Stellingen

behorende bij het proefschrift

A TIME-DOMAIN FINITE-ELEMENT METHOD FOR THE COMPUTATION OF THREE-DIMENSIONAL ACOUSTIC WAVE FIELDS IN INHOMOGENEOUS FLUIDS AND SOLIDS

Hans Stam

Delft, 21 juni 1990

1. Voor het berekenen van akoestische golfvelden in sterk inhomogene media is de eindige-elementenmethode zoals beschreven in dit proefschrift, wanneer optimaal geprogrammeerd, een belangrijke concurrent voor de bestaande eindige-elementenmethoden die slechts van continue benaderingen van de onbekende veldgrootheden gebruik maken.

   Dit proefschrift, hoofdstuk 13.

2. Bij het toepassen van het reciprociteitstheorema voor de numerieke oplossing van golfproblemen geeft substitutie van testvelden met bronnen waarvan de drager gelijk is aan de grootte van de karakteristieke gebieden een even nauwkeurig resultaat als de substitutie van puntbronoplossingen als testvelden. De eerstgenoemde testvelden hebben als voordeel, dat de resulterende veldgrootheden overal begrensd zijn, zodat de numerieke problemen die bij de substitutie van puntbronoplossingen bestaan, worden vermeden.

3. Voor het testen van de nauwkeurigheid van een numerieke methode is het van wezenlijk belang over een niet-triviaal testprobleem uit de categorie waarop de numerieke methode van toepassing is te beschikken, waarvan de oplossing langs onafhankelijke (bij voorkeur analytische) weg bekend is.

4. De methode van Cagniard en De Hoop voor het oplossen van gepulste golfproblemen, die doorgaans op golven geëxciteerd door puntbronnen is toegepast, is gemakkelijk uit te breiden tot het geval van excitatie door uitgebreide bronnen.

   Stam, H.J., The two-dimensional elastodynamic distributed surface load problem, accepted for publication in Wave Motion, Vol. 12, 1990 (zie ook dit proefschrift, hoofdstuk 11).

5. De systematiek van de in dit proefschrift beschreven eindige-elementenmethode is ook van toepassing op n-dimensionale eindige- elementenmethoden met $n > 3$. Daarbij wordt het rekengebied opgedeeld in simplices in R^n en worden de onbekende grootheden in deze simplices lineair geïnterpoleerd tussen hun waarden in de hoekpunten.

6. De uitbreiding van de in dit proefschrift beschreven eindige-elementen methode tot een gekoppelde ruimte-tijdeindige-elementenformulering van akoestische golfproblemen in sterk inhomogene, in de tijd veranderende media is niet mogelijk, omdat er geen voorwaarden voor de continuiteit van de golfgrootheden door vlakken van discontinuiteit in de media-eigenschappen in het gediscretiseerde ruimte-tijdgebied bekend zijn.

7. De werking van alternatieve geneeswijzen dient te worden aangetoond met behulp van statistische methoden en niet met de aanname van vage niet-meetbare structuren (zoals het bestaan van meridianen in de acupunctuur of de werking die een stof volgens het model van Barnard (1965) in de homoeopathie nog bij zeer sterke verdunning kan hebben).

   P. van Dijk, Geneeswijzen in Nederland en Vlaanderen, 1986, 7de druk, pp. 25-46 (acupunctuur) en pp. 143-164 (homoeopathie).

8. Aangezien de huidige promovendi geen tijd hebben om zich naast het gebied waarop hun promotieonderwerp betrekking heeft nog op andere gebieden van de cultuur goed te ontwikkelen, is de eis dat zij tenminste zes stellingen aan hun proefschrift toevoegen die niet op het onderwerp van het proefschrift betrekking hebben, uit de tijd. Deze eis dient dan ook te vervallen.

9. Op beginnersniveau is de linkshandige badmintonspeler in het voordeel ten op zichte van de rechtshandige.

10. Bij het schaken is de openingszet 1.d4 sterker dan 1.e4.

    Bondsdorff, E., Fabel, K., Riihimaa, O., 1971. Schach und Zahl, Walter Rau Verlag, Düsseldorf, tweede druk.

11. Aangezien bij het bridgen de kans op een gelijkmatige verdeling van de kaarten, wanneer met de hand geschud, groter is dan wanneer deze aselect verdeeld zijn, verdient het aanbeveling agressiever te bieden dan in de leerboeken - die van de aselecte verdeling uitgaan - wordt aangegeven.

    Sint, C. en Schipperheyn, T., 1985, Het moderne Acol boek, Elsevier, Amsterdam.

12. De invoering van het 'Keep-your-lane'systeem verhoogt de verkeersveiligheid op autosnelwegen en zou daarom ook in Nederland ingevoerd moeten worden.

    Verkeerskunde 41, 1989, nr.3, p. 101.

A Time-Domain Finite-Element Method for the Computation of Three-Dimensional Acoustic Wave Fields in Inhomogeneous Fluids and Solids

H.J. Stam

A Time-Domain Finite-Element Method for the Computation of Three-Dimensional Acoustic Wave Fields in Inhomogeneous Fluids and Solids

Proefschrift

ter verkrijging van de graad van doctor aan de
Technische Universiteit Delft, op gezag van
de Rector Magnificus, Prof. drs. P.A. Schenck,
in het openbaar te verdedigen ten overstaan van
een commissie aangewezen door het College van Dekanen
op donderdag 21 juni 1990 te 14.00 uur

door

Hendrik Johannes Stam

geboren te 's-Gravenhage

wiskundig ingenieur

Dit proefschrift is goedgekeurd door de promotor
prof. dr. ir. A.T. de Hoop

aan Janke

The research presented in this thesis has been sponsored through a Research Grant from Royal/Dutch Shell Exploration and Production Laboratories, Rijswijk, the Netherlands. This financial support is gratefully acknowledged.

Voorkant: Annelies Alewijnse

Contents

Chapter 1

INTRODUCTION

The computational modeling of acoustic wave problems has numerous applications. As examples we mention: exploration geophysics, acoustic imaging for medical purposes, and non-destructive evaluation of mechanical structures. In all these applications one is interested in space-time acoustic wave phenomena in strongly inhomogeneous, and possibly anisotropic, fluids and solids, and the quantitative evaluation of the quantities that characterize the wave motion (the scalar traction in fluids, the stress in solids and the particle velocities in both of these media) is the ultimate goal. For simple configurations, such as the geometries that comply with coordinate systems in which the governing acoustic wave equations are separable, analytical solutions to wave propagation and scattering problems can be constructed (Pao and Mow 1973); for more complicated configurations, however, it is necessary to turn to numerical methods. One of the numerical methods that is known for its simplicity is the finite-difference method. Finite-difference discretizations of the second-order elastodynamic wave equation in two spatial dimensions that are explicit in time have been given by Alterman and Loewenthal (1972), Boore (1972), and Kelly et al. (1976). Emerman, Schmidt and Stephen (1982) and Virieux (1984; 1986) have solved the coupled first-order elastodynamic wave equations in two dimensions numerically with the aid of both an implicit and an explicit finite-difference method as far as the time coordinate is concerned. Although the finite-difference method with its coordinate-line grid structure has the advantage of its simplicity, it has difficulties with taking into account arbitrarily shaped boundaries and interfaces of discontinuity in the mechanical properties that do not comply with

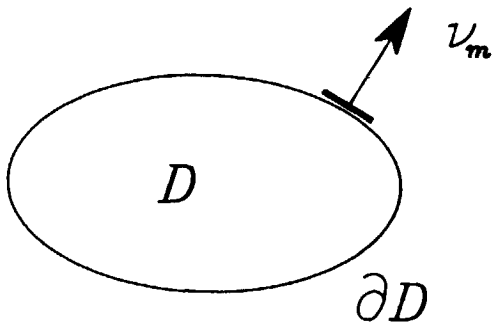

Figure 1.1: The bounded domain D of computation with boundary ∂D and unit vector along the outward normal ν_m.

the prevailing grid (see, for example, Boore 1972; Ilan et al. 1975; Ilan and Loewenthal 1976; Ilan 1978; and Kummer and Behle 1982). Now, arbitrarily oriented boundaries and interfaces can be handled without difficulty by the more intricate finite-element method, which is not restricted to a particular grid structure. Finite-element solutions of elastodynamic wave problems have been given by Smith (1975), and Smith and Bolt (1976). Further, in the work of Marfurt (1984) a comparison between the finite-element and the finite-difference methods has been given in the solution of scalar wave problems and elastodynamic wave problems.

Because of the limitations on computer storage capacity and computation time, one has to restrict, both in the finite-difference and in the finite-element method, the domain of the numerical computation in size as much as possible. Now, for a solution of the wave problem in some bounded domain D (see Figure 1.1) to be unique, conditions at the boundary ∂D of D are required in addition to the partial differential equations that hold in D. To compute wave motions that have not progressed yet that far from the sources that generate them, appropriate zero-value boundary conditions suffice, provided that

∂D is chosen outside the region where the wave motion has penetrated thus far. Admissible zero-value boundary conditions are either of the Dirichlet or the Neumann type. The distinction is as follows. For the Neumann-type boundary condition the normal component of the particle velocity is prescribed on that part of the boundary that is adjacent to a fluid and the traction is prescribed on that part of the boundary that is adjacent to a solid; for the Dirichlet-type boundary condition the scalar traction is prescribed on that part of the boundary that is adjacent to a fluid, while the particle velocity is prescribed on that part of the boundary that is adjacent to a solid. In most cases, the domain of computation D becomes, for such a procedure to apply, prohibitively large. Consequently, the domain D has to be smaller and one has to take into account that the wave motion has reached ∂D and that across ∂D acoustic radiation takes place away from D. The type of boundary condition that models this radiation into an unbounded exterior domain with known, simple acoustic properties is an important subject of present theoretical research. Some aspects of this are discussed below.

To construct boundary conditions that model the radiation of waves across ∂D away from D, the domain D of computation is embedded in a surrounding medium, the embedding, whose properties are so simple that its Green's function can be constructed by analytical methods. This enables us to make use of the corresponding surface-source or contrast volume-source integral representations of the wave field in the embedding. The surface-source integral representations of the acoustic wave field in the embedding, with the sources located on ∂D, produce boundary integral equations upon taking the points of observation on ∂D, while upon taking in them the point of observation in the interior of D, the Oseen extinction theorem leads to the null-field condition. Both types of integral relations yield (non-local) relations between the (scalar) traction and the particle velocity at the boundary ∂D. The discretization of these relations can provide the basis for the construction of non-local absorbing boundary conditions that can be used in the finite-element scheme. The difficulty with the boundary integral equations is that the Green's functions occurring in them have singularities in the point where the integration point coincides with the point of observation; these singularities have to be handled analytically. The null-field

condition has no such difficulty, but here the arbitrariness of the points at which it is invoked yields a problem.

Another way to arrive at an absorbing boundary condition is to represent the acoustic wave field quantities on ∂D by a volume integral that contains the contrast volume-source densities with respect to the embedding in D, where the latter differ from zero in any subdomain where the medium in D differs in properties from the one in the embedding. This representation relates the wave field quantities on ∂D to those in the domain D. Taking ∂D at some distance from the contrast sources in D, the singular points in the Green's function in the volume integral representations are avoided. Again, the relations yield a basis for non-local absorbing boundary conditions.

The methods described above discuss exact integral relations between the acoustic wave field quantities at the boundary ∂D of D (arising from the boundary integral equations) or between the ones at the boundary ∂D and those in the interior of D (arising from the contrast volume-source integral representations). Non-local boundary conditions to be used in the computational method then could follow upon discretizing these relations. However, the singularity of the Green's functions involved may present difficulties in this discretization. To circumvent these difficulties we make use of another procedure that can equally well be argued to approximate the relations that mutually exist between the wave field values at ∂D or exist between the wave field values at the boundary ∂D and those in the interior of D. The basis for the analysis lies in the application of the acoustic space-time reciprocity theorem of the time-convolution type to the discretized version $[D]$ of D and its embedding D_0. In a reciprocity theorem of this kind two states occur that can be present in one and the same domain in space-time. We identify one of the states with the actual acoustic wave field, while the other is regarded as a computational one that remains to be chosen appropriately. For the sources that occur in the computational state, a sequence of localized source distributions is chosen that are defined in $[D]$. Each of them has as its support one of the elementary regions into which D is discretized. The computational state has, like the actual wave field, no sources in the embedding D_0. For the medium properties in D and D_0 of the computational state the ones of the embedding are taken. The corresponding wave field quantities that

are related to the localized source distribution in a medium like the embedding are our discretized Green's functions. It is assumed that these can be calculated analytically. Substitution of these choices for the computational state in the reciprocity theorem yields relationships between the values of the acoustic wave field quantities weighted over each of the supports of the localized sources, and the contrast and generating sources in $[D]$. These relations serve as the non-local boundary conditions for our finite-element method. Due to the finite magnitude of the localized source solutions (discretized Green's functions) in the embedding, no difficulties of the type that would be met in the discretization of the exact integral relations for the acoustic wave field quantities occur.

The combination of two solution methods, a finite-difference or a finite-element one for the bounded domain with an intricate medium and an analytical one for the simple embedding, is known as a hybrid method. Wilton (1978) computes the acoustic radiation and scattering of a submerged elastic structure by combining a finite-element method with a mixed form of the boundary integral-equation method and the null-field method. Murakami et al. (1981) have presented a scheme that combines a finite-element method with a null-field method for the computation of time-harmonic elastodynamic waves. Van den Berg (1987) has solved two-dimensional SH-wave problems in the frequency domain by using a hybrid method that combines a finite-element formulation with a boundary integral-equation method.

In the present monograph, a hybrid method is presented that solves numerically space-time acoustic wave problems in a configuration that may consist of fluid and solid parts. The fluids and solids are taken to be linear, locally and instantaneously reacting, and time invariant in their mechanical behavior. In some bounded domain D^{SC} the medium is arbitrarily inhomogeneous and anisotropic. The embedding of this domain is a fluid or a solid whose properties are so simple that its Green's function can be constructed by analytical methods. The fluid-domain acoustic wave fields are characterized by their particle velocity and their scalar traction; the solid-domain acoustic wave fields are characterized by their particle velocity and their stress; these quantities are regarded as the fundamental state variables and will henceforth be referred to as the acoustic state quantities. We take the bounded domain of numerical computation D such

that $D^{SC} \subset D$. The computation of the wave fields in D is carried out by a finite-element method that is suited to handle, in particular, the conditions at arbitrarily shaped boundaries and interfaces of the solid/solid, fluid/fluid and the solid/fluid types.

In a number of engineering problems, mostly of the static, i.e., time-independent, type, the finite-element method can be based on a variational principle (Reddy 1987, p.258; Zienkiewicz and Taylor 1989, p.32). Such a principle states that the solution of the problem is a stationary point of a judiciously constructed functional (for example, the minimum of the potential energy stored in the system). For problems for which no variational principle is available, the methods of weighted residuals is commonly employed to lead to a finite-element formulation (Reddy 1987, p.287; Zienkiewicz and Taylor 1989, p.210). In our approach we shall use an acoustic space-time reciprocity theorem of the time-correlation type (De Hoop 1988; De Hoop and Stam 1988) as point of departure. In such a reciprocity theorem two acoustic states occur that can be present in one and the same domain in space-time. One of the states is identified with the actual acoustic wave field for which a numerical approximation is to be constructed, while the other is regarded as a computational one that remains to be chosen appropriately. Particular choices for the computational states are shown to lead to a formulation that is equivalent to a certain weighting procedure applied to the first-order equations that govern the wave motion, i.e., the equation of motion and the deformation rate equation. Next, particular local representations for the acoustic wave field are developed that are typically adapted to handle the conditions at interfaces in strongly inhomogeneous structures.

In view of the time invariance of the configuration in which the wave field occurs, we discretize the geometry into elementary subdomains that are cylindrical in the time direction in four-dimensional space-time. In three-dimensional space we take the tetrahedron as the elementary subdomain (see Figure 1.2). With this choice, the discretized geometry consists of prisms in space-time. In accordance with this, the local expansion functions are taken to be the product of a function of space and a function of time. The vertices of the tetrahedra form the nodes of the spatial discretization. In each vertex of a tetrahedron that coincides with a nodal point that is not on an interface (a 'simple' node),

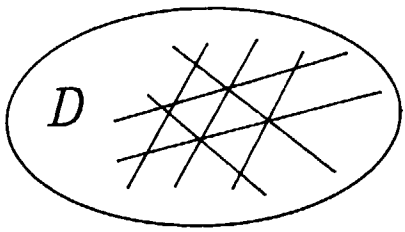

Figure 1.2: The spatial discretization of the domain D of computation into a union of tetrahedra.

the vectorial and tensorial state quantities are represented through their components with respect to the chosen Cartesian background reference frame. In each vertex of a tetrahedron that coincides with a nodal point that is on an interface (a 'multiple' node), the vectorial and tensorial state quantities that are continuous across this interface are again represented through their components with respect to the chosen Cartesian background reference frame while the ones that have one or more components that may jump by finite amounts across this interface are represented with respect to appropriate local base vectors. The directions of these local base vectors are chosen such that in the resulting representations of the state quantities, the continuity conditions at the interfaces are satisfied exactly (i.e., in machine precision).

For a unique (numerical) solution of the wave problem in the inhomogeneous and anisotropic bounded domain of computation D we need boundary conditions at its outer boundary ∂D. In our hybrid method we represent the state quantities on ∂D by integral representations containing the "discretized" Green's functions of the embedding and localized source distributions that represent the inhomogeneities in D. Suppose the embedding is a fluid, then we

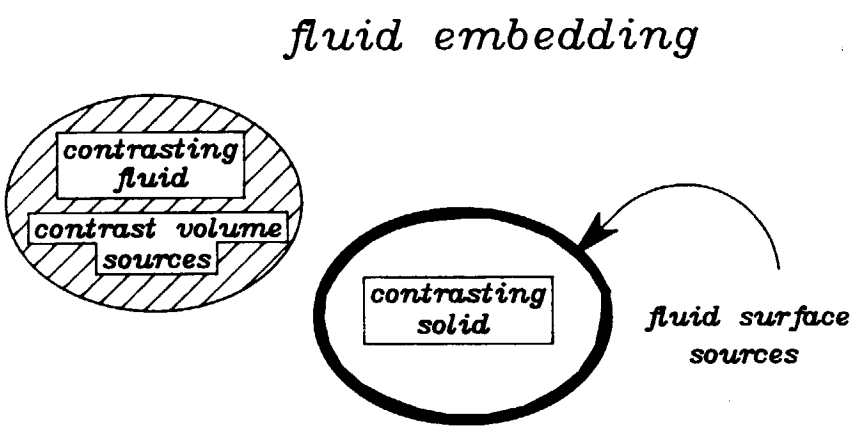

Figure 1.3: The contrast volume-sources and the fluid-type surface sources in the fluid embedding.

define in the fluid parts of D^{SC} contrast volume sources that are non-zero in those subdomains where the fluid properties show a contrast with respect to the embedding. Because the action of the solid parts in D^{SC} cannot be given in the form of fluid contrast volume sources, it is represented by fluid-type surface sources at the fluid/solid interfaces (see Figure 1.3). If the embedding is a solid, we define in the solid parts of D^{SC} contrast volume-sources that are non-zero in those subdomains where the solid properties show a contrast with respect to the embedding and the action of the fluid parts in D^{SC} are modeled by solid-type surface sources at the solid/fluid interfaces (see Figure 1.4). The relevant integral representations follow from the acoustic space-time reciprocity theorems of the time-convolution type (De Hoop 1988; De Hoop and Stam 1988) upon

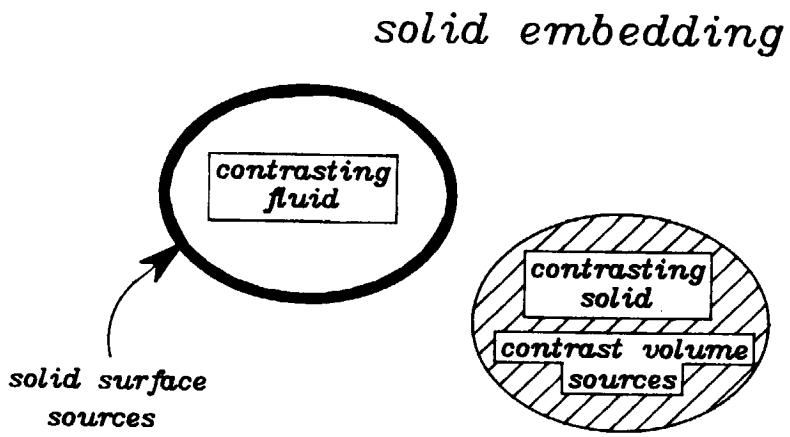

Figure 1.4: The contrast volume-sources and the solid-type surface sources in the solid embedding.

choosing in these theorems computational states that correspond to appropriate localized source distributions (the "discretized" Green's functions) of the embedding, which for a homogeneous embedding can be constructed analytically (De Hoop 1958; Achenbach 1973; De Hoop 1984; De Hoop 1985). In the implementation there is no need to put the boundary at some distance from the contrast sources since the discretized Green's functions are no longer singular. Supplemented with these relations, the finite-element method produces a unique solution of the wave problem in the domain D of computation. To determine the acoustic wave field in the embedding, we subsequently employ the surface- and volume-source integral representation, using the now known values of the acoustic wave fields at the boundaries of the surface sources and in the contrast volume-source densities.

Chapter 2

BASIC EQUATIONS OF ACOUSTICS

In this chapter the basic equations of low-velocity linearized acoustics are summarized. In the linear theory of acoustic waves, it is presupposed that the convective term in the co-moving time derivatives occurring in the equations can be neglected and that the media are linear in their acoustic behavior (Achenbach 1973).

The position of observation in three-dimensional space R^3 is specified by the coordinates $\{x_1, x_2, x_3\}$ with respect to a fixed, orthogonal, Cartesian reference frame with origin O and the three mutually perpendicular base vectors $\{\boldsymbol{i}_1, \boldsymbol{i}_2, \boldsymbol{i}_3\}$ of unit length each. In the indicated order the base vectors form a right-handed system. The subscript notation for Cartesian vectors and tensors in R^3 is employed and the summation convention applies. The corresponding lower-case Latin subscripts are to be assigned the values $1, 2, 3$. Whenever appropriate, the position vector will be denoted by $\boldsymbol{x} = x_p \boldsymbol{i}_p$. The time coordinate is denoted by t. Partial differentiation is denoted by ∂; ∂_p denotes differentiation with respect to x_p; ∂_t is a reserved symbol for differentiation with respect to t. The symbols $\cap$ and $\cup$ are used to denote the intersection and the union of sets, respectively, while $D_1 \subset D_2$ denotes that D_1 is a proper subset of D_2. SI-units are used throughout.

The geometrical configuration that we study is taken to be time invariant. The fluids and solids present in it are assumed to be linear, locally and instantaneously reacting, and time invariant in their mechanical behavior. They may

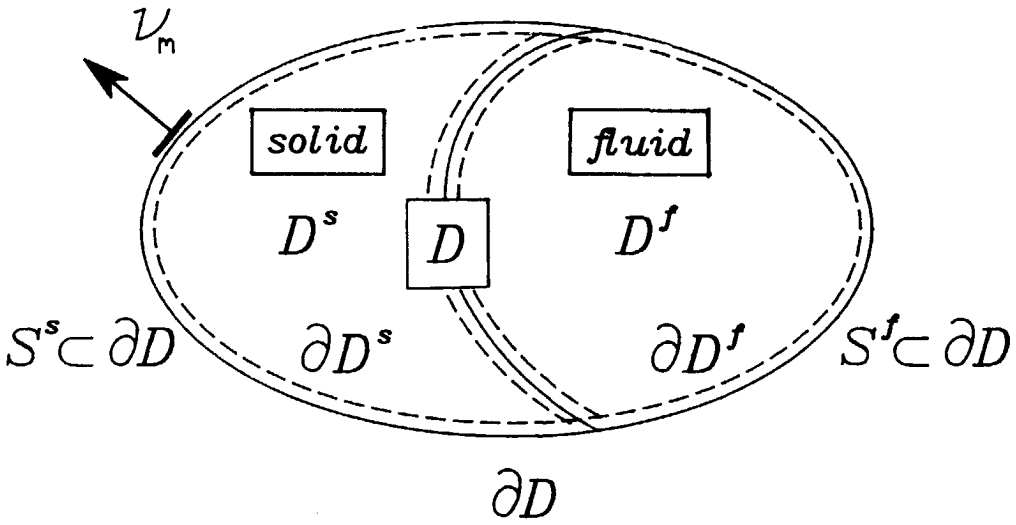

Figure 2.1: Domain D consisting of the subdomains D^s and D^f, respectively, with closed outer boundary ∂D, and its outwardly directed unit normal vector ν_m. The part of ∂D in the solid is denoted by S^s and the part of ∂D in the fluid by S^f; ∂D^s is the closed boundary of D^s, ∂D^f is the closed boundary of D^f.

be arbitrarily inhomogeneous and anisotropic. Let the configuration occupy the bounded domain $D \subset R^3$, and let D^s be the subdomain of D occupied by the solid and D^f the subdomain of D occupied by the fluid. The boundary of D is denoted by ∂D; the part of ∂D in the fluid is denoted by S^f and the part of ∂D in the solid by S^s (Figure 2.1). The closed boundary of D^s is ∂D^s and the closed boundary of D^f is ∂D^f . The acoustic wave field in the domain D^s occupied by the solid is characterized by its solid particle velocity v_r and its stress τ_{pq}. The physical properties of the solid are characterized by its tensorial volume density of solid mass ρ^s_{kr} (Lord Rayleigh 1899; Bromwhich 1902) and its compliance s_{ijpq} (the inverse of its stiffness). In each subdomain of D^s where the acoustic properties vary continuously with position, the acoustic wave field quantities are continuously differentiable and satisfy the (linearized) equation of

motion (Love 1944, Achenbach 1973, Aki and Richards 1980)

$$-\Delta_{kmpq}\partial_m\tau_{pq} + \rho^s_{kr}\partial_t v_r = f^s_k, \tag{2.1}$$

and the (linearized) deformation rate equation

$$\Delta_{ijmr}\partial_m v_r - s_{ijpq}\partial_t\tau_{pq} = h_{ij}, \tag{2.2}$$

in which

v_r = solid particle velocity (m/s),
τ_{pq} = solid stress (Pa),
ρ^s_{kr} = tensorial volume density of solid mass (kg/m^3),
s_{ijpq} = compliance (Pa^{-1}),
f^s_k = volume source density of solid force (N/m^3),
h_{ij} = volume source density of strain rate (s^{-1}).

Here, $\Delta_{kmpq} = (\delta_{kp}\delta_{mq} + \delta_{kq}\delta_{mp})/2$ is the unit tensor of rank four that specifically occurs in elastodynamics (δ_{kp} is the Kronecker tensor: $\delta_{kp} = 1$ if $k = p$ and $\delta_{kp} = 0$ if $k \neq p$); it has the symmetry properties $\Delta_{kmpq} = \Delta_{mkpq} = \Delta_{mkqp} = \Delta_{kmqp}$ and $\Delta_{kmpq} = \Delta_{pqkm}$, and it selects out of any tensor of rank two with which it is contracted, the symmetrical part. Thus

$$\Delta_{kmpq}\tau_{pq} = (\tau_{km} + \tau_{mk})/2 \quad \text{and} \quad \Delta_{ijmr}\partial_m v_r = (\partial_i v_j + \partial_j v_i)/2. \tag{2.3}$$

The compliance accounts for the, possibly anisotropic, elastic properties of the medium. The latter is related to the stiffness c_{ijpq} in the following way (Herman 1981):

$$c_{ijkl}s_{klpq} = \Delta_{ijpq}. \tag{2.4}$$

The tensorial volume density of solid mass accounts for the anisotropy in the inertia properties of the solid (Bromwich 1902). For an isotropic medium, the tensorial volume density of solid mass reduces to

$$\rho^s_{kr} = \rho^s\delta_{kr}, \tag{2.5}$$

where

ρ^s = scalar volume density of solid mass (kg/m^3),

and the compliance to

$$s_{ijpq} = \Lambda\delta_{ij}\delta_{pq} + 2M\Delta_{ijpq}, \tag{2.6}$$

where Λ and M are two scalar coefficients. The corresponding stiffness is commonly written as (Achenbach 1973)

$$c_{pqij} = \lambda\delta_{pq}\delta_{ij} + 2\mu\Delta_{pqij}, \tag{2.7}$$

where

λ, μ = Lamé coefficients (Pa).

From (2.6) and (2.7) it follows that the coefficients Λ and M are related to the Lamé coefficients through (Achenbach 1973, Herman 1981)

$$\Lambda = -\lambda[2\mu(3\lambda + 2\mu)]^{-1}, \quad M = (4\mu)^{-1}, \tag{2.8}$$

and

$$\lambda = -\Lambda[2M(3\Lambda + 2M)]^{-1}, \quad \mu = (4M)^{-1}. \tag{2.9}$$

The quantities ρ^s_{kr}, s_{ijpq} and c_{pqij} are referred to as the constitutive coefficients of the solid. They are assumed to be independent of time. In a (sub)domain of the solid where they vary with position, the solid is inhomogeneous or heterogeneous; in a (sub)domain where they are constant, the medium is homogeneous. At interfaces between two different solids the constitutive coefficients in general jump by finite amounts. In all applications that we consider we shall assume that at a solid/solid interface the media are rigidly bonded (neither rupture of nor mixing between the media takes place); then, the solid particle velocity and the solid traction are continuous across the interface. Let $\boldsymbol{\nu} = \nu_m \boldsymbol{i}_m$ denote a unit vector normal to the interface at the position $\boldsymbol{x}$ on the interface, then we have (Figure 2.2)

$$\lim_{h\uparrow 0} v_r(\boldsymbol{x} + h\boldsymbol{\nu}, t) = \lim_{h\downarrow 0} v_r(\boldsymbol{x} + h\boldsymbol{\nu}, t) \text{ for all } t, \tag{2.10}$$

and

$$\lim_{h\uparrow 0} t_k(\boldsymbol{x} + h\boldsymbol{\nu}, t) = \lim_{h\downarrow 0} t_k(\boldsymbol{x} + h\boldsymbol{\nu}, t) \text{ for all } t, \tag{2.11}$$

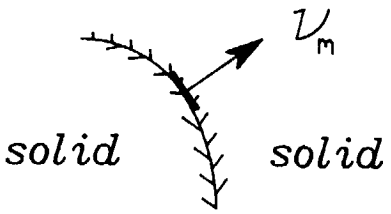

Figure 2.2: Solid/solid interface with unit normal vector ν_m.

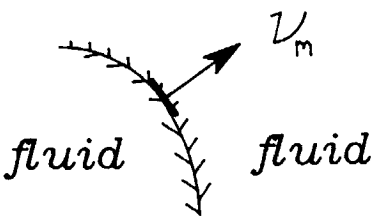

Figure 2.3: Fluid/fluid interface with unit normal vector ν_m.

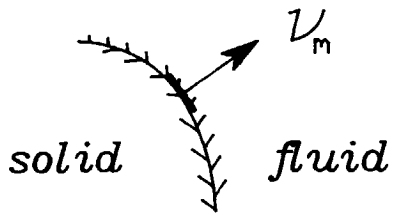

Figure 2.4: Fluid/solid interface with unit normal vector ν_m pointing away from the solid.

where the solid traction t_k is defined as

$$t_k = \Delta_{kmpq}\nu_m\tau_{pq}. \tag{2.12}$$

The acoustic wave field in the domain D^f occupied by the fluid is characterized by its fluid particle velocity w_k and its scalar fluid traction σ (the opposite of the pressure). The physical properties of the fluid are characterized by its tensorial volume density of fluid mass ρ^f_{kr} (Lord Rayleigh 1899) and its compressibility κ. In each subdomain of D^f where the acoustic properties vary continuously with position, the acoustic wave field quantities are continuously differentiable and satisfy the (linearized) equation of motion (Lamb 1957)

$$-\delta_{km}\partial_m\sigma + \rho^f_{kr}\partial_t w_r = f^f_k \tag{2.13}$$

and the (linearized) deformation rate equation

$$\delta_{mr}\partial_m w_r - \kappa\partial_t\sigma = q, \tag{2.14}$$

in which

w_r = fluid particle velocity (m/s),
σ = scalar fluid traction (Pa),
ρ^f_{kr} = tensorial volume density of fluid mass (kg/m^3),
κ = compressibility (Pa^{-1}),
f^f_k = volume source density of fluid force (N/m^3),
q = volume density of injection rate (s^{-1}).

Although (2.13) and (2.14) could be written in a simpler manner (note that $\delta_{km}\partial_m = \partial_k$), we have for reasons of symmetry with the acoustic equations for a solid retained in the first term on the left-hand side the Kronecker tensor. The inverse of the compressibility κ is denoted as the modulus of compression K, i.e. (Herman 1981),

$$\kappa K = 1. \tag{2.15}$$

The tensorial volume density of fluid mass acounts for anisotropy in the inertia properties of the fluid. For an isotropic fluid, the tensorial volume of mass reduces to

$$\rho^f_{kr} = \rho^f \delta_{kr}, \tag{2.16}$$

where

ρ^f = scalar volume density of fluid mass (kg/m^3).

The quantities ρ^f_{kr}, κ and K are referred to as the constitutive coefficients of the fluid. They are assumed to be independent of time. In a (sub)domain where they vary with position, the fluid is inhomogeneous or heterogeneous; in a (sub)domain where they are constant, the fluid is homogeneous. At an interface between two different fluids the constitutive coefficients in general jump by finite amounts. Across a fluid/fluid interface the normal component of the fluid particle velocity and the scalar fluid traction are continuous, i.e., at each point $\boldsymbol{x}$ of a fluid/fluid interface we have (Figure 2.3)

$$\lim_{h \downarrow 0} \nu_r w_r(\boldsymbol{x} + h\boldsymbol{\nu}, t) = \lim_{h \downarrow 0} \nu_r w_r(\boldsymbol{x} + h\boldsymbol{\nu}, t) \text{ for all } t, \tag{2.17}$$

and

$$\lim_{h \downarrow 0} \sigma(\boldsymbol{x} + h\boldsymbol{\nu}, t) = \lim_{h \downarrow 0} \sigma(\boldsymbol{x} + h\boldsymbol{\nu}, t) \text{ for all } t, \tag{2.18}$$

Table 2.1: The admissible explicit boundary conditions on ∂D.

part of exterior boundary surface	adjacent to	prescribed value of	type of boundary-value problem
S_1^f	fluid	scalar traction	Dirichlet
S_2^f	fluid	normal velocity	Neumann
S_1^s	solid	velocity	Dirichlet
S_2^s	solid	traction	Neumann

where $\boldsymbol{\nu} = \nu_m \boldsymbol{i}_m$ is a unit vector along the normal to the fluid/fluid interface at the point $\boldsymbol{x}$.

The last type of interface that can occur in the configuration is a fluid/solid interface. Across such an interface the normal component of the fluid particle velocity is equal to the normal component of the solid particle velocity and the scalar fluid traction equals the normal component of the solid traction, while the tangential component of the solid traction is equal to zero, i.e., at each point $\boldsymbol{x}$ of a fluid/solid interface we have (Figure 2.4)

$$\lim_{h \downarrow 0} \nu_r v_r(\boldsymbol{x} + h\boldsymbol{\nu}, t) = \lim_{h \downarrow 0} \nu_r w_r(\boldsymbol{x} + h\boldsymbol{\nu}, t) \text{ for all } t, \tag{2.19}$$

$$\lim_{h \downarrow 0} \nu_k t_k(\boldsymbol{x} + h\boldsymbol{\nu}, t) = \lim_{h \downarrow 0} \sigma(\boldsymbol{x} + h\boldsymbol{\nu}, t) \text{ for all } t, \tag{2.20}$$

and

$$\lim_{h \downarrow 0} [t_k(\boldsymbol{x} + h\boldsymbol{\nu}, t) - \nu_k \nu_q t_q(\boldsymbol{x} + h\boldsymbol{\nu}, t)] = 0 \text{ for all } t, \tag{2.21}$$

where $\boldsymbol{\nu} = \nu_m \boldsymbol{i}_m$ is a unit vector along the normal to the fluid/solid interface at the point $\boldsymbol{x}$ pointing away from the solid.

For a solution of the acoustic wave problem in a bounded configuration D (Figure 2.1) to be unique, the acoustic wave equations and the interface conditions must be supplemented by boundary conditions at ∂D. Admissible boundary conditions of the explicit type are presented in Table 2.1 (see also Figure 2.5).

As far as the time dependence is concerned, only causal solutions of the differential equations (2.1)-(2.2) and (2.13)-(2.14) are physically acceptable, i.e., the acoustic wave motion must be causally related to the action of the sources. Assuming that the sources start to act at the instant $t = t_0$, the causality of

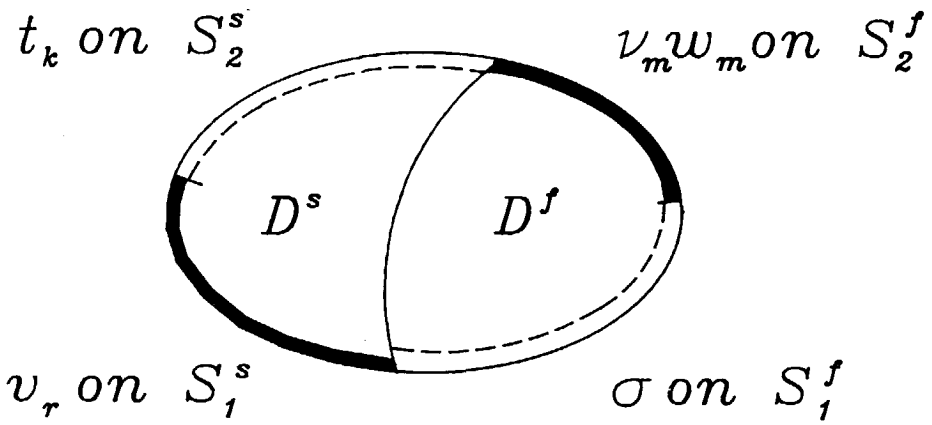

Figure 2.5: The four types of explicit boundary conditions prescribed at the different parts of the outer boundary ∂D.

the wave motion is ensured by putting the values w_r, σ, v_r and τ_{pq} equal to zero when $t < t_0$. To account for the possible action of other sources that were active up to the instant t_0, we can introduce the initial conditions

$$v_r(\boldsymbol{x}, t_0) = v_r^I(\boldsymbol{x}), \text{ and } \tau_{pq}(\boldsymbol{x}, t_0) = \tau_{pq}^I(\boldsymbol{x}) \text{ for } \boldsymbol{x} \in D^s \tag{2.22}$$

and

$$w_r(\boldsymbol{x}, t_0) = w_r^I(\boldsymbol{x}), \text{ and } \sigma(\boldsymbol{x}, t_0) = \sigma^I(\boldsymbol{x}) \text{ for } \boldsymbol{x} \in D^f. \tag{2.23}$$

In most of our applications we start from a medium at rest, in which case the right-hand sides of (2.22) and (2.23) vanish.

Uniqueness

To prove the uniqueness of the solution of the acoustic wave problem in the bounded domain D, subject to the boundary conditions of Table 2.1 at ∂D and the initial conditions of (2.22)-(2.23), we make use of the energy balance associated with the linearized acoustic wave equations, viz. (Achenbach 1973)

$$P + \partial_t(W_{\text{kin}} + W_{\text{def}}) = \dot{W}, \tag{2.24}$$

where

$$P = -\int_{\boldsymbol{x} \in S^s} \Delta_{mrpq} \nu_m v_r \tau_{pq} dA - \int_{\boldsymbol{x} \in S^f} \delta_{mk} \nu_m w_k \sigma dA \tag{2.25}$$

is the acoustic power flow across the boundary ∂D away from D,

$$W_{\text{kin}} = \int_{\boldsymbol{x} \in D^s} (1/2) v_k \rho_{kr}^s v_r dV + \int_{\boldsymbol{x} \in D^f} (1/2) w_k \rho_{kr}^f w_r dV \tag{2.26}$$

is the kinetic energy associated with the wave motion in D,

$$W_{\text{def}} = \int_{\boldsymbol{x} \in D^s} (1/2) \tau_{ij} s_{ijpq} \tau_{pq} dV + \int_{\boldsymbol{x} \in D^f} (1/2) \sigma \kappa \sigma dV \tag{2.27}$$

is the complementary energy (=elastic deformation energy for the linear medium) of the wave motion stored in the material in D, and

$$\dot{W} = \int_{\boldsymbol{x} \in D^s} (f_k^s v_k - h_{ij} \tau_{ij}) dV + \int_{\boldsymbol{x} \in D^f} (f_k^f w_k - q\sigma) dV \tag{2.28}$$

is the time rate at which work is done by the sources present in D. Equation (2.24) follows from (2.1)-(2.2) and (2.13)-(2.14) under the condition that both the volume densities of mass in the fluid and in the solid and the compliance

are symmetrical tensors, i.e., $\rho^f_{kr} = \rho^f_{rk}$, $\rho^s_{kr} = \rho^s_{rk}$ and $s_{ijpq} = s_{pqij}$. For W_{kin} and W_{def} actually to represent stored energies, they must be positive for any non-vanishing wave field; hence ρ^f_{kr}, ρ^s_{kr} and s_{ijpq} must be symmetrical, positive definite tensors and κ is a positive scalar.

For the uniqueness proof we assume the existence of at least one solution that satisfies the equations (2.1)-(2.2), (2.13)-(2.14), the boundary conditions of Table 2.1, and the initial conditions (2.22)-(2.23); we denote this solution by the superscript I: $\{w^I_r, \sigma^I, v^I_r, \tau^I_{pq}\}$. Suppose there is a different solution to the problem that satisfies the same system of equations in D, the same boundary conditions at ∂D and the same initial conditions in D; we denote it by the superscript II : $\{w^{II}_r, \sigma^{II}, v^{II}_r, \tau^{II}_{pq}\}$. Then, because of the linearity of the wave problem, the difference field $\{w^\Delta_r, \sigma^\Delta, v^\Delta_r, \tau^\Delta_{pq}\} = \{w^I_r - w^{II}_r, \sigma^I - \sigma^{II}, v^I_r - v^{II}_r, \tau^I_{pq} - \tau^{II}_{pq}\}$ satisfies the equations (2.1)-(2.2), (2.13)-(2.14) with zero right-hand sides, the boundary conditions

$$\sigma^\Delta = 0 \quad \text{when } \boldsymbol{x} \in S^f_1, \tag{2.29}$$

$$\nu_r w^\Delta_r = 0 \quad \text{when } \boldsymbol{x} \in S^f_2, \tag{2.30}$$

$$v^\Delta_r = 0 \quad \text{when } \boldsymbol{x} \in S^s_1, \tag{2.31}$$

$$t^\Delta_r = 0 \quad \text{when } \boldsymbol{x} \in S^s_2, \tag{2.32}$$

and the initial conditions

$$\{w^\Delta_r(\boldsymbol{x}, t_0), \sigma^\Delta(\boldsymbol{x}, t_0)\} = 0 \quad \text{when } \boldsymbol{x} \in D^f, \tag{2.33}$$

$$\{v^\Delta_r(\boldsymbol{x}, t_0), \tau^\Delta_{pq}(\boldsymbol{x}, t_0)\} = 0 \quad \text{when } \boldsymbol{x} \in D^s. \tag{2.34}$$

Using these results in (2.24) we obtain

$$\begin{aligned} &\partial_t \int_{\boldsymbol{x} \in D^s} (1/2) v^\Delta_k \rho^s_{kr} v^\Delta_r \, dV + \partial_t \int_{\boldsymbol{x} \in D^f} (1/2) w^\Delta_k \rho^f_{kr} w^\Delta_r \, dV \\ &+ \partial_t \int_{\boldsymbol{x} \in D^s} (1/2) \tau^\Delta_{ij} s_{ijpq} \tau^\Delta_{pq} dV + \partial_t \int_{\boldsymbol{x} \in D^f} (1/2) \sigma^\Delta \kappa \sigma^\Delta dV = 0. \end{aligned} \tag{2.35}$$

Integrating (2.35) with respect to t, and using (2.33) and (2.34), we arrive at

$$\begin{aligned}
&\int_{\boldsymbol{x}\in D^s}(1/2)v_k^{\Delta}(\boldsymbol{x},t)\rho_{kr}^s(\boldsymbol{x})v_r^{\Delta}(\boldsymbol{x},t)dV \\
&+\int_{\boldsymbol{x}\in D^f}(1/2)w_k^{\Delta}(\boldsymbol{x},t)\rho_{kr}^f(\boldsymbol{x})w_r^{\Delta}(\boldsymbol{x},t)dV \\
&+\int_{\boldsymbol{x}\in D^s}(1/2)\tau_{ij}^{\Delta}(\boldsymbol{x},t)s_{ijpq}(\boldsymbol{x})\tau_{pq}^{\Delta}(\boldsymbol{x},t)dV \qquad (2.36)\\
&+\int_{\boldsymbol{x}\in D^f}(1/2)\sigma^{\Delta}(\boldsymbol{x},t)\kappa(\boldsymbol{x})\sigma^{\Delta}(\boldsymbol{x},t)dV=0 \quad \text{for all } t\geq t_0.
\end{aligned}$$

Now, for a non-vanishing difference wave field all the terms in (2.36) are positive. Hence, the energy identity (2.36) can only be satisfied if

$$\{w_r^{\Delta}(\boldsymbol{x},t),\sigma^{\Delta}(\boldsymbol{x},t)\}=0 \qquad \text{when } \boldsymbol{x}\in D^f \text{ for all } t>t_0, \qquad (2.37)$$

$$\{v_r^{\Delta}(\boldsymbol{x},t),\tau_{pq}^{\Delta}(\boldsymbol{x},t)\}=0 \qquad \text{when } \boldsymbol{x}\in D^s \text{ for all } t>t_0. \qquad (2.38)$$

Consequently, the initial assumption that $\{w_r^I,\sigma^I,v_r^I,\tau_{pq}^I\}$ and $\{w_r^{II},\sigma^{II},v_r^{II},\tau_{pq}^{II}\}$ were two non-identical solutions of the acoustic wave problem leads to a contradiction, and the solution to the problem, provided that it exists, is unique. This completes the proof.

The uniqueness of the acoustic wave problem is a prerequisite for the meaningfulness of the construction of analytical or numerical solutions to it. In this respect it is noteworthy that in many cases in practice the configuration does not contain a bounded closed surface on which explicit boundary values are given. Frequently, the configuration is of the scattering type where a certain strongly inhomogeneous configuration of bounded extent is embedded in a so-called "invariant embedding" (Bellman and Kalaba 1956). The properties of this embedding are taken to be relatively simple ones (for example, homogeneous and isotropic), such that the Green's functions (point-excitation solutions to the wave problem) can be constructed analytically. If such a model applies, the contrast-source formulation of the inhomogeneities with respect to the embedding leads to non-local boundary conditions on ∂D that force the scattered wave to radiate into the embedding. The corresponding initial/boundary value problem can, in this case, too, be shown to have a unique solution.

Chapter 3

SPACE-TIME ACOUSTIC RECIPROCITY THEOREM OF THE TIME-CONVOLUTION TYPE

In the present chapter we present the space-time acoustic reciprocity theorem of the time-convolution type on which part of our later analysis is based. A reciprocity theorem interrelates in a specific way two physical states that could be present in one and the same domain in space-time. In our case we have a relation between two acoustic wave fields. Their characteristic quantities are distinguished by the superscripts $'A'$ and $'B'$, respectively (Figure 3.1). The reciprocity theorems of the time-convolution type for acoustic waves in a fluid and in a solid have been derived in papers by De Hoop (1988) and De Hoop and Stam (1988), respectively. In them, also a historical survey of the development of these theorems is given. The fluid and solid configurations considered in these papers were time invariant and the media in them were linear, and instantaneously and locally reacting in their acoustic behaviour. Inhomogeneity, anisotropy, and arbitrary relaxation effects were included. For our instanteneously reacting fluids and solids we derive the reciprocity theorems in a simpler way. In a solid medium of the type specified in Chapter 2, the field quantities in State $'A'$ satisfy the equations (cf. (2.1) and (2.2))

$$-\Delta_{kmpq}\partial_m\tau_{pq}^{A}(\boldsymbol{x},t)+\rho_{kr}^{s,A}(\boldsymbol{x})\partial_t v_r^{A}(\boldsymbol{x},t)=f_k^{s,A}(\boldsymbol{x},t) \tag{3.1}$$

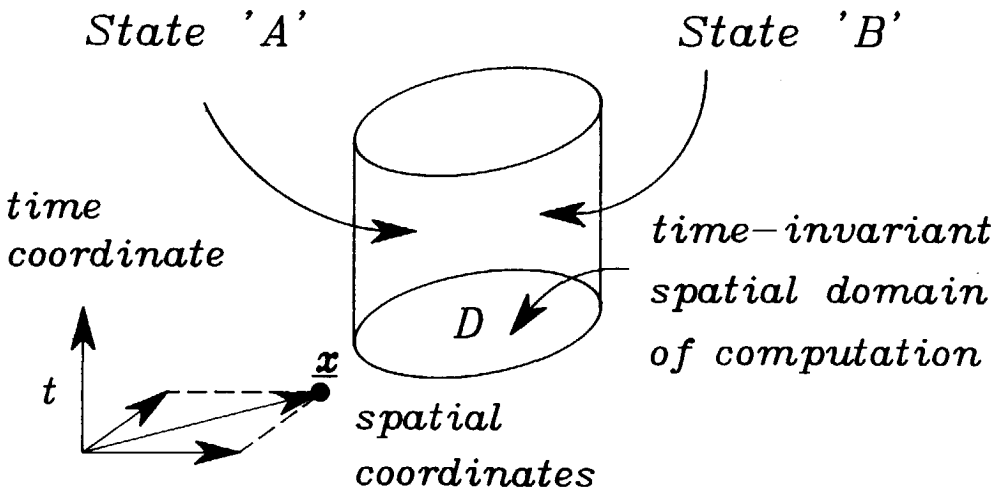

Figure 3.1: Space-time domain with the two admissible acoustic states 'A' and 'B'.

and

$$\Delta_{ijmr}\partial_m v_r^A(\boldsymbol{x},t) - s_{ijpq}^A(\boldsymbol{x})\partial_t \tau_{pq}^A(\boldsymbol{x},t) = h_{ij}^A(\boldsymbol{x},t), \tag{3.2}$$

and the quantities of the time-shifted and time-reversed field in State 'B' satisfy the equations (cf. (2.1) and (2.2))

$$-\Delta_{rmij}\partial_m \tau_{ij}^B(\boldsymbol{x},\tau-t) + \rho_{rk}^{s,B}(\boldsymbol{x})\partial_{\tau-t} v_k^B(\boldsymbol{x},\tau-t) = f_r^{s,B}(\boldsymbol{x},\tau-t) \tag{3.3}$$

and

$$\Delta_{pqmk}\partial_m v_k^B(\boldsymbol{x},\tau-t) - s_{pqij}^B(\boldsymbol{x})\partial_{\tau-t}\tau_{ij}^B(\boldsymbol{x},\tau-t) = h_{pq}^B(\boldsymbol{x},\tau-t). \tag{3.4}$$

As regards the space-time geometry in which the two admissible solid states occur, the time invariance implies that the geometry is the Cartesian product $D^s \times R$ of a time-invariant spatial domain $D^s \subset R^3$ where a solid medium is present, and the real axis R. The theorem will be derived for bounded domains D^s. The reciprocity theorem of the time-convolution type follows upon considering the interaction quantity

$$\int_{t\in R} \Delta_{mrpq}\partial_m [v_r^A(\boldsymbol{x},t)\tau_{pq}^B(\boldsymbol{x},\tau-t) - v_r^B(\boldsymbol{x},\tau-t)\tau_{pq}^A(\boldsymbol{x},t)]dt. \tag{3.5}$$

The first term in (3.5) is evaluated in the following way:

$$\begin{aligned}
&\int_{t\in R} \Delta_{mrpq}\partial_m[v_r^A(\boldsymbol{x},t)\tau_{pq}^B(\boldsymbol{x},\tau-t)]dt \\
&= \int_{t\in R} \Delta_{ijmr}[\partial_m v_r^A(\boldsymbol{x},t)]\tau_{ij}^B(\boldsymbol{x},\tau-t) \\
&+ v_r^A(\boldsymbol{x},t)\Delta_{rmij}[\partial_m\tau_{ij}^B(\boldsymbol{x},\tau-t)]dt \qquad (3.6)\\
&= \int_{t\in R}[s_{ijpq}^A(\boldsymbol{x})\partial_t\tau_{pq}^A(\boldsymbol{x},t) + h_{ij}^A(\boldsymbol{x},t)]\tau_{ij}^B(\boldsymbol{x},\tau-t)dt \\
&+ \int_{t\in R} v_r^A(\boldsymbol{x},t)[\rho_{rk}^{s,B}(\boldsymbol{x})\partial_{\tau-t}v_k^B(\boldsymbol{x},\tau-t) - f_r^{s,B}(\boldsymbol{x},\tau-t)]dt,
\end{aligned}$$

where (3.2) and (3.3) have been used. Similarly, the second term in (3.5) is evaluated as

$$\begin{aligned}
&\int_{t\in R} \Delta_{mrpq}\partial_m[v_r^B(\boldsymbol{x},\tau-t)\tau_{pq}^A(\boldsymbol{x},t)]dt \\
&= \int_{t\in R} \Delta_{pqmk}[\partial_m v_k^B(\boldsymbol{x},\tau-t)]\tau_{pq}^A(\boldsymbol{x},t) \\
&+ v_k^B(\boldsymbol{x},\tau-t)\Delta_{kmpq}[\partial_m\tau_{pq}^A(\boldsymbol{x},t)]dt \qquad (3.7)\\
&= \int_{t\in R}[s_{pqij}^B(\boldsymbol{x})\partial_{\tau-t}\tau_{ij}^B(\boldsymbol{x},\tau-t) + h_{pq}^B(\boldsymbol{x},\tau-t)]\tau_{pq}^A(\boldsymbol{x},t)dt \\
&+ \int_{t\in R} v_k^B(\boldsymbol{x},\tau-t)[\rho_{kr}^{s,A}(\boldsymbol{x})\partial_t v_r^A(\boldsymbol{x},t) - f_k^{s,A}(\boldsymbol{x},t)]dt,
\end{aligned}$$

where (3.1) and (3.4) have been used. Subtracting (3.7) from (3.6), and using the properties of the time convolution of two space-time functions, we arrive at

$$\begin{aligned}
&\int_{t\in R} \Delta_{mrpq}\partial_m[v_r^A(\boldsymbol{x},t)\tau_{pq}^B(\boldsymbol{x},\tau-t) - v_r^B(\boldsymbol{x},\tau-t)\tau_{pq}^A(\boldsymbol{x},t)]dt \\
&= \partial_\tau \int_{t\in R} \tau_{ij}^B(\boldsymbol{x},\tau-t)[s_{ijpq}^A(\boldsymbol{x}) - s_{pqij}^B(\boldsymbol{x})]\tau_{pq}^A(\boldsymbol{x},t)dt \\
&- \partial_\tau \int_{t\in R} v_k^B(\boldsymbol{x},\tau-t)[\rho_{kr}^{s,A}(\boldsymbol{x}) - \rho_{rk}^{s,B}(\boldsymbol{x})]v_r^A(\boldsymbol{x},t)dt \qquad (3.8)\\
&+ \int_{t\in R}[\tau_{ij}^B(\boldsymbol{x},\tau-t)h_{ij}^A(\boldsymbol{x},t) + v_k^B(\boldsymbol{x},\tau-t)f_k^{s,A}(\boldsymbol{x},t) \\
&- \tau_{pq}^A(\boldsymbol{x},t)h_{pq}^B(\boldsymbol{x},\tau-t) - v_r^A(\boldsymbol{x},t)f_r^{s,B}(\boldsymbol{x},\tau-t)]dt.
\end{aligned}$$

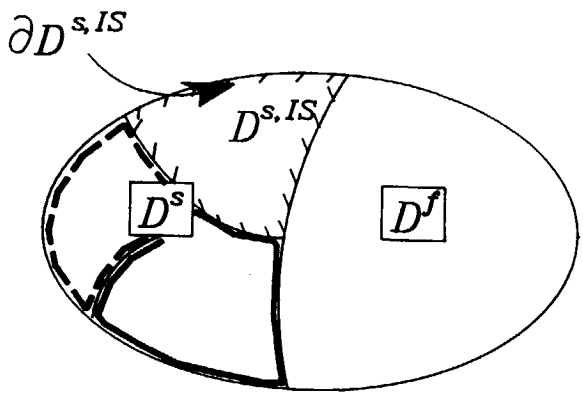

Figure 3.2: Domain $D^s = \bigcup_{IS=1}^{NS} D^{s,IS}$ consisting of the subdomains $\{ D^{s,IS};\ IS = 1, \ldots, NS \}$ with boundaries $\partial D^{s,IS}$.

Equation (3.8) is the local form of the space-time acoustic reciprocity theorem of the time-convolution type in a solid. The first two terms at the right-hand side of (3.8) are representative for the differences in the properties of the media present in the two states; they vanish at those locations where $\rho_{kr}^{s,A} = \rho_{rk}^{s,B}$ and $s_{ijpq}^{A} = s_{pqij}^{B}$. In case the latter conditions hold, the two media are denoted as each other's adjoints. In case the conditions hold for one and the same solid, the solid is denoted as self-adjoint. The last four terms at the right-hand side are associated with the source distributions; they vanish at those locations where no sources are present.

To arrive at the global form of the reciprocity theorem (for the domain D^s), we integrate (3.8) over D^s. Applying Gauss' divergence theorem to the resulting left-hand side for all subdomains $D^{s,IS}$, with $IS = 1, \ldots, NS$, out of which D^s is composed (Figure 3.2) and where the solid particle velocity and the stress are

continuously differentiable, and adding the relevant results, we end up with

$$\begin{aligned}
&\sum_{IS=1}^{NS} \int_{t\in R} dt \int_{\boldsymbol{x}\in\partial D^{s,IS}} \Delta_{mrpq}\nu_m^{(IS)}[v_r^A(\boldsymbol{x},t)\tau_{pq}^B(\boldsymbol{x},\tau-t) \\
&- v_r^B(\boldsymbol{x},\tau-t)\tau_{pq}^A(\boldsymbol{x},t)]dA \\
&= \partial_\tau \int_{t\in R} dt \int_{\boldsymbol{x}\in D^s} \tau_{ij}^B(\boldsymbol{x},\tau-t)[s_{ijpq}^A(\boldsymbol{x}) - s_{pqij}^B(\boldsymbol{x})]\tau_{pq}^A(\boldsymbol{x},t)dV \\
&- \partial_\tau \int_{t\in R} dt \int_{\boldsymbol{x}\in D^s} v_k^B(\boldsymbol{x},\tau-t)[\rho_{kr}^{s,A}(\boldsymbol{x}) - \rho_{rk}^{s,B}(\boldsymbol{x})]v_r^A(\boldsymbol{x},t)dV \qquad (3.9) \\
&+ \int_{t\in R} dt \int_{\boldsymbol{x}\in D^s} [\tau_{ij}^B(\boldsymbol{x},\tau-t)h_{ij}^A(\boldsymbol{x},t) + v_k^B(\boldsymbol{x},\tau-t)f_k^{s,A}(\boldsymbol{x},t) \\
&- \tau_{pq}^A(\boldsymbol{x},t)h_{pq}^B(\boldsymbol{x},\tau-t) - v_r^A(\boldsymbol{x},t)f_r^{s,B}(\boldsymbol{x},\tau-t)]dV,
\end{aligned}$$

where $D^s = \bigcup_{IS=1}^{NS} D^{s,IS}$ and $\partial D^{s,IS}$ is the boundary of $D^{s,IS}$. The unit vector along the normal to $\partial D^{s,IS}$ is denoted by $\boldsymbol{\nu}^{(IS)}$; it points away from $D^{s,IS}$. Equation (3.9) is the global form of the space-time reciprocity theorem of the time-convolution type in a solid and is known as Graffi's reciprocity theorem (Graffi 1939). The integrals over the internal surfaces account for possible jumps in the quantities across interfaces. For physical wave fields in the two States $'A'$ and $'B'$, the contributions from interfaces between different media present in D^s cancel in view of the interface conditions (2.10) and (2.11), but for computational states that do not necessarily satisfy these conditions, the interface integrals in general remain.

In a fluid medium of the type specified in Chapter 2, the field quantities of the State $'A'$ satisfy the equations (cf. (2.13) and (2.14))

$$-\delta_{km}\partial_m\sigma^A(\boldsymbol{x},t) + \rho_{kr}^{f,A}(\boldsymbol{x})\partial_t w_r^A(\boldsymbol{x},t) = f_k^{f,A}(\boldsymbol{x},t) \qquad (3.10)$$

and

$$\delta_{mr}\partial_m w_r^A(\boldsymbol{x},t) - \kappa^A(\boldsymbol{x})\partial_t\sigma^A(\boldsymbol{x},t) = q^A(\boldsymbol{x},t), \qquad (3.11)$$

and the quantities of the time-shifted and time-reversed field in State $'B'$ satisfy the equations (cf. (2.13) and (2.14))

$$-\delta_{rm}\partial_m\sigma^B(\boldsymbol{x},\tau-t) + \rho_{rk}^{f,B}(\boldsymbol{x})\partial_{\tau-t}w_k^B(\boldsymbol{x},\tau-t) = f_r^{f,B}(\boldsymbol{x},\tau-t) \qquad (3.12)$$

and

$$\delta_{mk}\partial_m w_k^B(\boldsymbol{x},\tau-t)-\kappa^B(\boldsymbol{x})\partial_{\tau-t}\sigma^B(\boldsymbol{x},\tau-t)=q^B(\boldsymbol{x},\tau-t). \tag{3.13}$$

As regards the space-time geometry in which the two admissible fluid states occur, the time invariance implies that the geometry is the Cartesian product $D^f \times R$ of a time-invariant spatial domain $D^f \subset R^3$ where a fluid medium is present and the real axis R. The theorem will be derived for bounded domains D^f. The reciprocity theorem of the time-convolution type follows upon considering the interaction quantity

$$\int_{t\in R}\delta_{mr}\partial_m[w_r^A(\boldsymbol{x},t)\sigma^B(\boldsymbol{x},\tau-t)-w_r^B(\boldsymbol{x},\tau-t)\sigma^A(\boldsymbol{x},t)]dt. \tag{3.14}$$

The first term in (3.14) is evaluated in the following way:

$$\begin{aligned}
&\int_{t\in R}\delta_{mr}\partial_m[w_r^A(\boldsymbol{x},t)\sigma^B(\boldsymbol{x},\tau-t)]dt\\
&=\int_{t\in R}\delta_{mr}[\partial_m w_r^A(\boldsymbol{x},t)]\sigma^B(\boldsymbol{x},\tau-t)+w_r^A(\boldsymbol{x},t)\delta_{rm}[\partial_m\sigma^B(\boldsymbol{x},\tau-t)]dt\\
&=\int_{t\in R}[\kappa^A(\boldsymbol{x})\partial_t\sigma^A(\boldsymbol{x},t)+q^A(\boldsymbol{x},t)]\sigma^B(\boldsymbol{x},\tau-t)dt \qquad (3.15)\\
&+\int_{t\in R}w_r^A(\boldsymbol{x},t)[\rho_{rk}^{f,B}(\boldsymbol{x})\partial_{\tau-t}w_k^B(\boldsymbol{x},\tau-t)-f_r^{f,B}(\boldsymbol{x},\tau-t)]dt,
\end{aligned}$$

where (3.11) and (3.12) have been used. Similarly, the second term in (3.14) is evaluated as

$$\begin{aligned}
&\int_{t\in R}\delta_{mr}\partial_m[w_r^B(\boldsymbol{x},\tau-t)\sigma^A(\boldsymbol{x},t)]dt\\
&=\int_{t\in R}\delta_{mk}[\partial_m w_k^B(\boldsymbol{x},\tau-t)]\sigma^A(\boldsymbol{x},t)+w_k^B(\boldsymbol{x},\tau-t)\delta_{km}[\partial_m\sigma^A(\boldsymbol{x},t)]dt\\
&=\int_{t\in R}[\kappa^B(\boldsymbol{x})\partial_{\tau-t}\sigma^B(\boldsymbol{x},\tau-t)+q^B(\boldsymbol{x},\tau-t)]\sigma^A(\boldsymbol{x},t)dt \qquad (3.16)\\
&+\int_{t\in R}w_k^B(\boldsymbol{x},\tau-t)[\rho_{kr}^{f,A}(\boldsymbol{x})\partial_t w_r^A(\boldsymbol{x},t)-f_k^{f,A}(\boldsymbol{x},t)]dt,
\end{aligned}$$

where (3.10) and (3.13) have been used. Subtracting (3.16) from (3.15), and using the properties of the time convolution of two space-time functions, we

arrive at

$$\begin{aligned}
&\int_{t\in R} \delta_{mr}\partial_m[w_r^A(\boldsymbol{x},t)\sigma^B(\boldsymbol{x},\tau-t) - w_r^B(\boldsymbol{x},\tau-t)\sigma^A(\boldsymbol{x},t)]dt \\
&= \partial_\tau \int_{t\in R} \sigma^B(\boldsymbol{x},\tau-t)[\kappa^A(\boldsymbol{x}) - \kappa^B(\boldsymbol{x})]\sigma^A(\boldsymbol{x},t)dt \\
&- \partial_\tau \int_{t\in R} w_k^B(\boldsymbol{x},\tau-t)[\rho_{kr}^{f,A}(\boldsymbol{x}) - \rho_{rk}^{f,B}(\boldsymbol{x})]w_r^A(\boldsymbol{x},t)dt \qquad (3.17) \\
&+ \int_{t\in R} [\sigma^B(\boldsymbol{x},\tau-t)q^A(\boldsymbol{x},t) + w_k^B(\boldsymbol{x},\tau-t)f_k^{f,A}(\boldsymbol{x},t) \\
&- \sigma^A(\boldsymbol{x},t)q^B(\boldsymbol{x},\tau-t) - w_r^A(\boldsymbol{x},t)f_r^{f,B}(\boldsymbol{x},\tau-t)]dt.
\end{aligned}$$

Equation (3.17) is the local form of the space-time acoustic reciprocity theorem of the time-convolution type in a fluid. The first two terms at the right-hand side of (3.17) are representative for the differences in the properties of the media present in the two states; they vanish at those locations where $\rho_{kr}^{f,A} = \rho_{rk}^{f,B}$ and $\kappa^A = \kappa^B$. In case the latter conditions hold, the two fluids are denoted as each other's adjoints. In case the conditions hold for one and the same fluid, the fluid is denoted as self-adjoint. The last four terms at the right-hand side are associated with the source distributions; they vanish at those locations where no sources are present.

To arrive at the global form of the reciprocity theorem (for the domain D^f), we integrate (3.17) over D^f. Applying Gauss' divergence theorem to the resulting left-hand side for all subdomains $D^{f,IF}$, with $IF = 1,\ldots,NF$, out of which D^f is composed (Figure 3.3) and where the fluid particle velocity and the scalar traction are continuously differentiable, and adding the relevant results, we end up with

$$\begin{aligned}
&\sum_{IF=1}^{NF} \int_{t\in R} dt \int_{\boldsymbol{x}\in\partial D^{f,IF}} \delta_{mr}\nu_m^{(IF)}[w_r^A(\boldsymbol{x},t)\sigma^B(\boldsymbol{x},\tau-t) - w_r^B(\boldsymbol{x},\tau-t)\sigma^A(\boldsymbol{x},t)]dA \\
&= \partial_\tau \int_{t\in R} dt \int_{\boldsymbol{x}\in D^f} \sigma^B(\boldsymbol{x},\tau-t)[\kappa^A(\boldsymbol{x}) - \kappa^B(\boldsymbol{x})]\sigma^A(\boldsymbol{x},t)dV \\
&- \partial_\tau \int_{t\in R} dt \int_{\boldsymbol{x}\in D^f} w_k^B(\boldsymbol{x},\tau-t)[\rho_{kr}^{f,A}(\boldsymbol{x}) - \rho_{rk}^{f,B}(\boldsymbol{x})]w_r^A(\boldsymbol{x},t)dV \qquad (3.18) \\
&+ \int_{t\in R} dt \int_{\boldsymbol{x}\in D^f} [\sigma^B(\boldsymbol{x},\tau-t)q^A(\boldsymbol{x},t) + w_k^B(\boldsymbol{x},\tau-t)f_k^{f,A}(\boldsymbol{x},t)
\end{aligned}$$

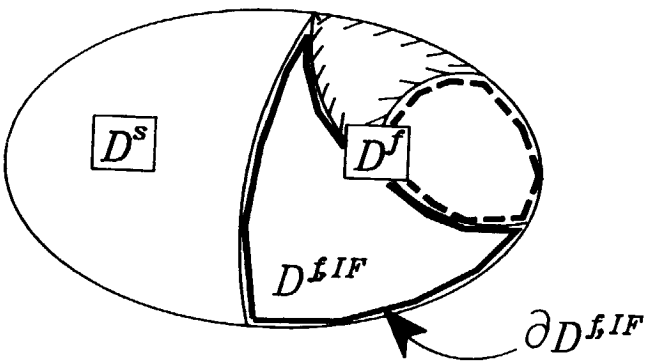

Figure 3.3: Domain $D^f = \bigcup_{IF=1}^{NF} D^{f,IF}$ consisting of the subdomains $\{ D^{f,IF};\ IF = 1,\ldots,NF \}$ with boundaries $\partial D^{f,IF}$.

$$- \sigma^A(\boldsymbol{x},t)q^B(\boldsymbol{x},\tau-t) - w_r^A(\boldsymbol{x},t)f_r^{f,B}(\boldsymbol{x},\tau-t)]dV,$$

where $D^f = \bigcup_{IF=1}^{NF} D^{f,IF}$ and $\partial D^{f,IF}$ is the boundary of $D^{f,IF}$. The unit vector along the normal to $\partial D^{f,IF}$ is denoted by $\boldsymbol{\nu}^{(IF)}$; it points away from $D^{f,IF}$. Equation (3.18) is the global form of the space-time reciprocity theorem of the time-convolution type in a fluid. The integrals over the internal surfaces account for possible jumps in the quantities across interfaces. For physical wave fields in the States $'A'$ and $'B'$, the contributions from interfaces between different media present in D^f cancel in view of the interface conditions (2.17) and (2.18), but for computational states that do not necessarily satisfy these conditions, the interface integrals in general remain.

To obtain the reciprocity theorems for an unbounded domain, they are applied to the ball D_Δ, interior to the sphere ∂D_Δ with radius Δ around the origin O; after which the limit $\Delta \to \infty$ is taken.

Equations (3.9) and (3.18) will serve as a basis for the development of appropriate integral representations of the acoustic wave field, especially for the

surface and (contrast) volume source representations that will later be employed in the embedding.

Chapter 4

SPACE-TIME ACOUSTIC RECIPROCITY THEOREM OF THE TIME-CORRELATION TYPE

In this chapter, for the same type of solid and fluid configurations as in Chapter 3, the space-time acoustic reciprocity theorems of the time-correlation type are presented. These reciprocity theorems are derived in De Hoop (1988) and De Hoop and Stam (1988) for the more general case that the media show relaxation. For our instantaneously reacting fluids and solids we derive the relevant theorems in a simpler way. Again the characteristic quantities of the two acoustic wave fields are denoted by the superscripts $'A'$ and $'B'$, respectively (Figure 4.1). In a solid medium of this type, the field quantities in State $'A'$ satisfy the equations (cf. (2.1) and (2.2))

$$-\Delta_{kmpq}\partial_m\tau^A_{pq}(\boldsymbol{x},t)+\rho^{s,A}_{kr}(\boldsymbol{x})\partial_t v^A_r(\boldsymbol{x},t)=f^{s,A}_k(\boldsymbol{x},t) \tag{4.1}$$

and

$$\Delta_{ijmr}\partial_m v^A_r(\boldsymbol{x},t)-s^A_{ijpq}(\boldsymbol{x})\partial_t\tau^A_{pq}(\boldsymbol{x},t)=h^A_{ij}(\boldsymbol{x},t), \tag{4.2}$$

and the quantities of the time-shifted (but now not time-reversed) field in State $'B'$ satisfy the equations (cf. (2.1) and (2.2))

$$-\Delta_{rmij}\partial_m\tau^B_{ij}(\boldsymbol{x},t-\tau)+\rho^{s,B}_{rk}(\boldsymbol{x})\partial_{t-\tau}v^B_k(\boldsymbol{x},t-\tau)=f^{s,B}_r(\boldsymbol{x},t-\tau) \tag{4.3}$$

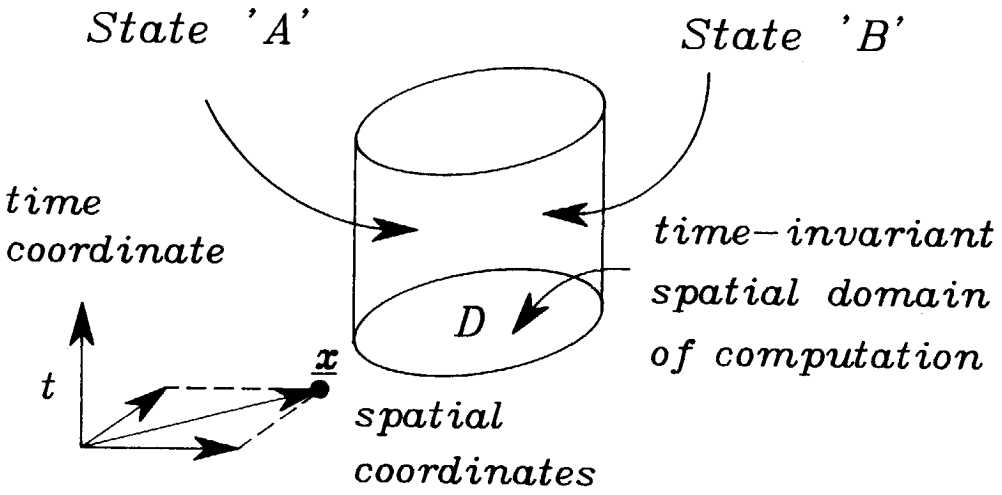

Figure 4.1: Space-time domain with the two admissible acoustic States 'A' and 'B'.

and

$$\Delta_{pqmk}\partial_m v_k^B(\boldsymbol{x},t-\tau) - s_{pqij}^B(\boldsymbol{x})\partial_{t-\tau}\tau_{ij}^B(\boldsymbol{x},t-\tau) = h_{pq}^B(\boldsymbol{x},t-\tau). \tag{4.4}$$

As regards the space-time geometry in which the two admissible solid states occur, the time invariance implies that the geometry is the Cartesian product $D^s \times R^3$ of a time-invariant spatial domain $D^s \subset R^3$ where a solid medium is present, and the real axis R. The theorem will be derived for bounded domains D^s. The reciprocity theorem of the time-correlation type follows upon considering the interaction quantity

$$\int_{t\in R} \Delta_{mrpq}\partial_m[v_r^A(\boldsymbol{x},t)\tau_{pq}^B(\boldsymbol{x},t-\tau) + v_r^B(\boldsymbol{x},t-\tau)\tau_{pq}^A(\boldsymbol{x},t)]dt. \tag{4.5}$$

The first term in (4.5) is evaluated in the following way:

$$\int_{t\in R} \Delta_{mrpq}\partial_m[v_r^A(\boldsymbol{x},t)\tau_{pq}^B(\boldsymbol{x},t-\tau)]dt$$

$$= \int_{t\in R} \Delta_{ijmr}[\partial_m v_r^A(\boldsymbol{x},t)]\tau_{ij}^B(\boldsymbol{x},t-\tau)$$

$$
\begin{aligned}
&+ v_r^A(\boldsymbol{x},t)\Delta_{rmij}[\partial_m \tau_{ij}^B(\boldsymbol{x},t-\tau)]dt \qquad (4.6)\\
&= \int_{t\in R}[s_{ijpq}^A(\boldsymbol{x})\partial_t \tau_{pq}^A(\boldsymbol{x},t) + h_{ij}^A(\boldsymbol{x},t)]\tau_{ij}^B(\boldsymbol{x},t-\tau)dt\\
&+ \int_{t\in R} v_r^A(\boldsymbol{x},t)[\rho_{rk}^{s,B}(\boldsymbol{x})\partial_{t-\tau} v_k^B(\boldsymbol{x},t-\tau) - f_r^{s,B}(\boldsymbol{x},t-\tau)]dt,
\end{aligned}
$$

where (4.2) and (4.3) have been used. Similarly, the second term in (4.5) is evaluated as

$$
\begin{aligned}
&\int_{t\in R}\Delta_{mrpq}\partial_m[v_r^B(\boldsymbol{x},t-\tau)\tau_{pq}^A(\boldsymbol{x},t)]dt\\
&= \int_{t\in R}\Delta_{pqmk}[\partial_m v_k^B(\boldsymbol{x},t-\tau)]\tau_{pq}^A(\boldsymbol{x},t)\\
&+ v_k^B(\boldsymbol{x},t-\tau)\Delta_{kmpq}[\partial_m \tau_{pq}^A(\boldsymbol{x},t)]dt \qquad (4.7)\\
&= \int_{t\in R}[s_{pqij}^B(\boldsymbol{x})\partial_{t-\tau}\tau_{ij}^B(\boldsymbol{x},t-\tau) + h_{pq}^B(\boldsymbol{x},t-\tau)]\tau_{pq}^A(\boldsymbol{x},t)dt\\
&+ \int_{t\in R} v_k^B(\boldsymbol{x},t-\tau)[\rho_{kr}^{s,A}(\boldsymbol{x})\partial_t v_r^A(\boldsymbol{x},t) - f_k^{s,A}(\boldsymbol{x},t)]dt,
\end{aligned}
$$

where (4.1) and (4.4) have been used. Adding (4.6) to (4.7) and using the properties of the time correlation of two space-time functions, we arrive at

$$
\begin{aligned}
&\int_{t\in R}\Delta_{mrpq}\partial_m[v_r^A(\boldsymbol{x},t)\tau_{pq}^B(\boldsymbol{x},t-\tau) + v_r^B(\boldsymbol{x},t-\tau)\tau_{pq}^A(\boldsymbol{x},t)]dt\\
&= \partial_\tau\int_{t\in R}\tau_{ij}^B(\boldsymbol{x},t-\tau)[s_{ijpq}^A(\boldsymbol{x}) - s_{pqij}^B(\boldsymbol{x})]\tau_{pq}^A(\boldsymbol{x},t)dt\\
&+ \partial_\tau\int_{t\in R} v_k^B(\boldsymbol{x},t-\tau)[\rho_{kr}^{s,A}(\boldsymbol{x}) - \rho_{rk}^{s,B}(\boldsymbol{x})]v_r^A(\boldsymbol{x},t)dt \qquad (4.8)\\
&+ \int_{t\in R}[\tau_{ij}^B(\boldsymbol{x},t-\tau)h_{ij}^A(\boldsymbol{x},t) - v_k^B(\boldsymbol{x},t-\tau)f_k^{s,A}(\boldsymbol{x},t)\\
&+ \tau_{pq}^A(\boldsymbol{x},t)h_{pq}^B(\boldsymbol{x},t-\tau) - v_r^A(\boldsymbol{x},t)f_r^{s,B}(\boldsymbol{x},t-\tau)]dt.
\end{aligned}
$$

Equation (4.8) is the local form of the space-time acoustic reciprocity theorem of the time correlation type in a solid. The first two terms at the right-hand side of (4.8) are representative for the differences in the properties of the media present in the two states; they vanish at those locations where $\rho_{kr}^{s,A} = \rho_{rk}^{s,B}$ and

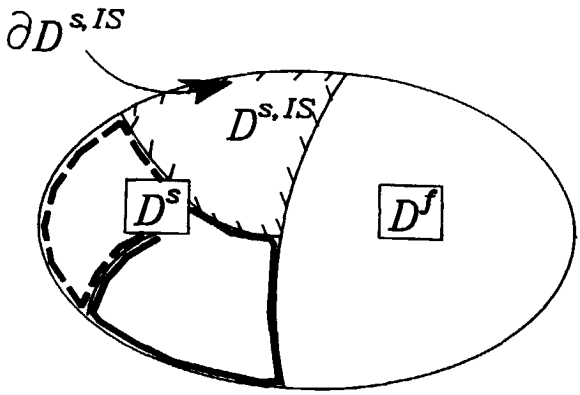

Figure 4.2: Domain $D^s = \bigcup_{IS=1}^{NS} D^{s,IS}$ consisting of the subdomains $\{ D^{s,IS};\ IS = 1, \ldots, NS \}$ with boundaries $\partial D^{s,IS}$.

$s^A_{ijpq} = s^B_{pqij}$. In case the latter conditions hold, the two media are denoted as each other's adjoints. In case the conditions hold for one and the same solid, the solid is denoted as self-adjoint. The last four terms at the right-hand side are associated with the source distributions; they vanish at those locations where no sources are present.

To arrive at the global form of the reciprocity theorem (for the domain D^s), we integrate (4.8) over D^s. Applying Gauss' divergence theorem to the resulting left-hand side for all subdomains $D^{s,IS}$, with $IS = 1, \ldots, NS$, out of which D^s is composed (Figure 4.2) and where the solid particle velocity and the stress are continuously differentiable, and adding the relevant results, we end up with

$$\sum_{IS=1}^{NS} \int_{t\in R} dt \int_{\boldsymbol{x}\in\partial D^{s,IS}} \Delta_{mrpq}\nu_m^{(IS)}[v_r^A(\boldsymbol{x},t)\tau_{pq}^B(\boldsymbol{x},t-\tau)$$

$$+ v_r^B(\boldsymbol{x},t-\tau)\tau_{pq}^A(\boldsymbol{x},t)]dA$$

$$= \partial_\tau \int_{t\in R} dt \int_{\boldsymbol{x}\in D^s} \tau_{ij}^B(\boldsymbol{x},t-\tau)[s_{ijpq}^A(\boldsymbol{x}) - s_{pqij}^B(\boldsymbol{x})]\tau_{pq}^A(\boldsymbol{x},t)dV$$

$$+ \partial_\tau \int_{t\in R} dt \int_{\boldsymbol{x}\in D^s} v_k^B(\boldsymbol{x}, t-\tau)[\rho_{kr}^{s,A}(\boldsymbol{x}) - \rho_{rk}^{s,B}(\boldsymbol{x})]v_r^A(\boldsymbol{x}, t)dV \qquad (4.9)$$

$$+ \int_{t\in R} dt \int_{\boldsymbol{x}\in D^s} [\tau_{ij}^B(\boldsymbol{x}, t-\tau)h_{ij}^A(\boldsymbol{x}, t) - v_k^B(\boldsymbol{x}, t-\tau)f_k^{s,A}(\boldsymbol{x}, t)$$

$$+ \tau_{pq}^A(\boldsymbol{x}, t)h_{pq}^B(\boldsymbol{x}, t-\tau) - v_r^A(\boldsymbol{x}, t)f_r^{s,B}(\boldsymbol{x}, t-\tau)]dV,$$

where $D^s = \bigcup_{IS=1}^{NS} D^{s,IS}$ and $\partial D^{s,IS}$ is the boundary of $D^{s,IS}$. The unit vector along the normal to $\partial D^{s,IS}$ is denoted by $\boldsymbol{\nu}^{(IS)}$; it points away from $D^{s,IS}$. Equation (4.9) is the global form of the space-time reciprocity theorem of the time-correlation type. The integrals over the internal surfaces account for possible jumps in the quantities across interfaces. For physical wave fields in the States $'A'$ and $'B'$, the contributions from interfaces between different media present in D^s cancel in view of the boundary conditions (2.10) and (2.11), but for computational states that do not necessarily satisfy these conditions, the interface integrals remain.

In a fluid medium of the type specified in Chapter 2, the field quantities of the State $'A'$ satisfy the equations (cf. (2.13) and (2.14))

$$-\delta_{km}\partial_m\sigma^A(\boldsymbol{x}, t) + \rho_{kr}^{f,A}(\boldsymbol{x})\partial_t w_r^A(\boldsymbol{x}, t) = f_k^{f,A}(\boldsymbol{x}, t) \qquad (4.10)$$

and

$$\delta_{mr}\partial_m w_r^A(\boldsymbol{x}, t) - \kappa^A(\boldsymbol{x})\partial_t\sigma^A(\boldsymbol{x}, t) = q^A(\boldsymbol{x}, t), \qquad (4.11)$$

and the quantities of the time-shifted (but now not time-reversed) field in state $'B'$ satisfy the equations (cf. (2.13) and (2.14))

$$-\delta_{rm}\partial_m\sigma^B(\boldsymbol{x}, t-\tau) + \rho_{rk}^{f,B}(\boldsymbol{x})\partial_{t-\tau} w_k^B(\boldsymbol{x}, t-\tau) = f_r^{f,B}(\boldsymbol{x}, t-\tau) \qquad (4.12)$$

and

$$\delta_{mk}\partial_m w_k^B(\boldsymbol{x}, t-\tau) - \kappa^B(\boldsymbol{x})\partial_{t-\tau}\sigma^B(\boldsymbol{x}, t-\tau) = q^B(\boldsymbol{x}, t-\tau). \qquad (4.13)$$

As regards the space-time geometry in which the two admissible fluid states occur, the time invariance implies that the geometry is the Cartesian product $D^f \times R^3$ of a time-invariant spatial domain $D^f \subset R^3$ where a fluid medium is present, and the real axis R. The theorem will be derived for bounded domains D^f. The reciprocity theorem of the time-correlation type follows upon

considering the interaction quantity

$$\int_{t\in R} \delta_{mr}\partial_m[w_r^A(\boldsymbol{x},t)\sigma^B(\boldsymbol{x},t-\tau) + w_r^B(\boldsymbol{x},t-\tau)\sigma^A(\boldsymbol{x},t)]dt. \tag{4.14}$$

The first term in (4.14) is evaluated in the following way:

$$\begin{aligned}
&\int_{t\in R} \delta_{mr}\partial_m[w_r^A(\boldsymbol{x},t)\sigma^B(\boldsymbol{x},t-\tau)]dt \\
&= \int_{t\in R} \delta_{mr}[\partial_m w_r^A(\boldsymbol{x},t)]\sigma^B(\boldsymbol{x},t-\tau) + w_r^A(\boldsymbol{x},t)\delta_{rm}[\partial_m\sigma^B(\boldsymbol{x},t-\tau)]dt \\
&= \int_{t\in R}[\kappa^A(\boldsymbol{x})\partial_t\sigma^A(\boldsymbol{x},t) + q^A(\boldsymbol{x},t)]\sigma^B(\boldsymbol{x},t-\tau)dt \qquad (4.15)\\
&+ \int_{t\in R} w_r^A(\boldsymbol{x},t)[\rho_{rk}^{f,B}(\boldsymbol{x})\partial_{t-\tau}w_k^B(\boldsymbol{x},t-\tau) - f_r^{f,B}(\boldsymbol{x},t-\tau)]dt,
\end{aligned}$$

where (4.11) and (4.12) have been used. Similarly, the second term in (4.14) is evaluated as

$$\begin{aligned}
&\int_{t\in R} \delta_{mr}\partial_m[w_r^B(\boldsymbol{x},t-\tau)\sigma^A(\boldsymbol{x},t)]dt \\
&= \int_{t\in R} \delta_{mk}[\partial_m w_k^B(\boldsymbol{x},t-\tau)]\sigma^A(\boldsymbol{x},t) + w_k^B(\boldsymbol{x},t-\tau)\delta_{km}[\partial_m\sigma^A(\boldsymbol{x},t)]dt \\
&= \int_{t\in R}[\kappa^B(\boldsymbol{x})\partial_{t-\tau}\sigma^B(\boldsymbol{x},t-\tau) + q^B(\boldsymbol{x},t-\tau)]\sigma^A(\boldsymbol{x},t)dt \qquad (4.16)\\
&+ \int_{t\in R} w_k^B(\boldsymbol{x},t-\tau)[\rho_{kr}^{f,A}(\boldsymbol{x})\partial_t w_r^A(\boldsymbol{x},t) - f_k^{f,A}(\boldsymbol{x},t)]dt,
\end{aligned}$$

where (4.10) and (4.13) have been used. Adding (4.15) to (4.16), and using the properties of the time correlation of two space-time functions, we arrive at

$$\begin{aligned}
&\int_{t\in R} \delta_{mr}\partial_m[w_r^A(\boldsymbol{x},t)\sigma^B(\boldsymbol{x},t-\tau) + w_r^B(\boldsymbol{x},t-\tau)\sigma^A(\boldsymbol{x},t)]dt \\
&= \partial_\tau \int_{t\in R} \sigma^B(\boldsymbol{x},t-\tau)[\kappa^A(\boldsymbol{x}) - \kappa^B(\boldsymbol{x})]\sigma^A(\boldsymbol{x},t)dt \\
&+ \partial_\tau \int_{t\in R} w_k^B(\boldsymbol{x},t-\tau)[\rho_{kr}^{f,A}(\boldsymbol{x}) - \rho_{rk}^{f,B}(\boldsymbol{x})]w_r^A(\boldsymbol{x},t)dt \qquad (4.17)\\
&+ \int_{t\in R}[\sigma^B(\boldsymbol{x},t-\tau)q^A(\boldsymbol{x},t) - w_k^B(\boldsymbol{x},t-\tau)f_k^{f,A}(\boldsymbol{x},t) \\
&+ \sigma^A(\boldsymbol{x},t)q^B(\boldsymbol{x},t-\tau) - w_r^A(\boldsymbol{x},t)f_r^{f,B}(\boldsymbol{x},t-\tau)]dt.
\end{aligned}$$

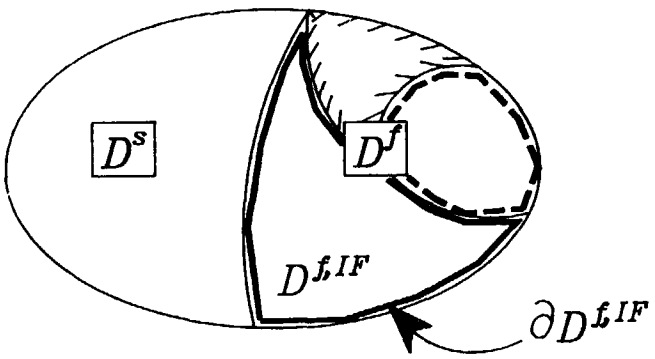

Figure 4.3: Domain $D^f = \bigcup_{IF=1}^{NF} D^{f,IF}$ consisting of the subdomains $\{ D^{f,IF};\ IF = 1,\ldots,NF \}$ with boundaries $\partial D^{f,IF}$.

Equation (4.17) is the local form of the space-time acoustic reciprocity theorem of the time-correlation type in a fluid. The first two terms at the right-hand side of (4.17) are representative for the differences in the properties of the media present in the two states; they vanish at those locations where $\rho_{kr}^{f,A} = \rho_{rk}^{f,B}$ and $\kappa^A = \kappa^B$. In case the latter conditions hold, the two media are denoted as each other's adjoints. In case the conditions hold for one and the same fluid, the fluid is denoted as self-adjoint. The last four terms at the right-hand side are associated with the source distributions; they vanish at those locations where no sources are present.

To arrive at the global form of the reciprocity theorem (for the domain D^f), we integrate (4.17) over D^f. Applying Gauss' divergence theorem to the resulting left-hand side for all subdomains $D^{f,IF}$, with $IF = 1,\ldots,NF$, out of which D^f is composed (Figure 4.3) and where the fluid particle velocity and the scalar traction are continuously differentiable, and adding the relevant results,

we end up with

$$\begin{aligned}
&\sum_{IF=1}^{NF} \int_{t\in R} dt \int_{\boldsymbol{x}\in\partial D^{f,IF}} \delta_{mr}\nu_m^{(IF)}[w_r^A(\boldsymbol{x},t)\sigma^B(\boldsymbol{x},t-\tau) + w_r^B(\boldsymbol{x},t-\tau)\sigma^A(\boldsymbol{x},t)]dA \\
&= \partial_\tau \int_{t\in R} dt \int_{\boldsymbol{x}\in D^f} \sigma^B(\boldsymbol{x},t-\tau)[\kappa^A(\boldsymbol{x}) - \kappa^B(\boldsymbol{x})]\sigma^A(\boldsymbol{x},t)dV \\
&+ \partial_\tau \int_{t\in R} dt \int_{\boldsymbol{x}\in D^f} w_k^B(\boldsymbol{x},t-\tau)[\rho_{kr}^{f,A}(\boldsymbol{x}) - \rho_{rk}^{f,B}(\boldsymbol{x})]w_r^A(\boldsymbol{x},t)dV \qquad (4.18) \\
&+ \int_{t\in R} dt \int_{\boldsymbol{x}\in D^f} [\sigma^B(\boldsymbol{x},t-\tau)q^A(\boldsymbol{x},t) - w_k^B(\boldsymbol{x},t-\tau)f_k^{f,A}(\boldsymbol{x},t) \\
&+ \sigma^A(\boldsymbol{x},t)q^B(\boldsymbol{x},t-\tau) - w_r^A(\boldsymbol{x},t)f_r^{f,B}(\boldsymbol{x},t-\tau)]dV,
\end{aligned}$$

where $D^f = \bigcup_{IF=1}^{NF} D^{f,IF}$ and $\partial D^{f,IF}$ is the boundary of $D^{f,IF}$. The unit vector along the normal to $\partial D^{f,IF}$ is denoted by $\boldsymbol{\nu}^{(IF)}$; it points away from $D^{f,IF}$. Equation (4.18) is the global form of the space-time reciprocity theorem of the time-correlation type in a fluid. The integrals over the internal surfaces account for possible jumps in the quantities across interfaces. For physical wave fields in the States 'A' and 'B', the contributions from interfaces between different media present in D^f cancel in view of the boundary conditions (2.17) and (2.18), but for computational states that do not necessarily satisfy these conditions, the interface integrals remain.

Equations (4.9) and (4.18) will serve as a basis for the development of the finite-element method for the elastodynamic wave problem.

Chapter 5

THE FINITE-ELEMENT METHOD BASED ON RECIPROCITY

In this chapter a finite-element method to solve acoustic wave problems is presented that is based on reciprocity. It amounts to a particular type of discretization of the acoustic wave problem associated with the partial differential equations (2.1)-(2.2) and (2.13)-(2.14). The finite-element method is a powerful tool for analyzing problems numerically in engineering and the applied sciences. The method is extensively described in the textbooks by, for example, Zienkiewicz and Taylor (1989) and Strang and Fix (1973). One of the advantages of the finite-element method as contrasted with finite-difference schemes on coordinate-line grids is that it can handle, without difficulty, boundary conditions at arbitrarily shaped boundaries and interfaces.

On many occasions where the finite-element method is applied to space-time problems, the method is only used for the spatial part of the analysis. Such a discretization in part of the problem produces a system of ordinary differential equations in time. The solution method of the latter equations in the time direction is then still free to be chosen; one can either use analytical or numerical methods (see, for example, Smith 1975; Zienkiewicz 1983; Zienkiewicz and Morgan 1983; Zienkiewicz et al., 1984).

A recent development in the application of the finite-element method to

[0]The theory developed in this chapter has been presented in Stam and De Hoop (1990)

space-time problems is its extension to the time domain as well. This so-called space-time finite-element method applies to a fully discretized space-time domain. The property of the finite-element method that it is able to handle irregular grids, makes this method also suited for problems defined in time-dependent configurations. Mitchell (1977) presents such a method for a one-dimensional wave problem. Bajer (1986) describes the application to vibration analysis, where the space-time domain is discretized into triangular, tetrahedral and hyper-tetrahedral space-time elements. In the present monograph we consider wave problems in a time-invariant configuration. Notwithstanding this time invariance, we make use of a space-time finite-element formulation, because it treats the dependence on the time coordinate in the same way as the dependence on the spatial ones, which can, for the analysis of wave phenomena, be argued to be a desirable feature.

Finite-element solutions of physical problems are mathematically based on so-called weak formulations of the relevant problems. Especially when solving static, i.e., time-independent problems, variational principles furnish such formulations (Reddy 1986, p.258; Zienkiewicz and Taylor 1989, p.32). In it, a functional is constructed that is stationary and, in case the functional is positive definite, a minimum for the exact solution of the problem. Achenbach (1973, p.61) presents such a variational principle for the elastostatic problem with regard to a perfectly elastic body. For problems where no variational principle is available, the method of weighted residuals furnishes the method for constructing weak solutions. In this method the governing partial differential equations are weighted, i.e., multiplied through by some weighting function and integrated over the domain of computational interest, the latter being the domain in which the problem has to be solved numerically. Selecting a certain sequence of linearly independent weighting functions, this procedure leads to relations that are in fact weighted forms of the pertaining differential equations.

In our approach we introduce as the starting point for the construction of a finite-element solution of the wave problem the reciprocity theorem of the time-correlation type derived in Chapter 4. Of the two states occurring in this theorem, State $'A'$, is identified with the actual wave field that is to be approximated, while the other state, State $'B'$, is considered as a computational

one that remains to be chosen appropriately. For the acoustic waves in the solid parts, the theorem is applied to the bounded subdomain D^s of D where the solid medium is present. We have (cf. (4.9))

$$\begin{aligned}
&\sum_{IS=1}^{NS} \int_{t\in R} dt \int_{\boldsymbol{x}\in\partial D^{s,IS}} \Delta_{mrpq}\nu_m^{(IS)}[v_r^A(\boldsymbol{x},t)\tau_{pq}^B(\boldsymbol{x},t-\tau) \\
&+ v_r^B(\boldsymbol{x},t-\tau)\tau_{pq}^A(\boldsymbol{x},t)]dA \\
&= \partial_\tau \int_{t\in R} dt \int_{\boldsymbol{x}\in D^s} \tau_{ij}^B(\boldsymbol{x},t-\tau)[s_{ijpq}^A(\boldsymbol{x}) - s_{pqij}^B(\boldsymbol{x})]\tau_{pq}^A(\boldsymbol{x},t)dV \\
&+ \partial_\tau \int_{t\in R} dt \int_{\boldsymbol{x}\in D^s} v_k^B(\boldsymbol{x},t-\tau)[\rho_{kr}^{s,A}(\boldsymbol{x}) - \rho_{rk}^{s,B}(\boldsymbol{x})]v_r^A(\boldsymbol{x},t)dV \qquad (5.1) \\
&+ \int_{t\in R} dt \int_{\boldsymbol{x}\in D^s} \tau_{ij}^B(\boldsymbol{x},t-\tau)h_{ij}^A(\boldsymbol{x},t) - v_k^B(\boldsymbol{x},t-\tau)f_k^{s,A}(\boldsymbol{x},t) \\
&+ \tau_{pq}^A(\boldsymbol{x},t)h_{pq}^B(\boldsymbol{x},t-\tau) - v_r^A(\boldsymbol{x},t)f_r^{s,B}(\boldsymbol{x},t-\tau)dV.
\end{aligned}$$

Equation (5.1) can, from a particular point of view, also be regarded as a "weighted" form of the acoustic wave equations (2.1) and (2.2) pertaining to State 'A'. To show this, we take State 'B' to be any sequence of piecewise continuously differentiable functions $\{v_k^B(\boldsymbol{x},t;IWS), \tau_{ij}^B(\boldsymbol{x},t;IWS)\}$ defined on D^s, with $IWS = 1,\ldots,NWS$, and take $\{f_r^{s,B}(\boldsymbol{x},t;IWS), h_{pq}^B(\boldsymbol{x},t;IWS)\}$ as (cf. (4.3))

$$\begin{aligned}
f_r^{s,B}(\boldsymbol{x},t-\tau;IWS) &= -\Delta_{rmij}\partial_m\tau_{ij}^B(\boldsymbol{x},t-\tau;IWS) \qquad (5.2) \\
&\quad +\rho_{rk}^{s,B}(\boldsymbol{x})\partial_{t-\tau}v_k^B(\boldsymbol{x},t-\tau;IWS)
\end{aligned}$$

and (cf. (4.4))

$$\begin{aligned}
h_{pq}^B(\boldsymbol{x},t-\tau;IWS) &= \Delta_{pqmk}\partial_m v_k^B(\boldsymbol{x},t-\tau;IWS) \qquad (5.3) \\
&\quad -s_{pqij}^B(\boldsymbol{x})\partial_{t-\tau}\tau_{ij}^B(\boldsymbol{x},t-\tau;IWS),
\end{aligned}$$

for given $\{\rho_{rk}^{s,B}, s_{pqij}^B\}$. Substitution of these expressions for $f_r^{s,B}$ and h_{pq}^B in (5.1)

leads to

$$\begin{aligned}
&\sum_{IS=1}^{NS} \int_{t\in R} dt \int_{x\in\partial D^{s,IS}} \Delta_{mrpq}\nu_m^{(IS)}[v_r^A(x,t)\tau_{pq}^B(x,t-\tau;IWS) \\
&+ v_r^B(x,t-\tau;IWS)\tau_{pq}^A(x,t)]dA \\
&= \partial_\tau \int_{t\in R} dt \int_{x\in D^s} \tau_{ij}^B(x,t-\tau;IWS)s_{ijpq}^A(x)\tau_{pq}^A(x,t)dV \\
&+ \partial_\tau \int_{t\in R} dt \int_{x\in D^s} v_k^B(x,t-\tau;IWS)\rho_{kr}^{s,A}(x)v_r^A(x,t)dV \qquad (5.4) \\
&+ \int_{t\in R} dt \int_{x\in D^s} \tau_{ij}^B(x,t-\tau;IWS)h_{ij}^A(x,t) - v_k^B(x,t-\tau;IWS)f_k^{s,A}(x,t)dV \\
&+ \int_{t\in R} dt \int_{x\in D^s} \Delta_{pqmk}[\partial_m v_k^B(x,t-\tau;IWS)]\tau_{pq}^A(x,t) \\
&+\Delta_{rmij}v_r^A(x,t)[\partial_m\tau_{ij}^B(x,t-\tau;IWS)]dV.
\end{aligned}$$

Next, by applying Gauss' divergence theorem to the subdomains $D^{s,IS}$, with $IS = 1,\ldots,NS$, in the interiors of which both sides are continuously differentiable, we replace the surface integrals on the left-hand side by a volume integral. Adding the results, we end up with the desired relation

$$\begin{aligned}
&\int_{t\in R} dt \int_{x\in D^s} v_k^B(x,t-\tau;IWS) \\
&[-\Delta_{kmpq}\partial_m\tau_{pq}^A(x,t) + \rho_{kr}^{s,A}(x)\partial_t v_r^A(x,t) - f_k^{s,A}(x,t)]dV \qquad (5.5) \\
&- \int_{t\in R} dt \int_{x\in D^s} \tau_{ij}^B(x,t-\tau;IWS) \\
&[\Delta_{ijmr}\partial_m v_r^A(x,t) - s_{ijpq}^A(x)\partial_t\tau_{pq}^A(x,t) - h_{ij}^A(x,t)]dV = 0 \\
&\text{for } IWS = 1,\ldots,NWS.
\end{aligned}$$

Upon choosing in (5.5) the test functions $\tau_{ij}^B = 0$ throughout D^s and $v_k^B \neq 0$, we obtain a number of NWS weighted forms of the equation of motion over the space-time domain $D^s \times R$ with the arbitrary piecewise continuously differentiable weighting functions v_k^B :

$$\int_{t\in R} dt \int_{x\in D^s} v_k^B(x,t-\tau;IWS)$$

$$[-\Delta_{kmpq}\partial_m\tau^A_{pq}(\boldsymbol{x},t)+\rho^{s,A}_{kr}(\boldsymbol{x})\partial_t v^A_r(\boldsymbol{x},t)-f^{s,A}_k(\boldsymbol{x},t)]dV=0 \qquad (5.6)$$

for $IWS=1,\ldots,NWS$.

Note that the choice $\tau^B_{ij}=0$ is compatible with (5.2) and (5.3), provided that we take $\rho^{s,B}_{rk}=0, f^{s,B}_r=0$ and $h^B_{pq}=\Delta_{pqmk}\partial_m v^B_k$. Upon choosing the test functions $v^B_k=0$ throughout D^s and $\tau^B_{ij}\neq 0$ in (5.5) we obtain a number of NWS weighted forms of the deformation rate equation over the space-time domain $D^s\times R$ with the arbitrary piecewise continuously differentiable weighting functions τ^B_{ij} :

$$\int_{t\in R}dt\int_{\boldsymbol{x}\in D^s}\tau^B_{ij}(\boldsymbol{x},t-\tau;IB)$$

$$[\Delta_{ijmr}\partial_m v^A_r(\boldsymbol{x},t)-s^A_{ijpq}(\boldsymbol{x})\partial_t\tau^A_{pq}(\boldsymbol{x},t)-h^A_{ij}(\boldsymbol{x},t)]dV=0 \qquad (5.7)$$

for $IWS=1,\ldots,NWS$.

Note that the choice $v^B_k=0$ is compatible with (5.2) and (5.3), provided that we take $s^B_{pqij}=0, h^B_{pq}=0$ and $f^{s,B}_r=-\Delta_{rmij}\partial_m\tau^B_{ij}$.

For the acoustic waves in the fluid parts, the theorem is applied to the bounded subdomain D^f of D where a fluid medium is present. We have (cf. (4.18))

$$\begin{aligned}
&\sum_{IF=1}^{NF}\int_{t\in R}dt\int_{\boldsymbol{x}\in\partial D^{f,IF}}\delta_{mr}\nu^{(IF)}_m[w^A_r(\boldsymbol{x},t)\sigma^B(\boldsymbol{x},t-\tau)+w^B_r(\boldsymbol{x},t-\tau)\sigma^A(\boldsymbol{x},t)]dA\\
&=\partial_\tau\int_{t\in R}dt\int_{\boldsymbol{x}\in D^f}\sigma^B(\boldsymbol{x},t-\tau)[\kappa^A(\boldsymbol{x})-\kappa^B(\boldsymbol{x})]\sigma^A(\boldsymbol{x},t)dV\\
&+\partial_\tau\int_{t\in R}dt\int_{\boldsymbol{x}\in D^f}w^B_k(\boldsymbol{x},t-\tau)[\rho^{f,A}_{kr}(\boldsymbol{x})-\rho^{f,B}_{rk}(\boldsymbol{x})]w^A_r(\boldsymbol{x},t)dV \qquad (5.8)\\
&+\int_{t\in R}dt\int_{\boldsymbol{x}\in D^f}\sigma^B(\boldsymbol{x},t-\tau)q^A(\boldsymbol{x},t)-w^B_k(\boldsymbol{x},t-\tau)f^{f,A}_k(\boldsymbol{x},t)\\
&+\sigma^A(\boldsymbol{x},t)q^B(\boldsymbol{x},t-\tau)-w^A_r(\boldsymbol{x},t)f^{f,B}_r(\boldsymbol{x},t-\tau)dV.
\end{aligned}$$

Equation (5.8) can, from a particular point of view, also be regarded as a "weighted" form of the acoustic equations (2.13) and (2.14) pertaining to State $'A'$. To show this, we take State $'B'$ to be any sequence of piecewise continuously differentiable functions $\{w^B_k(\boldsymbol{x},t;IWF),\sigma^B(\boldsymbol{x},t;IWF)\}$ defined on D^f,

with $IWF = 1, \ldots, NWF$, and take $\{f_r^{f,B}(\boldsymbol{x}, t; IWF), q^B(\boldsymbol{x}, t; IWF)\}$ as (cf. (4.12))

$$\begin{aligned} f_r^{f,B}(\boldsymbol{x}, t-\tau; IWF) &= -\delta_{rm}\partial_m \sigma^B(\boldsymbol{x}, t-\tau; IWF) \\ &\quad +\rho_{rk}^{f,B}(\boldsymbol{x})\partial_{t-\tau} w_k^B(\boldsymbol{x}, t-\tau; IWF) \end{aligned} \tag{5.9}$$

and (cf. (4.13))

$$\begin{aligned} q^B(\boldsymbol{x}, t-\tau; IWF) &= \delta_{mk}\partial_m w_k^B(\boldsymbol{x}, t-\tau; IWF) \\ &\quad -\kappa^B(\boldsymbol{x})\partial_{t-\tau}\sigma^B(\boldsymbol{x}, t-\tau; IWF), \end{aligned} \tag{5.10}$$

for given $\{\rho_{rk}^{f,B}, \kappa\}$. Substitution of these expressions for $f_r^{f,B}$ and q^B in (5.8) leads to

$$\begin{aligned} &\sum_{IF=1}^{NF} \int_{t\in R} dt \int_{\boldsymbol{x}\in\partial D^{f,IF}} \delta_{mr}\nu_m^{(IF)}[w_r^A(\boldsymbol{x}, t)\sigma^B(\boldsymbol{x}, t-\tau; IWF) \\ &+ w_r^B(\boldsymbol{x}, t-\tau; IWF)\sigma^A(\boldsymbol{x}, t)]dA \\ &= \int_{t\in R} dt \int_{\boldsymbol{x}\in D^f} \sigma^B(\boldsymbol{x}, t-\tau; IWF)\kappa^A(\boldsymbol{x})\partial_t\sigma^A(\boldsymbol{x}, t)dV \\ &+ \int_{t\in R} dt \int_{\boldsymbol{x}\in D^f} w_k^B(\boldsymbol{x}, t-\tau; IWF)\rho_{kr}^{f,A}(\boldsymbol{x})\partial_t w_r^A(\boldsymbol{x}, t)dV \\ &+ \int_{t\in R} dt \int_{\boldsymbol{x}\in D^f} \sigma^B(\boldsymbol{x}, t-\tau; IWF)q^A(\boldsymbol{x}, t) - w_k^B(\boldsymbol{x}, t-\tau; IWF)f_k^{f,A}(\boldsymbol{x}, t)dV \\ &+ \int_{t\in R} dt \int_{\boldsymbol{x}\in D^f} \delta_{mk}[\partial_m w_k^B(\boldsymbol{x}, t-\tau; IWF)]\sigma^A(\boldsymbol{x}, t) \\ &+\delta_{mr}w_r^A(\boldsymbol{x}, t)[\partial_m\sigma^B(\boldsymbol{x}, t-\tau; IWF)]dV \\ &\text{for } IWF = 1, \ldots, NWF. \end{aligned} \tag{5.11}$$

Next, by applying Gauss' divergence theorem to the subdomains $D^{f,IF}$, with $IF = 1, \ldots, NF$, in the interiors of which both sides are continuously differentiable, we replace the surface integrals on the left-hand side by a volume integral.

Adding the results, we end up with the desired relation

$$\int_{t\in R} dt \int_{\boldsymbol{x}\in D^f} w_k^B(\boldsymbol{x}, t-\tau; IWF)$$
$$[-\delta_{km}\partial_m \sigma^A(\boldsymbol{x},t) + \rho_{kr}^{f,A}(\boldsymbol{x})\partial_t w_r^A(\boldsymbol{x},t) - f_k^{f,A}(\boldsymbol{x},t)]dV$$
$$-\int_{t\in R} dt \int_{\boldsymbol{x}\in D^f} \sigma^B(\boldsymbol{x}, t-\tau; IWF) \tag{5.12}$$
$$[\delta_{mr}\partial_m w_r^A(\boldsymbol{x},t) - \kappa^A(\boldsymbol{x})\partial_t \sigma^A(\boldsymbol{x},t) - q^A(\boldsymbol{x},t)]dV = 0$$
$$\text{for } IWF = 1,\ldots,NWF.$$

Upon choosing in (5.12) the test function $\sigma^B = 0$ throughout D^f and $w_k^B \neq 0$, we obtain a number of NWF weighted forms of the equation of motion over the space-time domain $D^f \times R$ with the arbitrary piecewise continuously differentiable weighting function w_k^B:

$$\int_{t\in R} dt \int_{\boldsymbol{x}\in D^f} w_k^B(\boldsymbol{x}, t-\tau; IWF)$$
$$[-\delta_{km}\partial_m \sigma^A(\boldsymbol{x},t) + \rho_{kr}^{f,A}(\boldsymbol{x})\partial_t w_r^A(\boldsymbol{x},t) - f_k^{f,A}(\boldsymbol{x},t)]dV = 0 \tag{5.13}$$
$$\text{for } IWF = 1,\ldots,NWF.$$

Note that the choice $\sigma^B = 0$ is compatible with (5.9) and (5.10), provided that we take $\rho_{rk}^{f,B} = 0$, $f_r^{f,B} = 0$ and $q^B = \delta_{mk}\partial_m w_k^B$. Upon choosing the test function $w_k^B = 0$ throughout D^f and $\sigma^B \neq 0$ in (5.12), we obtain a number of NWF weighted forms of the deformation rate equation over the space-time domain $D^f \times R$ with the arbitrary weighting function σ^B:

$$\int_{t\in R} dt \int_{\boldsymbol{x}\in D^f} \sigma^B(\boldsymbol{x}, t-\tau; IWF)$$
$$[\delta_{mr}\partial_m w_r^A(\boldsymbol{x},t) - \kappa^A(\boldsymbol{x})\partial_t \sigma^A(\boldsymbol{x},t) - q^A(\boldsymbol{x},t)]dV = 0 \tag{5.14}$$
$$\text{for } IWF = 1,\ldots,NWF.$$

Note that the choice $w_k^B = 0$ is compatible with (5.9) and (5.10), provided that we take $\kappa^B = 0$, $q^B = 0$ and $f_r^{f,B} = -\delta_{rm}\partial_m \sigma^B$.

Equations (5.5) and (5.12) form the basis of a space-time finite-element method. In these equations the Field $'A'$ remains to be identified with an approximation to the actual wave field, given the chosen sequence of the States $'B'$. Upon taking a reciprocity relation as the point of departure of setting up a numerical scheme, it seems more or less natural to treat the States $'A'$ and $'B'$ in an equivalent manner, which implies that each specimen of the weighted State $'B'$ is also taken as a specimen of the sequence of functions into which State $'A'$ is expanded . As far as (5.5) and (5.12) are concerned, this implies that the sequence of weighting functions is taken to be the same as the sequence of expansion functions. This procedure leads to a square system of linear algebraic equations with the expansion coefficients of State $'A'$ as the unknowns. Boundary conditions of the explicit type are accounted for by prescribing those expansion coefficients that are related to the relevant field values of State $'A'$ at the boundary of D. The above method is known as the method of weighted residuals (see, for example, Dhatt and Touzot (1984); Reddy (1986); Zienkiewicz and Taylor (1989)).

To model an acoustic wave field that radiates into an exterior unbounded domain the Green's function (point-source excitation) of which is known, non-local absorbing acoustic boundary conditions are applied. These boundary conditions relate the wave field quantities at the boundary ∂D to their values in the interior of D via the pertaining (discretized) contrast source-type integral representations. In the solution of the wave problem these relations are added to the equations that follow from using the finite-element method for the interior field in D and the so-called hybrid finite-element method results. The source-type integral representations of the acoustic quantities occurring in this formulation will be discussed in Chapter 6.

Chapter 6

INTEGRAL RELATIONS FOR THE HYBRID FINITE-ELEMENT METHOD

In this chapter, the integral relations for the acoustic wave field quantities that are needed for the hybrid finite-element method are discussed. In their discretized form they lead to non-local absorbing boundary conditions that will simulate the causal radiation of acoustic waves into a sourcefree unbounded embedding of the bounded domain of computation. The geometry to which the integral representations apply is a so-called scattering geometry. Such a geometry consists of a bounded domain D^{SC} whose wave properties show a contrast with those of a given unbounded embedding D_0. The domain D^{SC} is built up of fluid and/or solid parts that may be arbitrarily inhomogeneous and anisotropic. The domain occupied by the fluid parts is denoted by D^f ($D^f \subset D^{SC}$); the domain occupied by the solid parts is denoted by D^s ($D^s \subset D^{SC}$). Obviously, $D^f \cup D^s = D^{SC}$. The embedding D_0 consists of either a fluid or a solid (Figure 6.1). In the case that in D_0 a fluid is present, the medium properties of the embedding are given by its tensorial volume density of fluid mass $\rho^{f,0}_{rk}(\boldsymbol{x})$ and its compressibility $\kappa^0(\boldsymbol{x})$. In the case that in D_0 a solid is present, the medium properties of the embedding are given by its tensorial volume density of solid mass $\rho^{s,0}_{rk}(\boldsymbol{x})$ and its compliance $s^0_{pqij}(\boldsymbol{x})$.

For the construction of the non-local boundary conditions we use the global forms of the reciprocity theorems of the time-convolution type ((3.9) and (3.18)),

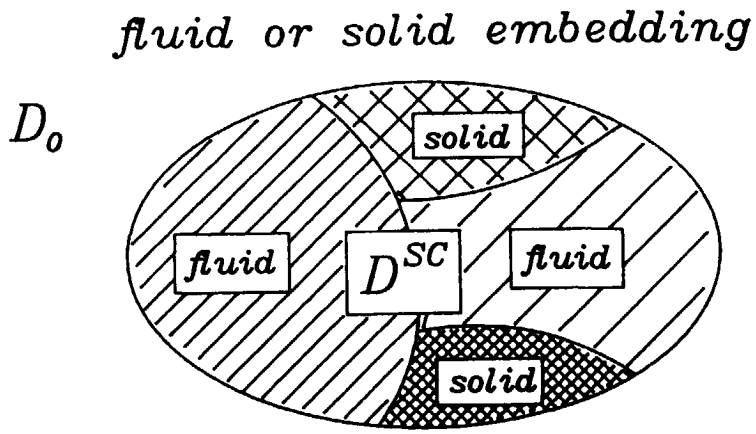

Figure 6.1: The scattering geometry with bounded domain D^{SC} consisting of fluid and/or solid parts in which the wave properties show a contrast with those of the fluid or solid embedding in D_0.

presented in Chapter 3. Which of the two theorems is applied in a particular scattering problem, depends on the type of medium present in the embedding. In the case of a fluid embedding, the reciprocity theorem (3.18) is applied to both the domain D^f and the domain D_0. The results are subsequently combined (in the same way as in which the results for the subdomains $D^{f,IF}$ were combined in Chapter 3 to give an integral relation applying to D^f) to a single integral relation that holds for the fluid part of the scattering configuration. Similarly, in the case of a solid embedding, the reciprocity theorem (3.9) is applied to both the domain D^s and the domain D_0. The results are subsequently combined (in the same way as in which the results for the subdomains $D^{s,IS}$ were combined in Chapter 3 to give an integral relation applying to D^s) to a single integral relation that holds for the solid part of the scattering configuration.

Now, the reciprocity theorems in Chapter 3 have been derived for bounded domains D^s and D^f. In the above described procedure, however, we need them also for the unbounded fluid or solid embeddings. In order to obtain the theorems for the unbounded domain D_0, we first apply them to the bounded domain $D_0 \cap D_\Delta (= D_\Delta \setminus D^{SC})$ where D_Δ is the ball interior to the sphere ∂D_Δ with radius Δ around the origin O. The radius Δ is taken so large that $D^{SC} \subset D_\Delta$ (Figure 6.2). In the relevant result, we finally let $\Delta \to \infty$. For causal acoustic states the contribution from ∂D_Δ then vanishes in the limit $\Delta \to \infty$.

Fluid embedding

In the case of a fluid embedding, the reciprocity theorem (3.18) is applied to the domain $(D_0 \cap D_\Delta) \cup D^f$ $(= D_\Delta \setminus D^s)$. Upon taking $\Delta \to \infty$, we have $(D_0 \cap D_\Delta) \cup D^f \to D_0 \cup D^f$ $(= D_0 \setminus D^s)$. We assume that in D_0 both states correspond to waves that radiate causally away from sources of bounded extent that are located in D^{SC}. Under this condition the surface integral over ∂D_Δ vanishes in the limit $\Delta \to \infty$. The medium properties in D_0 are in both states taken to be the ones applying to the embedding. The volume source distributions of State $'A'$ are taken to be located in D^f, while for the source distributions of State $'B'$ we take sequences of localized sources whose supports are the elements of the discretized version of D^f. Hence, the domain D_0 is sourcefree for both states. The only surface integrals that in the limit $\Delta \to \infty$ remain in the

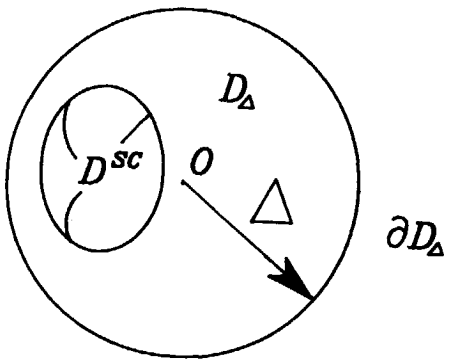

Figure 6.2: The ball D_Δ interior to the sphere ∂D_Δ with radius Δ around the origin O. The domain D^{SC} is a proper subdomain of D_Δ.

reciprocity theorem are then the ones over the fluid/solid boundaries ∂D^s and possibly the ones over the fluid/fluid interfaces, depending on the discontinuities in the wave field quantities in the States 'A' and 'B' (Figure 6.3).

In the reciprocity theorem we now identify State 'A' in D^f with an approximation of the actual acoustic wave field that exists in D^f and assume that this approximation satisfies the boundary conditions (2.17) and (2.18) at the interfaces. Henceforth, the superscript A will be dropped. The medium properties in State 'B' in D^f are also taken to be the ones of the embedding. For the specification of the wave field quantities of State 'B', we first define two finite sequences of localized source distributions. The first sequence consists of localized source distributions in the fluid of the body force type $f_r^f = SF_r^f(\boldsymbol{x}, t; IGF^f)$ with $IGF^f = 1, \ldots, NGF^f$; the second one consists of localized source distributions in the fluid of the injection rate type $q = SF^q(\boldsymbol{x}, t; IGF^q)$ with $IGF^q = 1, \ldots, NGF^q$. Each of these localized source distributions has as its support one of the elements of the discretized geometry that is used in the finite-element modeling of the wave motion in D^f, and has a bounded magnitude. Now, we choose in State 'B' for the sources successively one of these

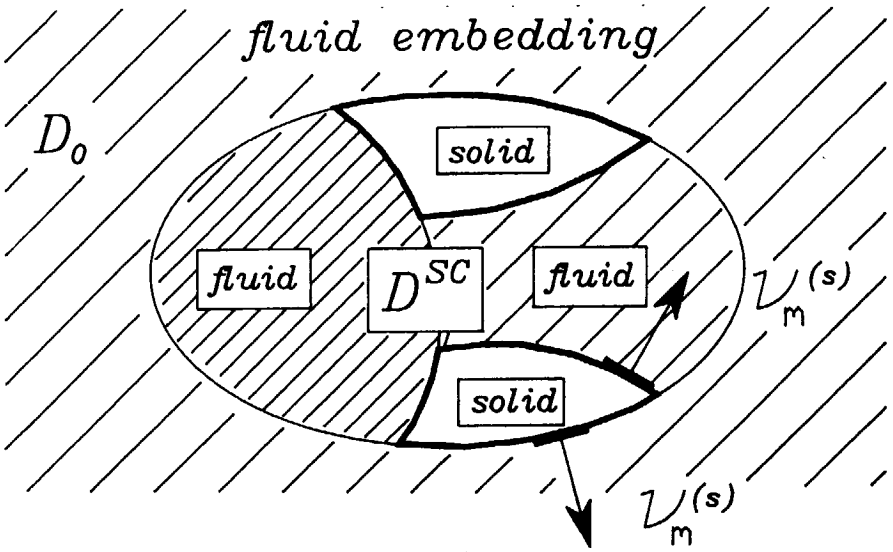

Figure 6.3: The fluid domains (hatched) to which the reciprocity theorem is applied; $\nu_m^{(s)}$ is the unit normal vector at the fluid/solid boundaries pointing away from the solid.

localized source distributions and for the wave field quantities the ones that correspond to the causal wave fields $\{GF_k^{w,f}(\boldsymbol{x},t;IGF^f), GF^{\sigma,f}(\boldsymbol{x},t;IGF^f)\}$ and $\{GF_k^{w,q}(\boldsymbol{x},t;IGF^q),\ GF^{\sigma,q}(\boldsymbol{x},t;IGF^q)\}$, respectively, radiated by these sources and located in a medium with the acoustic wave properties of the embedding. The relevant radiated wave fields are defined in the entire R^3 and satisfy the interface conditions (2.17) and (2.18) everywhere. Henceforth, the relevant radiated wave fields will also be denoted as "discretized" Green's functions because of their similarity to point-source solutions in the non-discretized geometry. Substituting the choices for State 'A' and State 'B' into Equation (3.18), we obtain

$$\int_{t\in R} dt \int_{\boldsymbol{x}\in D^f} w_r(\boldsymbol{x},t) SF_r^f(\boldsymbol{x},\tau-t;IGF^f)dV$$

$$= \int_{t\in R} dt \int_{\boldsymbol{x}\in\partial D^*} \delta_{mr}\nu_m^{(s)}[w_r(\boldsymbol{x},t)GF^{\sigma,f}(\boldsymbol{x},\tau-t;IGF^f)$$

$$- GF_r^{w,f}(\boldsymbol{x},\tau-t;IGF^f)\sigma(\boldsymbol{x},t)]dA$$

$$+ \partial_\tau \int_{t\in R} dt \int_{\boldsymbol{x}\in D^f} GF^{\sigma,f}(\boldsymbol{x},\tau-t;IGF^f)[\kappa(\boldsymbol{x})-\kappa^0(\boldsymbol{x})]\sigma(\boldsymbol{x},t)dV$$

$$
\begin{aligned}
&-\partial_\tau \int_{t\in R} dt \int_{\boldsymbol{x}\in D^f} GF_k^{w,f}(\boldsymbol{x},\tau-t;IGF^f)[\rho_{kr}^f(\boldsymbol{x})-\rho_{rk}^{f,0}(\boldsymbol{x})]w_r(\boldsymbol{x},t)dV \qquad (6.1)\\
&+\int_{t\in R} dt \int_{\boldsymbol{x}\in D^f} [GF^{\sigma,f}(\boldsymbol{x},\tau-t;IGF^f)q(\boldsymbol{x},t)+GF_k^{w,f}(\boldsymbol{x},\tau-t;IGF^f)f_k^f(\boldsymbol{x},t)]dV,\\
&\text{for } IGF^f=1,\ldots,NGF^f,
\end{aligned}
$$

and

$$
\begin{aligned}
&\int_{t\in R} dt \int_{\boldsymbol{x}\in D^f} \sigma(\boldsymbol{x},t)SF^q(\boldsymbol{x},\tau-t;IGF^q)dV\\
&=\int_{t\in R} dt \int_{\boldsymbol{x}\in \partial D^s} \delta_{mr}\nu_m^{(s)}[w_r(\boldsymbol{x},t)GF^{\sigma,q}(\boldsymbol{x},\tau-t;IGF^q)\\
&-GF_r^{w,q}(\boldsymbol{x},\tau-t;IGF^q)\sigma(\boldsymbol{x},t)]dA\\
&+\partial_\tau \int_{t\in R} dt \int_{\boldsymbol{x}\in D^f} GF^{\sigma,q}(\boldsymbol{x},\tau-t;IGF^q)[\kappa(\boldsymbol{x})-\kappa^0(\boldsymbol{x})]\sigma(\boldsymbol{x},t)dV\\
&-\partial_\tau \int_{t\in R} dt \int_{\boldsymbol{x}\in D^f} GF_k^{w,q}(\boldsymbol{x},\tau-t;IGF^q)[\rho_{kr}^f(\boldsymbol{x})-\rho_{rk}^{f,0}(\boldsymbol{x})]w_r(\boldsymbol{x},t)dV \qquad (6.2)\\
&+\int_{t\in R} dt \int_{\boldsymbol{x}\in D^f} [GF^{\sigma,q}(\boldsymbol{x},\tau-t;IGF^q)q(\boldsymbol{x},t)+GF_k^{w,q}(\boldsymbol{x},\tau-t;IGF^q)f_k^f(\boldsymbol{x},t)]dV,\\
&\text{for } IGF^q=1,\ldots,NGF^q.
\end{aligned}
$$

In (6.1) and (6.2), ∂D^s is the fluid/solid boundary and $\nu_m^{(s)}$ the unit vector along its normal pointing away from ∂D^s.

In case the embedding is homogeneous, there exist analytic expressions for the radiated wave fields $\{GF_k^{w,f}, GF^{\sigma,f}\}$ and $\{GF_k^{w,q}, GF^{\sigma,q}\}$. To derive these, the basic wave equations, that now have constant coefficients, are subjected to a time-Laplace transformation and a spatial three-dimensional Fourier transformation. In the space-time transformed domain, the solutions corresponding to the localized body force and injection rate sources can in principle, and in case the embedding is also isotropic, very easily, be found. The corresponding space-time solutions are obtained after the successive application of the inverse spatial Fourier transformation and the inverse time-Laplace transformation. Note that for our discretized Green's functions, the inverse spatial Fourier integrals are uniformly convergent since the result is a bounded function of position.

Equations (6.1) and (6.2) yield relationships between the values of the state quantities in State $'A'$ weighted over each of the supports of the localized sources (the terms in the left-hand sides), the contrast and generating sources in D^f and the boundary values of the wave field at ∂D^s. This aspect lies at the root of the hybrid finite-element modeling to be discussed in Chapter 8.

Solid embedding

In the case of a solid embedding, the reciprocity theorem (3.9) is applied to the domain $(D_0 \cap D_\Delta) \cup D^s$ $(= D_\Delta \setminus D^f)$. Upon taking $\Delta \rightarrow \infty$, we have $(D_0 \cap D_\Delta) \cup D^s \rightarrow D_0 \cup D^s$ $(= D_0 \setminus D^f)$. We assume that in D_0 both states correspond to waves that radiate causally away from sources of bounded extent that are located in D^{SC}. Under this condition the surface integral over ∂D_Δ vanishes in the limit $\Delta \rightarrow \infty$. The medium properties in D_0 are in both states taken to be the ones applying to the embedding. The volume source distributions of State $'A'$ are taken to be located in D^s, while for the source distributions of State $'B'$ we take sequences of localized sources whose supports are the elements of the discretized version of D^s. Hence, the domain D_0 is sourcefree for both states. The only surface integrals that in the limit $\Delta \rightarrow \infty$ remain in the reciprocity theorem are then the ones over the solid/fluid boundaries ∂D^f and possibly the ones over the solid/solid interfaces, depending on the discontinuities in the wave field quantities in the States $'A'$ and $'B'$ (Figure 6.4).

In the reciprocity theorem we now identify State $'A'$ in D^s with an approximation of the actual acoustic wave field that exists in D^s and assume that this approximation satisfies the boundary conditions (2.10) and (2.11) at the interfaces. Henceforth, the superscript A will be dropped. The medium properties in State $'B'$ in D^s are also taken to be the ones of the embedding. For the specification of the other wave field quantities of State $'B'$, we first define two finite sequences of localized source distributions. The first sequence consists of localized source distributions in the solid of the body force type $f_r^s = SS_r^f(\boldsymbol{x}, t; IGS^f)$ with $IGS^f = 1, \ldots, NGS^f$; the second one consists of localized source distributions in the solid of the strain rate type $h_{pq} = SS_{pq}^h(\boldsymbol{x}, t; IGS^h)$ with $IGS^h = 1, \ldots, NGS^h$. Each of these localized source distributions has as its support one of the elements of the discretized geometry that is used in the

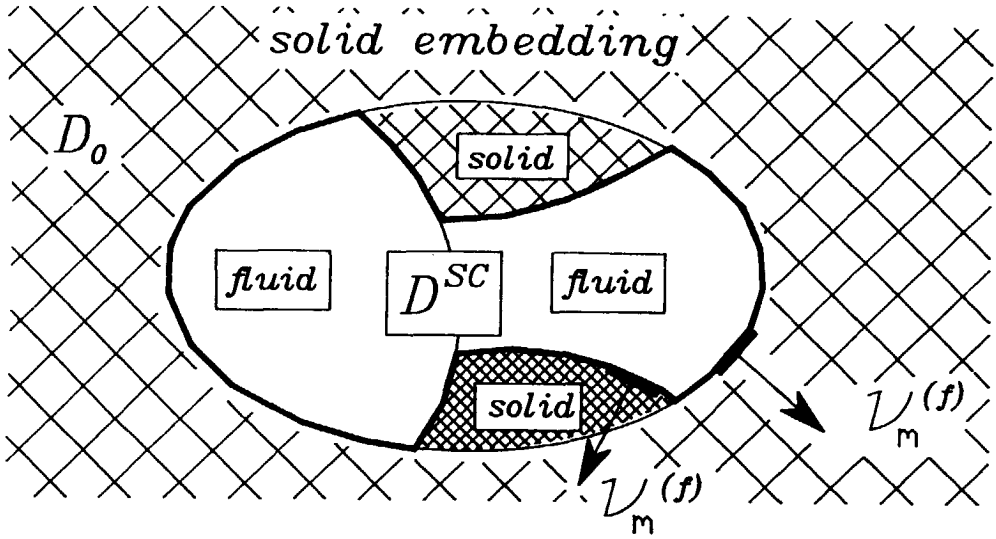

Figure 6.4: The solid domains (hatched) to which the reciprocity theorem is applied; $\nu_m^{(f)}$ is the unit normal vector at the solid/fluid boundaries pointing away from the fluid.

finite-element modeling of the wave motion in D^s, and has a bounded magnitude. Now, we choose in State 'B' for the sources successively one of these localized source distributions and for the wave field quantities the ones that correspond to the causal wave fields $\{GS_k^{v,f}(\boldsymbol{x},t;IGS^f), GS_{ij}^{\tau,f}(\boldsymbol{x},t;IGS^f)\}$ and $\{GS_k^{v,h}(\boldsymbol{x},t;IGS^h),\ GS_{ij}^{\tau,h}(\boldsymbol{x},t;IGS^h)\}$, respectively, radiated by these sources and located in a medium with the acoustic wave properties of the embedding. The relevant radiated wave fields are defined in the entire R^3 and satisfy the interface conditions (2.10) and (2.11) everywhere. Henceforth, the relevant radiated wave fields will also be denoted as "discretized" Green's functions because of their similarity to point-source solutions in the non-discretized geometry. Substituting these choices for State 'A' and State 'B' into Equation (3.9), we obtain

$$\int_{t\in R} dt \int_{\boldsymbol{x}\in D^s} v_r(\boldsymbol{x},t) SS_r^f(\boldsymbol{x},\tau-t)dV$$

$$= \int_{t\in R} dt \int_{\boldsymbol{x}\in\partial D^f} \Delta_{mrpq}\nu_m^{(f)}[v_r(\boldsymbol{x},t)GS_{pq}^{\tau,f}(\boldsymbol{x},\tau-t;IGS^f)$$

$$- GS_r^{v,f}(\boldsymbol{x},\tau-t;IGS^f)\tau_{pq}(\boldsymbol{x},t)]dA \qquad (6.3)$$

$$+\partial_\tau \int_{t\in R} dt \int_{\boldsymbol{x}\in D^s} GS_{ij}^{\tau,f}(\boldsymbol{x},\tau-t;IGS^f)[s_{ijpq}(\boldsymbol{x})-s^0_{pqij}(\boldsymbol{x})]\tau_{pq}(\boldsymbol{x},t)dV$$

$$-\partial_\tau \int_{t\in R} dt \int_{\boldsymbol{x}\in D^s} GS_k^{v,f}(\boldsymbol{x},\tau-t;IGS^f)[\rho^s_{kr}(\boldsymbol{x})-\rho^{s,0}_{rk}(\boldsymbol{x})]v_r(\boldsymbol{x},t)dV$$

$$+\int_{t\in R} dt \int_{\boldsymbol{x}\in D^s} [GS_{ij}^{\tau,f}(\boldsymbol{x},\tau-t;IGS^f)h_{ij}(\boldsymbol{x},t)+GS_k^{v,f}(\boldsymbol{x},\tau-t;IGS^f)f^s_k(\boldsymbol{x},t)]dV,$$

for $IGS^f = 1,\ldots,NGS^f$,

and

$$\int_{t\in R} dt \int_{\boldsymbol{x}\in D^s} \tau_{pq}(\boldsymbol{x},t)SS^h_{pq}(\boldsymbol{x},\tau-t)dV$$

$$=\int_{t\in R} dt \int_{\boldsymbol{x}\in\partial D^f} \Delta_{mrpq}\nu_m^{(f)}[v_r(\boldsymbol{x},t)GS_{pq}^{\tau,h}(\boldsymbol{x},\tau-t;IGS^h)$$

$$-GS_r^{v,h}(\boldsymbol{x},\tau-t;IGS^h)\tau_{pq}(\boldsymbol{x},t)]dA \qquad (6.4)$$

$$+\partial_\tau \int_{t\in R} dt \int_{\boldsymbol{x}\in D^s} GS_{ij}^{\tau,h}(\boldsymbol{x},\tau-t;IGS^h)[s_{ijpq}(\boldsymbol{x})-s^0_{pqij}(\boldsymbol{x})]\tau_{pq}(\boldsymbol{x},t)dV$$

$$-\partial_\tau \int_{t\in R} dt \int_{\boldsymbol{x}\in D^s} GS_k^{v,h}(\boldsymbol{x},\tau-t;IGS^h)[\rho^s_{kr}(\boldsymbol{x})-\rho^{s,0}_{rk}(\boldsymbol{x})]v_r(\boldsymbol{x},t)dV$$

$$+\int_{t\in R} dt \int_{\boldsymbol{x}\in D^s} [GS_{ij}^{\tau,h}(\boldsymbol{x},\tau-t;IGS^h)h_{ij}(\boldsymbol{x},t)+GS_k^{v,h}(\boldsymbol{x},\tau-t;IGS^h)f^s_k(\boldsymbol{x},t)]dV,$$

for $IGS^h = 1,\ldots,NGS^h$.

In (6.3) and (6.4), ∂D^f is the solid/fluid boundary and $\nu_m^{(f)}$ the unit vector along its normal pointing away from ∂D^f.

In case the embedding is homogeneous, there exist analytic expressions for the radiated wave fields $\{GS_k^{v,f}, GS_{ij}^{\tau,f}\}$ and $\{GS_k^{v,h}, GS_{ij}^{\tau,h}\}$. To derive these, the basic wave equations, that now have constant coefficients, are subjected to a time-Laplace transformation and a spatial three-dimensional Fourier transformation. In the space-time transformed domain, the solutions corresponding to the localized body force and strain rate sources can in principle, and in case the embedding is also isotropic, easily, be found. The corresponding space-time solutions are obtained after the successive application of the inverse spatial Fourier transformation and the inverse time-Laplace transformation. Note that for our

discretized Green's functions, the inverse spatial Fourier integrals are uniformly convergent since the result is a bounded function of position.

Equations (6.3) and (6.4) yield relationships between the values of the state quantities in State $'A'$ weighted over each of the supports of the localized sources (the terms in the left-hand sides), the contrast and generating sources in D^s and the boundary values of the wave field at ∂D^J. This aspect lies at the root of the hybrid finite-element modeling to be discussed in Chapter 8.

Chapter 7

EXPANSION AND WEIGHTING FUNCTIONS FOR THE FINITE-ELEMENT METHOD

Discretization Procedure

In the hybrid finite-element method for the scattering geometry introduced in Chapter 6, the finite-element computations are restricted to the bounded domain D^{SC}. The numerical handling of our acoustic wave problem in D^{SC} implies that some discretized version of it is used to 'approximate' the actual analytic one defined through the partial differential equations, the boundary conditions and the initial conditions presented in Chapter 2. We observe that each fluid quantity $QF = QF(\boldsymbol{x}, t)$ occurring in the acoustic wave problem (which can be a scalar, a vector, or a tensor of arbitrary rank) and defined on the domain D^f has, after discretization, a discretized counterpart $[QF] = [QF](\boldsymbol{x}, t)$ defined on the discretized version $[D^f]$ of D^f. Similarly, each solid quantity $QS = QS(\boldsymbol{x}, t)$ occurring in the acoustic wave problem (which can also be a scalar, a vector, or a tensor of arbitrary rank) and defined on the domain D^s has, after discretization, a discretized counterpart $[QS] = [QS](\boldsymbol{x}, t)$ defined on the discretized version $[D^s]$ of D^s. In the applied discretization procedure the discretized version $[D^{SC}]$ of D^{SC} is the union of the domains $[D^f]$ and $[D^s]$, i.e., $[D^{SC}] = [D^f] \cup [D^s]$.

[0]The theory developed in this chapter has been presented in Stam and De Hoop (1990)

To define in what sense the discretized wave field quantities approximate the actual ones in the domains $[D^f]$ and $[D^s]$ we use the relations (5.12) and (5.5), respectively, that have been derived from the reciprocity theorems of the time-correlation type for a fluid and a solid. In the application of the relation (5.12) to the discretized fluid domain $[D^f]$, we first choose an appropriate sequence of piecewise continuously differentiable weighting functions $\{w_k^B(\boldsymbol{x},t;IWF),\sigma^B(\boldsymbol{x},t;IWF)\}$ with $IWF = 1,\ldots,NWF$, defined on $[D^f]$. Next, the discretized fluid quantities $[QF]$ are substituted. Now, the discretized fluid wave field quantities are considered to be an approximation of the exact ones in $[D^f]$ if they satisfy the relation (5.12) for the whole sequence of chosen weighting functions in the State $'B'$. Similarly, in the application of the relation (5.5) to the discretized solid domain $[D^s]$, we first choose an appropriate sequence of piecewise continuously differentiable weighting functions $\{v_k^B(\boldsymbol{x},t;IWS),\tau_{ij}^B(\boldsymbol{x},t;IWS)\}$ with $IWS = 1,\ldots,NWS$, defined on $[D^s]$. Next, the discretized solid quantities $[QS]$ are substituted. Now, again, the discretized solid wave field quantities are considered to be an approximation of the exact ones in $[D^s]$ if they satisfy the relation (5.5) for the whole sequence of chosen weighting functions in the State $'B'$.

The approximation of the acoustic wave field in the whole scattering domain $[D^{SC}]$ is obtained by linking the ones in $[D^f]$ to the ones in $[D^s]$ along the fluid/solid interfaces occurring in $[D^{SC}]$, where the relevant interface conditions are required.

Discretization of the Computational Domain

The domain of computation D^{SC} is discretized by taking it to be the union $[D^{SC}] = \bigcup_{IT=1}^{NT} T(IT)$ of a finite number of tetrahedra $\{T(IT); IT = 1,\ldots,NT\}$ (simplices in R^3) that all have vertices, edges and faces in common (see, Naber 1980). The vertices of the tetrahedra will also be denoted as the nodes of the (geometrical) mesh and the supremum h of the maximum diameters of the tetrahedra will be denoted as the mesh size.

Except for the (discretized) Green's functions that have been introduced in Chapter 6, each quantity $QF = QF(\boldsymbol{x},t)$ and $QS = QS(\boldsymbol{x},t)$ occurring in the acoustic wave-field problem will, in the interior of each tetrahedron, be

approximated by the linear interpolation of its values at the vertices. We use a local numbering that applies to each of the tetrahedra. The four vertices of a tetrahedron T are denoted by $\{P(0),\ P(1),\ P(2),\ P(3)\}$ and their position vectors by $\{x_l(0), x_l(1), x_l(2), x_l(3)\}$, respectively. The position in the interior of T or on its boundary ∂T can be specified by the barycentric coordinates $\{\lambda(0), \lambda(1), \lambda(2), \lambda(3)\}$ defined through

$$x_l = \sum_{I^V=0}^{3} \lambda(I^V) x_l(I^V) \quad \text{with} \quad 0 \leq \lambda(I^V) \leq 1 \quad \text{and} \quad \sum_{I^V=0}^{3} \lambda(I^V) = 1. \tag{7.1}$$

We observe that the barycentric coordinates $\lambda(I^V)$ do perform the linear interpolation in the tetrahedron (viz. of the position vector) we are looking for. To express the barycentric coordinates in terms of x_l, some geometrical quantities associated with T are needed. First, the vectorial areas $\{A_l(0), A_l(1), A_l(2), A_l(3)\}$ of the faces of T that are directed along the outward normals to the faces of T are introduced; they are given by (for the numbering we refer to Figure 7.1)

$$\begin{aligned}
A_l(0) &= \varepsilon_{lmn}(x_m(1)x_n(2) + x_m(2)x_n(3) + x_m(3)x_n(1))/2, \\
A_l(1) &= -\varepsilon_{lmn}(x_m(2)x_n(3) + x_m(3)x_n(0) + x_m(0)x_n(2))/2, \\
A_l(2) &= \varepsilon_{lmn}(x_m(3)x_n(0) + x_m(0)x_n(1) + x_m(1)x_n(3))/2, \\
A_l(3) &= -\varepsilon_{lmn}(x_m(0)x_n(1) + x_m(1)x_n(2) + x_m(2)x_n(0))/2,
\end{aligned} \tag{7.2}$$

where ε_{lmn} is the completely antisymmetric unit tensor of rank three (Levi-Civita tensor). The magnitude of the vectorial surface $A_l(I^V)$ is denoted by $A(I^V)$. From (7.2) it follows that

$$\sum_{I^V=0}^{3} A_l(I^V) = 0. \tag{7.3}$$

The volume of T is given by

$$\begin{aligned}
V &= \varepsilon_{lmn}(-x_l(0)x_m(1)x_n(2) + x_l(1)x_m(2)x_n(3) \\
&\quad -x_l(2)x_m(3)x_n(0) + x_l(3)x_m(0)x_n(1))/6.
\end{aligned} \tag{7.4}$$

Now, we observe that at each vertex of T, the three vectorial edges leaving that vertex and the three vectorial faces meeting at that vertex form, apart from

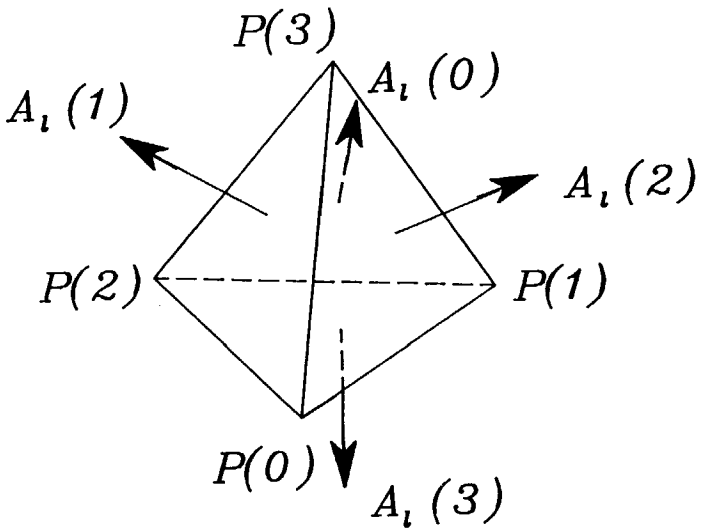

Figure 7.1: Tetrahedron T with its four vertices $\{P(0), P(1), P(2), P(3)\}$ and the outwardly directed vectorial areas $\{A_l(0), A_l(1), A_l(2), A_l(3)\}$ of its faces.

a constant factor, a set of (oblique) reciprocal base vectors. Let us consider the vertex $P(0)$. The three vectorial edges leaving this vertex are $\{x_l(1) - x_l(0), x_l(2) - x_l(0), x_l(3) - x_l(0)\}$ and the three vectorial areas of the faces meeting at this vertex are $\{A_l(1), A_l(2), A_l(3)\}$. Now, it is easily verified that

$$[x_l(I^V) - x_l(0)]A_l(J^V) = -3V\delta(I^V, J^V) \quad \text{with} \quad I^V = 1,2,3 \quad \text{and} \quad J^V = 1,2,3, \tag{7.5}$$

where $\delta(I^V, I^V) = 1$ and $\delta(I^V, J^V) = 0$ if $I^V \neq J^V$. From (7.5) it follows that, at the vertex with position vector $x_l(0)$, the set of vectors $\{-[x_l(1) - x_l(0)]/3V, -[x_l(2) - x_l(0)]/3V, -[x_l(3) - x_l(0)]/3V\}$ is reciprocal to the set $\{A_l(1), A_l(2), A_l(3)\}$, and the set $\{-A_l(1)/3V, -A_l(2)/3V, -A_l(3)/3V\}$ is reciprocal to the set $\{x_l(1) - x_l(0), x_l(2) - x_l(0), x_l(3) - x_l(0)\}$. Returning to (7.1), we can, by letting $\lambda(0) = 1 - \lambda(1) - \lambda(2) - \lambda(3)$, write

$$x_l - x_l(0) = \sum_{I^V=1}^{3} \lambda(I^V)[x_l(I^V) - x_l(0)]. \tag{7.6}$$

Upon multiplying this equation by $-(3V)^{-1}A_l(J^V)$ and using (7.5) we obtain

$$-(3V)^{-1}[x_l - x_l(0)]A_l(J^V) = \lambda(J^V) \quad \text{for } J^V = 1,2,3. \tag{7.7}$$

Since further, on account of (7.3) and (7.7)

$$-(3V)^{-1}[x_l - x_l(0)]A_l(0) = -\sum_{I^V=1}^{3} \lambda(I^V), \tag{7.8}$$

(7.6) leads to

$$x_l - x_l(0) = -(3V)^{-1} \sum_{J^V=0}^{3} [x_m - x_m(0)]A_m(J^V)x_l(J^V). \tag{7.9}$$

Similar results hold for the other vertices as well. By combining the results we have

$$x_l - x_l(I^V) = -(3V)^{-1} \sum_{J^V=0}^{3} [x_m - x_m(I^V)]A_m(J^V)x_l(J^V) \quad \text{for} \quad I^V = 0,1,2,3. \tag{7.10}$$

Summing the results for $I^V = 0,1,2,3$, respectively, and introducing the position vector b_l of the barycenter of T through

$$b_l = (1/4) \sum_{I^V=0}^{3} x_l(I^V), \tag{7.11}$$

we arrive at the symmetrical expression

$$x_l = b_l - (3V)^{-1} \sum_{I^V=0}^{3} (x_m - b_m) A_m(I^V) x_l(I^V). \tag{7.12}$$

On account of this relation, we can write

$$x_l = \sum_{I^V=0}^{3} x_l(I^V) \phi(I^V; \boldsymbol{x}), \tag{7.13}$$

where

$$\phi(I^V; \boldsymbol{x}) = 1/4 - (3V)^{-1} (x_m - b_m) A_m(I^V). \tag{7.14}$$

Comparing (7.13) with (7.1), we see that $\{\phi(I^V; \boldsymbol{x}); I^V = 0, 1, 2, 3\}$ are nothing but the barycentric coordinates of a point in T or on its boundary. On the other hand, $\phi(I^V; \boldsymbol{x})$ performs a linear interpolation between the value one at the vertex $x_l = x_l(I^V)$ and the value zero at the remaining vertices of T.

In the tetrahedron T we use the functions $\phi(I^V; \boldsymbol{x})$ as local expansion functions. The linear interpolation of a quantity $QF(\boldsymbol{x}, t)$ in a tetrahedron T present in $[D^f]$ is correspondingly given by

$$[QF](\boldsymbol{x}, t) = \sum_{I^V=0}^{3} A^{QF}(I^V; t) \phi(I^V; \boldsymbol{x}) \quad \text{for } \boldsymbol{x} \in T, \tag{7.15}$$

in which

$$A^{QF}(I^V; t) = QF(\boldsymbol{x}(I^V); t) \tag{7.16}$$

is the value of QF at the vertex with ordinal number I^V. The linear interpolation of a quantity $QS(\boldsymbol{x}, t)$ in a tetrahedron T present in $[D^s]$ is given by

$$[QS](\boldsymbol{x}, t) = \sum_{I^V=0}^{3} A^{QS}(I^V; t) \phi(I^V; \boldsymbol{x}) \quad \text{for } \boldsymbol{x} \in T, \tag{7.17}$$

in which

$$A^{QS}(I^V; t) = QS(\boldsymbol{x}(I^V); t) \tag{7.18}$$

is the value of QS at the vertex with ordinal number I^V. The global expansions, for the domain $[D^{SC}]$, of the quantities $[QF]$ and $[QS]$ follow by combining all the local expansions. For the fluid quantities the latter are written as

$$[QF](\boldsymbol{x}, t) = \sum_{IT=1}^{NT} \sum_{I^V=0}^{3} A^{QF}(IT, I^V; t) \Phi(IT, I^V; \boldsymbol{x}) \quad \text{for } \boldsymbol{x} \in [D^{SC}], \tag{7.19}$$

in which

$$A^{QF}(IT, I^V; t) = QF(\boldsymbol{x}(I^V); t) \text{ for } \boldsymbol{x} \in T(IT) \tag{7.20}$$

is the value of QF in the tetrahedron $T(IT)$ at its vertex with ordinal number I^V. For the solid quantities they are written as

$$[QS](\boldsymbol{x}, t) = \sum_{IT=1}^{NT} \sum_{I^V=0}^{3} A^{QS}(IT, I^V; t)\Phi(IT, I^V; \boldsymbol{x}) \quad \text{for } \boldsymbol{x} \in [D^{SC}], \tag{7.21}$$

in which

$$A^{QS}(IT, I^V; t) = QS(\boldsymbol{x}(I^V); t) \text{ for } \boldsymbol{x} \in T(IT) \tag{7.22}$$

is the value of QS in the tetrahedron $T(IT)$ at its vertex with ordinal number I^V. In (7.19) and (7.21), the global expansion functions Φ are defined by

$$\Phi(IT, I^V; \boldsymbol{x}) = \phi(I^V; \boldsymbol{x})\chi_{T(IT)}(\boldsymbol{x}) \quad \text{for } \boldsymbol{x} \in [D^{SC}], \tag{7.23}$$

where $\chi_D(\boldsymbol{x})$ is the characteristic function of the set D, defined as

$$\chi_D(\boldsymbol{x}) = \begin{cases} 0 & \text{when } \boldsymbol{x} \notin D \\ 1 & \text{when } \boldsymbol{x} \in D. \end{cases} \tag{7.24}$$

Discretization of the Medium Parameters

In the discretization of the medium parameters a distinction must be made between subdomains in which these parameters vary continuously with position and subdomains in which surfaces of discontinuity in these parameters occur. It is assumed that across such surfaces of discontinuity in medium parameters, the parameter values jump by finite amounts. Especially in applications where accurate values of the wave-field quantities up to these surfaces are needed (such as, for example, in the modeling of borehole measurement situations in exploration geophysics, and in the non-destructive evaluation of mechanical structures), special measures have to be taken to model the behavior of these quantities accurately. In principle, the medium properties can jump across any face of any tetrahedron of the discretized geometry. To accomodate this feature, all nodes of the geometrical mesh are considered as multiple nodes, where the multiplicity of each node is equal to the number of tetrahedra that meet at that node (Figure 7.2). The values of the constitutive parameters at the vertices follow

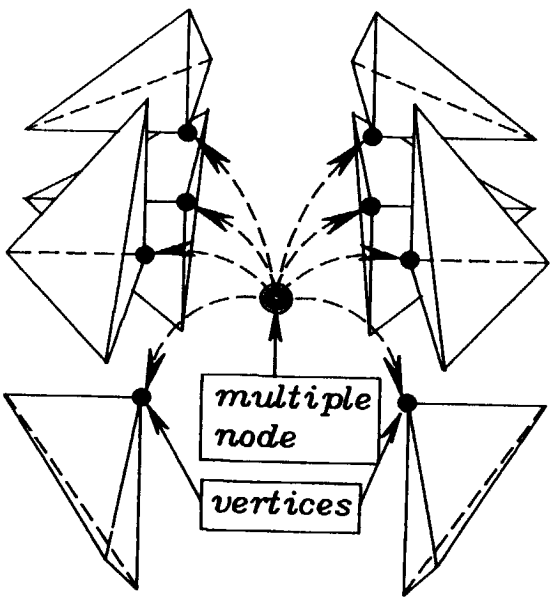

Figure 7.2: A multiple node in the discretized geometry and the tetrahedra that meet in this node. The multiplicity of the node in the figure is equal to eight.

from user-supplied input expressions that are spatially sampled in the interior of each tetrahedron close to each of its vertices. Out of the thus constructed local expansions of the medium parameters, their global expansions over the domain of computation are composed. In these global representations a global numbering is applied which is related to the local numbering by

$$I = IT * I^V \quad \text{for } IT = 1, \ldots, NT, I^V = 0, \ldots, 3. \tag{7.25}$$

For a non-scalar constitutive parameter (such as the tensorial volume density of mass for a fluid or a solid) the components with respect to the background Cartesian reference frame are used in the discretization procedure. The relevant global expansions for the fluid properties are written as

$$[\rho^f_{kr}(\boldsymbol{x})] = \sum_{I^{\rho;f}=1}^{N^{\rho;f}} A^{\rho;f}_{kr}(I^{\rho;f}) \Phi^{\rho;f}(I^{\rho;f}; \boldsymbol{x}) \quad \text{for } \boldsymbol{x} \in [D^{SC}] \tag{7.26}$$

for the fluid's tensorial density of mass, where $\{\Phi^{\rho;f}(I^{\rho;f}; \boldsymbol{x}); I^{\rho;f} = 1, \ldots, N^{\rho;f}\}$ is the sequence of its global linear expansion functions and $\{A^{\rho;f}_{kr}(I^{\rho;f}); I^{\rho;f} = 1, \ldots, N^{\rho;f}\}$ is the sequence of its global tensorial expansion coefficients, and

$$[\kappa(\boldsymbol{x})] = \sum_{I^\kappa=1}^{N^\kappa} A^\kappa(I^\kappa) \Phi^\kappa(I^\kappa, \boldsymbol{x}) \quad \text{for } \boldsymbol{x} \in [D^{SC}] \tag{7.27}$$

for the fluid's compressibility, where $\{\Phi^\kappa(I^\kappa; \boldsymbol{x}); I^\kappa = 1, \ldots, N^\kappa\}$ is the sequence of its global linear expansion functions and $\{A^\kappa(I^\kappa); I^\kappa = 1, \ldots, N^\kappa\}$ is the sequence of its global scalar expansion coefficients. The relevant global expansions for the solid properties are written as

$$[\rho^s_{kr}(\boldsymbol{x})] = \sum_{I^{\rho;s}=1}^{N^{\rho;s}} A^{\rho;s}_{kr}(I^{\rho;s}) \Phi^{\rho;s}(I^{\rho;s}; \boldsymbol{x}) \quad \text{for } \boldsymbol{x} \in [D^{SC}] \tag{7.28}$$

for the solid's volume density of mass, where $\{\Phi^{\rho;s}(I^{\rho;s}; \boldsymbol{x}); I^{\rho;s} = 1, \ldots, N^{\rho;s}\}$ is the sequence of its global linear expansion functions and $\{A^{\rho;s}_{kr}(I^{\rho;s}); I^{\rho;s} = 1, \ldots, N^{\rho;s}\}$ is the sequence of its global tensorial expansion coefficients, and

$$[s_{ijpq}(\boldsymbol{x})] = \sum_{I^s=1}^{N^s} A^s_{ijpq}(I^s) \Phi^s(I^s; \boldsymbol{x}) \quad \text{for } \boldsymbol{x} \in [D^{SC}] \tag{7.29}$$

for the solid's compliance, where $\{\Phi^s(I^s;\boldsymbol{x}); I^s = 1,\ldots,N^s\}$ is the sequence of its global linear expansion functions and $\{A^s_{ijpq}(I^s); I^s = 1,\ldots,N^s\}$ is the sequence of its global tensorial expansion coefficients.

Discretization of the Volume Source Densities

For the discretization of the volume source densities the same procedure as for the discretization of the medium parameters is followed. The values of the volume source densities at the vertices of the tetrahedra out of which the discretized geometry is composed, follow from user-supplied input expressions that are sampled in the interior of each tetrahedron close to each of its vertices. Out of the thus constructed local expansions of the volume source densities, their global expansions over the domain of computation are composed in the same way as is done for the medium parameters (with the same global numbering (cf. (7.25))). Here, too, for the non-scalar volume source densities the components with respect to the background Cartesian reference frame are used in the discretization procedure. The relevant global expansions for the volume source densities in the fluid are written as

$$[f^f_k(\boldsymbol{x},t)] = \sum_{I^{f;f}=1}^{N^{f;f}} A^{f;f}_k(I^{f;f};t)\Phi^{f;f}(I^{f;f};\boldsymbol{x}) \quad \text{for } \boldsymbol{x}\in[D^{SC}] \tag{7.30}$$

for the volume source density of body force in a fluid, where $\{\Phi^{f;f}(I^{f;f};\boldsymbol{x}); I^{f;f} = 1,\ldots,N^{f;f}\}$ is the sequence of its global linear expansion functions and $\{A^{f;f}_k(I^{f;f};t); I^{f;f} = 1,\ldots,N^{f;f}\}$ is the sequence of its global vectorial expansion coefficients, and

$$[q(\boldsymbol{x},t)] = \sum_{I^q=1}^{N^q} A^q(I^q;t)\Phi^q(I^q;\boldsymbol{x}) \quad \text{for } \boldsymbol{x}\in[D^{SC}] \tag{7.31}$$

for the volume source density of injection rate, where $\{\Phi^q(I^q;\boldsymbol{x}); I^q = 1,\ldots,N^q\}$ is the sequence of its global linear expansion functions and $\{A^q(I^q;t); I^q = 1,\ldots,N^q\}$ is the sequence of its global scalar expansion coefficients. The relevant global expansions for the volume source densities in the solid are written as

$$[f^s_k(\boldsymbol{x},t)] = \sum_{I^{f;s}=1}^{N^{f;s}} A^{f;s}_k(I^{f;s};t)\Phi^{f;s}(I^{f;s};\boldsymbol{x}) \quad \text{for } \boldsymbol{x}\in[D^{SC}] \tag{7.32}$$

for the volume source density of body force in a solid where $\{\Phi^{f;s}(I^{f;s};\boldsymbol{x}); I^{f;s} = 1,\ldots,N^{f;s}\}$ is the sequence of its global linear expansion functions and $\{A^{f;s}_k(I^{f;s};t);$

$I^{f;s} = 1, \ldots, N^{f;s}\}$ is the sequence of its global vectorial expansion coefficients, and

$$[h_{ij}(\boldsymbol{x}, t)] = \sum_{I^h=1}^{N^h} A_{ij}^h(I^h; t)\Phi^h(I^h; \boldsymbol{x}) \quad \text{for } \boldsymbol{x} \in [D^{SC}] \tag{7.33}$$

for the volume source density of injection rate, where $\{\Phi^h(I^h; \boldsymbol{x}); I^h = 1, \ldots, N^h\}$ is the sequence of its global linear expansion functions and $\{A_{ij}^h(I^h; t);\ I^h = 1, \ldots, N^h\}$ is the sequence of its global expansion tensorial expansion coefficients.

Discretization of the Wave-Field Quantities

In the discretization of the acoustic wave field quantities the situation is more complicated. Here, some components are by necessity continuous across an interface of discontinuity in material properties, while other components show a finite jump across such a discontinuity surface. To preserve accuracy in the computational results, it is necessary to take computational measures that enforce the continuity conditions across an interface (in machine precision) and leave the non-continuous components free to jump by finite amounts. The procedure we apply is explained for an arbitrary non-scalar wave field quantity Q that has to be approximated. This quantity can represent the fluid particle velocity w_r in $[D^f]$, the solid particle velocity v_r in $[D^s]$ or the stress τ_{pq} in $[D^s]$. The non-scalar expansion coefficients in (7.15) and (7.17) have at each vertex to be decomposed along a certain base consisting of three linearly independent vectors. In a number of circumstances, the base vectors of the global Cartesian background reference frame serve this purpose. Depending on the indicated continuity requirements it may, however, be necessary to use local base vectors instead of the global ones. As such, the three edges that leave the vertex under consideration are candidates, as well as the three vectorial areas of the faces that meet at that vertex. These two systems form, locally, a set of reciprocal base vectors. (cf. (7.5)). The actual choice to be made depends on the behavior of the medium properties in the neighborhood of the vertex (node) under consideration.

The interfaces of discontinuity in the material properties that may occur in the scattering domain D^{SC} are of the fluid/fluid, the solid/solid, or the

fluid/solid type. The relevant continuity conditions for a fluid/fluid interface are given by (2.17) and (2.18), for a solid/solid interface by (2.10) and (2.11), and for a fluid/solid interface by (2.19), (2.20) and (2.21). The specific choices of the vectorial/tensorial decompositions of the wave field quantities at the vertices of a tetrahedron are displayed below. Note that for a scalar quantity no base of decomposition is required.

Choice of the vectorial/tensorial decompositions at the vertices of a tetrahedron

Vertex coincides with nodal point not on an interface

In a vertex that coincides with a nodal point that is not on an interface we decompose the field quantities along the axes of the background Cartesian reference frame.

Vertex coincides with nodal point on a solid/solid interface

Across a solid/solid interface all components of the solid particle velocity and the normal component of the stress (the traction) are to be continuous, while the tangential components of the stress may jump by finite amounts. Accordingly, in a vertex $P(I^V)$ of a tetrahedron T that coincides with a nodal point located on a solid/solid interface, the solid particle velocity is decomposed along the axes of the background Cartesian reference frame, and the stress $\tau_{pq}(I^V;t)$ is written as

$$\tau_{pq}(I^V;t) = -(3V)^{-1} \sum_{J^V=0}^{3} T_p(I^V,J^V;t)[x_q(J^V) - x_q(I^V)]A(J^V). \tag{7.34}$$

Equation (7.34) implies that the second subscript of $\tau_{pq}(I^V;t)$ is decomposed along the local base vectors $\{-(3V)^{-1}[x_q(J^V)-x_q(I^V)]A(J^V); J^V = 0,1,2,3, J^V \neq I^V\}$ that are directed along the edges meeting in $P(I^V)$. Using (7.5), it follows that the expansion coefficient

$$T_p(I^V,J^V;t) = \tau_{pq}(I^V;t)A_q(J^V)/A(J^V) \quad \text{with } I^V \neq J^V, \tag{7.35}$$

is the traction at the face with vectorial area $A_q(J^V)$ in the vertex $P(I^V)$. Obviously, the term with $J^V = I^V$ drops automatically from the summation (7.34); for later purposes it is, however, advantageous to put

$$T_p(I^V,I^V;t) = 0. \tag{7.36}$$

The factor $A(J^V)$ in (7.34) and (7.35) drops out in the final result but is introduced for the computational reason that the expansion coefficients truly have the magnitude and dimension of a traction.

Vertex coincides with nodal point on a fluid/fluid interface

Across a fluid/fluid interface the normal component of the fluid particle velocity is to be continuous, while its tangential components may jump by finite amounts. Accordingly, in a vertex $P(I^V)$ of a tetrahedron T that coincides with a nodal point located on a fluid/fluid interface, the fluid particle velocity is written as

$$w_r(I^V;t) = -(3V)^{-1} \sum_{J^V=0}^{3} W(I^V, J^V;t)[x_r(J^V) - x_r(I^V)]A(J^V). \tag{7.37}$$

Equation (7.37) implies that the particle velocity $w_r(I^V;t)$ is decomposed along the local base vectors $\{-(3V)^{-1}\,[x_r(J^V) - x_r(I^V)]\,A(J^V), J^V = 0,1,2,3, J^V \neq I^V\}$ that are directed along the edges meeting in $P(I^V)$. Using (7.5), it follows that the expansion coefficient

$$W(I^V, J^V;t) = w_r(I^V;t)A_r(J^V)/A(J^V) \quad \text{with } I^V \neq J^V, \tag{7.38}$$

is the magnitude of the normal component of the fluid particle velocity at the face with vectorial area $A_r(J^V)$ in the vertex $P(I^V)$. Obviously, the term with $J^V = I^V$ drops automatically from the summation (7.37); for later purposes it is, however, advantageous to put

$$W(I^V, I^V;t) = 0 \tag{7.39}$$

Here, too, the factor $A(J^V)$ is introduced for the computational convenience that the expansion coefficients truly have the magnitude and the dimension of a velocity.

Vertex coincides with nodal point on a fluid/solid interface

At a fluid/solid interface the normal component of the fluid particle velocity is equal to the normal component of the solid particle velocity while their tangential components may differ by finite amounts. Further, the normal component of the traction in the solid is equal to the scalar traction in the fluid, while the tangential components of the traction in the solid are equal to zero. Accordingly,

in a vertex $P(I^V)$ of a tetrahedron T situated in the solid part that coincides with a nodal point that is located on a fluid/solid interface, the solid particle velocity is written as

$$v_r(I^V;t) = -(3V)^{-1} \sum_{J^V=0}^{3} V(I^V,J^V;t)[x_r(J^V) - x_r(I^V)]A(J^V). \tag{7.40}$$

In (7.40), the particle velocity $v_r(I^V;t)$ is decomposed along the local base vectors $\{-(3V)^{-1}[x_r(J^V)-x_r(I^V)]A(J^V), J^V = 0,1,2,3, J^V \neq I^V\}$ that are directed along the edges meeting in $P(I^V)$. Using (7.5), it follows that the expansion coefficient

$$V(I^V,J^V;t) = v_r(I^V;t)A_r(J^V)/A(J^V) \quad \text{with } I^V \neq J^V, \tag{7.41}$$

is the magnitude of the normal component of the solid particle velocity at the face with vectorial area $A_r(J^V)$ in the vertex $P(I^V)$. Obviously, the term with $J^V = I^V$ drops automatically from the summation (7.40); for later purposes it is, however, advantageous to put

$$V(I^V,I^V;t) = 0. \tag{7.42}$$

In a vertex $P(I^V)$ of a tetrahedron T situated in the fluid part that coincides with a nodal point that is located on a fluid/solid interface, the fluid particle velocity is, again, represented by (7.37). Finally, the stress $\tau_{pq}(I^V;t)$ is represented by (7.34) where the coefficient $T_p(I^V,J^V;t)$ is now given by

$$\begin{aligned} T_p(I^V,J^V;t) &= \sum_{K^V=0}^{3} T(I^V,J^V,K^V;t)\{\delta(J^V,K^V)A_p(K^V)/A(K^V) \\ &+ [1-\delta(J^V,K^V)]\varepsilon_{pkl}A_k(J^V)[x_l(K^V) - x_l(I^V)]/[2(A(J^V))^2]\} \end{aligned} \tag{7.43}$$

where ε_{pkl} is the completely antisymmetric unit tensor of rank three (Levi-Civita tensor). With the representation (7.43), the traction at the face with vectorial area $A_p(J^V)$ in the vertex $P(I^V)$ is decomposed along the base vectors $A_p(J^V)/A(J^V)$, and $\{\varepsilon_{pkl}A_k(J^V)[x_l(K^V) - x_l(I^V)], K^V = 0,1,2,3, K^V \neq I^V, K^V \neq J^V\}$. The first one is nothing but the unit normal vector of the face with vectorial area $A_p(J^V)$; the two other ones are perpendicular to the normal vector of this face and one of its two edges that meet in the vertex $P(I^V)$.

Obviously, the expansion coefficient

$$T(I^V, J^V, J^V; t) = T_p(I^V, J^V; t) A_p(J^V)/A(J^V) \quad \text{with } J^V \neq I^V, \tag{7.44}$$

is the magnitude of the normal component of the traction at the face with vectorial area $A_p(J^V)$ in $P(I^V)$. Further, the two expansion coefficients

$$\begin{aligned} T(I^V, J^V, K^V; t) \;=\; & T_p(I^V, J^V; t)[x_p(L^V) - x_p(I^V)] \\ & \text{with } K^V \neq I^V, K^V \neq J^V, L^V \neq I^V, L^V \neq J^V \\ & \text{and } K^V \neq L^V, \end{aligned} \tag{7.45}$$

are the innerproducts of the traction at the face with vectorial area $A_p(J^V)$ in the vertex $P(I^V)$ with the two edges of this face that meet in $P(I^V)$ and completely determine the tangential component of the traction in $P(I^V)$. Substitution of (7.43) into (7.34) gives the representation of the stress $\tau_{pq}(I^V; t)$ in the vertex $P(I^V)$ as

$$\begin{aligned} \tau_{pq}(I^V; t) \;=\; & -(3V)^{-1} \sum_{J^V=0}^{3} \sum_{K^V=0}^{3} T(I^V, J^V, K^V; t)\{\delta(J^V, K^V)[A_p(K^V)/A(K^V)] \\ & [x_q(J^V) - x_q(I^V)]A(J^V) + [1 - \delta(J^V, K^V)] \\ & \varepsilon_{pkl} A_k(J^V)[x_l(K^V) - x_l(I^V)][x_q(J^V) - x_q(I^V)]/[2A(J^V)]\}. \end{aligned} \tag{7.46}$$

Obviously, the terms with $K^V = I^V$ and $J^V = I^V$ in (7.46) drop automatically from the summation. It is advantageous however, to put

$$T(I^V, I^V, K^V; t) = T(I^V, J^V, I^V; t) = T(I^V, I^V, I^V; t) = 0. \tag{7.47}$$

With this, for each nodal point located on either of the interfaces under consideration, appropriate expansions for the acoustic state quantities have been defined.

Global Representations

The global representation of each wave field quantity is again composed out of all its local representations. In this process, the relationships between the local representations in the different tetrahedra in the geometrical mesh that exist on

account of the continuity conditions that hold on their common faces, are taken into account. Due to the way in which in a vertex of a tetrahedron the vectorial and tensorial wave field quantities are decomposed, the required continuity is simply accounted for by taking the proper local expansion coefficients occurring in the local expansions in the two adjacent tetrahedra to be equal. Subsequently, the resulting value is used to represent a single expansion coefficient in the global representation. The related global expansion function is then the combination of all the local expansion functions in the different tetrahedra that are "supervised" by this global expansion coefficient. In the domain outside the union of the supports of all these local expansion functions, the global expansion function is defined to be zero. Summing the thus constructed global expansion functions, the global representations of the wavefield quantities are arrived at. Note that in these global expansions the number of global expansion coefficients is, in general, less than the number of local expansion coefficients. For the fluid wave field quantities we write the global expansions as

$$[w_r](\boldsymbol{x},t) = \sum_{I^w=0}^{N^w} A^w(I^w;t)\Phi_r(I^w;\boldsymbol{x}) \quad \text{when } \boldsymbol{x} \in [D^f], \tag{7.48}$$

for the fluid particle velocity in $[D^f]$, and

$$[\sigma](\boldsymbol{x},t) = \sum_{I^\sigma=0}^{N^\sigma} A^\sigma(I^\sigma;t)\Phi(I^\sigma;\boldsymbol{x}) \quad \text{when } \boldsymbol{x} \in [D^f]. \tag{7.49}$$

for the scalar traction in $[D^f]$. For the solid wave field quantities we write

$$[v_r](\boldsymbol{x},t) = \sum_{I^v=0}^{N^v} A^v(I^v;t)\Phi_r(I^v;\boldsymbol{x}) \quad \text{when } \boldsymbol{x} \in [D^s]. \tag{7.50}$$

for the solid particle velocity in $[D^s]$, and

$$[\tau_{pq}](\boldsymbol{x},t) = \sum_{I^\tau=0}^{N^\tau} A^\tau(I^\tau;t)\Phi_{pq}(I^\tau;\boldsymbol{x}) \quad \text{when } \boldsymbol{x} \in [D^s]. \tag{7.51}$$

for the solid stress in $[D^s]$. Note that the zero value of the tangential component of the traction at a fluid/solid interface is accounted for by putting the relevant local expansion coefficients of the type (7.45) equal to zero.

The presented global representations of the acoustic medium parameters, the acoustic sources and the acoustic wave field quantities in $[D^{SC}]$ are the discrete

counterparts of the corresponding piecewise analytic exact wave field quantities in this domain and are used as their approximations in the hybrid finite-element method.

The expressions (7.35) and (7.46) do not exihibit explicitly the symmetry of the tensorial stress at each vertex. This implies that not all nine coefficients that can be globalized are linearly independent. In fact, three relationships exist between them. The latter follow from contracting the expressions with appropriate vectorial geometrical quantities associated with the vertex under consideration and using the orthogonality relationship (7.5).

Chapter 8

THE IMPLEMENTATION OF THE HYBRID FINITE-ELEMENT METHOD

In this chapter a hybrid finite-element method is described for the computation of the acoustic wave field in the scattering geometry introduced in Chapter 6. We repeat that in this configuration D^{SC} is the bounded domain that contains fluid and/or solid parts that may be arbitrarily inhomogeneous and anisotropic and D_0 is the fluid or solid embedding, in general with simple medium properties. In the hybrid finite-element method, the acoustic wave field in D^{SC} is computed numerically with the finite-element presented in Chapter 5. As was already mentioned in Chapter 7, we in fact approximate the exact acoustic wave field by a discretized representation defined in the discretized version $[D^{SC}]$ of D^{SC}.

As the starting point for the finite-element computation in the discretized fluid domain $[D^f] \subset [D^{SC}]$ and the discretized solid domain $[D^s] \subset [D^{SC}]$ the integral relations (5.12) and (5.5) are taken. In (5.12) we substitute for the medium properties of State $'A'$ the global representations (7.26) and (7.27), for the sources of State $'A'$ the global representations (7.30) and (7.31) and, finally, for the wave field quantities of State $'A'$ the global representations (7.48) and (7.49). Similarly, we substitute in (5.5) for the medium properties of State $'A'$ the global representations (7.28) and (7.29), for the sources of State $'A'$ the global representations (7.32) and (7.33) and, finally, for the wave field quantities of State $'A'$ the global representations (7.50) and (7.51).

Next, in each of the two integral relations an appropriate sequence of weighting functions is substituted for State $'B'$. Upon taking a reciprocity relation as the point of departure of setting up a numerical scheme, it seems more or less natural to treat the States $'A'$ and $'B'$ in an equivalent manner, which implies that each specimen of the sequence into which State $'A'$ is expanded is also taken as a specimen of the State $'B'$. Thus each global expansion function is used as a weighting function (Galerkin method). We note that with this choice the number of global expansion functions and therefore also the number of the global expansion coefficients of the wave field quantities of the State $'A'$ is equal to the number of weighting functions that are substituted for the State $'B'$. The different integrals that show up in our finite-element formulation of the space-time acoustic wave problem are evaluated in Appendix A.

To have a unique solution for the discretized version of the acoustic wave field problem in $[D^{SC}]$, boundary conditions are required at the boundary $[\partial D^{SC}]$. To approximate the exact wave problem in D^{SC} as much as possible, the type of boundary conditions that guarantee its uniqueness are also used in its discretized version. We distinguish two cases. In the first case, the generated waves in $[D^{SC}]$ do not reach the boundary $[\partial D^{SC}]$ within the chosen time window. In this case, zero-valued boundary conditions suffice. In agreement with the analytical wave problem in D^{SC}, these explicit boundary conditions are either of the Dirichlet or the Neumann type. In the finite-element scheme they are applied to the discretized versions $[S_1^f]$, $[S_2^f]$, $[S_1^s]$ and $[S_2^s]$ of the surface parts S_1^f, S_2^f, S_1^s and S_2^s of D^{SC}, respectively. The zero-valued boundary conditions are accounted for by just setting the global expansion coefficients related to the prescribed wave field quantities at the boundary $[D^{SC}]$ equal to zero. In fact, in the case of zero-valued boundary conditions, each combination of Dirichlet and Neumann boundary conditions can be taken. They all yield a solution of the wave problem in the discretized geometry. In general, these solutions differ. The discrepancy between them is indicative of the discretization error as far as this is due to the discretization of the boundary conditions. Next, the global expansion functions that are related to a prescribed global expansion coefficient are omitted from the sequence of the weighting functions in the computational scheme. In this manner, the number of weighting functions substituted for the State $'B'$ remains

equal to the number of the unknown global expansion coefficients of the acoustic wave field quantities.

In the second case, the acoustic waves generated by the (contrast) sources in $[D^{SC}]$, have reached the boundary $[\partial D^{SC}]$ within the chosen time window. In the exact acoustic wave problem in the infinite scattering geometry, the acoustic waves generated in D^{SC} radiate across the boundary ∂D^{SC} into the embedding D_0. To preserve this feature in the discretized version of the acoustic wave problem, non-local boundary conditions are constructed to model the radiation of the acoustic wave field across the boundary $[\partial D^{SC}]$ into the embedding D_0. For the fluid and for the solid embedding these non-local boundary conditions have different forms.

In the case of a fluid embedding, we start with the Equations (6.1) and (6.2) in which the discretized Green's functions for a fluid medium occur. They yield relationships between the values of the fluid state quantities weighted over each of the supports of the localized source distributions, the contrast and generating sources of the acoustic wave field in $[D^f]$, and its values at the boundary $[\partial D^s]$. Without loss of generality, we take the boundary $[\partial D^{SC}]$ at some distance from the solid parts $[D^s]$ in $[D^{SC}]$, i.e. $[\partial D^{SC}] = [S^f]$ so that all nodal points on the discretized boundary $[\partial D^{SC}]$ are present in the fluid medium. Next, we construct the non-local boundary conditions for these nodal points at $[\partial D^{SC}]$ with the aid of the relations (6.1) and (6.2). For this purpose, the global expansion functions related to the acoustic wave field quantities at the nodal points on the boundary $[S^f]$ are used as the sequence of localized source distributions in these equations. For the medium properties and the sources in $[D^f]$ we substitute the global representations (7.26), (7.27) and (7.30),(7.31), respectively. Finally, for the acoustic wave field quantities the global representations (7.48) and (7.49) are substituted. With these substitutions, we obtain a relationship between the global expansion coefficients of the acoustic wave field quantities at the nodal points on $[\partial D^{SC}]$, the ones at the interior nodal points of $[D^f]$ and the ones at the nodal points on $[\partial D^s]$.

In the case of a solid embedding, we start with the Equations (6.3) and (6.4) in which the discretized Green's functions for a solid medium occur. They yield relationships between the values of the solid state quantities weighted over each

of the supports of the localized source distributions, the contrast and generating sources of the acoustic wave field in $[D^s]$, and its values at the boundary $[\partial D^f]$. Without loss of generality, we take the boundary $[\partial D^{SC}]$ at some distance from the fluid parts $[D^f]$ in $[D^{SC}]$, i.e. $[\partial D^{SC}] = [S^s]$, so that all nodal points on the discretized boundary $[\partial D^{SC}]$ are present in a solid medium. Next, we construct the non-local boundary conditions for these nodal points at $[\partial D^{SC}]$ with the aid of the relations (6.3) and (6.4). For this purpose, the global expansion functions related to the acoustic wave field quantities at the nodal points on the boundary $[S^s]$ are used as the sequence of localized source distributions in these equations. For the medium properties and the sources in $[D^s]$ we substitute the global representations (7.28), (7.29) and (7.32), (7.33), respectively. Finally, for the acoustic wave field quantities the global representations (7.50) and (7.51) are substituted. With these substitutions, we obtain a relationship between the global expansion coefficients of the acoustic wave field quantities at the nodal points on $[\partial D^{SC}]$, the ones at the interior nodal points of $[D^s]$ and the ones at the nodal points on $[\partial D^f]$.

The relations derived above for a fluid and a solid embedding are the non-local boundary conditions that simulate the causal radiation of the acoustic waves, generated in $[D^{SC}]$, into the sourcefree embedding D_0. They are only useful in our computational scheme if the discretized Green's functions related to our chosen sequence of localized source distributions can be found analytically. For a homogeneous fluid or solid embedding this is the case. The relations are next added to the system of equations provided by the finite-element method in $[D^{SC}]$, in which we omit from the sequence of weighting functions the global expansion functions that were used as localized source distributions in the relations (6.1) and (6.2) or (6.3) and (6.4). In this manner, the number of weighting functions substituted for the State $'B'$ remains equal to the number of the unknown global expansion coefficients of the acoustic wave field quantities.

In our computational scheme, the finite-element method is only applied in the spatial direction, because in this direction we may have inhomogeneities. This so-called partial discretization procedure (Zienkiewicz and Morgan 1983, p.266) of our space-time acoustic wave problem leads to a square system of linear, first-order, ordinary differential equations as far as the time coordinate t is

concerned. In it, the global expansion coefficients used in the global representations of the acoustic wave field quantities occur as the unknown time functions. In principle, this system can, since it has constant (i.e., time-independent coefficients), be solved analytically. The analytic solution is just a linear combination of exponential time functions, each term having in its exponent one of the eigenvalues of the system matrix. Although such analytic solutions are possible they may be so complex that one has to resort to a numerical solution method instead. Besides the numerous finite-difference methods that are available for the solution of general systems of linear, first-order differential equations, we can also make use of a finite-element method in the time direction. This method is discussed in Zienkiewicz (1983, p.405) and in Zienkiewicz and Morgan (1983, p.283). First, the time domain (determined by the chosen time window) is discretized into a union of time intervals of equal length. Next, piecewise linear expansion functions ('hat' functions) are defined to be used in the representation of the unknown time functions on the discretized time interval. Finally, the system of differential equations is weighted over the discretized time domain for a particular sequence of weighting functions leading to a marching-on-in-time scheme. Several schemes can be found in this framework by making different choices for the time-weighting functions (Zienkiewicz 1983, p.411, Zienkiewicz and Morgan 1983, p.287). In our computational method we apply this finite-element discretization in the time direction where we take the time weighting functions to be equal to the time expansion functions, i.e., we take for the time weighting functions also 'hat' functions. The relevant procedure leads to a discretization of the four-dimensional space-time geometry into a union of prisms in space-time in which the acoustic wave field quantities are approximated by local expansion functions, each of which is the product of a linear function of space and a linear function of time.

Chapter 9

THE TWO-DIMENSIONAL ACOUSTIC WAVE PROBLEM

Introduction

To avoid the extensive use of computer storage capacity and computation time for testing our finite-element method, it is tested for some two-dimensional acoustic wave problems. For them, it is still possible to illustrate the specific advantages of the use of our elements. The main difference with the three-dimensional case is the construction of the local expansion functions. The elementary regions into which the domain of computation is discretized are now triangles (simplices in R^2) instead of tetrahedra (simplices in R^3). In each triangle, the quantities associated with the wave motion are again approximated linearly. The local expansion functions for the triangle will be presented. The same type of arguments as in Chapter 7 are used to construct from the local expansions the global ones. For simplicity, the media in the test problems are taken to be istropic. Substituting the expressions (2.5) and (2.6) for the tensorial volume density of mass and the compliance of the solid, we obtain for the equation of motion in the solid D^s

$$-\Delta_{kmpq}\partial_m\tau_{pq} + \rho^s\partial_t v_k = f_k^s, \tag{9.1}$$

and for the equation of deformation rate in the solid D^s

$$\Delta_{ijmr}\partial_m v_r - (\Lambda\delta_{ij}\delta_{pq} + 2M\Delta_{ijpq})\partial_t\tau_{pq} = h_{ij}. \tag{9.2}$$

Substituting the expression (2.16) for the tensorial volume density of mass of the fluid, we obtain for the equation of motion in the fluid D^f

$$-\delta_{km}\partial_m\sigma + \rho^f\partial_t w_k = f_k^f \tag{9.3}$$

and for the equation of deformation rate in the fluid D^f

$$\delta_{mr}\partial_m w_r - \kappa\partial_t\sigma = q. \tag{9.4}$$

Two-dimensional Acoustic Wave equations

A wave motion in three-dimensional space is called two-dimensional if all physical quantities associated with the wave motion are independent of one of the Cartesian coordinates. As a consequence, the geometrical configuration as well as the physical properties of the material in which the wave motion occurs are independent of that particular coordinate. Let x_2 be that coordinate, then we have $\partial_2 = 0$ (see Figure 9.1). In what follows, the subscript 2 will be indicated explicitly, while Greek subscripts will be used to denote the remaining subscripts 1 and 3. In the solid the wave motion now consists of two uncoupled wave motions. The first is a horizontally polarized shear wave motion ($SH-$wave) characterized by the non-zero quantities $\tau_{\alpha 2}, v_2, f_2^s$ and $h_{\alpha 2}$ that satisfy the equation of motion

$$-\Delta_{2\beta\gamma 2}\partial_\beta\tau_{\gamma 2} - \Delta_{2\beta 2\delta}\partial_\beta\tau_{2\delta} + \rho^s\partial_t v_2 = f_2^s, \tag{9.5}$$

and the equation of deformation rate

$$\Delta_{\alpha 2\gamma 2}\partial_\gamma v_2 - 2M\partial_t\tau_{\alpha 2} = h_{\alpha 2}. \tag{9.6}$$

The wave motion is a horizontally polarized two-dimensional (shear) wave motion in a solid. The second one is a vertically polarized combined $P-$ and $SV-$wave motion characterized by the non-zero quantities $\tau_{\alpha\beta}, \tau_{22}, v_\alpha, f_\alpha^s, h_{\alpha\beta}$ and h_{22} that satisfy the equation of motion

$$-\Delta_{\alpha\beta\gamma\delta}\partial_\beta\tau_{\gamma\delta} + \rho^s\partial_t v_\alpha = f_\alpha^s, \tag{9.7}$$

and the equation of deformation rate

$$\Delta_{\alpha\beta\gamma\delta}\partial_\gamma v_\delta - (\Lambda\delta_{\alpha\beta}\delta_{\gamma\delta} + 2M\Delta_{\alpha\beta\gamma\delta})\partial_t\tau_{\gamma\delta} - \Lambda\delta_{\alpha\beta}\partial_t\tau_{22} = h_{\alpha\beta}, \tag{9.8}$$

$$-\Lambda\delta_{\gamma\delta}\partial_t\tau_{\gamma\delta} - (\Lambda + 2M)\partial_t\tau_{22} = h_{22}. \tag{9.9}$$

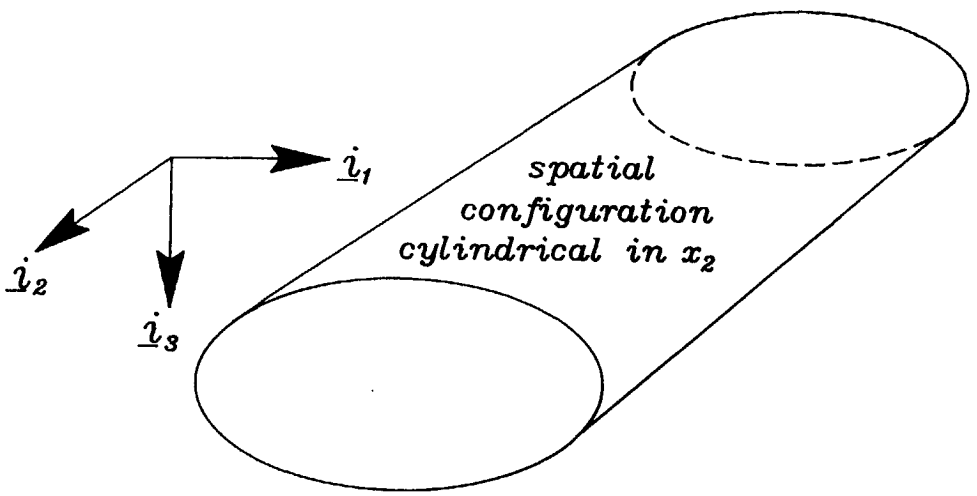

Figure 9.1: The two-dimensional spatial configuration that is cylindrical in the x_2-direction.

Elimination of τ_{22} from Equations (9.8) and (9.9) leads to

$$\Delta_{\alpha\beta\gamma\delta}\partial_\gamma v_\delta - \{[2\Lambda M/(\Lambda+2M)]\delta_{\alpha\beta}\delta_{\gamma\delta} + 2M\Delta_{\alpha\beta\gamma\delta}\}\partial_t\tau_{\gamma\delta} = h_{\alpha\beta} - [\Lambda\delta_{\alpha\beta}/(\Lambda+2M)]h_{22}. \tag{9.10}$$

Equations (9.7) and (9.10) are rewritten as

$$-(1/2)\partial_\beta(\tau_{\alpha\beta} + \tau_{\beta\alpha}) + \rho^s\partial_t v_\alpha = f^s_\alpha, \tag{9.11}$$

and

$$(1/2)(\partial_\alpha v_\beta + \partial_\beta v_\alpha) - [2\Lambda M/(\Lambda + 2M)]\delta_{\alpha\beta}\partial_t\tau_{\gamma\gamma} - M\partial_t(\tau_{\alpha\beta} + \tau_{\beta\alpha}) =$$

$$h_{\alpha\beta} - [\Lambda\delta_{\alpha\beta}/(\Lambda + 2M)]h_{22}. \tag{9.12}$$

Contracting Equation (9.12) with the Kronecker tensor $\delta_{\alpha\beta}$ we find

$$\begin{aligned}\partial_t\tau_{\gamma\gamma} &= \{(\Lambda + 2M)/[2M(3\Lambda + 2M)]\}\partial_\gamma v_\gamma \\ &\quad - \{(\Lambda + 2M)/[2M(3\Lambda + 2M)]\}h_{\gamma\gamma} + \{\Lambda/[M(3\Lambda + 2M)]\}h_{22}.\end{aligned} \tag{9.13}$$

Substitution in (9.12) gives

$$(1/2)(\partial_\alpha v_\beta + \partial_\beta v_\alpha) - [\Lambda/(3\Lambda + 2M)]\delta_{\alpha\beta}\partial_\gamma v_\gamma - M\partial_t(\tau_{\alpha\beta} + \tau_{\beta\alpha}) =$$

$$h_{\alpha\beta} - \delta_{\alpha\beta}[\Lambda/(3\Lambda + 2M)](h_{\gamma\gamma} + h_{22}). \tag{9.14}$$

Equations (9.11) and (9.14) are taken as starting point for the computation of the horizontally polarized two-dimensional wave motion. Eliminating the stress from them leads to a second order wave equation for the particle velocity v_α in which the wave speed of the $P-$wave

$$c_P = [(\lambda + 2\mu)/\rho]^{1/2} = \{(\Lambda + M)/[M(3\Lambda + 2M)\rho]\}^{1/2} \tag{9.15}$$

and the wave speed of the $S-$wave

$$c_S = (\mu/\rho)^{1/2} = (4M\rho)^{-1/2} \tag{9.16}$$

occur. In the fluid the two-dimensional wave motion satisfies the equation of motion that decomposes into

$$-\delta_{\alpha\beta}\partial_\beta\sigma + \rho^f\partial_t w_\alpha = f^f_\alpha, \tag{9.17}$$

$$\rho^f\partial_t w_2 = f^f_2, \tag{9.18}$$

and the equation of deformation rate is

$$\delta_{\alpha\beta}\partial_\alpha w_\beta - \kappa\partial_t\sigma = q. \tag{9.19}$$

Expansion and Weighting Functions for the Two-dimensional Finite-element Method

The two-dimensional domain of computation D^{SC} is discretized by taking it to be the union $[D^{SC}] = \bigcup_{IT=1}^{NT} T(IT)$ of a finite number of triangles $\{T(IT); IT = 1,\ldots,NT\}$ (simplices in R^2) that all have vertices and edges in common (see, Naber 1980). The vertices of the triangle will also be denoted as the nodes of the (geometrical) mesh and the supremum h of the maximum diameters of the triangles will be denoted as the mesh size.

Each fluid and solid quantity $QF = QF(\boldsymbol{x},t)$ and $QS = QS(\boldsymbol{x},t)$, respectively, occurring in the acoustic wave-field problem will, in the interior of each triangle, be approximated by the linear interpolation of its values at the vertices. We use a local numbering that applies for each triangle. The three vertices of a triangle T are denoted by $\{P(0),\ P(1),\ P(2)\}$ and their respective position vectors by $\{x_\alpha(0), x_\alpha(1), x_\alpha(2)\}$. The position in the interior of T or on its boundary ∂T can be specified by the barycentric coordinates $\{\lambda(0), \lambda(1), \lambda(2)\}$ defined through

$$x_\alpha = \sum_{I^V=0}^{2} \lambda(I^V)x_\alpha(I^V) \text{ with } 0 \le \lambda(I^V) \le 1 \text{ and } \sum_{I^V=0}^{2} \lambda(I^V) = 1. \tag{9.20}$$

We observe that the barycentric coordinates $\lambda(I^V)$ do perform the linear interpolation in the triangle (viz. of the position vector) we are looking for. To express the barycentric coordinates in terms of x_α, some geometrical quantities associated with T are needed. First, the vectorial lengths $\{L_\alpha(0), L_\alpha(1), L_\alpha(2)\}$ of the edges of T that are directed along the outward normals to the edges of T are introduced; they are given by (for the numbering we refer to Figure 9.2)

$$\begin{aligned} L_\alpha(0) &= \varepsilon_{\alpha 2\beta}[(x_\beta(1) - x_\beta(2)], \\ L_\alpha(1) &= \varepsilon_{\alpha 2\beta}[(x_\beta(2) - x_\beta(0)], \\ L_\alpha(2) &= \varepsilon_{\alpha 2\beta}[(x_\beta(0) - x_\beta(1)], \end{aligned} \tag{9.21}$$

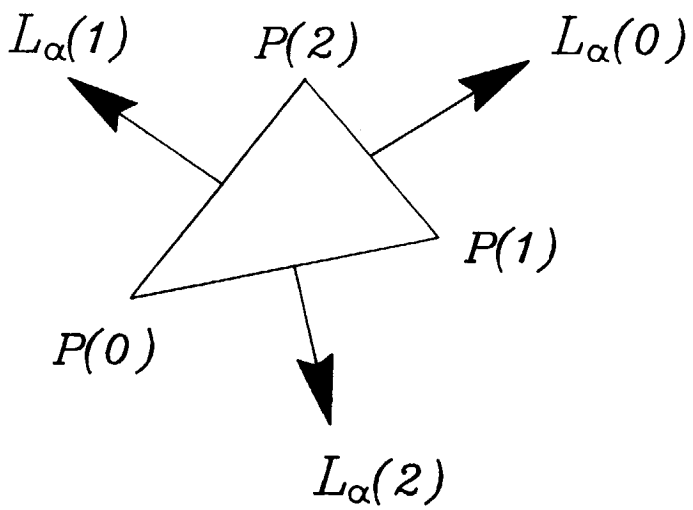

Figure 9.2: Triangle T with its three vertices $\{P(0), P(1), P(2)\}$ and the outwardly directed vectorial lengths $\{L_\alpha(0), L_\alpha(1), L_\alpha(2)\}$ of its edges.

where ε_{lmn} is the completely antisymmetric unit tensor of rank three (Levi-Civita tensor). The magnitude of the vectorial length $L_\alpha(I^V)$ is denoted by $L(I^V)$. It follows that

$$\sum_{I^V=0}^{2} L_\alpha(I^V) = 0. \tag{9.22}$$

The area of T is given by

$$A = \varepsilon_{2\alpha\beta}[x_\alpha(0)x_\beta(1) + x_\alpha(1)x_\beta(2) + x_\alpha(2)x_\beta(0)]/2. \tag{9.23}$$

Now, we observe that at each vertex of T, the two edges that leave that vertex and their two vectorial lengths form, apart from a constant factor, a set of (oblique) reciprocal base vectors. Let us consider the vertex $P(0)$. The two edges leaving this vertex are $\{x_\alpha(1)-x_\alpha(0), x_\alpha(2)-x_\alpha(0)\}$ and their two vectorial lengths are $\{L_\alpha(1), L_\alpha(2)\}$. Now, it is easily verified that

$$[x_\alpha(I^V) - x_\alpha(0)]L_\alpha(J^V) = -2A\delta(I^V, J^V) \text{ with } I^V = 1,2 \text{ and } J^V = 1,2, \tag{9.24}$$

where $\delta(I^V, I^V) = 1$ and $\delta(I^V, J^V) = 0$ if $I^V \neq J^V$. From (9.24) it follows that, at the vertex with position vector $x_\alpha(0)$, the set of vectors $\{-[x_\alpha(1) - x_\alpha(0)]/2A, -[x_\alpha(2) - x_\alpha(0)]/2A\}$ is reciprocal to the set $\{L_\alpha(1), L_\alpha(2)\}$, and the set $\{-L_\alpha(1)/2A, -L_\alpha(2)/2A\}$ is reciprocal to the set $\{x_\alpha(1) - x_\alpha(0), x_\alpha(2) - x_\alpha(0)\}$. Returning to (9.20), we can, by letting $\lambda(0) = 1 - \lambda(1) - \lambda(2)$, write

$$x_\alpha - x_\alpha(0) = \sum_{I^V=1}^{2} \lambda(I^V)[x_\alpha(I^V) - x_\alpha(0)]. \tag{9.25}$$

Upon multiplying this equation by $-(2A)^{-1}L_\alpha(J^V)$ and using (9.24) we obtain

$$-(2A)^{-1}[x_\alpha - x_\alpha(0)]L_\alpha(J^V) = \lambda(J^V) \text{ for } J^V = 1,2. \tag{9.26}$$

Since further, on account of (9.22) and (9.26)

$$-(2A)^{-1}[x_\alpha - x_\alpha(0)]L_\alpha(0) = -\sum_{I^V=1}^{2} \lambda(I^V), \tag{9.27}$$

(9.25) leads to

$$x_\alpha - x_\alpha(0) = -(2A)^{-1} \sum_{J^V=0}^{2} [x_\beta - x_\beta(0)]L_\beta(J^V)x_\alpha(J^V). \tag{9.28}$$

Similar results hold for the other vertices as well. By combining the results we have

$$x_\alpha - x_\alpha(I^V) = -(2A)^{-1} \sum_{J^V=0}^{2} [x_\beta - x_\beta(I^V)] L_\beta(J^V) x_\alpha(J^V) \quad \text{for} \quad I^V = 0,1,2. \tag{9.29}$$

Summing the results for $I^V = 0,1,2$, respectively, and introducing the position vector b_α of the barycenter of T through

$$b_\alpha = (1/3) \sum_{I^V=0}^{2} x_\alpha(I^V), \tag{9.30}$$

we arrive at the symmetrical expression

$$x_\alpha = b_\alpha - (2A)^{-1} \sum_{I^V=0}^{2} [x_\beta - b_\beta] L_\beta(I^V) x_\alpha(I^V). \tag{9.31}$$

On account of this relation, we can write

$$x_\alpha = \sum_{I^V=0}^{2} x_\alpha(I^V) \phi(I^V; \boldsymbol{x}), \tag{9.32}$$

where

$$\phi(I^V; \boldsymbol{x}) = 1/3 - (2A)^{-1} (x_\beta - b_\beta) L_\beta(I^V). \tag{9.33}$$

Comparing (9.32) with (9.20), we see that $\{\phi(I^V; \boldsymbol{x}); I^V = 0,1,2\}$ are nothing but the barycentric coordinates of a point in T or on its boundary. On the other hand, $\phi(I^V; \boldsymbol{x})$ performs a linear interpolation between the value one at the vertex $x_\alpha = x_\alpha(I^V)$ and the value zero at the remaining vertices of T.

In the triangle T we use the functions $\phi(I^V; \boldsymbol{x})$ as local expansion functions. The linear interpolation of a quantity $QF(\boldsymbol{x}, t)$ in a triangle T present in $[D^J]$ is correspondingly given by

$$[QF](\boldsymbol{x}, t) = \sum_{I^V=0}^{2} A^{QF}(I^V; t) \phi(I^V; \boldsymbol{x}) \quad \text{for } \boldsymbol{x} \in T, \tag{9.34}$$

in which

$$A^{QF}(I^V; t) = QF(\boldsymbol{x}(I^V); t) \tag{9.35}$$

is the value of QF at the vertex with ordinal number I^V. The linear interpolation of a quantity $QS(\boldsymbol{x}, t)$ in a triangle T present in $[D^s]$ is given by

$$[QS](\boldsymbol{x}, t) = \sum_{I^V=0}^{2} A^{QS}(I^V; t) \phi(I^V; \boldsymbol{x}) \quad \text{for } \boldsymbol{x} \in T, \tag{9.36}$$

in which

$$A^{QS}(I^V;t) = QS(\boldsymbol{x}(I^V);t) \tag{9.37}$$

is the value of QS at the vertex with ordinal number I^V. The global expansions of the quantities $[QF]$ and $[QS]$ follow by combining all the local expansions. For the fluid quantities they are written as

$$[QF](\boldsymbol{x},t) = \sum_{IT=1}^{NT} \sum_{I^V=0}^{2} A^{QF}(IT,I^V;t)\Phi(IT,I^V;\boldsymbol{x}) \quad \text{for } \boldsymbol{x} \in [D^{SC}], \tag{9.38}$$

in which

$$A^{QF}(IT,I^V;t) = QF(\boldsymbol{x}(I^V);t) \text{ for } \boldsymbol{x} \in T(IT) \tag{9.39}$$

is the value of QF in triangle $T(IT)$ at its vertex with ordinal number I^V. For the solid quantities they are written as

$$[QS](\boldsymbol{x},t) = \sum_{IT=1}^{NT} \sum_{I^V=0}^{2} A^{QS}(IT,I^V;t)\Phi(IT,I^V;\boldsymbol{x}) \quad \text{for } \boldsymbol{x} \in [D^{SC}], \tag{9.40}$$

in which

$$A^{QS}(IT,I^V;t) = QS(\boldsymbol{x}(I^V);t) \text{ for } \boldsymbol{x} \in T(IT) \tag{9.41}$$

is the value of QS in triangle $T(IT)$ at its vertex with ordinal number I^V. In (9.38) and (9.40), the global expansion functions Φ are defined by

$$\Phi(IT,I^V;\boldsymbol{x}) = \phi(I^V;\boldsymbol{x})\chi_{T(IT)}(\boldsymbol{x}) \quad \text{for } \boldsymbol{x} \in [D^{SC}], \tag{9.42}$$

where $\chi_D(\boldsymbol{x})$ is the characteristic function of the set D, defined as

$$\chi_D(\boldsymbol{x}) = \begin{cases} 0 & \text{when } \boldsymbol{x} \notin D \\ 1 & \text{when } \boldsymbol{x} \in D. \end{cases} \tag{9.43}$$

The specific choices of the vectorial/tensorial decompositions of the wave field quantities at the vertices of a triangle are displayed below. Note that for a scalar quantity no base of decomposition is required.

Choice of the vectorial/tensorial decompositions at the vertices of a triangle

Vertex coincides with nodal point not on an interface

In a vertex that coincides with a nodal point that is not on an interface, we decompose the field quantities along the axes of the background Cartesian reference frame.

Vertex coincides with nodal point on a solid/solid interface

Across a solid/solid interface all components of the solid particle velocity and the normal component of the stress (the traction) are to be continuous, while the tangential component of the stress may jump by a finite amount. Accordingly, at a vertex $P(I^V)$ of a triangle T that coincides with a nodal point located on a solid/solid interface, the solid particle velocity is decomposed along the axes of the background Cartesian reference frame, and the stress $\tau_{\alpha\beta}(I^V;t)$ is written as

$$\tau_{\alpha\beta}(I^V;t) = -(2A)^{-1} \sum_{J^V=0}^{2} T_\alpha(I^V, J^V;t)[x_\beta(J^V) - x_\beta(I^V)]L(J^V). \tag{9.44}$$

As far as the second subscript of $\tau_{\alpha\beta}(I^V;t)$ is concerned it is decomposed along the local base vectors $\{-(2A)^{-1}[x_\beta(J^V) - x_\beta(I^V)]L(J^V), J^V = 0,1,2, J^V \neq I^V\}$ that are directed along the edges meeting in $P(I^V)$. Using (9.24), it follows that the expansion coefficient

$$T_\alpha(I^V, J^V;t) = \tau_{\alpha\beta}(I^V;t)L_\beta(J^V)/L(J^V), \quad \text{with } I^V \neq J^V, \tag{9.45}$$

is the traction at the edge with vectorial length $L_\beta(J^V)$ at the vertex $P(I^V)$. Obviously, the term with $J^V = I^V$ drops automatically from the summation (9.44); for later purposes it is, however, advantageous to put

$$T_\alpha(I^V, I^V;t) = 0. \tag{9.46}$$

Vertex coincides with nodal point on a fluid/fluid interface

Across a fluid/fluid interface the normal component of the fluid particle velocity is to be continuous, while its tangential component may jump by a finite amount. Accordingly, at a vertex $P(I^V)$ of a triangle T that coincides with a nodal point located on a fluid/fluid interface, the fluid particle velocity is written as

$$w_\alpha(I^V;t) = -(2A)^{-1} \sum_{J^V=0}^{2} W(I^V, J^V;t)[x_\alpha(J^V) - x_\alpha(I^V)]L(J^V). \tag{9.47}$$

The particle velocity $w_\alpha(I^V;t)$ is decomposed along the local base vectors $\{-(2A)^{-1}[x_\alpha(J^V)-x_\alpha(I^V)]\,L(J^V), J^V = 0,1,2, J^V \neq I^V\}$ that are directed along the edges meeting at $P(I^V)$. Using (9.24), it follows that the expansion coefficient

$$W(I^V,J^V;t) = w_\alpha(I^V;t)L_\alpha(J^V)/L(J^V), \quad \text{with } I^V \neq J^V, \tag{9.48}$$

is the length of the normal component of the fluid particle velocity at the edge with vectorial length $L_\alpha(J^V)$ at the vertex $P(I^V)$. Obviously, the term with $J^V = I^V$ drops automatically from the summation (9.47); for later purposes it is, however, advantageous to put

$$W(I^V,I^V;t) = 0. \tag{9.49}$$

Vertex coincides with nodal point on a fluid/solid interface

At a fluid/solid interface the normal component of the fluid particle velocity is equal to the normal component of the solid particle velocity while their tangential components may differ by a finite amount. Further, the normal component of the traction in the solid is equal to the scalar traction in the fluid, while the tangential components of the traction in the solid are equal to zero. Accordingly, at a vertex $P(I^V)$ of a triangle T situated in the solid part that coincides with a nodal point that is located on a fluid/solid interface, the solid particle velocity is written as

$$v_\alpha(I^V;t) = -(2A)^{-1}\sum_{J^V=0}^{2} V(I^V,J^V;t)[x_\alpha(J^V) - x_\alpha(I^V)]L(J^V). \tag{9.50}$$

In (9.50), the particle velocity $v_\alpha(I^V;t)$ is decomposed along the local base vectors $\{-(2A)^{-1}[x_\alpha(J^V) - x_\alpha(I^V)]L(J^V), J^V = 0,1,2, J^V \neq I^V\}$ that are directed along the edges meeting in $P(I^V)$. Using (9.24), it follows that the expansion coefficient

$$V(I^V,J^V;t) = v_\alpha(I^V;t)L_\alpha(J^V)/L(J^V), \quad \text{with } I^V \neq J^V, \tag{9.51}$$

is the length of the normal component of the solid particle velocity at the edge with vectorial length $L_\alpha(J^V)$ at the vertex $P(I^V)$. Obviously, the term with $J^V = I^V$ drops automatically from the summation (9.50); for later purposes it is, however, advantageous to put

$$V(I^V,I^V;t) = 0. \tag{9.52}$$

At a vertex $P(I^V)$ of a triangle T situated in the fluid part that coincides with a nodal point that is located on a fluid/solid interface, the fluid particle velocity is, again, represented by (9.47). Finally, the stress $\tau_{\alpha\beta}(I^V;t)$ is represented by (9.44) where the coefficient $T_\alpha(I^V,J^V;t)$ is now given as

$$\begin{aligned} T_\alpha(I^V,J^V;t) &= \sum_{K^V=0}^{2} T(I^V,J^V,K^V;t)\{\delta(J^V,K^V)L_\alpha(K^V)/L(K^V) \\ &\quad + [1-\delta(J^V,K^V)][x_\alpha(K^V)-x_\alpha(I^V)]/(L(J^V))^2\}. \end{aligned} \tag{9.53}$$

With the representation (9.53), the stress is decomposed along the base vectors $L_\alpha(J^V)/L(J^V)$ and $\{[x_\alpha(K^V)-x_\alpha(I^V)], K^V=0,1,2, K^V\neq I^V, K^V\neq J^V\}$. The first one is nothing but the unit normal vector of the edge with vectorial length $L_\alpha(J^V)$; the other one is directed along this edge. Obviously, the expansion coefficient

$$T(I^V,J^V,J^V;t) = T_\alpha(I^V,J^V;t)L_\alpha(J^V)/L(J^V), \quad \text{with } J^V\neq I^V \tag{9.54}$$

is the length of the normal component of the traction at the edge with vectorial length $L_\alpha(J^V)$ in $P(I^V)$. Further, the expansion coefficient

$$T(I^V,J^V,K^V;t) = T_\alpha(I^V,J^V;t)[x_\alpha(K^V)-x_\alpha(I^V)], \quad \text{with } K^V\neq I^V, J^V\neq K^V \tag{9.55}$$

is the innerproduct of the traction at the edge with vectorial length $L_\alpha(J^V)$ in the point $P(I^V)$ and completely determines the tangential component of this traction. Substitution of (9.53) into (9.44) gives the representation of the stress $\tau_{\alpha\beta}(I^V;t)$ in the vertex $P(I^V)$:

$$\begin{aligned} \tau_{\alpha\beta}(I^V;t) &= \sum_{J^V=0}^{2}\sum_{K^V=0}^{2} T(I^V,J^V,K^V;t)\{\delta(J^V,K^V) \\ &\quad [L_\alpha(K^V)/L(K^V)][x_\beta(J^V)-x_\beta(I^V)]/L(J^V) \\ &\quad + [1-\delta(J^V,K^V)][x_\alpha(K^V)-x_\alpha(I^V)][x_\beta(J^V)-x_\beta(I^V)]/L(J^V)\}. \end{aligned} \tag{9.56}$$

Obviously, the terms with $K^V=I^V$ and $J^V=I^V$ in (9.56) drop from the summation. It is advantageous however, to put

$$T(I^V,I^V,K^V;t) = T(I^V,J^V,I^V;t) = T(I^V,I^V,I^V;t) = 0. \tag{9.57}$$

With this, for nodal points located on either of the interfaces that occur in our problem, appropriate expansions for the acoustic state quantities have been defined.

The global representation of each wave field quantity is again composed out of all its local representations. In this process, the relationships between the local representations in the different triangles in the geometrical mesh that exist due to the continuity conditions that hold on their common edges, are taken into account.

Chapter 10

TWO-DIMENSIONAL ACOUSTIC WAVES GENERATED BY A STRIP LOAD AT THE BOUNDARY OF A SEMI-INFINITE FLUID

Introduction

The two-dimensional acoustic wave motion generated by an arbitrary distributed impulsive surface load on the boundary of a semi-infinite lossless fluid is investigated theoretically. With the aid of the Cagniard-De Hoop method closed-form expressions are obtained for the particle velocity and the scalar traction of the generated wave motion. For details of the Cagniard-De Hoop method see, for example, Achenbach (1973), Miklowitz (1978), Aki and Richards (1980), De Hoop and Van der Hijden (1985), or De Hoop (1988).

The practically important case is considered where the strip exerts on the boundary surface of the fluid a normal force. The case of a uniformly distributed impulsive strip load of the normal-load type is worked out in detail. Synthetic seismograms are presented for an array of shallow receivers close to the strip source, where a plane wave contribution is manifest in addition to the cylindrical body wave. For the time shape (source signature) of the exerting force, a damped sinusoid is taken. The results are of importance as test cases for the accuracy

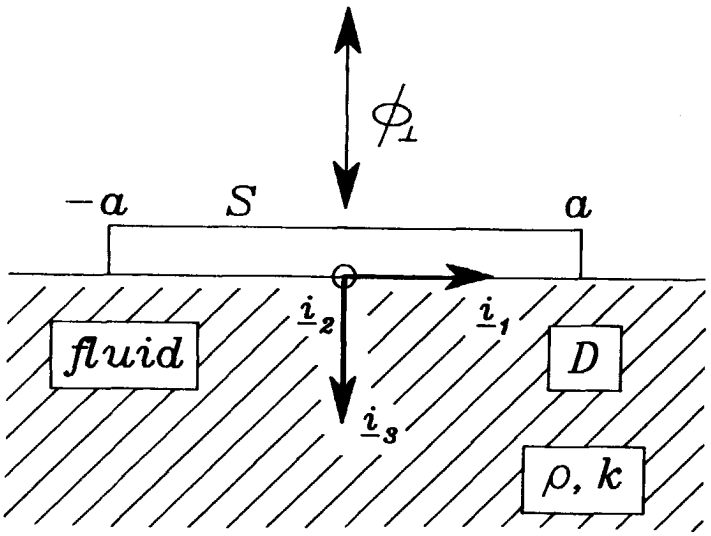

Figure 10.1: Semi-infinite, homogeneous, isotropic, lossless fluid with medium parameters ρ and κ and the strip source of extension $[-a, a]$ at its boundary. The strip source exerts a normal force $\phi_\perp$.

in the computational modeling of acoustic wave problems by, for example, time-domain finite-difference or finite-element methods (see, Alterman and Karal, 1968; Kelly et al., 1976; Emerman et al., 1982; Marfurt, 1984; Virieux, 1984, 1986).

Basic Equations

The acoustic waves under consideration are small-amplitude disturbances traveling in a semi-infinite, homogeneous, isotropic, and lossless fluid. The physical properties of the fluid are characterized by its volume density of mass ρ and its compressibility κ. To specify the position in the configuration we employ the coordinates $\{x_1, x_2, x_3\}$ with respect to a fixed, orthogonal, Cartesian reference frame with origin O and the three mutually perpendicular base vectors $\{\boldsymbol{i}_1, \boldsymbol{i}_2, \boldsymbol{i}_3\}$ of unit length each. In the indicated order, the base vectors form a right-handed system. In accordance with the geophysical convention, $\boldsymbol{i}_3$ points vertically downwards (Figure 10.1). The subscript notation for Cartesian vectors and tensors is used and the summation convention applies. The structure is shift-invariant in the direction of $\boldsymbol{i}_2$. The time coordinate is denoted by t.

Partial differentiation is denoted by ∂; ∂_p denotes differentiation with respect to x_p, ∂_t is a reserved symbol for partial differentiation with respect to t.

The fluid medium occupies the half-space

$$D = \{x_m \in R^3; x_3 > 0\}. \tag{10.1}$$

A force is applied to the surface of the fluid; it is taken to be independent of x_2. As a consequence, all physical quantities associated with the wave motion are independent of x_2 as well, and $\partial_2 = 0$. The resulting two-dimensional wave motion is characterized by the non-zero particle velocity components w_1 and w_3 and the non-zero scalar traction σ. The corresponding components of the (sourcefree) equation of motion in the interior of D are

$$\begin{aligned} -\partial_1\sigma + \rho\partial_t w_1 &= 0, \\ -\partial_3\sigma + \rho\partial_t w_3 &= 0. \end{aligned} \tag{10.2}$$

The scalar traction is related to the non-zero components of the particle velocity through the (sourcefree) deformation rate equation (constitutive relation)

$$\partial_t\sigma = (1/\kappa)(\partial_1 w_1 + \partial_3 w_3). \tag{10.3}$$

At the boundary of D, a surface load is applied to the fluid. Its (prescribed) normal force has the vertical component $\phi_\perp$. Hence, the boundary condition

$$-\lim_{x_3\downarrow 0}\sigma = \phi_\perp(x_1, t) \text{ for all } x_1 \text{ and } t, \tag{10.4}$$

is to be satisfied. Let the source start to act at the instant $t = 0$, then $\phi_\perp(x_1, t) = 0$ when $t < 0$, while

$$\{w_1, w_3, \sigma\}(x_1, x_3, t) = 0 \text{ when } t < 0. \tag{10.5}$$

Equation (10.5) describes the causality of the generated wave motion.

Method of Solution

The Cagniard-De Hoop method is used to obtain analytical expressions for the particle velocity and the scalar traction. The first step in this method consists

of carrying out a one-sided Laplace transformation with respect to time. To show the notation we give the transformation for the particle velocity:

$$\hat{w}_k(x_1, x_3, s) = \int_{t=0}^{\infty} \exp(-st) w_k(x_1, x_3, t) dt. \tag{10.6}$$

In (10.6), s is a real, positive parameter that is chosen large enough to ensure the convergence of integrals of the indicated type. The next step consists of carrying out a one-dimensional Fourier transformation with respect to the horizontal coordinate x_1. For the particle velocity this transformation is given by

$$\tilde{w}_k(i\alpha, x_3, s) = \int_{x_1=-\infty}^{\infty} \exp(is\alpha x_1) \hat{w}_k(x_1, x_3, s) dx_1, \tag{10.7}$$

where $\alpha \in R$. The corresponding inverse transformation is given by (note that the actual Fourier-transform variable in (10.7) is $s\alpha$)

$$\hat{w}_k(x_1, x_3, s) = (s/2\pi) \int_{\alpha=-\infty}^{\infty} \exp(-is\alpha x_1) \tilde{w}_k(i\alpha, x_3, s) d\alpha. \tag{10.8}$$

Subjecting the equation of motion (10.2) and the equation of deformation rate (10.3) to these transformations, ∂_t can be replaced by s and ∂_1 by $-is\alpha$, and a system of ordinary differential equations in x_3 is arrived at (Van der Hijden, 1988):

$$\partial_3 \underline{\tilde{F}} = -s \underline{A}\, \underline{\tilde{F}}, \tag{10.9}$$

where the field matrix $\underline{\tilde{F}}$ is the column matrix with the elements

$$\tilde{F}_1 = -\tilde{\sigma}, \quad \tilde{F}_2 = \tilde{w}_3, \tag{10.10}$$

and the system matrix $\underline{A}$ is the square matrix with the elements

$$A_{11} = A_{22} = 0,$$

$$A_{12} = \rho, \quad A_{21} = (1/\rho)[1/c_f^2 - (i\alpha)^2], \tag{10.11}$$

where $c_f = (\rho\kappa)^{-1/2}$ is the fluid wave speed. Note that $\underline{A}$ is independent of s. Equation (10.9) represents a system of linear first-order ordinary differential equations in x_3. The eigenvalues of $\underline{A}$ are found to be $\pm\gamma_f$, with

$$\gamma_f = \gamma_f(i\alpha) = [1/c_f^2 - (i\alpha)^2]^{1/2}, \quad \mathrm{Re}(\gamma_f) \geq 0. \tag{10.12}$$

The solution of (10.9) that is bounded as $x_3 \to \infty$ can be written as

$$\tilde{\underline{F}} = W(i\alpha, s)\tilde{\underline{e}}(i\alpha)\exp(-s\gamma_f x_3), \tag{10.13}$$

in which

$$\tilde{\underline{e}} = \tilde{\underline{e}}(i\alpha) = \{\rho, \gamma_f\}^T \tag{10.14}$$

is a normalized eigenvector of $\underline{\underline{A}}$ corresponding to the eigenvalue γ_f. Note that $\tilde{\underline{e}}(i\alpha)$ is independent of s. The amplitude coefficient $W(i\alpha, s)$ in (10.13) follows from the application of the boundary conditions (10.4) at $x_3 = 0$. It is obtained as

$$W(i\alpha, s) = W(i\alpha)\phi_\perp(i\alpha, s) = (\rho^{-1})\phi_\perp(i\alpha, s). \tag{10.15}$$

Transforming the solution (10.13) back to the $(x_1, x_3, s)-$domain, the $s-$domain wave field constituent

$$\hat{\underline{F}} = (s/2\pi)\int_{\alpha=-\infty}^{\infty} W(i\alpha, s)\tilde{\underline{e}}(i\alpha)\exp[-s(i\alpha x_1 + \gamma_f x_3)]d\alpha \tag{10.16}$$

is obtained. Starting from the expression (10.16), the case of a uniformly distributed strip load of the normal-force type is further investigated in the next section.

Cagniard-De Hoop Method for the Uniformly Distributed Normal Strip Load

In this section the case of the uniformly distributed strip load of the normal-load type is worked out in detail. First the ray parameter $p = i\alpha$ is introduced in the integral representation (10.16). This leads to the expression

$$\hat{\underline{F}} = (s/2\pi i)\int_{p=-i\infty}^{i\infty} W(p, s)\tilde{\underline{e}}(p)\exp[-s(px_1 + \gamma x_3)]dp. \tag{10.17}$$

Now, along the strip

$$S = \{x_m \in R^3;\ -a < x_1 < a,\ x_3 = 0\} \tag{10.18}$$

of width $2a$ a spatially uniformly distributed normal-load is exerted on the fluid (Figure 10.1). The spatial dependence on x_1 of the strip load is modeled by the difference of two unit step loads; one of which is active on the interval $(-a, \infty)$, the other one being active on the interval (a, ∞). The combination of

the two equals unity on the interval $(-a, a)$ and vanishes outside this interval. Correspondingly, the distribution of the surface load has the form

$$\phi_\perp(x_1, t) = \Phi_\perp(t)[H(x_1 + a) - H(x_1 - a)], \tag{10.19}$$

where

$$H(x_1) = \{0, 1/2, 1\} \text{ for } \{ x_1 < 0, x_1 = 0, x_1 > 0\} \tag{10.20}$$

is the Heaviside unit step function. The space-time transformed expression corresponding to (10.19) is

$$\tilde{\phi}_\perp(p, s) = \hat{\Phi}_\perp(s)[\exp(spa) - \exp(-spa)]/sp. \tag{10.21}$$

The expression (10.21) is substituted into (10.15) giving the amplitude coefficient that is substituted into (10.16). We observe that in the integrand in this expression the point $p = 0$ is a regular point as long as the two terms in the numerator are kept together. However, in the application of the Cagniard-De Hoop method, we have to separate these two terms and each of them has a simple pole at $p = 0$. To handle this singularity, the integrand in (10.16) is continued analytically into the complex $p-$plane away from the imaginary axes. Using Cauchy's theorem, the path of integration is, before the separation of the two terms in (10.21), deformed into the path L^+ that deviates from the imaginary axes along a semi-circle of vanishingly small radius around $p = 0$ in the right half of the $p-$plane (Figure 10.2). (A semi-circle around $p = 0$ in the left half of the $p-$plane could have served as well; the two types of deviation lead to the same final results.)

With the above, we obtain for the wave-field contribution

$$\hat{\underline{F}}(x_1, x_3, s) = -[\hat{\underline{FE}}(x_1 + a, x_3, s) - \hat{\underline{FE}}(x_1 - a, x_3, s)], \tag{10.22}$$

where

$$\hat{\underline{FE}}(\chi, x_3, s) =$$

$$[\hat{\Phi}_\perp(s)/2\pi i] \int_{p \in L^+} [W(p)/p] \tilde{\underline{e}}(p) \exp[-s(p\chi + \gamma_f x_3)] dp, \tag{10.23}$$

in which χ stands for $x_1 + a$ or $x_1 - a$, respectively, and the expressions for $W(p)$ and $\tilde{\underline{e}}(p)$ are given in (10.15) and (10.14), respectively.

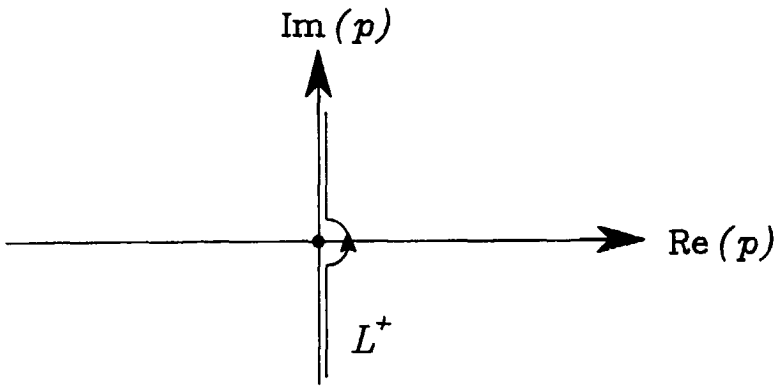

Figure 10.2: The contour L^+ in the complex $p-$plane.

Next, we take advantage of the symmetry of the configuration with respect to the plane $x_1 = 0$. In the present case, we have the symmetry relations

$$\begin{aligned} w_1(x_1, x_3, t) &= -w_1(-x_1, x_3, t), \\ w_3(x_1, x_3, t) &= w_3(-x_1, x_3, t), \\ \sigma(x_1, x_3, t) &= \sigma(-x_1, x_3, t). \end{aligned} \tag{10.24}$$

Once the wave field has been determined in the domain

$$D^+ = \{x_m \in R^3; x_1 \geq 0, x_3 > 0\}, \tag{10.25}$$

its values in the entire half-space D are known via (10.24).

Body Wave Constituent

The first step in the Cagniard-De Hoop method consists of deforming, in each of the two terms in (10.22), the path of integration L^+ in the complex $p-$plane into a path L^B along which

$$p\chi + \gamma_f x_3 = \tau, \tag{10.26}$$

where τ is real and positive. By virtue of Jordan's lemma (Whittaker and Watson 1950, p.115) the contribution from joining circular axes at infinity vanishes, and hence Cauchy's theorem ensures that the integral along the imaginary $p-$axes is equal to the integral along L^B. In (10.26), $\chi = x_1 + a$ for the first term in (10.22) and $\chi = x_1 - a$ for the second term in (10.22). Such a path is denoted as a Cagniard-De Hoop path. In the process of deformation we encounter the singularities in $W(p)/p, \underline{\varepsilon}(p)$ and $\gamma_f(p) = (1/c_f^2 - p^2)^{1/2}$. These are: the branch points $p = \pm 1/c_f$ of γ_f that also occur in $\tilde{\underline{\varepsilon}}(p)$, and the pole $p = 0$. The pole $p = 0$ will be shown to be associated with the downgoing plane wave that exists in the vertical region below the strip S. Since the application of Cauchy's theorem in connection with the deformation of the path of integration in the complex $p-$plane requires the integrands to be single-valued, branch cuts are, in accordance with (10.12), introduced along $\mathrm{Im}(p) = 0$ and $1/c_f < |\mathrm{Re}(p)| < \infty$, i.e., where $\mathrm{Re}(\gamma_f) = 0$. In the cut $p-$plane, we then have $\mathrm{Re}[\gamma_f(p)] > 0$. Depending on the position of the point of observation, three cases are distinghuised for the deformation of the contour L^+ in (10.22) in the complex $p-$plane (Figure 10.3). First, if $\chi > 0$ the contour is deformed into the right half of the complex $p-$plane. Secondly, if $\chi = 0$ the contour remains unchanged and runs along L^+ . Finally, if $\chi < 0$ the contour is deformed into the left half of the complex $p-$plane, in which case the contribution from the pole $p = 0$ is to be taken into account. In this procedure the deformed path of integration in (10.23) is obtained as $p = p^B(\chi, x_3, \tau)$ in the upper half of the $p-$plane, together with its image $p = p^{B^*}$ with respect to the real axis in the lower half of the $p-$plane, where p^B is given by

$$p^B(\chi, x_3, \tau) = \chi\tau/(\chi^2 + x_3^2) + i(\tau^2 - T_f^2)^{1/2} x_3/(\chi^2 + x_3^2), \tag{10.27}$$

with $T_f < \tau < \infty$, where $T_f = (\chi^2 + x_3^2)^{1/2}/c_f$ is the arrival time of the body wave. Introducing τ as the variable of integration, we rewrite (10.23) in the form

$$\hat{\underline{F}}\hat{\underline{E}} = \hat{\Phi}_\perp(s)\hat{\underline{G}}(\chi, x_3, s) + H(-\chi)\hat{\Phi}_\perp(s) W(0)\tilde{\underline{\varepsilon}}(0) \exp(-s x_3/c_f), \tag{10.28}$$

where H denotes again the Heaviside unit step function (cf. (10.20)), and

$$\hat{\underline{G}}(\chi, x_3, s) = \int_{\tau=T_f}^{\infty} \underline{g}(\chi, x_3, t) \exp(-s\tau) d\tau, \tag{10.29}$$

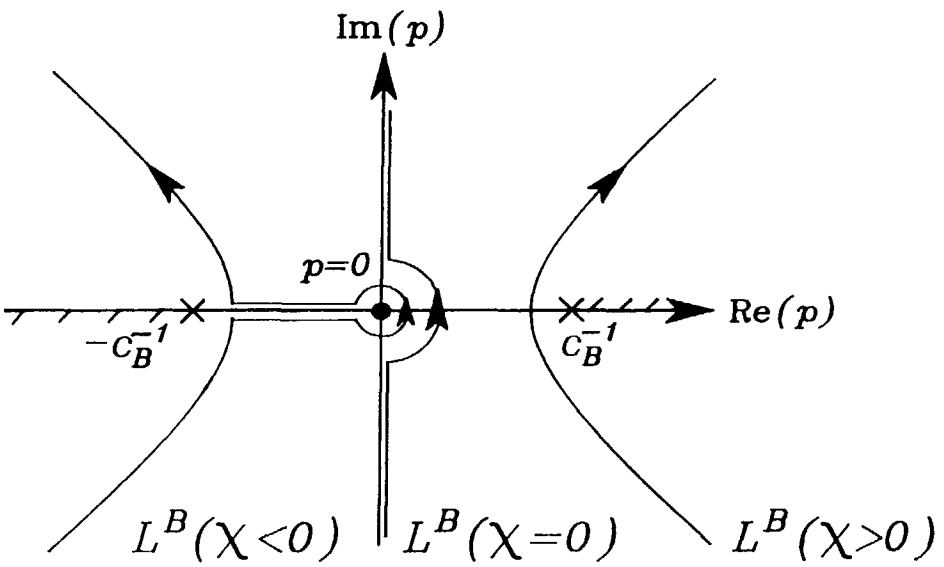

Figure 10.3: The contour L^B in the complex $p-$plane for the three different cases of $\chi < 0, \chi = 0, \chi > 0$.

in which

$$\underline{g}(\chi, x_3, \tau) = (1/\pi)\mathrm{Im}\{[W(p^B)/p^B]\tilde{\underline{\varepsilon}}^B(p^B)(\partial p^B/\partial\tau)\}H(\tau - T_f). \tag{10.30}$$

In (10.30), $\partial p^B/\partial\tau$ is the one-dimensional Jacobian given by

$$\partial p^B/\partial\tau = \chi/(\chi^2 + x_3^2) + i[\tau/(\tau^2 - T_f^2)^{1/2}]x_3/(\chi^2 + x_3^2). \tag{10.31}$$

In the derivation of (10.28), the parts associated with $p = p^B$ and $p = p^{B^*}$ are taken together and Schwarz's reflection principle has been used in the integrand. In equation (10.28), the first term is the contribution from the integration along the contour L^B; it is identified as a cylindrical body wave motion. The second term is the contribution from the residue of the integrand in (10.17) at the simple pole $p = 0$; it is identified as the plane body wave that is excited below the strip source. (Note that in the domain D^+ given by (10.25), the region below the strip source $0 \leq x_1 < a$ leads to $\chi < 0$ in the term for which $\chi = x_1 - a$.) The space-time expression for the body wave follows by applying the convolution theorem to (10.28) and Lerch's theorem (see Widder, 1946):

$$\underline{FE} = H(t - T_f^{PL})\underline{PW}(\chi, x_3, t) + H(t - T_f)\int_{\tau=T_f}^{t} \Phi_\perp(t-\tau)\underline{g}(\chi, x_3, \tau)d\tau, \tag{10.32}$$

where $T_f^{PL} = x_3/c_f$ is the arrival time of the plane body wave and

$$\underline{PW}(\chi, x_3, t) = H(-\chi)W(0)\tilde{\underline{\varepsilon}}(0)\Phi_\perp(t - x_3/c_f). \tag{10.33}$$

Equation (10.32) is the space-time expression for the body wave that is generated in the semi-infinite fluid by the strip load of normal force. The wave motion consists of cylindrical body waves originating from the two edges of the strip source (cf. (10.22)). In addition, we have an extra plane body wave in the region below the strip source. As an illustration of the wave motion in the semi-infinite fluid generated by the strip source at its boundary, synthetic seismograms have been computed. The results are presented below.

Numerical Results

Synthetic seismograms of the particle velocity close to the strip source are presented for the normal strip load problem. The medium properties are taken to

be $\rho = 1.0 * 10^3$ kg/m^3 and $\kappa = 4.4 * 10^{-10}$ Pa^{-1}. The corresponding fluid wave speed is $c_f = 1507$ m/s. Along the strip

$$S = \{-a < x_1 < a, x_3 = 0\} \tag{10.34}$$

the strip load exerts a spatially uniformly distributed normal force on the fluid. The force per unit length in the x_2-direction and unit width in the x_1-direction is $\Phi(t)/2a$ with $\Phi(t)$ as the wavelet. For the test problem we took a source signature that is representative for a loaded mass-spring system, viz.

$$\Phi_\perp(t) = A \exp(-\delta t) \sin(\omega t) H(t), \tag{10.35}$$

where $H(t)$ is the Heaviside unit step function (cf. (11.27)), A the source strength amplitude, δ the damping coefficient and ω the angular frequency. In our computations we take a strip load for which a=1 m. Two synthetic seismograms are presented that represent the particle velocity close to the strip source. They apply to an array of 21 receivers that are located 0.15 m apart at a depth of 1 m. The first receiver of this array is located below the center of the strip source (Figure 10.4). For the computation of these seismograms we took as source parameters $A = 1$ N/m, $\delta = 2 * 10^4$ s^{-1} and $\omega = 2\pi * 5 * 10^3$ rad/s; this wavelet has a frequency of $5 * 10^3$ Hz and its first peak dominates the wave shape (see Figure 10.5). The seismograms in Figures 10.6 and 10.7 represent the horizontal and vertical particle velocities w_1 and w_3, respectively.

In the seismograms a scale is used such that the different wave phenomena are clearly visible. As a consequence, some of the wave peaks in the seismograms had to be clipped.

The computer program was written in Fortran 77. The time convolutions occurring in the expressions for the particle velocity were evaluated numerically with the aid of a subroutine of the NAG library (NAG (1988)). The relative accuracy for the determination of these time convolutions was set to 10^{-6}. To avoid numerical difficulties in the computation of the fluid waves in case the Cagniard-De Hoop contour runs closely along the pole $p = 0$ in the complex p−plane, an analytically integrable part was separated off from the relevant Green's function so that the remaining part was easy to integrate numerically.

For each receiver the synthetic data were computed at 300 time intervals of $2\pi/30\omega$ m · s. Because the source signature is a highly damped sinusoid,

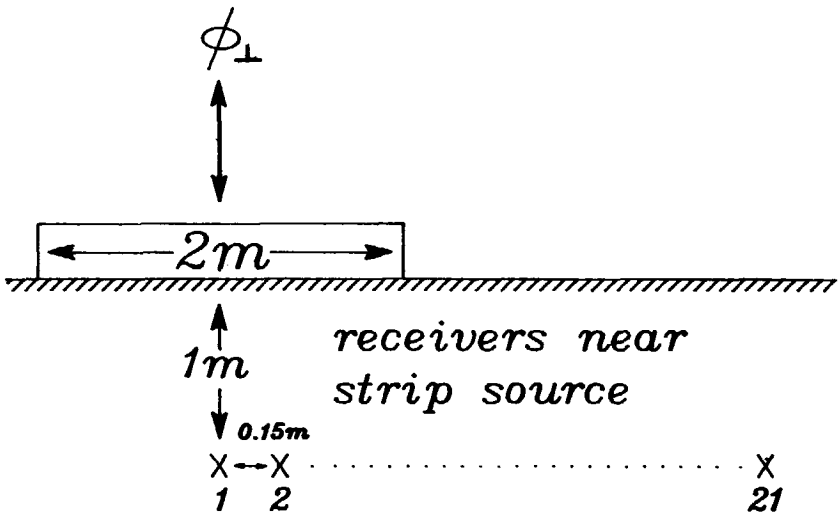

Figure 10.4: The array of 21 receivers near the strip source.

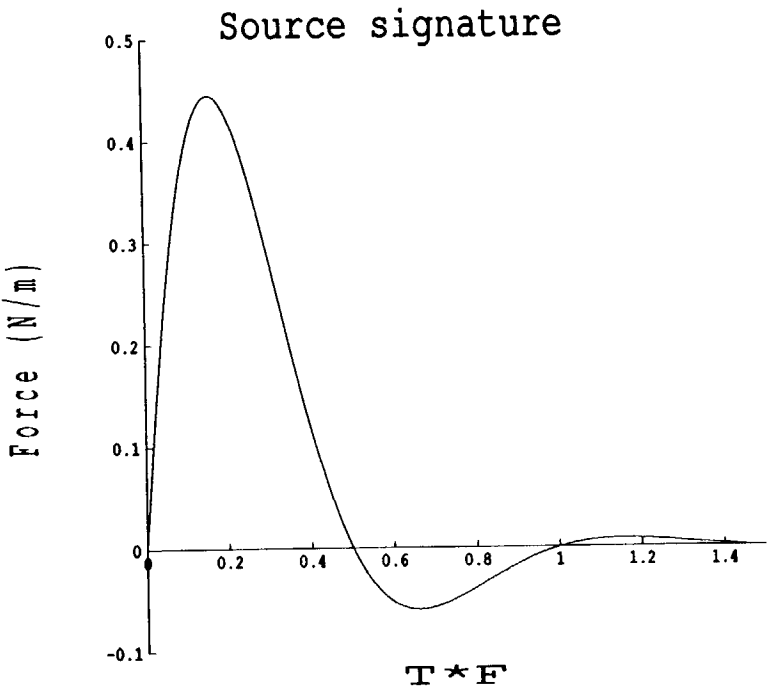

Figure 10.5: The source signature of the strip source for the source parameters $A = 1$ N/m, $\delta = 2 * 10^4$ s^{-1} and $\omega = 2\pi * 5 * 10^3$ rad/s (f=$5 * 10^3$ Hz).

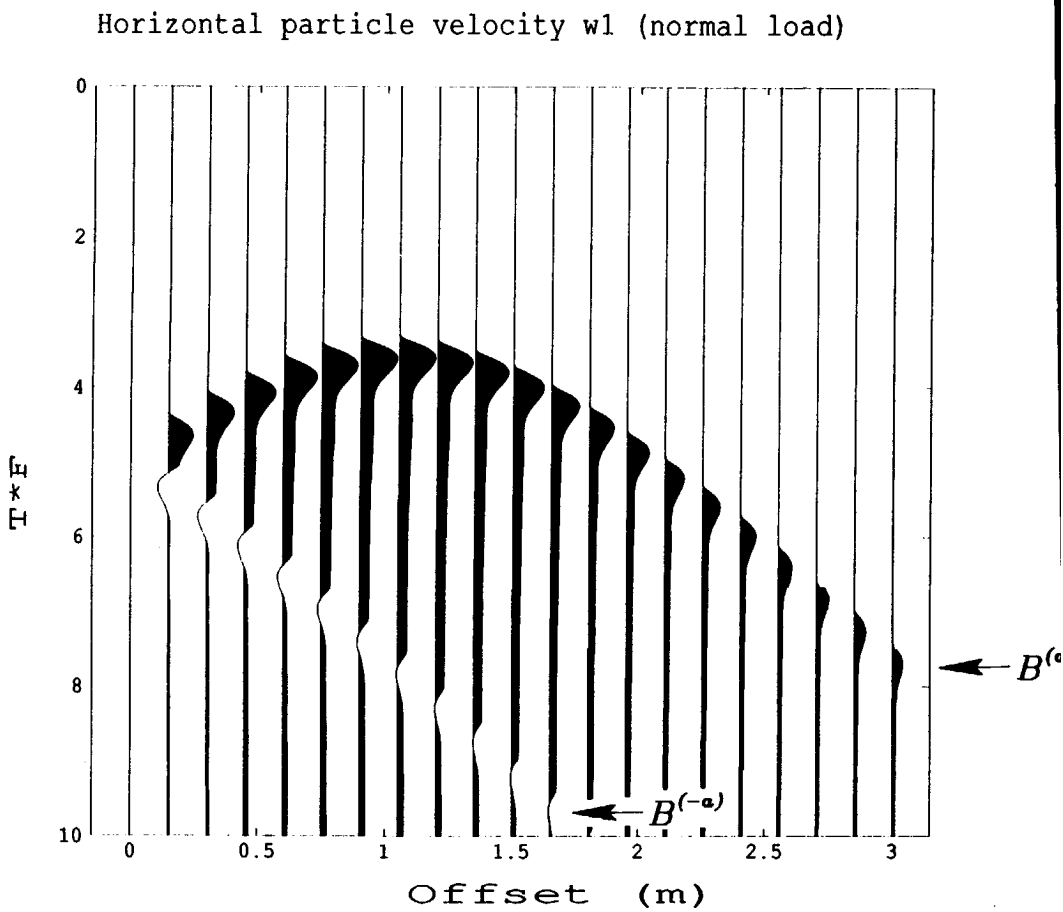

Figure 10.6: The horizontal component of the particle velocity for the 21 shallow receivers for the normal load. The fluid waves are indicated by B. The wave originating from the left edge of the strip source has the superscript $(-a)$, the one originating from the right edge of the strip source has the superscript (a).

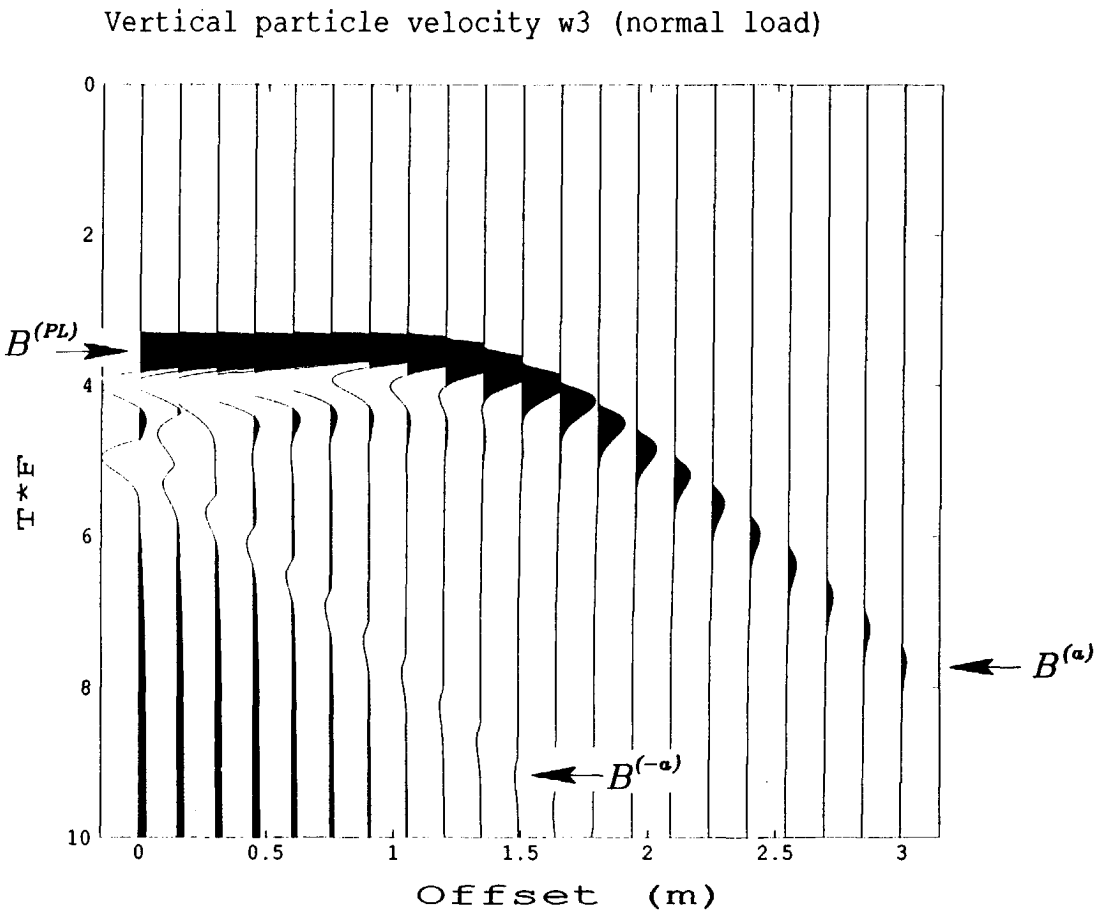

Figure 10.7: The vertical component of the particle velocity for the 21 shallow receivers for the normal load. The fluid waves are indicated by B. The wave originating from the left edge of the strip source has the superscript $(-a)$, the one originating from the right edge of the strip source has the superscript (a). The plane fluid wave is indicated by $B^{(PL)}$.

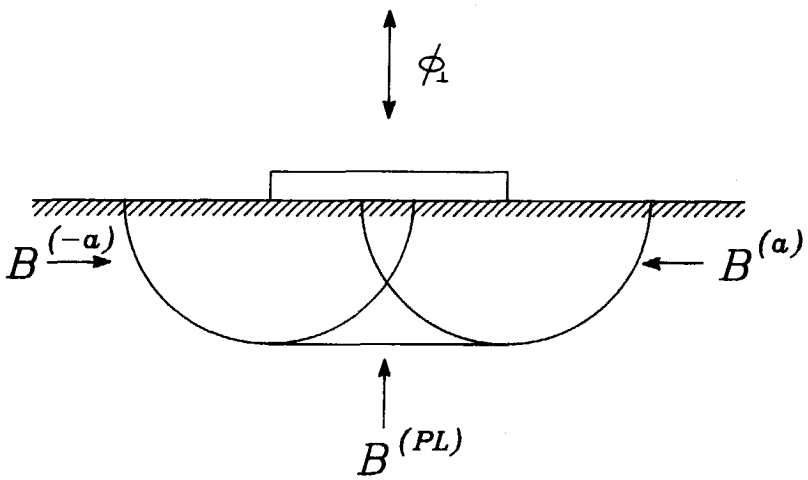

Figure 10.8: The different wave fronts generated by the normal load. The wave fronts of the fluid waves are indicated by B. The waves originating from the left edge of the strip source have the superscript $(-a)$, the ones originating from the right edge of the strip source have the superscript (a). The wave front of the plane fluid wave is indicated by $B^{(PL)}$.

the wave field quantities at a point of observation are expected to drop to a very small value shortly after the arrival of the first peak of the different wave constituents. To save a lot of computation time, the negligibly small field values at these instants have been automatically put equal to zero. With the above measures, the CPU-time needed for each of the two seismograms was about 1 hour on a Vax 8250 computer. The main part of the computation time was spent on the evaluation of the time convolutions of the source signature with the relevant Green's functions.

In the seismogram of the vertical component of the particle velocity w_3 we see the plane fluid wave contribution that exists below the strip source. The corresponding wave fronts are drawn in Figure 10.8.

The synthetic seismograms in Figures 10.6 and 10.7 have been computed for a source with a high frequency (5 kHz), in order to bring out clearly the characteristics of the wave motions generated. In problems of applied geophysics much lower frequencies usually occur. Since the presented solution method is suited for all frequencies, it can be used for low-frequency problems as well.

Chapter 11

TWO-DIMENSIONAL ACOUSTIC WAVES GENERATED BY A STRIP LOAD AT THE BOUNDARY OF A SEMI-INFINITE SOLID

Introduction

The two-dimensional acoustic $P-$ and $SV-$wave motion generated by an arbitrary distributed impulsive surface load on the boundary of a semi-infinite perfectly elastic solid is investigated theoretically. With the aid of the Cagniard-De Hoop method closed-form expressions are obtained for the particle velocity and the stress of the generated wave motion. For details of the Cagniard-De Hoop method see, for example, Achenbach (1973), Miklowitz (1978), Aki and Richards (1980), De Hoop and Van der Hijden (1985), or De Hoop (1988). The case of a uniformly distributed impulsive strip load of the normal-load and the shear-load types are worked out in detail. Synthetic seismograms are presented for an array of receivers close to the strip source, where a plane wave contribution is manifest in addition to the cylindrical $P-$ and $SV-$waves. For the time shape (source signature) of the exerting forces, a damped sinusoid is taken. The results are

[0] A manuscript containing the theory developed in this chapter has been accepted for publication in Geophysics, 1990, Vol. 50, Nr. 8

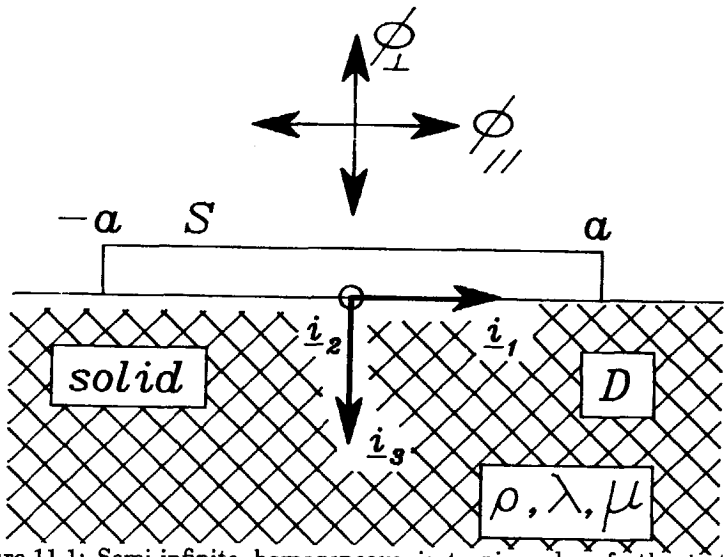

Figure 11.1: Semi-infinite, homogeneous, isotropic and perfectly elastic solid with medium parameters λ, μ, ρ and the strip source of extension $[-a, a]$ at its boundary. The strip source either exerts a normal force $\phi_\perp$ or a tangential force $\phi_{//}$.

of importance as test cases for the accuracy in the computational modeling of acoustic wave problems by, for example, time-domain finite-difference or finite-element methods (see, Alterman and Karal, 1968; Kelly et al., 1976; Emerman et al., 1982; Marfurt, 1984; Virieux, 1984, 1986).

Basic Equations

The elastic waves under consideration are small-amplitude disturbances traveling in a semi-infinite, homogeneous, isotropic, and perfectly elastic solid. The physical properties of the solid are characterized by its volume density of mass ρ and its Lamé coefficients λ and μ, which are real, positive constants. To specify the position in the configuration we employ the coordinates $\{x_1, x_2, x_3\}$ with respect to a fixed, orthogonal, Cartesian reference frame with origin O and the three mutually perpendicular base vectors $\{\boldsymbol{i}_1, \boldsymbol{i}_2, \boldsymbol{i}_3\}$ of unit length each. In the indicated order, the base vectors form a right-handed system. In accordance with the geophysical convention, $\boldsymbol{i}_3$ points vertically downwards (Figure 11.1). The subscript notation for Cartesian vectors and tensors is used and the sum-

mation convention applies. The structure is shift-invariant in the direction of i_2. The time coordinate is denoted by t. Partial differentiation is denoted by ∂; ∂_p denotes differentiation with respect to x_p, ∂_t is a reserved symbol for partial differentiation with respect to t.

The elastic medium occupies the half-space

$$D = \{x_m \in R^3; x_3 > 0\}. \tag{11.1}$$

A force is applied to the surface of the solid; it is taken to be independent of x_2. Consequently, all physical quantities associated with the wave motion are independent of x_2 as well, and $\partial_2 = 0$. The resulting two-dimensional wave motion is characterized by the non-zero particle velocity components v_1 and v_3 and the non-zero stress components $\tau_{11}, \tau_{22}, \tau_{33}$ and $\tau_{13} = \tau_{31}$. The corresponding components of the equation of motion in the interior of D are

$$\begin{aligned} -\partial_1\tau_{11} - \partial_3\tau_{13} + \rho\partial_t v_1 &= 0, \\ -\partial_1\tau_{31} - \partial_3\tau_{33} + \rho\partial_t v_3 &= 0. \end{aligned} \tag{11.2}$$

The non-zero stress components are related to the non-zero components of the particle velocity through the (sourcefree) deformation rate equation (constitutive relation)

$$\begin{aligned} \partial_t\tau_{11} &= \lambda(\partial_1 v_1 + \partial_3 v_3) + 2\mu\partial_1 v_1, \\ \partial_t\tau_{22} &= \lambda(\partial_1 v_1 + \partial_3 v_3), \\ \partial_t\tau_{33} &= \lambda(\partial_1 v_1 + \partial_3 v_3) + 2\mu\partial_3 v_3, \\ \partial_t\tau_{13} &= \mu(\partial_1 v_3 + \partial_3 v_1). \end{aligned} \tag{11.3}$$

At the surface of D, a surface load is applied to the solid. Its (prescribed) force has the horizontal component $\phi_{//}$ and the vertical component $\phi_\perp$. Hence, the boundary conditions

$$-\lim_{x_3 \downarrow 0} \tau_{13} = \phi_{//}(x_1, t) \text{ for all } x_1 \text{ and } t,$$

(11.4)

$$-\lim_{x_3 \downarrow 0} \tau_{33} = \phi_\perp(x_1, t) \text{ for all } x_1 \text{ and } t,$$

are to be satisfied. Let the source start to act at the instant $t = 0$, then $\phi_{//}(x_1, t) = 0$ and $\phi_\perp(x_1, t) = 0$ when $t < 0$, while

$$\{v_1, v_3, \tau_{11}, \tau_{22}, \tau_{33}, \tau_{13}\}(x_1, x_3, t) = 0 \text{ when } t < 0. \tag{11.5}$$

Equation (11.5) describes the causality of the generated wave motion.

Method of Solution

The Cagniard-De Hoop method is used to obtain analytical expressions for the particle velocity and the stress. The first step in this method consists of carrying out a one-sided Laplace transformation with respect to time. To show the notation we give the transformation for the particle velocity:

$$\hat{v}_k(x_1, x_3, s) = \int_{t=0}^{\infty} \exp(-st) v_k(x_1, x_3, t) dt. \tag{11.6}$$

In (11.6), s is a real, positive parameter that is chosen large enough to ensure the convergence of integrals of the indicated type. The next step consists of carrying out a one-dimensional Fourier transformation with respect to the horizontal coordinate x_1 . For the particle velocity this transformation is given by

$$\tilde{v}_k(i\alpha, x_3, s) = \int_{x_1=-\infty}^{\infty} \exp(is\alpha x_1) \hat{v}_k(x_1, x_3, s) dx_1, \tag{11.7}$$

where $\alpha \in R$. The corresponding inverse transformation is given by (note that the actual Fourier-transform variable in (11.7) is $s\alpha$)

$$\hat{v}_k(x_1, x_3, s) = (s/2\pi) \int_{\alpha=-\infty}^{\infty} \exp(-is\alpha x_1) \tilde{v}_k(i\alpha, x_3, s) d\alpha. \tag{11.8}$$

Subjecting the equation of motion (11.2) and the equation of deformation rate (11.3) to these transformations, ∂_t can be replaced by s and ∂_1 by $-is\alpha$, and a system of partial differential equations in x_3 is arrived at (Van der Hijden, 1988). Elimination of $\tilde{\tau}_{11}$ from this system leads to

$$\partial_3 \tilde{\underline{F}} = -s \underline{\underline{A}} \, \tilde{\underline{F}}, \tag{11.9}$$

where the field matrix $\underline{\tilde{F}}$ is the column matrix with the elements

$$\tilde{F}_1 = -\tilde{\tau}_{13}, \quad \tilde{F}_2 = -\tilde{\tau}_{33}, \quad \tilde{F}_3 = \tilde{v}_1, \quad \tilde{F}_4 = \tilde{v}_3, \tag{11.10}$$

and the system matrix $\underline{\underline{A}}$ is the square matrix with the elements

$$\begin{aligned} &A_{11} = A_{14} = A_{22} = A_{23} = A_{32} = A_{33} = A_{41} = A_{44} = 0, \\ &A_{12} = -i\alpha\lambda/(\lambda + 2\mu), \quad A_{13} = \rho - (i\alpha)^2 4\mu(\lambda + \mu)/(\lambda + 2\mu), \\ &A_{21} = -i\alpha, \quad A_{24} = \rho, \quad A_{31} = 1/\mu, \quad A_{34} = -i\alpha, \\ &A_{42} = 1/(\lambda + 2\mu), \quad A_{43} = -i\alpha\lambda/(\lambda + 2\mu). \end{aligned} \tag{11.11}$$

Note that $\underline{\underline{A}}$ is independent of s. Equation (11.9) represents a system of linear first-order ordinary differential equations in x_3. The eigenvalues of $\underline{\underline{A}}$ are found to be $\pm\gamma_P$ and $\pm\gamma_S$, with

$$\gamma_{P,S} = \gamma_{P,S}(i\alpha) = [1/c_{P,S}^2 - (i\alpha)^2]^{1/2}, \quad \mathrm{Re}(\gamma_{P,S}) \geq 0, \tag{11.12}$$

where $c_P = [(\lambda+2\mu)/\rho]^{1/2}$ is the $P-$wave speed and $c_S = (\mu/\rho)^{1/2}$ is the $S-$wave speed. The solution of (11.9) that is bounded as $x_3 \to \infty$ can be written as

$$\underline{\tilde{F}} = \underline{\tilde{F}}^P(i\alpha, x_3, s) + \underline{\tilde{F}}^S(i\alpha, x_3, s), \tag{11.13}$$

where

$$\underline{\tilde{F}}^P = W^P(i\alpha, s)\underline{\tilde{e}}^P(i\alpha)\exp(-s\gamma_P x_3) \tag{11.14}$$

is the $P-$wave in which

$$\underline{\tilde{e}}^P = \underline{\tilde{e}}^P(i\alpha) = \{2\mu i\alpha\gamma_P, 2\mu[1/2c_S^2 - (i\alpha)^2], i\alpha, \gamma_P\}^T \tag{11.15}$$

is a normalized eigenvector of $\underline{\underline{A}}$ corresponding to the eigenvalue γ_P, and

$$\underline{\tilde{F}}^S = W^S(i\alpha, s)\underline{\tilde{e}}^S(i\alpha)\exp(-s\gamma_S x_3) \tag{11.16}$$

is the $SV-$wave in which

$$\underline{\tilde{e}}^S = \underline{\tilde{e}}^S(i\alpha) = \{2\mu[1/2c_S^2 - (i\alpha)^2], -2\mu i\alpha\gamma_S, \gamma_S, -i\alpha\}^T \tag{11.17}$$

is a normalized eigenvector of $\underline{\underline{A}}$ corresponding to the eigenvalue γ_S. Note that $\tilde{\underline{e}}^P(i\alpha)$ and $\tilde{\underline{e}}^S(i\alpha)$ are independent of s. The amplitude coefficients $W^P = W^P(i\alpha, s)$ and $W^S = W^S(i\alpha, s)$ in (11.14) and (11.16) follow from the application of the boundary conditions (11.4) at $x_3 = 0$. They are obtained as

$$W^P(i\alpha, s) = W^P_{//}(i\alpha)\tilde{\phi}_{//}(i\alpha, s) + W^P_{\perp}(i\alpha)\tilde{\phi}_{\perp}(i\alpha, s), \tag{11.18}$$

$$W^S(i\alpha, s) = W^S_{//}(i\alpha)\tilde{\phi}_{//}(i\alpha, s) + W^S_{\perp}(i\alpha)\tilde{\phi}_{\perp}(i\alpha, s), \tag{11.19}$$

where

$$W^P_{//}(i\alpha) = i\alpha\gamma_S/2\mu\Delta_R, \quad W^P_{\perp}(i\alpha) = [1/2c_S^2 - (i\alpha)^2]/2\mu\Delta_R, \tag{11.20}$$

and

$$W^S_{//}(i\alpha) = [1/2c_S^2 - (i\alpha)^2]/2\mu\Delta_R, \quad W^S_{\perp}(i\alpha) = -i\alpha\gamma_P/2\mu\Delta_R, \tag{11.21}$$

in which

$$\Delta_R(i\alpha) = [1/2c_S^2 - (i\alpha)^2]^2 + (i\alpha)^2\gamma_P\gamma_S \tag{11.22}$$

is the Rayleigh determinant. Transforming the solution (11.13) back to the (x_1, x_3, s)−domain, the s−domain $P-$ and $SV-$wave field constituents

$$\hat{\underline{F}}^{P,S} = (s/2\pi)\int_{\alpha=-\infty}^{\infty} W^{P,S}(i\alpha, s)\tilde{\underline{e}}^{P,S}(i\alpha)\exp[-s(i\alpha x_1 + \gamma_{P,S}x_3)]d\alpha. \tag{11.23}$$

are obtained. Starting from the expressions (11.23), the case of a uniformly distributed strip load is further investigated in the next section.

Cagniard-De Hoop Method for the Uniformly Distributed Strip Load

In this section the case of the uniformly distributed strip load is worked out in detail. First the ray parameter $p = i\alpha$ is introduced in the integral representations (11.23). This leads to the expressions

$$\hat{\underline{F}}^{P,S} = (s/2\pi i)\int_{p=-i\infty}^{i\infty} W^{P,S}(p, s)\tilde{\underline{e}}^{P,S}(p)\exp[-s(px_1 + \gamma_{P,S}x_3)]dp. \tag{11.24}$$

Now, along the strip

$$S = \{x_m \in R^3;\ -a < x_1 < a,\ x_3 = 0\} \tag{11.25}$$

of width $2a$ a spatially uniformly distributed load is exerted on the solid (Figure 11.1). The spatial dependence on x_1 of the strip load is modeled by the difference of two unit step loads; one of which is active on the interval $(-a, \infty)$, the other one being active on the interval (a, ∞). The combination of the two equals unity on the interval $(-a, a)$ and vanishes outside this interval. Correspondingly, the distribution of the surface load has the form

$$\{\phi_{//}, \phi_{\perp}\}(x_1, t) = \{\Phi_{//}, \Phi_{\perp}\}(t)[H(x_1 + a) - H(x_1 - a)], \tag{11.26}$$

where

$$H(x_1) = \{0, 1/2, 1\} \text{ for } \{ x_1 < 0, x_1 = 0, x_1 > 0\} \tag{11.27}$$

is the Heaviside unit step function. The space-time transformed expression corresponding to (11.26) is

$$\{\tilde{\phi}_{//}, \tilde{\phi}_{\perp}\}(p, s) = \{\hat{\Phi}_{//}, \hat{\Phi}_{\perp}\}(s)[\exp(spa) - \exp(-spa)]/sp. \tag{11.28}$$

The expression (11.28) is substituted into (11.18) and (11.19) thus giving the amplitude coefficients that are substituted into (11.24). We observe that in the integrand in this expression the point $p = 0$ is a regular point as long as the two terms in the numerator are kept together. However, in the application of the Cagniard-De Hoop method, we have to separate these two terms and each of them has a simple pole at $p = 0$. To handle this singularity, the integrand in (11.24) is continued analytically into the complex p–plane away from the imaginary axes. Using Cauchy's theorem, the path of integration is, before the separation of the two terms in (11.28) has taken place, deformed into the path L^+ that deviates from the imaginary axes along a semi-circle of vanishingly small radius around $p = 0$ in the right half of the p–plane (Figure 11.2). (A semi-circle around $p = 0$ in the left half of the p–plane could have served as well; the two types of deviation lead to the same final results.)

In view of the linearity of our wave problem, the field $\underline{F}$ generated by a combined normal and shear load is the superposition of a field $\underline{F}_{\perp}$ generated by a normal load and a field $\underline{F}_{//}$ generated by a shear load:

$$\underline{F} = \underline{F}_{\perp} + \underline{F}_{//}, \tag{11.29}$$

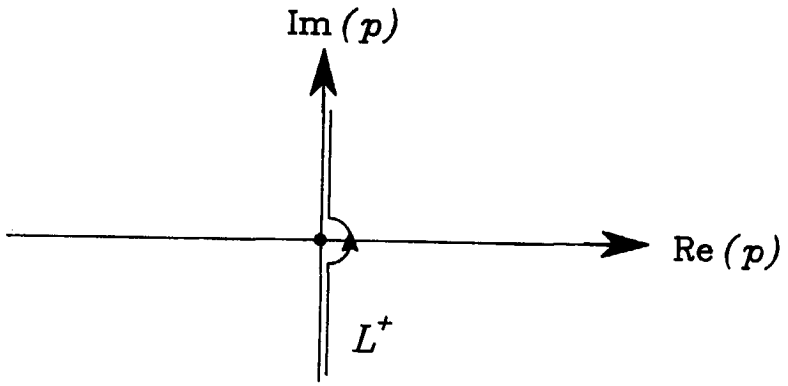

Figure 11.2: The contour L^+ in the complex $p-$plane

while we have the additional separation into a $P-$wave and an $SV-$wave which I express by

$$\underline{E}_{\perp} = \underline{E}^P_{\perp} + \underline{E}^S_{\perp}, \tag{11.30}$$

$$\underline{E}_{//} = \underline{E}^P_{//} + \underline{E}^S_{//}. \tag{11.31}$$

With the above, we obtain for the different wave-field contributions

$$\hat{\underline{E}}^{P,S}_{\perp,//}(x_1, x_3, s) = -[\underline{\hat{FE}}^{P,S}_{\perp,//}(x_1 + a, x_3, s) - \underline{\hat{FE}}^{P,S}_{\perp,//}(x_1 - a, x_3, s)], \tag{11.32}$$

where

$$[\underline{\hat{FE}}^{P,S}_{\perp,//}(\chi, x_3, s) =$$

$$[\hat{\Phi}_{\perp,//}(s)/2\pi i) \int_{p \in L^+} [W^{P,S}_{\perp,//}(p)/p] \tilde{\underline{\epsilon}}^{P,S}(p) \exp[-s(p\chi + \gamma_{P,S} x_3)] dp \tag{11.33}$$

in which χ stands for $x_1 + a$ or $x_1 - a$, respectively, and the expressions for $W^{P,S}_{\perp,//}(p)$ and $\tilde{\underline{\epsilon}}^{P,S}(p)$ are given in (11.20), (11.21) and (11.15), (11.17). In the case of a normal load, the factor p in the denominator of the integrand in (11.33) is, in the expression for the $SV-$wave, canceled by the factor p occurring in

$W_{\perp}^{S}(p)$, while in the case of a shear load it is canceled in the expression for the P–wave by the factor p occurring in $W_{//}^{P}(p)$.

Next, we take advantage of the symmetry of the configuration with respect to the plane $x_1 = 0$. For a normal load (i.e., $\Phi_{//} = 0, \Phi_{\perp} \neq 0$) we have the symmetry relations

$$v_1(x_1, x_3, t) = -v_1(-x_1, x_3, t), \quad v_3(x_1, x_3, t) = v_3(-x_1, x_3, t),$$

$$\tau_{13}(x_1, x_3, t) = -\tau_{13}(-x_1, x_3, t), \quad \tau_{33}(x_1, x_3, t) = \tau_{33}(-x_1, x_3, t). \tag{11.34}$$

For a shear load (i.e., $\Phi_{//} \neq 0, \Phi_{\perp} = 0$) we have the symmetry relations

$$v_1(x_1, x_3, t) = v_1(-x_1, x_3, t), \quad v_3(x_1, x_3, t) = -v_3(-x_1, x_3, t),$$

$$\tau_{13}(x_1, x_3, t) = \tau_{13}(-x_1, x_3, t), \quad \tau_{33}(x_1, x_3, t) = -\tau_{33}(-x_1, x_3, t). \tag{11.35}$$

Once the wave field has been determined in the domain

$$D^{+} = \{x_m \in R^3; x_1 \geq 0, x_3 > 0\}, \tag{11.36}$$

its values in the entire half-space D are known via (11.34) and (11.35).

P-wave Contribution

The Cagniard-De Hoop method is first elucidated for the P–wave expressions in the case of a spatially uniformly distributed normal strip load. The first step consists of deforming, in each of the two terms in (11.32), the path of integration L^{+} in the complex p–plane into a path L^{P} along which

$$p\chi + \gamma_P x_3 = \tau, \tag{11.37}$$

where τ is real and positive. By virtue of Jordan's lemma (Whittaker and Watson 1950, p.115) the contribution from joining circular axes at infinity vanishes, and hence Cauchy's theorem ensures that the integral along the imaginary p–axes is equal to the integral along L^{P}. In (11.37), $\chi = x_1 + a$ for the first

term in (11.32) and $\chi = x_1 - a$ for the second term in (11.32). Such a path is denoted as a Cagniard-De Hoop path. In the process of deformation we encounter the singularities in $W_\perp^P(p)/p, \underline{\varepsilon}^P(p)$ and $\gamma_{P,S}(p) = (1/c_{P,S}^2 - p^2)^{1/2}$. These are: the branch points $p = \pm 1/c_P$ of γ_P and $p = \pm 1/c_S$ of γ_S that also occur in $W_\perp^P(p)/p$ and $\underline{\varepsilon}^P(p)$, and the poles of $W_\perp^P(p)/p$, i.e., the zeros $p = \pm 1/c_R$ of Δ_R (cf. (11.22)) (c_R =Rayleigh wave speed), and the pole $p = 0$. The former two poles are associated with the Rayleigh waves along the traction-free boundary of the solid half-space; the pole $p = 0$ will be shown to be associated with the downgoing plane wave that exists in the vertical region below the strip S. Since the application of Cauchy's theorem in connection with the deformation of the path of integration in the complex $p-$plane requires the integrands to be single-valued, branch cuts are, in accordance with (11.12), introduced along $\mathrm{Im}(p) = 0$ and $1/c_{P,S} <| \mathrm{Re}(p) |< \infty$, i.e., where $\mathrm{Re}(\gamma_{P,S}) = 0$. In the cut $p-$plane, we then have $\mathrm{Re}[\gamma_{P,S}(p)] > 0$. Depending on the position of the point of observation, three cases are distinghuised for the deformation of the contour L^+ in (11.32) (Figure 11.3). First, if $\chi > 0$ the contour is deformed into the right half of the complex $p-$plane. Secondly, if $\chi = 0$ the contour remains unchanged and runs along L^+ . Finally, if $\chi < 0$ the contour is deformed into the left half of the complex $p-$plane, in which case the contribution from the pole $p = 0$ is to be taken into account. In this procedure the deformed paths of integration in (11.32) are obtained as $p = p^P(\chi, x_3, \tau)$ in the upper half of the $p-$plane, together with their images $p = p^{P*}$ with respect to the real axis, where p^P is given by

$$p^P(\chi, x_3, \tau) = \chi\tau/(\chi^2 + x_3^2) + i(\tau^2 - T_P^2)^{1/2} x_3/(\chi^2 + x_3^2), \tag{11.38}$$

with $T_P < \tau < \infty$, where $T_P = (\chi^2 + x_3^2)^{1/2}/c_P$ is the arrival time of the $P-$wave. Introducing τ as the variable of integration, we rewrite (11.33) in the form

$$\underline{\hat{E}}_\perp^P = \hat{\Phi}_\perp(s)\underline{\hat{G}}_\perp^P(\chi, x_3, s) + H(-\chi)\hat{\Phi}_\perp(s)W_\perp^P(0)\underline{\tilde{\varepsilon}}^P(0)\exp(-sx_3/c_P), \tag{11.39}$$

where H denotes again the Heaviside unit step function (cf. (11.27)), and

$$\underline{\hat{G}}_\perp^P(\chi, x_3, s) = \int_{\tau=T_P}^{\infty} \underline{g}_\perp^P(\chi, x_3, t)\exp(-s\tau)d\tau, \tag{11.40}$$

with

$$\underline{g}_\perp^P(\chi, x_3, \tau) = (1/\pi)\mathrm{Im}\{[W_\perp^P(p^P)/p^P]\underline{\tilde{\varepsilon}}^P(p^P)(\partial p^P/\partial\tau)\}H(\tau - T_P). \tag{11.41}$$

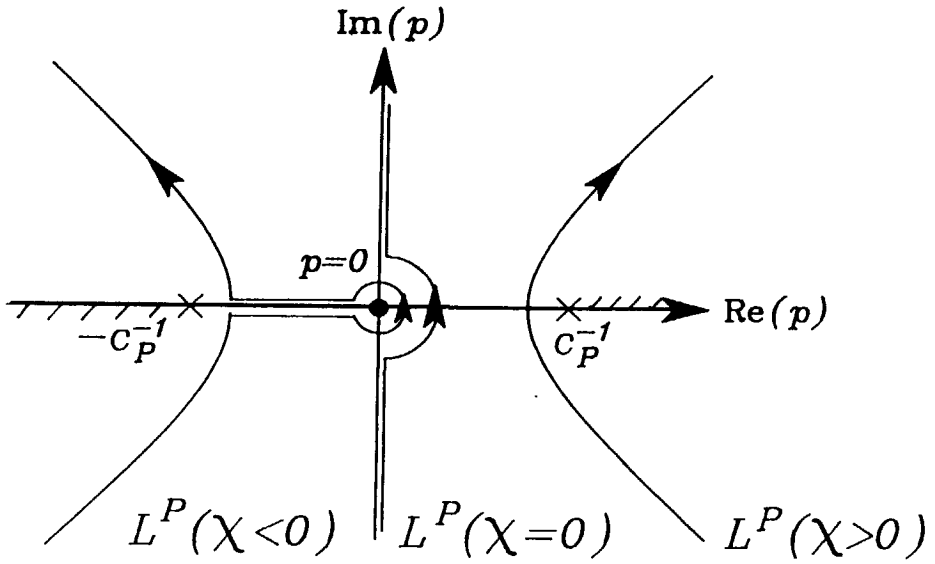

Figure 11.3: The contour L^P in the complex $p-$plane for the three different cases of $\chi < 0, \chi = 0, \chi > 0$.

In (11.41), $\partial p^P/\partial\tau$ is the one-dimensional Jacobian given by

$$\partial p^P/\partial\tau = \chi/(\chi^2 + x_3^2) + i[\tau/(\tau^2 - T_P^2)^{1/2}]x_3/(\chi^2 + x_3^2). \tag{11.42}$$

In the derivation of (11.39), the parts associated with $p = p^P$ and $p = p^{P^*}$ are taken together and Schwarz's reflection principle has been used in the integrand. In equation (11.39), the first term is the contribution from the integration along the contour L^P; it is identified as a cylindrical $P-$wave motion. The second term is the contribution from the residue of the integrand in (11.33) at the simple pole $p = 0$; it is identified as the plane $P-$wave that is excited below the strip source. (Note that in the domain D^+ given by (11.36), the region below the strip source $0 \le x_1 < a$ leads to $\chi < 0$ in the term for which $\chi = x_1 - a$ only.) The space-time expression for the $P-$wave follows by applying the convolution theorem to (11.39) and Lerch's theorem (see Widder, 1946):

$$\underline{FE}_\perp^P = H(t - T_P^{PL})\underline{PW}_\perp(\chi, x_3, t) + H(t - T_P)\int_{\tau=T_P}^{t} \Phi_\perp(t-\tau)\underline{g}_\perp^P(\chi, x_3, \tau)d\tau, \tag{11.43}$$

where $T_P^{PL} = x_3/c_P$ is the arrival time of the plane $P-$wave and

$$\underline{PW}_\perp(\chi, x_3, t) = H(-\chi)W_\perp^P(0)\tilde{\underline{\xi}}^P(0)\Phi_\perp(t - x_3/c_P). \tag{11.44}$$

We note that for $p = 0$ the first and third components of the eigenvector $\tilde{\underline{\xi}}^P$ are zero (see (11.15)). Consequently (cf. Eq. (11.10)), the only non-zero components of the plane $P-$wave existing below the strip are τ_{33} and v_3, as expected.

SV-wave Contribution

The $SV-$wave contribution is found in a similar manner, except that now the path of integration L^+ in each of the two terms of (11.32) is deformed in the complex $p-$plane into a path L^S along which

$$p\chi + \gamma_S x_3 = \tau, \tag{11.45}$$

where again τ is real and positive and $\chi = x_1 + a$ for the first term in (11.32) and $\chi = x_1 - a$ for the second term in (11.32). In the process of deformation we encounter the singularities in $W_\perp^S(p)/p, \tilde{\underline{\xi}}^S(p)$ and $\gamma_{P,S}(p) = (1/c_{P,S}^2 - p^2)^{1/2}$. These are: the branch points $p = \pm 1/c_P$ of γ_P and $p = \pm 1/c_S$ of γ_S, and the

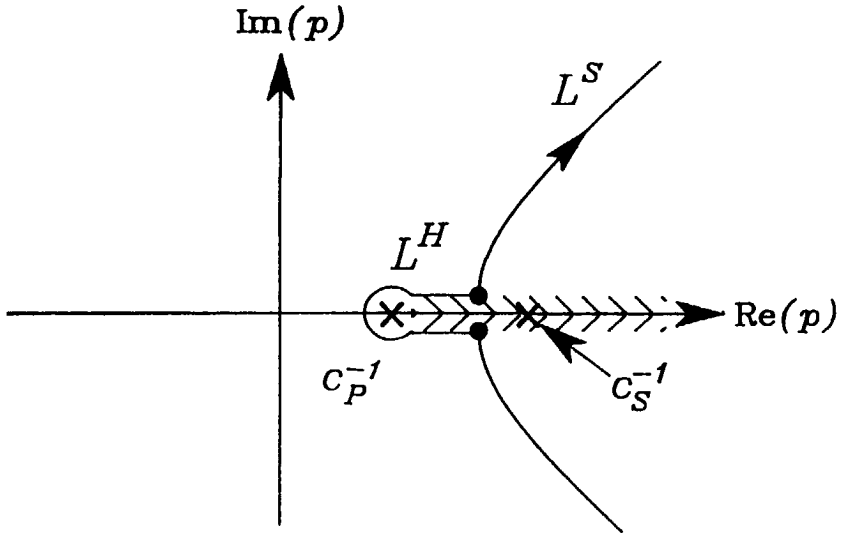

Figure 11.4: The contours L^H and L^S in the complex $p-$plane for the case $c_S/c_P < |\ \chi/(\chi^2+x_3^2)^{1/2}\ | \leq 1$.

poles of $W_\perp^S(p)/p$, i.e., the zeros $p = \pm 1/c_R$ of Δ_R. Note that in this case $p = 0$ is not a pole because the factor p in the denominator is canceled by the factor p occurring in $W_\perp^S(p)$ (see (11.21)). Hence, the corresponding integrand in (11.33) has no pole at $p = 0$ with the consequence that no plane $SV-$wave exists below the strip source. In deforming the path of integration from L^+ to a path where (11.45) holds, the deformed path is tempted to cross the branch cut associated with $p = 1/c_P$ in case $c_S/c_P < |\ \chi/(\chi^2+x_3^2)^{1/2}\ | \leq 1$. This has to be prevented and a loop integral L^H around this branch cut must be included (Figure 11.4). With this, the modified paths of integration in (11.32) generally exist of two parts: $p = p^H(\chi, x_3, \tau)$ and $p = p^S(\chi, x_3, \tau)$ both in the upper half of the p-plane, together with their images $p = p^{H^*}$ and $p = p^{S^*}$ with respect to the real axis, where p^H is given by

$$p^H(\chi, x_3, t) = \begin{cases} \chi\tau/(\chi^2+x_3^2) + (T_S^2-\tau^2)^{1/2}x_3/(\chi^2+x_3^2) + i0 & \text{when } \chi < 0, \\ \chi\tau/(\chi^2+x_3^2) - (T_S^2-\tau^2)^{1/2}x_3/(\chi^2+x_3^2) + i0, & \text{when } \chi > 0, \end{cases} \tag{11.46}$$

with $T_H < \tau < T_S$ where

$$T_H = T_P \mid \chi \mid /(\chi^2 + x_3^2)^{1/2} + T_S[1 - (c_S/c_P)^2]^{1/2} x_3/(\chi^2 + x_3^2)^{1/2},$$

$$T_S = (\chi^2 + x_3^2)^{1/2}/c_S, \tag{11.47}$$

and

$$p^S(\chi, x_3, \tau) = \chi\tau/(\chi^2 + x_3^2) + i(\tau^2 - T_S^2)^{1/2} x_3/(\chi^2 + x_3^2), \tag{11.48}$$

with $T_S < \tau < \infty$. Introducing τ as the variable of integration, we rewrite (11.33) in the form

$$\underline{\hat{F}\hat{E}}_\perp^S(\chi, x_3, s) = \hat{\Phi}_\perp(s)\underline{\hat{G}}_\perp^S(\chi, x_3, s), \tag{11.49}$$

where

$$\underline{\hat{G}}_\perp^S(\chi, x_3, s) = \int_{\tau=T_H}^{T_S} \underline{g}_\perp^H(\chi, x_3, \tau)\exp(-s\tau)d\tau + \int_{\tau=T_S}^{\infty} \underline{g}_\perp^S(\chi, x_3, \tau)\exp(-s\tau)d\tau, \tag{11.50}$$

in which

$$\underline{g}_\perp^H(\chi, x_3, \tau) = (1/\pi)\mathrm{Im}\{[W_\perp^S(p^H)/p^H]\underline{e}^S(p^H)(\partial p^H/\partial\tau)\}[H(\tau - T_H) - H(\tau - T_S)], \tag{11.51}$$

with $\partial p^H/\partial\tau$ being the one-dimensional Jacobian given by

$$\partial p^H/\partial\tau = \begin{cases} \chi/(\chi^2 + x_3^2) - [\tau/(T_S^2 - \tau^2)^{1/2}]x_3/(\chi^2 + x_3^2) & \text{when } \chi < 0, \\ \chi/(\chi^2 + x_3^2) + [\tau/(T_S^2 - \tau^2)^{1/2}]x_3/(\chi^2 + x_3^2) & \text{when } \chi > 0, \end{cases} \tag{11.52}$$

and

$$\underline{g}_\perp^S(\chi, x_3, \tau) = (1/\pi)\mathrm{Im}\{[W_\perp^S(p^S)/p^S]\underline{e}^S(p^S)(\partial p^S/\partial\tau)\}H(\tau - T_S), \tag{11.53}$$

with $\partial p^S/\partial\tau$ being the one-dimensional Jacobian given by

$$\partial p^S/\partial\tau = \chi/(\chi^2 + x_3^2) + i[\tau/(\tau^2 - T_S^2)^{1/2}]x_3/(\chi^2 + x_3^2). \tag{11.54}$$

The first term in (11.50) is the contribution from the integration along the contour L^H; it is identified as a cylindrical headwave (headwave arising from a

P to S conversion). The second term is the contribution from the integration along the contour L^S; it is identified as a cylindrical $SV-$ wave. In (11.47) and (11.48), T_H and T_S are the arrival times of the headwave and the $SV-$wave, respectively. The space-time expression for the $SV-$wave follows by applying the convolution theorem to (11.49) and Lerch's theorem (see Widder, 1946):

$$\underline{FE}_{\perp}^{S} = H(t-T_H)\int_{\tau=T_H}^{t} H(T_S-\tau)\Phi_{\perp}(t-\tau)\underline{g}_{\perp}^{H}(\chi,x_3,\tau)d\tau \tag{11.55}$$

$$+ H(t-T_S)\int_{\tau=T_S}^{t} \Phi_{\perp}(t-\tau)\underline{g}_{\perp}^{S}(\chi,x_3,\tau)d\tau.$$

Shear Load

In the case of a shear load, the $P-$ and $SV-$wave contributions are found in the same manner except that we have to replace $W_{\perp}^{P}(p)$ and $W_{\perp}^{S}(p)$ by $W_{//}^{P}(p)$ and $W_{//}^{S}(p)$, respectively, in (11.33). Then the factor p in the denominator of (11.28) is canceled for the $P-$wave expressions. (Note that $W_{//}^{P}(p)$ contains a factor p (see (11.20))), while it remains present in the $SV-$wave expressions ($W_{//}^{S}(p)$ does not contain a factor p (see (11.21))). Consequently, one of the important differences with the results for the normal load is the existence of a plane $SV-$wave in the region below the strip instead of a plane $P-$wave. The expression (11.39) is, for the case of a shear load, replaced by

$$\underline{\hat{FE}}_{//}^{P} = \hat{\Phi}_{//}(s)\underline{\hat{G}}_{//}^{P}(\chi,x_3,s), \tag{11.56}$$

where

$$\underline{\hat{G}}_{//}^{P}(\chi,x_3,s) = \int_{\tau=T_P}^{\infty} \underline{g}_{//}^{P}(\chi,x_3,t)\exp(-s\tau)d\tau, \tag{11.57}$$

in which

$$\underline{g}_{//}^{P}(\chi,x_3,\tau) = (1/\pi)\mathrm{Im}\{[W_{//}^{P}(p^P)/p^P]\underline{\varepsilon}^{P}(p^P)(\partial p^P/\partial\tau)\}H(\tau-T_P). \tag{11.58}$$

The relevant space-time expression for the $P-$wave follows by applying the convolution theorem to (11.56) and Lerch's theorem (see Widder, 1946):

$$\underline{FE}_{//}^{P} = H(t-T_P)\int_{\tau=T_P}^{t} \Phi_{//}(t-\tau)\underline{g}_{//}^{P}(\chi,x_3,\tau)d\tau. \tag{11.59}$$

Next, the expression (11.49) is for the case of a shear load, replaced by

$$\underline{\hat{FE}}^S_{//}(\chi, x_3, s) = \hat{\Phi}_{//}(s)\underline{\hat{G}}^S_{//}(\chi, x_3, s), \tag{11.60}$$

where

$$\underline{\hat{G}}^S_{//}(\chi, x_3, s) = \int_{\tau=T_H}^{T_S} \underline{g}^H_{//}(\chi, x_3, \tau)\exp(-s\tau)d\tau + \int_{\tau=T_S}^{\infty} \underline{g}^S_{//}(\chi, x_3, \tau)\exp(-s\tau)d\tau \tag{11.61}$$

$$+ H(-\chi)\hat{\Phi}_{//}(s)W^S_{//}(0)\underline{\tilde{e}}^S(0)\exp(-sx_3/c_S),$$

in which

$$\underline{g}^H_{//}(\chi, x_3, \tau) = (1/\pi)\mathrm{Im}\{[W^S_{//}(p^H)/p^H]\underline{e}^S(p^H)(\partial p^H/\partial\tau)\}[H(\tau - T_H) - H(\tau - T_S)], \tag{11.62}$$

and

$$\underline{g}^S_{//}(\chi, x_3, \tau) = (1/\pi)\mathrm{Im}\{[W^S_{//}(p^S)/p^S]\underline{e}^S(p^S)(\partial p^S/\partial\tau)\}H(\tau - T_S). \tag{11.63}$$

Again, the relevant space-time expression for the SV–wave follows by applying the convolution theorem to (11.60) and Lerch's theorem (see Widder, 1946):

$$\begin{aligned}\underline{FE}^S_{//} &= H(t - T^{PL}_S)\underline{PW}_{//}(\chi, x_3, t) \\ &+ H(t - T_H)\int_{\tau=T_H}^{t} H(T_S - \tau)\Phi_{//}(t - \tau)\underline{g}^H_{//}(\chi, x_3, \tau)d\tau \\ &+ H(t - T_S)\int_{\tau=T_S}^{t} \Phi_{//}(t - \tau)\underline{g}^S_{//}(\chi, x_3, \tau)d\tau,\end{aligned} \tag{11.64}$$

where $T^{PL}_S = x_3/c_S$ is the arrival time of the plane SV–wave and

$$\underline{PW}_{//}(\chi, x_3, t) = H(-\chi)W^S_{//}(0)\underline{\tilde{e}}^S(0)\Phi_{\perp}(t - x_3/c_S). \tag{11.65}$$

Equations (11.43), (11.55) and (11.59), (11.64) are the space-time expressions for the different waves that are generated in the semi-infinite solid by a strip load of the normal force and the shear force type, respectively. The wave motion consists in each of the two cases of cylindric P- and SV-waves originating from the two edges of the strip source (cf. (11.32)). In addition, in the case of a normal

strip load we have an extra plane $P-$wave, and in the case of a shear strip load an extra plane $SV-$wave, in the region below the strip source. As an illustration of the wave motion in the semi-infinite solid generated by the strip source at its boundary, synthetic seismograms for the uniformly distributed strip load of the normal force and the shear force type have been computed. The results are presented below.

Numerical Results

Synthetic seismograms of the particle velocity close to the strip source and at greater depths are presented, both for the normal strip load problem and for the shear strip load problem. The medium properties are taken to be $\rho = 2.5 * 10^3$ kg/m^3 and $\lambda = \mu = 10^{10}$ Pa. The corresponding $P-$ and $S-$wave speeds are: $c_P = 3464$ m/s and $c_S = 2000$ m/s. Along the strip

$$S = \{-a < x_1 < a, x_3 = 0\} \tag{11.66}$$

the strip load exerts either a spatially uniformly distributed normal force or a spatially uniformly distributed shear force on the solid. The force per unit length in the x_2-direction and unit width in the x_1-direction is $\Phi(t)/2a$ with $\Phi(t)$ as the wavelet. For the test problem we took a source signature that is representative for a loaded mass-spring system, viz.

$$\Phi_{\perp,//}(t) = A \exp(-\delta t) \sin(\omega t) H(t), \tag{11.67}$$

where $H(t)$ is the Heaviside unit step function (cf. (11.27)), A the source strength amplitude, δ the damping coefficient and ω the angular frequency. In our computations we take a strip load for which a=1 m. Four synthetic seismograms are presented that represent the particle velocity close to the strip source; two of them show the different waves generated by the strip source of the normal-load type and two of them show the different waves generated by the strip source of the shear-load type. They apply to an array of 21 receivers that are located 0.15 m apart at a depth of 1 m. The first receiver of this array is located below the center of the strip source (Figure 11.5). For the computation of these seismograms we took as source parameters $A = 1$ N/m, $\delta = 2 * 10^4$ s^{-1} and $\omega = 2\pi * 5 * 10^3$ rad/s; this wavelet has a frequency of $5 * 10^3$ Hz and its first

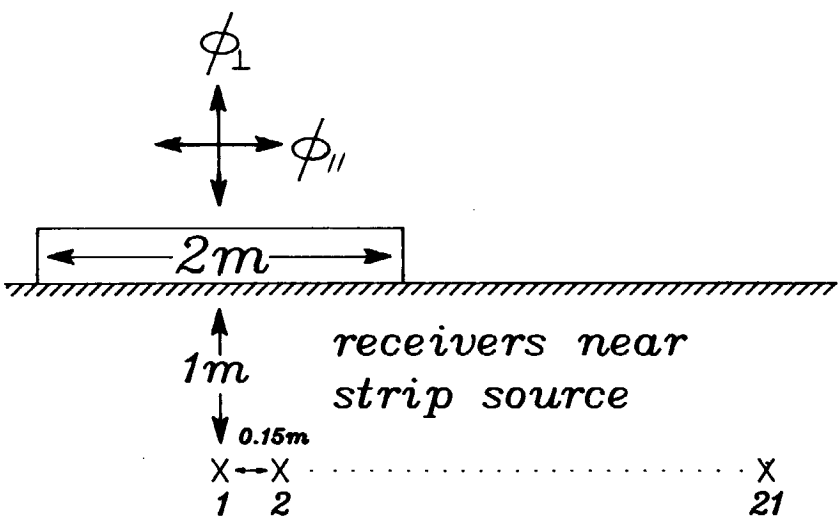

Figure 11.5: The array of 21 receivers near the strip source.

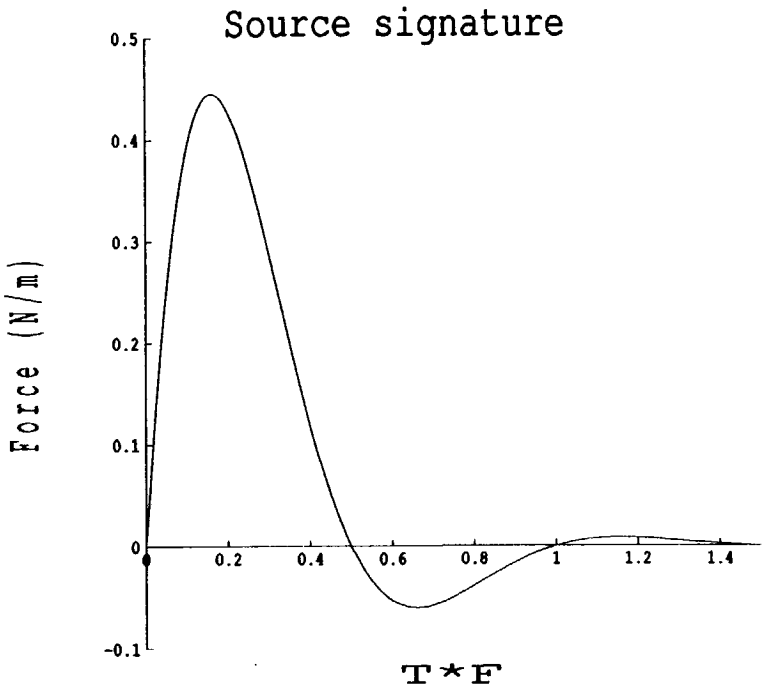

Figure 11.6: The source signature of the strip source for the source parameters $A = 1$ N/m, $\delta = 2 * 10^4$ s^{-1} and $\omega = 2\pi * 5 * 10^3$ rad/s (f=$5 * 10^3$ Hz) and for the source parameters $A = 1$ N/m, $\delta = 20$ s^{-1} and $\omega = 2\pi * 5$ rad/s (f = 5 Hz). Due to the scaled time axis, the figure shows the same source signature for both sets of source parameters.

peak dominates the wave shape (see Figure 11.6). The seismograms in Figures 11.7 and 11.8 represent the horizontal and vertical particle velocities v_1 and v_3, respectively, for the normal load. The seismograms in Figures 11.9 and 11.10 represent the horizontal and vertical particle velocities v_1 and v_3, respectively, for the shear load.

Next, another four synthetic seismograms are presented that represent the particle velocity at greater depths; again two of them show the waves generated by the strip source of the normal-load type and two of them show the waves generated by the strip source of the shear-load type. They apply to an array of 21 receivers that are located 150 m apart at a depth of 1000 m. The first receiver of this array is again located below the center of the strip source (Figure 11.11). For the computation of these seismograms we took as source parameters $A = 1$ N/m, $\delta = 2 * 10$ s^{-1} and $\omega = 2\pi * 5$ rad/s; this wavelet has a frequency of 5 Hz and its first peak dominates the wave shape (see Figure 11.6). The seismograms in Figures 11.12 and 11.13 represent the horizontal and vertical particle velocities v_1 and v_3, respectively, in the case of a normal load. The seismograms in Figures 11.14 and 11.15 represent the horizontal and vertical particle velocities v_1 and v_3, respectively, in the case of a shear load.

Both in the seismograms of the receivers near the strip source and in the seismograms of the receivers at greater depths a scale is used such that the different wave phenomena are clearly visible. As a consequence, some of the wave peaks in the seismograms had to be clipped.

The computer program was written in Fortran 77. The time convolutions occurring in the expressions for the particle velocity were evaluated numerically with the aid of a subroutine of the NAG library (NAG (1988)). The relative accuracy for the determination of these time convolutions was set to 10^{-6}. To avoid numerical difficulties in the computation of the P–wave for the normal load problem and in the computation of the SV–wave for the shear load problem in case the Cagniard-De Hoop contour runs closely along the pole $p = 0$ in the complex p–plane, for both problems an analytically integrable part was separated off from the relevant Green's function so that the remaining part was easy to integrate numerically.

For each receiver the synthetic data were computed at 300 time intervals

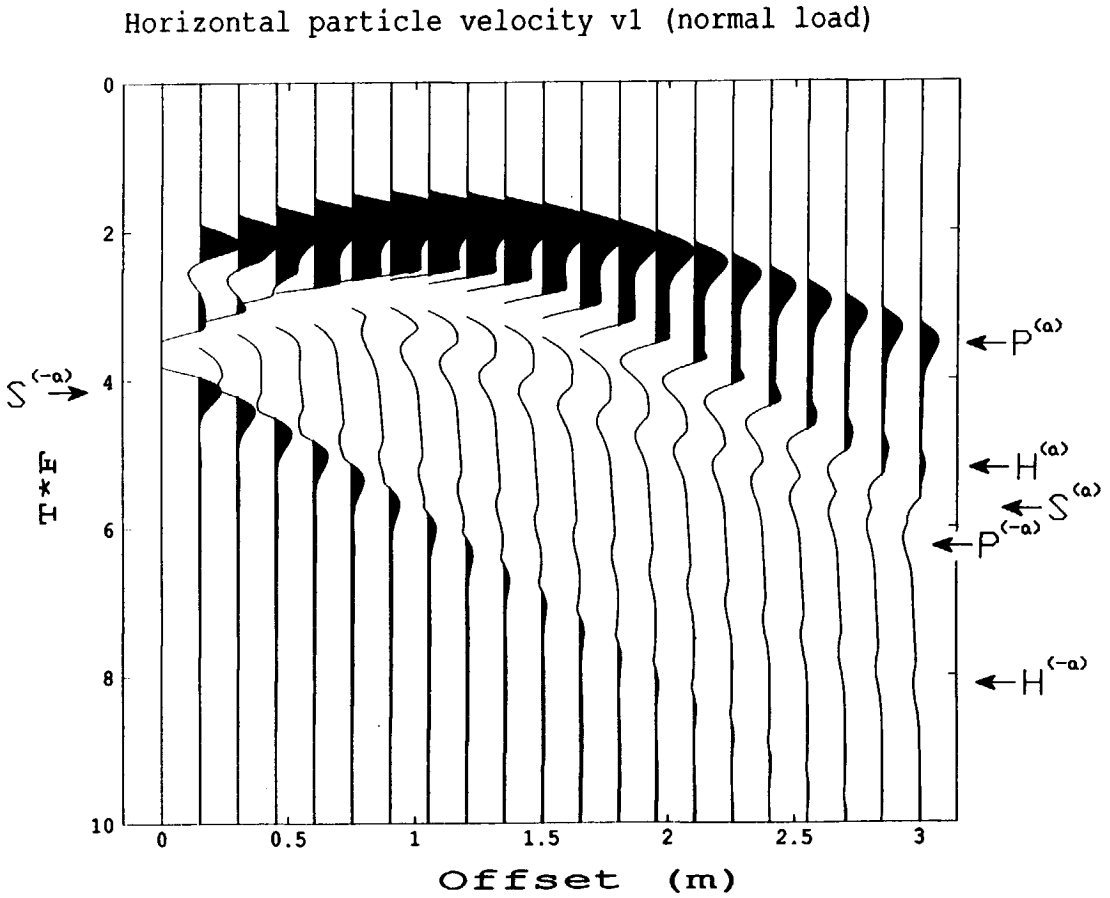

Figure 11.7: The horizontal component of the particle velocity for the 21 shallow receivers in the case of a normal load. The $P-, H-$, and $S-$waves are indicated by P, H and S, respectively. The waves originating from the left edge of the strip source have the superscript $(-a)$, the ones originating from the right edge of the strip source have the superscript (a). The Rayleigh waves have a too small amplitude to show up.

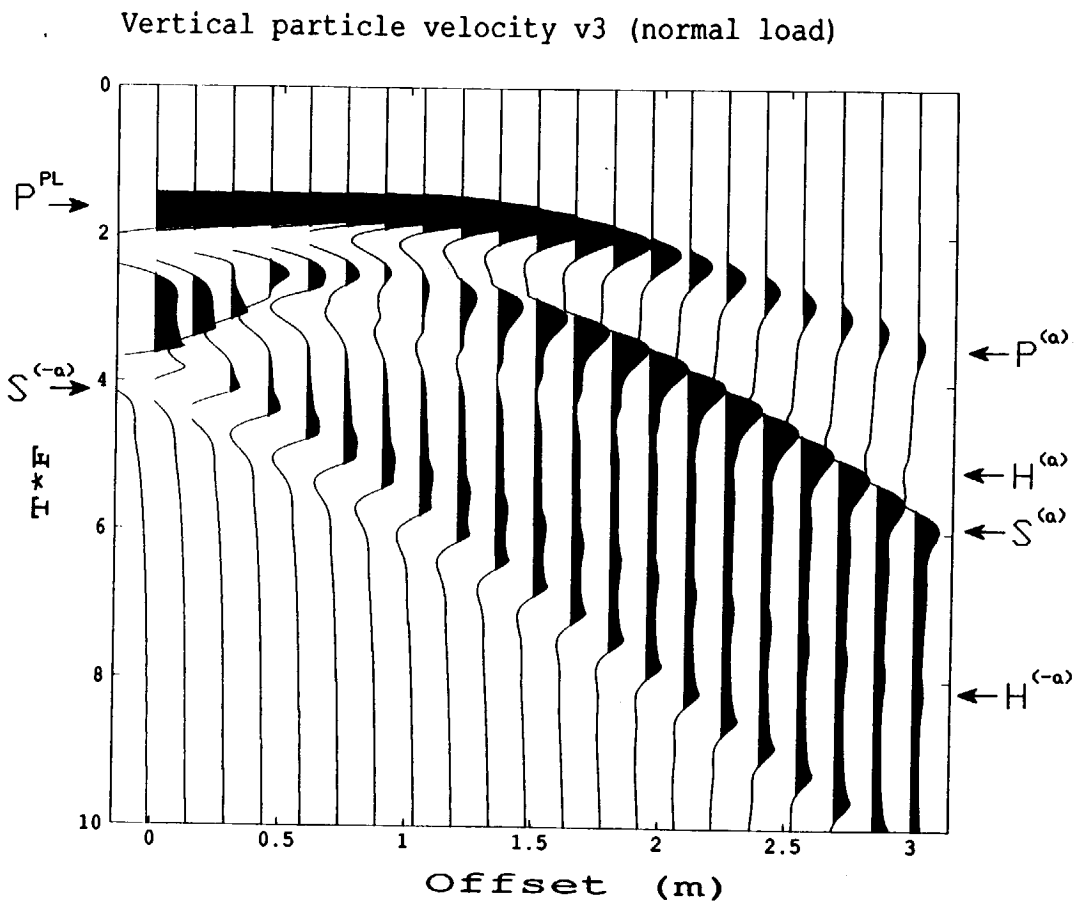

Figure 11.8: The vertical component of the particle velocity for the 21 shallow receivers in the case of a normal load. The $P-, H-$, and $S-$waves are indicated by P, H and S, respectively. The waves originating from the left edge of the strip source have the superscript $(-a)$, the ones originating from the right edge of the strip source have the superscript (a). The plane $P-$wave is indicated by P^{PL}. The Rayleigh waves have a too small amplitude to show up.

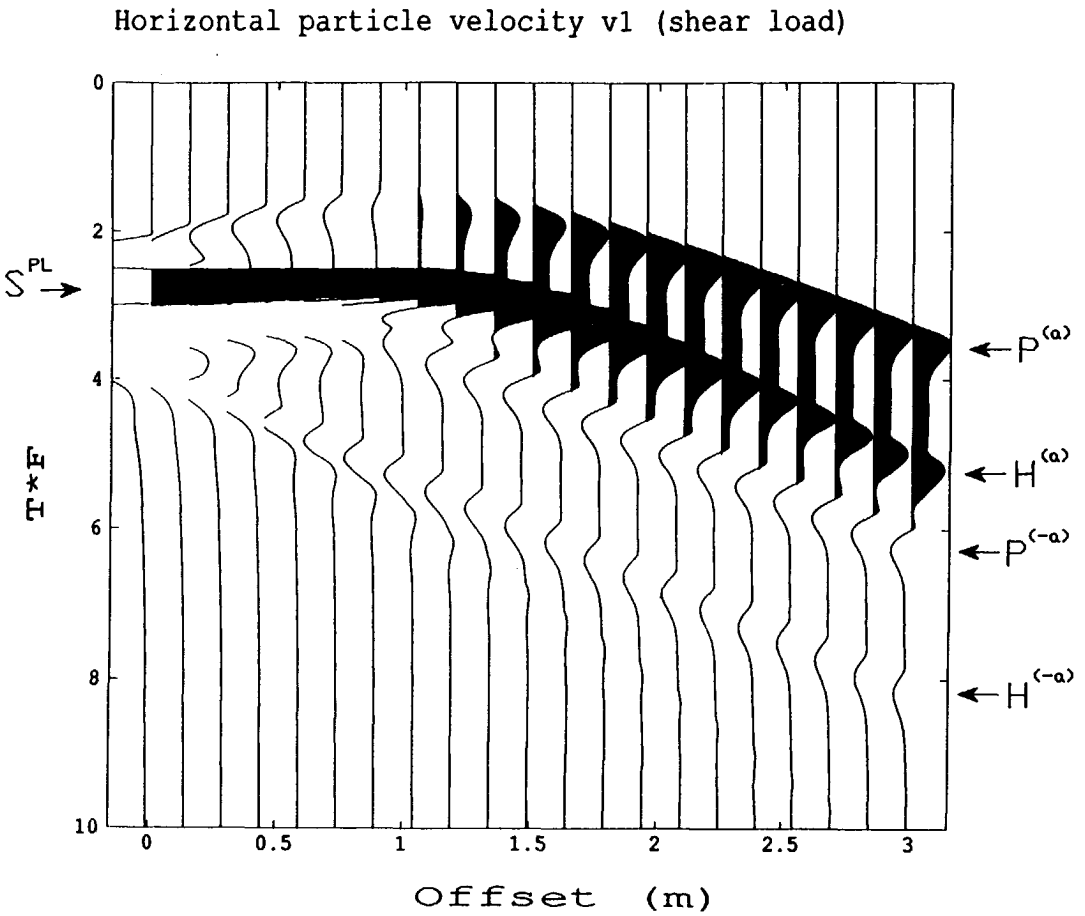

Figure 11.9: The horizontal component of the particle velocity for the 21 shallow receivers in the case of a shear load. The $P-$, $H-$, and $S-$waves are indicated by P, H and S, respectively. The waves originating from the left edge of the strip source have the superscript $(-a)$, the ones originating from the right edge of the strip source have the superscript (a). The plane $S-$wave is indicated by S^{PL}. The Rayleigh waves have a too small amplitude to show up.

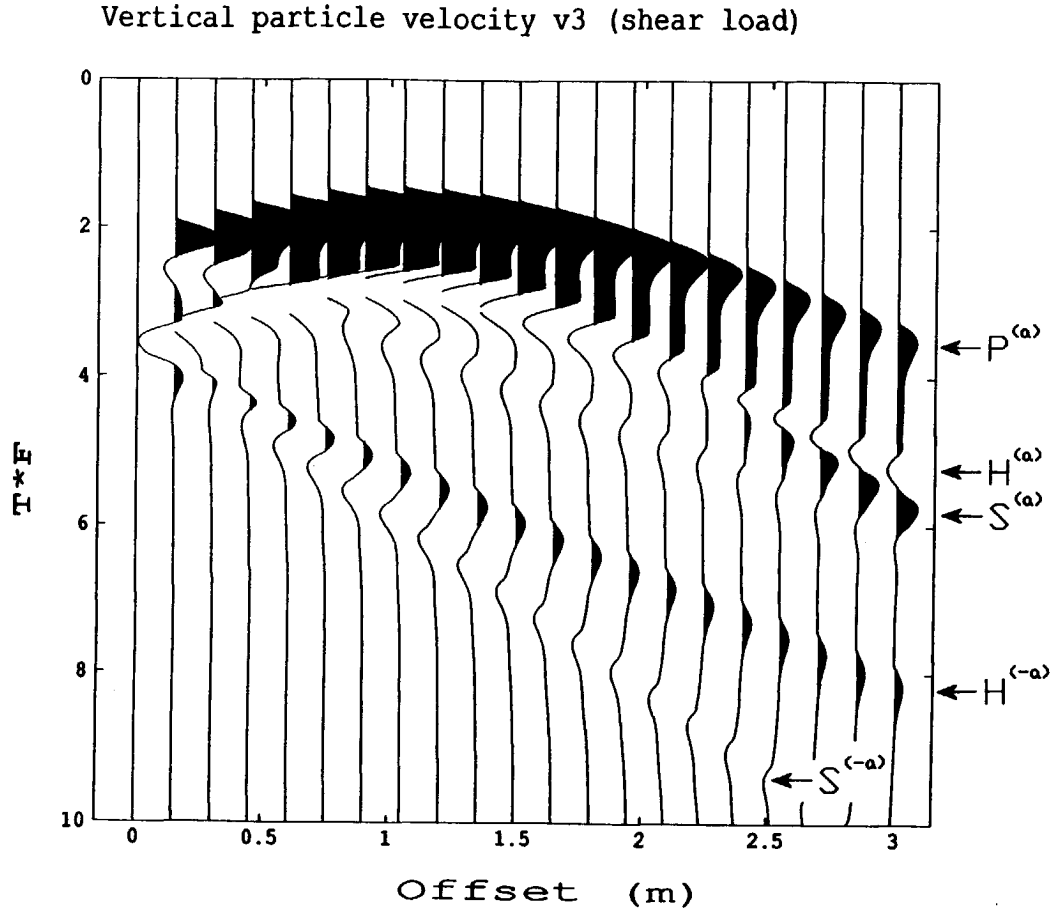

Figure 11.10: The vertical component of the particle velocity for the 21 shallow receivers in the case of a shear load. The $P-$, $H-$, and $S-$waves are indicated by P, H and S, respectively. The waves originating from the left edge of the strip source have the superscript $(-a)$, the ones originating from the right edge of the strip source have the superscript (a). The Rayleigh waves have a too small amplitude to show up.

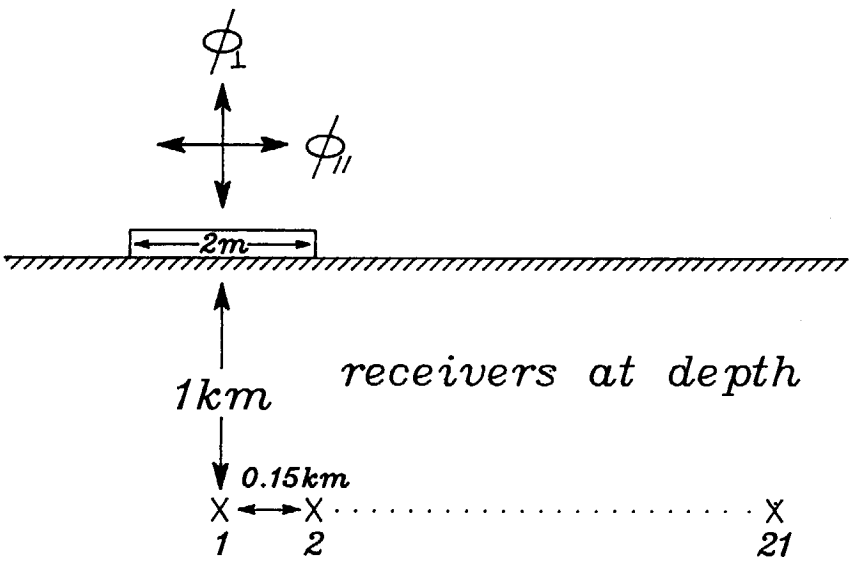

Figure 11.11: The array of 21 receivers at depth.

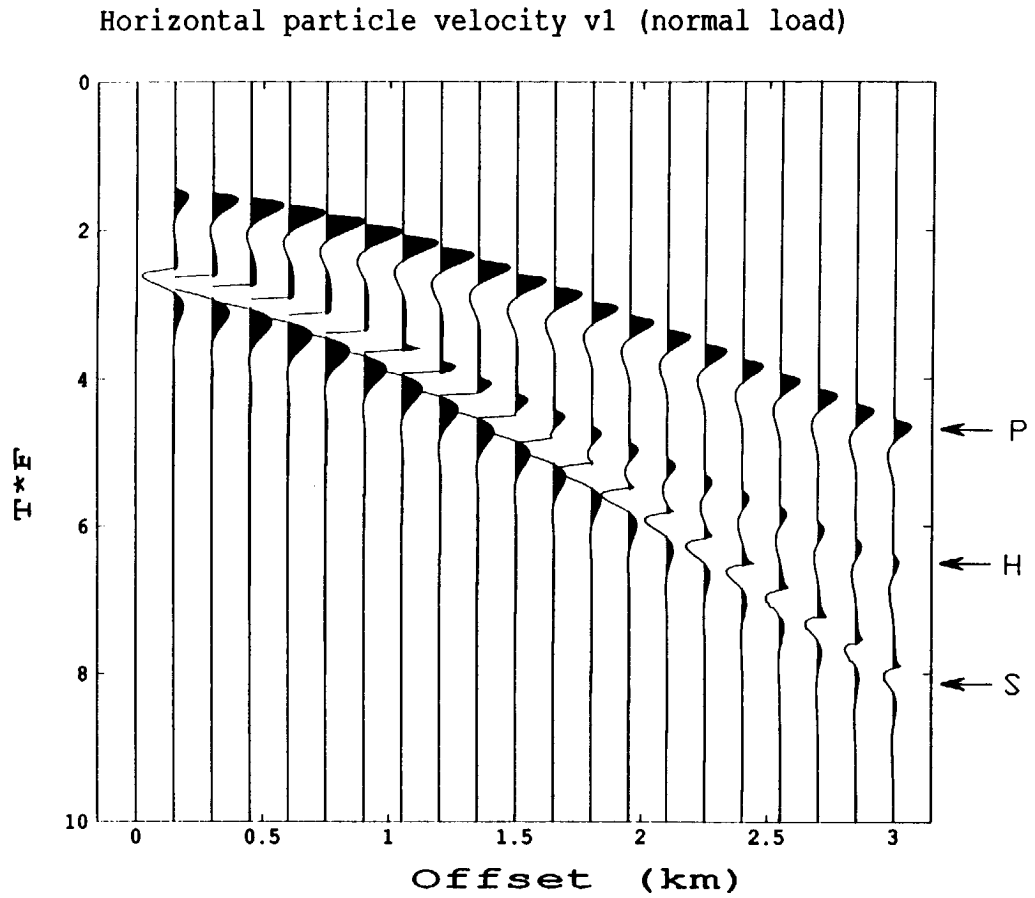

Figure 11.12: The horizontal component of the particle velocity for the 21 receivers at greater depths in the case of a normal load. The $P-, H-$, and $S-$waves are indicated by P, H and S, respectively. The Rayleigh waves have a too small amplitude to show up.

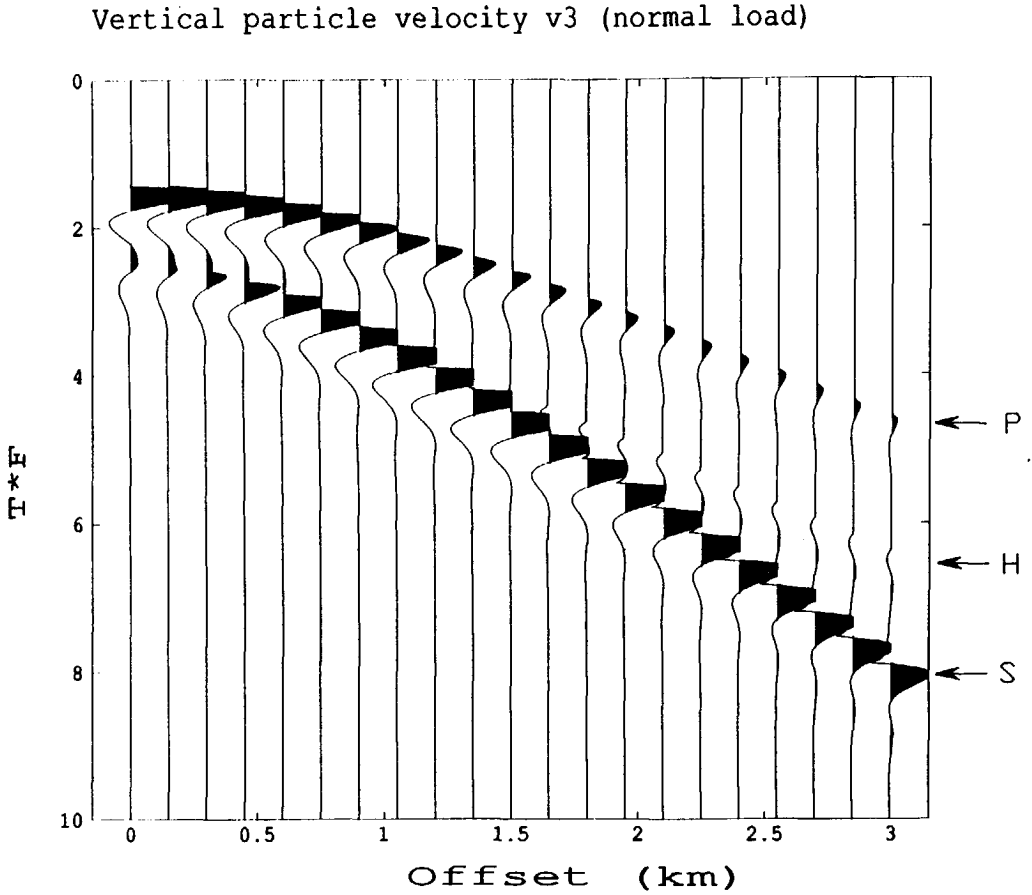

Figure 11.13: The vertical component of the particle velocity for the 21 receivers at greater depths in the case of a normal load. The $P-, H-$, and $S-$waves are indicated by P, H and S, respectively. The plane P-wave below the strip cannot be distinguished from the cylindrical P-wave emanating from the edges of the strip. The Rayleigh waves have a too small amplitude to show up.

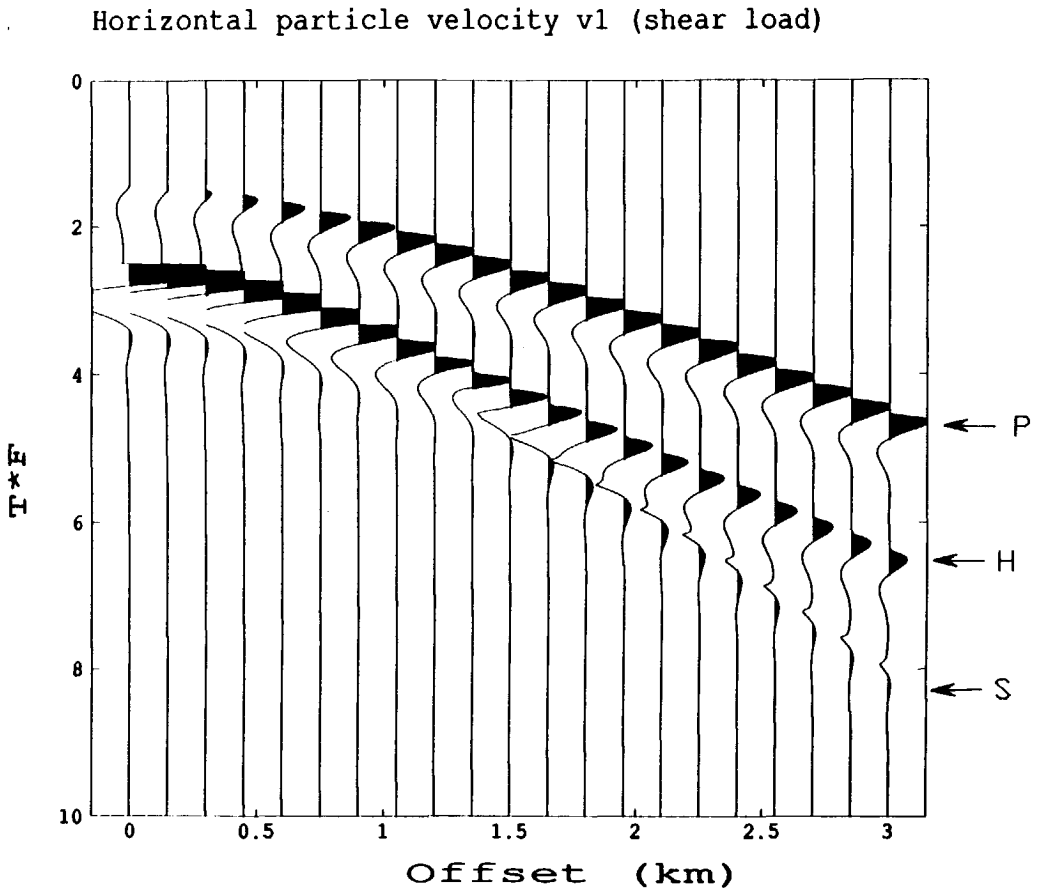

Figure 11.14: The horizontal component of the particle velocity for the 21 receivers at greater depths in the case of a shear load. The $P-, H-$, and $S-$waves are indicated by P, H and S, respectively. The plane S-wave below the strip cannot be distinguished from the cylindrical S-wave emanating from the edges of the strip. The Rayleigh waves have a too small amplitude to show up.

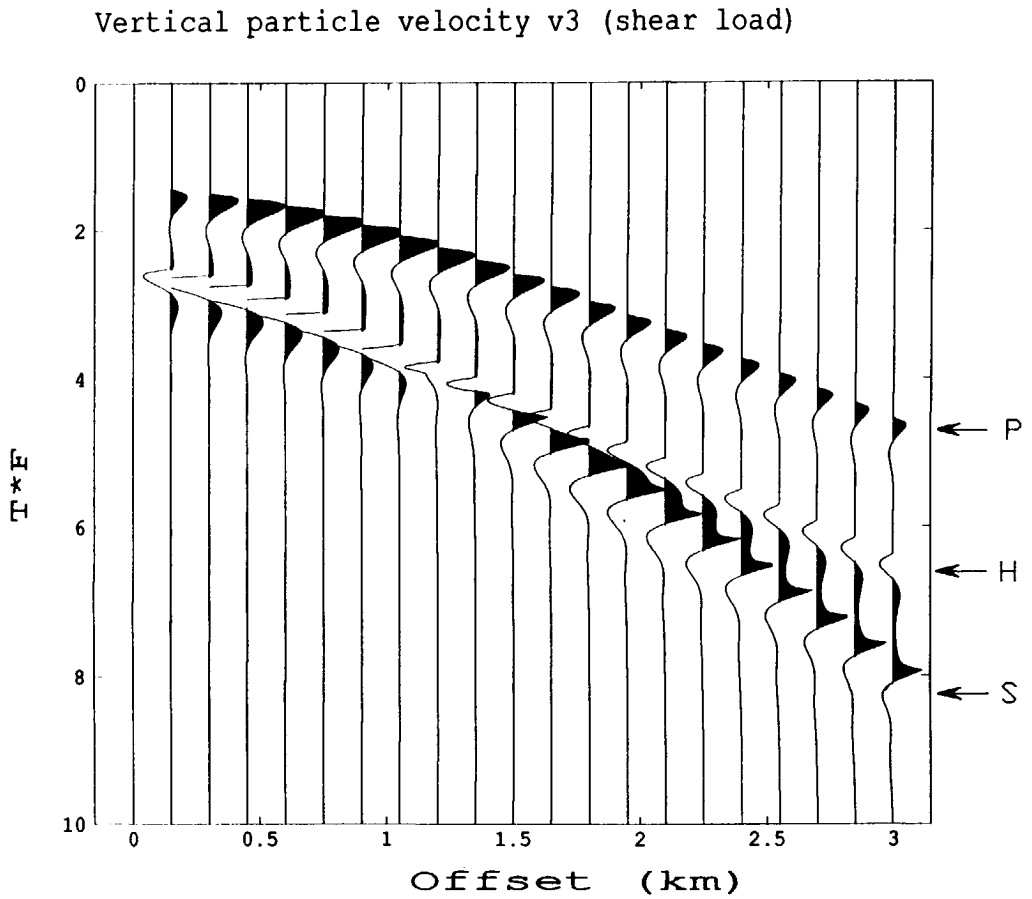

Figure 11.15: The vertical component of the particle velocity for the 21 receivers at greater depths in the case of a shear load. The $P-, H-$, and $S-$waves are indicated by P, H and S, respectively. The Rayleigh waves have a too small amplitude to show up.

of $2\pi/30\omega$ m · s. Because the source signature is a highly damped sinusoid, the wave field quantities at a point of observation are expected to drop to a very small value shortly after the arrival of the first peak of the different wave constituents. To save a lot of computation time, the negligibly small field values at these instants have been automatically put equal to zero. With the above measures, the CPU-time needed for each of the eight seismograms was about 1.5 hour on a Vax 8250 computer. The main part of the computation time was spent on the evaluation of the time convolutions of the source signature with the relevant Green's functions.

The seismograms in Figures 11.7-11.10 clearly show the different $P-, S-$ and P to S headwave conversion waves originating from the two edges of the strip source. In addition, we see for the case of a normal load in the seismogram of the vertical component of the particle velocity v_3 the plane $P-$wave contribution that exists below the strip source, while for the case of a shear load we see in the seismogram of the horizontal component of the particle velocity v_1 the plane $S-$wave contribution that now exists below the strip source. The Rayleigh waves have a too small amplitude to show up. The corresponding wave fronts for the normal load are drawn in Figure 11.16 and for the shear load in Figure 11.17.

The synthetic seismograms in Figures 11.7-11.10 have been computed for a source with a high frequency (5 kHz) in order to bring out clearly the characteristics of the wave motions generated. In problems of applied geophysics much lower frequencies usually occur. Since the presented solution method is suited for all frequencies, it can be used for low-frequency problems as well.

The seismograms in Figures 11.12-11.15 clearly show the $P-, S-$ and P to S headwave conversion waves generated by the strip source. The Rayleigh waves have a too small amplitude to show up. We see for the case of a normal load that the strip source outputs a lot of shear wave energy. From these seismograms it is observed that at a distance from the strip source that is large compared with its width, the particle velocity can be approximated by the particle velocity generated by a line source with the proper strength placed at the center of the strip source.

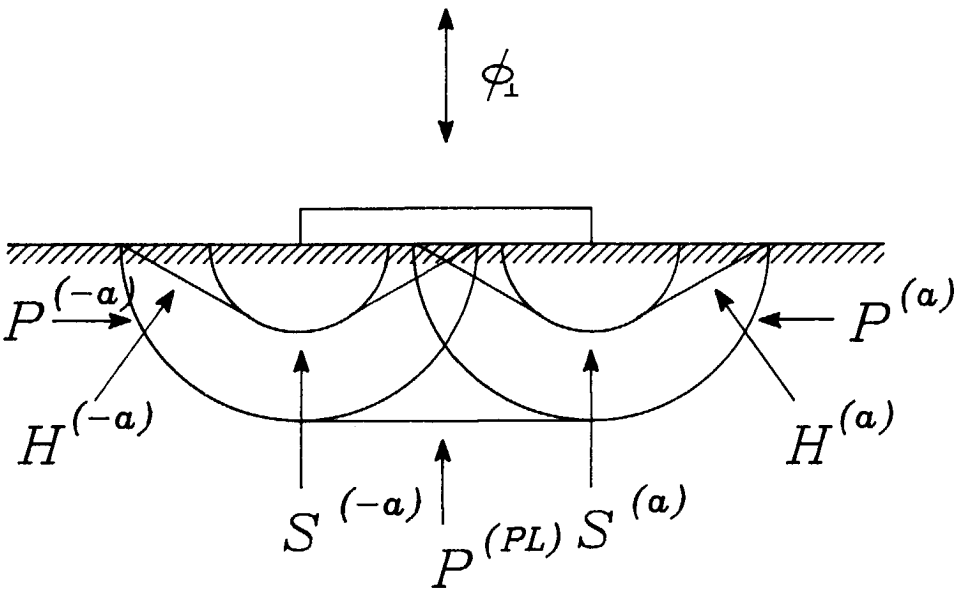

Figure 11.16: The different wave fronts generated by the normal load. The wave fronts of the $P-, H-$, and $S-$waves are indicated by P, H and S, respectively. The waves originating from the left edge of the strip source have the superscript $(-a)$, the ones originating from the right edge of the strip source have the superscript (a). The wave front of the plane $P-$wave is indicated by $P^{(PL)}$. The Rayleigh (surface) waves are indicated by R.

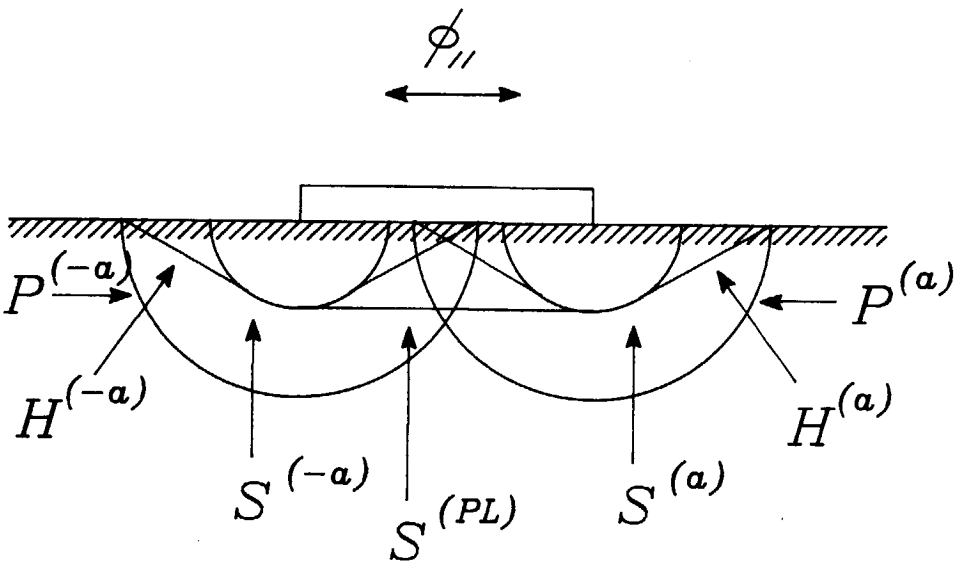

Figure 11.17: The different wave fronts generated by the shear load. The wave fronts of the $P-, H-$, and $S-$waves are indicated by P, H and S, respectively. The waves originating from the left edge of the strip source have the superscript $(-a)$, the ones originating from the right edge of the strip source have the superscript (a). The wave front of the plane $S-$wave is indicated by $S^{(PL)}$. The Rayleigh (surface) waves are indicated by R.

Chapter 12

TWO-DIMENSIONAL ACOUSTIC WAVES GENERATED BY A STRIP SOURCE AT A PLANE FLUID/SOLID INTERFACE

Introduction

The two-dimensional acoustic wave motion generated by an arbitrary distributed impulsive strip source at the plane interface between a semi-infinite solid and a semi-infinite fluid is investigated theoretically. Both media are homogeneous, isotropic and lossless. With the aid of the Cagniard-De Hoop method closed-form space-time expressions are obtained for the particle velocity and the scalar traction of the generated wave motion in the fluid and the particle velocity and the stress of the generated wave motion in the solid. For details of the Cagniard-De Hoop method see, for example, Achenbach (1973); Miklowitz (1978); Aki and Richards (1980); De Hoop and Van der Hijden (1985); or De Hoop (1988).

The case is considered where the strip source either introduces a distributed volume injection rate or exerts on the boundary surface of the fluid as well as the boundary surface of the solid a normal distributed force. The case of a uniformly distributed impulsive strip source is worked out in detail. Synthetic seismograms are presented for an array of receivers in the solid close to the

strip source where a plane $P-$wave contribution is manifest in addition to the cylindrical $P-$ and $SV-$waves, and for an array of receivers in the fluid close to the strip source where a plane $P-$wave contribution is manifest in addition to the cylindrical $P-$waves.

For the force and for the volume injection rate strip source strengths a damped sinusoid is taken as time shape (source signature). The results are of importance as test cases for the accuracy in the computational modeling of acoustic wave problems by, for example, time-domain finite-difference or finite-element methods (see, Alterman and Karal, 1968; Kelly et al., 1976; Emerman et al., 1982; Marfurt, 1984; Virieux, 1984, 1986).

Basic Equations

The acoustic waves under consideration are small-amplitude disturbances traveling in a fluid/solid configuration consisting of a semi-infinite fluid and a semi-infinite solid that are in touch along their plane interface. The fluid and the solid are both homogeneous, isotropic, and lossless. The physical properties of the fluid are characterized by its volume density of mass ρ^f and its compressibility κ; the physical properties of the solid are characterized by its volume density of mass ρ^s and its Lamé coefficients λ and μ. All constitutive coefficients are real, positive constants.

To specify the position in the configuration I employ, as before, the coordinates $\{x_1, x_2, x_3\}$ with respect to a fixed, orthogonal, Cartesian reference frame with origin O and the three mutually perpendicular base vectors $\{\boldsymbol{i}_1, \boldsymbol{i}_2, \boldsymbol{i}_3\}$ of unit length each. In the indicated order, the base vectors form a right-handed system. The origin O is taken to be on the plane interface and the unit base vectors $\boldsymbol{i}_1$ and $\boldsymbol{i}_2$ are taken to be parallel to the interface. The unit base vector $\boldsymbol{i}_3$ points vertically downwards into the solid (Figure 12.1). The subscript notation for Cartesian vectors and tensors is used and the summation convention applies. The time coordinate is denoted by t. Partial differentiation is denoted by $\partial; \partial_p$ denotes differentiation with respect to x_p, ∂_t is a reserved symbol for partial differentiation with respect to t.

The fluid/solid configuration occupies the domain $D = R^3$. In D, the fluid

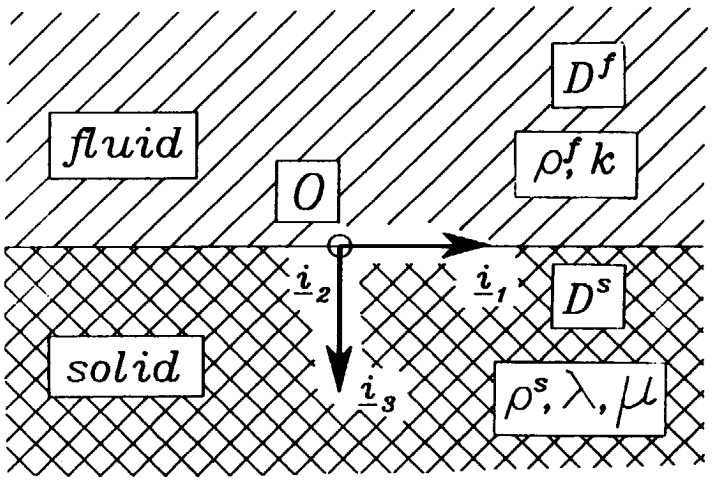

Figure 12.1: The semi-infinite fluid and the semi-infinite solid in touch along the infinite plane interface. The origin O of the Cartesian reference frame is taken to be at the interface, and the unit base vectors $\boldsymbol{i}_1$ and $\boldsymbol{i}_2$ are taken to be parallel to it.

occupies the halfspace

$$D^f = \{x_m \in R^3; x_3 < 0\} \tag{12.1}$$

and the solid occupies the halfspace

$$D^s = \{x_m \in R^3; x_3 > 0\}. \tag{12.2}$$

The plane interface between the fluid and the solid is given by

$$I = \{x_m \in R^3; x_3 = 0\}. \tag{12.3}$$

On the interface I a strip source is present that is parallel to the x_2-direction and exerts a normal force on the boundary surfaces of both the fluid and the solid. With this source, we have a structure that is shift-invariant in the x_2-direction. The force that is applied by the strip source is taken to be independent of x_2. As a consequence, all physical quantities associated with the wave motion are independent of x_2 as well, and $\partial_2 = 0$. The resulting two-dimensional wave motion in D is in the part D^f where the fluid is present, characterized by the non-zero particle velocity components w_1 and w_3 and the non-zero scalar traction σ, and in the part D^s where the solid is present, by the non-zero particle velocity components v_1 and v_3 and the non-zero stress components $\tau_{11}, \tau_{22}, \tau_{33}$ and $\tau_{13} = \tau_{31}$ (in-plane wave motion). The corresponding components of the (sourcefree) equation of motion in the interior of D^f are

$$\begin{aligned} -\partial_1\sigma + \rho^f\partial_t w_1 &= 0, \\ -\partial_3\sigma + \rho^f\partial_t w_3 &= 0. \end{aligned} \tag{12.4}$$

The scalar traction is related to the non-zero components of the particle velocity through the (sourcefree) deformation rate equation (constitutive relation)

$$\partial_t\sigma = (1/\kappa)(\partial_1 w_1 + \partial_3 w_3). \tag{12.5}$$

The corresponding components of the (sourcefree) equation of motion in the interior of D^s are

$$-\partial_1\tau_{11} - \partial_3\tau_{13} + \rho^s\partial_t v_1 = 0,$$

(12.6)

$$-\partial_1\tau_{31} - \partial_3\tau_{33} + \rho^s\partial_t v_3 = 0.$$

The non-zero stress tensor components are related to the non-zero components of the particle velocity through the (sourcefree) deformation rate equation (constitutive relation)

$$\begin{aligned}
\partial_t\tau_{11} &= \lambda(\partial_1 v_1 + \partial_3 v_3) + 2\mu\partial_1 v_1,\\
\partial_t\tau_{22} &= \lambda(\partial_1 v_1 + \partial_3 v_3),\\
\partial_t\tau_{33} &= \lambda(\partial_1 v_1 + \partial_3 v_3) + 2\mu\partial_3 v_3,\\
\partial_t\tau_{13} &= \mu(\partial_1 v_3 + \partial_3 v_1).
\end{aligned} \tag{12.7}$$

The wave fields that exist in the fluid and in the solid are interconnected by the interface conditions at I. The action of the strip source is represented by the difference across the interface I between the normal component of the particle velocity in the solid and the normal component of the particle velocity in the fluid, and the difference across the interface I between the normal component of the traction in the solid and the scalar traction in the fluid:

$$\lim_{x_3\downarrow 0} v_3 - \lim_{x_3\uparrow 0} w_3 = \phi_V(x_1,t) \text{ for all } x_1 \text{ and } t, \tag{12.8}$$

and

$$-\lim_{x_3\downarrow 0} \tau_{33} + \lim_{x_3\uparrow 0} \sigma = \phi_F(x_1,t) \text{ for all } x_1 \text{ and } t, \tag{12.9}$$

where $\phi_V(x_1,t)$ is the jump in the normal component of the particle velocity across the interface I and $\phi_F(x_1,t)$ is the jump in the normal component of the traction across the interface I. Since the fluid exerts only a normal force to the solid, the tangential traction in the solid is equal to zero at the interface:

$$\lim_{x_3\downarrow 0} \tau_{13} = 0 \text{ for all } x_1 \text{ and } t. \tag{12.10}$$

Let the source start to act at the instant $t = 0$, then $\phi_V(x_1,t) = 0$ and $\phi_F(x_1,t) = 0$ when $t < 0$, while

$$\{w_1, w_3, \sigma\}(x_1,x_3,t) = 0 \text{ when } t < 0 \text{ and } x_m \in D^f \tag{12.11}$$

and

$$\{v_1, v_3, \tau_{11}, \tau_{22}, \tau_{33}, \tau_{13}\}(x_1, x_3, t) = 0 \text{ when } t < 0 \text{ and } x_m \in D^s. \tag{12.12}$$

Equations (12.11) and (12.12) describe the causality of the generated wave motion.

Method of Solution

The Cagniard-De Hoop method is used to obtain analytical expressions for the particle velocity and the scalar traction in the fluid and the particle velocity and the stress in the solid. The first step in this method consists of carrying out a one-sided Laplace transformation with respect to time. To show the notation we give the transformation for the particle velocity in the fluid:

$$\hat{w}_k(x_1, x_3, s) = \int_{t=0}^{\infty} \exp(-st) w_k(x_1, x_3, t) dt. \tag{12.13}$$

In (12.13), s is a real, positive parameter that is chosen large enough to ensure the convergence of integrals of the indicated type. The next step consists of carrying out a one-dimensional Fourier transformation with respect to the horizontal coordinate x_1 . For the particle velocity in the fluid this transformation is given by

$$\tilde{w}_k(i\alpha, x_3, s) = \int_{x_1=-\infty}^{\infty} \exp(is\alpha x_1) \hat{w}_k(x_1, x_3, s) dx_1, \tag{12.14}$$

where $\alpha \in R$. The corresponding inverse transformation is given by (note that the actual Fourier-transform variable in (12.14) is $s\alpha$)

$$\hat{w}_k(x_1, x_3, s) = (s/2\pi) \int_{\alpha=-\infty}^{\infty} \exp(-is\alpha x_1) \tilde{w}_k(i\alpha, x_3, s) d\alpha. \tag{12.15}$$

Subjecting the basic equations (12.4)-(12.5) for the acoustic waves in the fluid and the basic equations (12.6)-(12.7) for the in-plane motion in the solid to these transformations, ∂_t can be replaced by s and ∂_1 by $-is\alpha$, and two systems of ordinary differential equations in x_3 are arrived at (Van der Hijden, 1988), one describing the propagation of the acoustic waves in the fluid and the other describing the propagation of the $P-$ and $SV-$waves in the solid. The two systems are given in two separate subsections to follow.

The transform domain expressions for the acoustic waves in the fluid

Upon applying the transformations (12.13) and (12.14) to the equation of motion (12.4) and the deformation rate equation (12.5), and eliminating $\tilde{w}_1$ from the resulting system of partial differential equations, the following system of ordinary differential equations is arrived at:

$$\partial_3 \underline{\tilde{F}}^f = -s\underline{\underline{A}}^f \, \underline{\tilde{F}}^f, \tag{12.16}$$

where the fluid field matrix $\underline{\tilde{F}}^f$ is the column matrix with the elements

$$\tilde{F}_1^f = -\tilde{\sigma}, \; \tilde{F}_2^f = \tilde{w}_3, \tag{12.17}$$

and the fluid system matrix $\underline{\underline{A}}^f$ is the square matrix with elements

$$A_{11}^f = A_{22}^f = 0, A_{12}^f = \rho^f, A_{21}^f = (1/\rho^f)[(1/c_f)^2 - (i\alpha)^2], \tag{12.18}$$

where $c_f = (\rho^f \kappa)^{-1/2}$ is the wave speed in the fluid. Note that $\underline{\underline{A}}^f$ is independent of s. Equation (12.16) represents a system of linear first-order ordinary differential equations in x_3. The eigenvalues of the matrix $\underline{\underline{A}}^f$ are found to be $\pm\gamma_f$ where

$$\gamma_f = \gamma_f(i\alpha) = [(1/c_f)^2 - (i\alpha)^2]^{1/2} \quad \text{with} \quad \mathrm{Re}(\gamma_f) \geq 0. \tag{12.19}$$

The solution of (12.16) that is bounded as $x_3 \to -\infty$ can be written as

$$\underline{\tilde{F}}^f = \underline{\tilde{F}}^f(i\alpha, x_3, s) = W^f(i\alpha, s)\underline{\tilde{e}}^f(ia) \exp(s\gamma_f x_3), \tag{12.20}$$

in which

$$\underline{\tilde{e}}^f(i\alpha) = (\rho^f, -\gamma_f)^T \tag{12.21}$$

is a suitably normalized eigenvector of the matrix $\underline{\underline{A}}^f$ corresponding to the eigenvalue $-\gamma_f$. Note that $\underline{\tilde{e}}^f$ is independent of s.

The transform domain expressions for the *P*– and *SV*–waves in the solid

Upon applying the transformations (12.13) and (12.14) to the equation of motion (12.6) and the deformation rate equation (12.7), and eliminating $\tilde{\tau}_{11}$ from the

resulting system of partial differential equations, the following system of ordinary differential equations is arrived at:

$$\partial_3 \tilde{\underline{F}}^s = -s\underline{\underline{A}}^s\, \tilde{\underline{F}}^s, \tag{12.22}$$

where the solid field matrix $\tilde{\underline{F}}^s$ is the column matrix with the elements

$$\tilde{F}_1^s = -\tilde{\tau}_{13}, \quad \tilde{F}_2^s = -\tilde{\tau}_{33}, \quad \tilde{F}_3^s = \tilde{v}_1, \quad \tilde{F}_4^s = \tilde{v}_3, \tag{12.23}$$

and the solid system matrix $\underline{\underline{A}}^s$ is the square matrix with the elements

$$\begin{aligned}
&A_{11}^s = A_{14}^s = A_{22}^s = A_{23}^s = A_{32}^s = A_{33}^s = A_{41}^s = A_{44}^s = 0,\\
&A_{12}^s = -i\alpha\lambda/(\lambda+2\mu), \quad A_{13}^s = \rho - (i\alpha)^2 4\mu(\lambda+\mu)/(\lambda+2\mu),\\
&A_{21}^s = -i\alpha, \quad A_{24}^s = \rho, \quad A_{31}^s = 1/\mu, \quad A_{34}^s = -i\alpha,\\
&A_{42}^s = 1/(\lambda+2\mu), \quad A_{43}^s = -i\alpha\lambda/(\lambda+2\mu).
\end{aligned} \tag{12.24}$$

Note that $\underline{\underline{A}}^s$ is independent of s. Equation (12.22) represents a system of linear first-order ordinary differential equations in x_3. The eigenvalues of $\underline{\underline{A}}^s$ are found to be $\pm\gamma_P$ and $\pm\gamma_S$, with

$$\gamma_{P,S} = \gamma_{P,S}(i\alpha) = [1/c_{P,S}^2 - (i\alpha)^2]^{1/2}, \quad \mathrm{Re}(\gamma_{P,S}) \geq 0, \tag{12.25}$$

where $c_P = [(\lambda+2\mu)/\rho^s]^{1/2}$ is the $P-$wave speed in the solid and $c_S = (\mu/\rho^s)^{1/2}$ is the $S-$wave speed in the solid. The solution of (12.22) that is bounded as $x_3 \to \infty$ can be written as

$$\tilde{\underline{F}}^s = \tilde{\underline{F}}^P(i\alpha, x_3, s) + \tilde{\underline{F}}^S(i\alpha, x_3, s), \tag{12.26}$$

where

$$\tilde{\underline{F}}^P = W^P(i\alpha, s)\tilde{\underline{\varepsilon}}^P(i\alpha)\exp(-s\gamma_P x_3) \tag{12.27}$$

is the $P-$wave in which

$$\tilde{\underline{\varepsilon}}^P = \tilde{\underline{\varepsilon}}^P(i\alpha) = \{2\mu i\alpha\gamma_P, 2\mu[1/2c_S^2 - (i\alpha)^2], i\alpha, \gamma_P\}^T \tag{12.28}$$

is a normalized eigenvector of $\underline{\underline{A}}^s$ corresponding to the eigenvalue γ_P, and

$$\tilde{\underline{F}}^S = W^S(i\alpha, s)\tilde{\underline{\varepsilon}}^S(i\alpha)\exp(-s\gamma_S x_3) \tag{12.29}$$

is the $SV-$wave in which

$$\tilde{\underline{e}}^S = \tilde{\underline{e}}^S(i\alpha) = \{2\mu[1/2c_S^2 - (i\alpha)^2], -2\mu i\alpha\gamma_S, \gamma_S, -i\alpha\}^T \tag{12.30}$$

is a normalized eigenvector of $\underline{\underline{A}}^s$ corresponding to the eigenvalue γ_S. Note that $\tilde{\underline{e}}^P(i\alpha)$ and $\tilde{\underline{e}}^S(i\alpha)$ are independent of s.

The amplitude coefficients $W^f = W^f(i\alpha, s), W^P = W^P(i\alpha, s)$ and $W^S = W^S(i\alpha, s)$ in (12.20), (12.27) and (12.29) follow from the application of the boundary conditions (12.8) - (12.10) at $x_3 = 0$. They are obtained as

$$W^f(i\alpha, s) = W_V^f(i\alpha)\tilde{\phi}_V(i\alpha, s) + W_F^f(i\alpha)\tilde{\phi}_F(i\alpha, s), \tag{12.31}$$

$$W^P(i\alpha, s) = W_V^P(i\alpha)\tilde{\phi}_V(i\alpha, s) + W_F^P(i\alpha)\tilde{\phi}_F(i\alpha, s), \tag{12.32}$$

$$W^S(i\alpha, s) = W_V^S(i\alpha)\tilde{\phi}_V(i\alpha, s) + W_F^S(i\alpha)\tilde{\phi}_F(i\alpha, s), \tag{12.33}$$

where

$$W_V^f(i\alpha) = \Delta_R/\gamma_f\Delta_{SCH}, \quad W_F^f(i\alpha) = \gamma_P/4\rho^s c_S^4\gamma_f\Delta_{SCH}, \tag{12.34}$$

and

$$\begin{aligned} W_V^P(i\alpha) &= \rho^f[1/2c_S^2 - (i\alpha)^2]/2\rho^s c_S^2\gamma_f\Delta_{SCH}, \\ W_F^P(i\alpha) &= -[1/2c_S^2 - (i\alpha)^2]/2\rho^s c_S^2\Delta_{SCH}, \end{aligned} \tag{12.35}$$

and

$$W_V^S(i\alpha) = -\rho^f i\alpha\gamma_P/2\rho^s c_S^2\gamma_f\Delta_{SCH}, \quad W_F^S(i\alpha) = i\alpha\gamma_P/2\rho^s c_S^2\Delta_{SCH}, \tag{12.36}$$

in which

$$\Delta_{SCH}(i\alpha) = \Delta_R + \rho^f\gamma_P/4\rho^s c_S^4\gamma_f, \tag{12.37}$$

is the "Scholte-wave determinant" and

$$\Delta_R(i\alpha) = [1/2c_S^2 - (i\alpha)^2]^2 + (i\alpha)^2\gamma_P\gamma_S \tag{12.38}$$

is the "Rayleigh-wave determinant". Transforming the solution (12.20) back to the $(x_1, x_3, s)-$domain, the $s-$domain expressions for the acoustic wave field in the fluid

$$\hat{\underline{F}}^f = (s/2\pi)\int_{\alpha=-\infty}^{\infty} W^f(i\alpha, s)\tilde{\underline{e}}^f(i\alpha)\exp[-s(i\alpha x_1 - \gamma_f x_3)]d\alpha \qquad (12.39)$$

are obtained. Transforming the solution (12.26) back to the $(x_1, x_3, s)-$domain, the $s-$domain expressions for the $P-$ and $SV-$wave field in the solid

$$\hat{\underline{F}}^{P,S} = (s/2\pi)\int_{\alpha=-\infty}^{\infty} W^{P,S}(i\alpha, s)\tilde{\underline{e}}^{P,S}(i\alpha)\exp[-s(i\alpha x_1 + \gamma_{P,S} x_3)]d\alpha \qquad (12.40)$$

are obtained. Starting from the expressions (12.39) and (12.40), the case of a uniformly distributed strip source is further investigated in the next section.

Cagniard-De Hoop Method for the Uniformly Distributed Strip Source

In this section the case of the uniformly distributed strip source is worked out in detail. First the "horizontal" ray parameter $p = i\alpha$ is introduced in the integral representations (12.39) and (12.40). This leads for each of the formulas to an expression of the form

$$\hat{\underline{F}} = (s/2\pi i)\int_{p=-i\infty}^{i\infty} W(p, s)\tilde{\underline{e}}(p)\exp[-s(px_1 + \gamma|x_3|)]dp, \qquad (12.41)$$

where $\hat{\underline{F}} = \hat{\underline{F}}^{f,P,S}, W = W^{f,P,S}, \tilde{\underline{e}} = \tilde{\underline{e}}^{f,P,S}$ and $\gamma = \gamma_{f,P,S}$. Now, along the strip

$$S = \{x_m \in R^3;\ -a < x_1 < a,\ x_3 = 0\} \qquad (12.42)$$

of width $2a$ a spatially uniformly distributed surface source is present (Figure 12.2). The spatial dependence on x_1 of the source strength is modeled by the difference of two unit step sources; one of which is active on the interval $(-a, \infty)$, the other being active on the interval (a, ∞). The combination of the two equals unity on the interval $(-a, a)$ and vanishes outside this interval. Correspondingly, the distribution of the surface source has the form

$$\phi(x_1, t) = \Phi(t)[H(x_1 + a) - H(x_1 - a)], \qquad (12.43)$$

where

$$H(x_1) = \{0, 1/2, 1\} \text{ for } \{\ x_1 < 0, x_1 = 0, x_1 > 0\} \qquad (12.44)$$

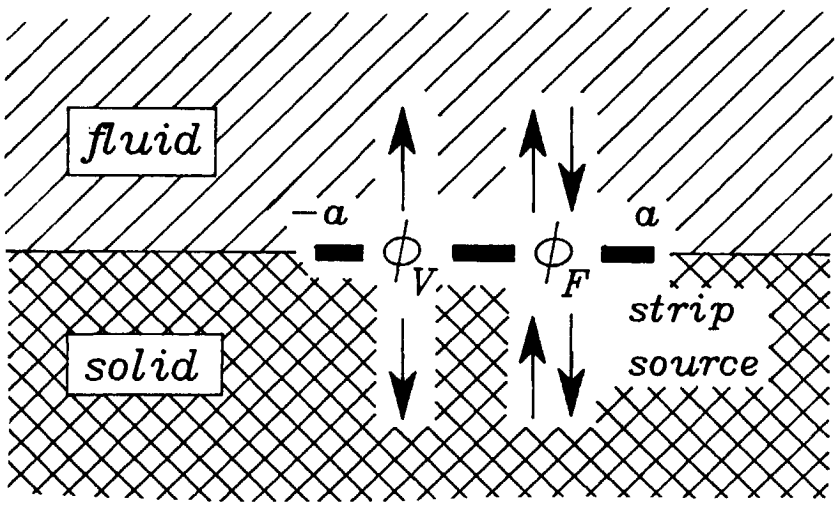

Figure 12.2: The uniformly distributed strip source of width $2a$ at the plane interface between the semi-infinite fluid and the semi-infinite solid.

is the Heaviside unit step function and $\phi = \phi_{V,F}$. The space-time transformed expression corresponding to (12.43) is

$$\tilde{\phi}(p,s) = \hat{\Phi}(s)[\exp(spa) - \exp(-spa)]/sp. \tag{12.45}$$

The expression (12.45) is substituted into (12.31), (12.32) and (12.33) giving the amplitude coefficients that are needed in (12.41). We observe that in the integrand in the latter expression the point $p = 0$ is a regular point as long as the two terms in the numerator of (12.45) are kept together. However, in the application of the Cagniard-De Hoop method, we have to separate these two terms and each of them may have a simple pole at $p = 0$. This pole is present in the integrands occurring in the expressions for the body wave components of $\hat{\sigma}$ and $\hat{w}_3$ in the fluid and for the P−wave components of $\hat{\tau}_{33}$ and $\hat{v}_3$ in the solid, while for the components of $\hat{\tau}_{13}$ and $\hat{v}_1$ in the solid the factor p is cancelled by the factor p occurring in the corresponding components of the eigenvector $\tilde{\underline{e}}^P$ (cf. (12.28)). The pole $p = 0$ is also not present in the integrands for the expressions of the SV−wave components in the solid because in the amplitude coefficient W^S a factor p occurs that cancels the one in the denominator (cf. (12.36)). To handle

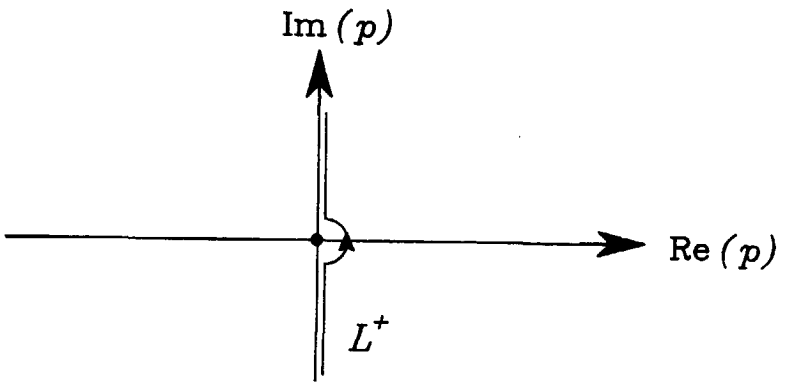

Figure 12.3: The contour L^+ in the complex $p-$plane

the possible singularity, the integrand in (12.41) is continued analytically into the complex $p-$plane away from the imaginary axes. Using Cauchy's theorem, the path of integration is, before the separation of the two terms in (12.45), deformed into the path L^+ that deviates from the imaginary axes along a semi-circle of vanishingly small radius around $p = 0$ in the right half of the $p-$plane (Figure 12.3). (A semi-circle around $p = 0$ in the left half of the $p-$plane could have served as well; the two types of deviation lead to the same final results.)

In view of the linearity of our wave problem, the field in $D^{f,s}$, generated by a combined volume injection rate and force strip source, is the superposition of a field $\underline{F}_V^{f,s}$ generated by a volume injection rate strip source and a field $\underline{F}_F^{f,s}$ generated by a force strip source:

$$\underline{F}^{f,s} = \underline{F}_V^{f,s} + \underline{F}_F^{f,s}, \tag{12.46}$$

while in the solid part D^s we have the additional separation into a $P-$wave and an $S-$wave which we express by

$$\underline{F}_V^s = \underline{F}_V^P + \underline{F}_V^S, \tag{12.47}$$

$$\underline{F}_F^s = \underline{F}_F^P + \underline{F}_F^S. \tag{12.48}$$

With the above, we obtain for the different wave-field contributions expressions of the form

$$\hat{\underline{F}}(x_1, x_3, s) = -[\hat{\underline{FE}}(x_1 + a, x_3, s) - \hat{\underline{FE}}(x_1 - a, x_3, s)], \tag{12.49}$$

where $\hat{\underline{FE}} = \hat{\underline{FE}}^{f,P,S}_{V,F}$ with

$$\hat{\underline{FE}}(\chi, x_3, s) = [\hat{\Phi}(s)/2\pi i] \int_{p \in L^+} [W(p)/p] \tilde{\underline{e}}(p) \exp[-s(p\chi + \gamma|x_3|)] dp, \tag{12.50}$$

in which χ stands for $x_1 + a$ or $x_1 - a$, respectively, $\Phi = \Phi_{V,F}$ and $W = W^{f,P,S}_{V,F}$. The expressions for $W^{f,P,S}_{V,F}(p)$ and $\tilde{\underline{e}}^{f,P,S}(p)$ are given in (12.34), (12.35), (12.36) and (12.21), (12.28), (12.30).

Next, we take advantage of the symmetry of the configuration with respect to the plane $x_1 = 0$. For the wave field in the fluid we have the symmetry relations

$$\begin{gathered} w_1(x_1, x_3, t) = -w_1(-x_1, x_3, t), \quad w_3(x_1, x_3, t) = w_3(-x_1, x_3, t), \\ \sigma(x_1, x_3, t) = \sigma(-x_1, x_3, t), \end{gathered} \tag{12.51}$$

and for the wave field in the solid we have the symmetry relations

$$\begin{gathered} v_1(x_1, x_3, t) = -v_1(-x_1, x_3, t), \quad v_3(x_1, x_3, t) = v_3(-x_1, x_3, t), \\ \tau_{13}(x_1, x_3, t) = -\tau_{13}(-x_1, x_3, t), \quad \tau_{33}(x_1, x_3, t) = \tau_{33}(-x_1, x_3, t). \end{gathered} \tag{12.52}$$

Once the wave field has been determined in the domain

$$D^+ = \{x_m \in R^3; x_1 > 0\}, \tag{12.53}$$

its values in the entire space D are known via (12.51) and (12.52).

The first step in the Cagniard-De Hoop method consists of deforming, in each of the two terms in (12.49), the path of integration L^+ in the complex p−plane into a path L^B along which

$$p\chi + \gamma|x_3| = \tau, \tag{12.54}$$

where τ is real and positive. By virtue of Jordan's lemma (Whittaker and Watson 1950, p.115) the contribution from joining circular axes at infinity vanishes, and hence Cauchy's theorem ensures that the integral along the imaginary $p-$axes is equal to the integral along L^B. In (12.54), $\chi = x_1 + a$ for the first term in (12.49) and $\chi = x_1 - a$ for the second term in (12.49). Such a path is denoted as a Cagniard-De Hoop path. In the process of deformation we encounter the singularities in $W(p)/p, \tilde{\underline{\xi}}(p)$ and $\gamma_{f,P,S}(p) = (1/c_{f,P,S}^2 - p^2)^{1/2}$. These are: the branch points $p = \pm 1/c_{f,P,S}$ of $\gamma_{f,P,S}$ that also occur in $W(p)/p$ and $\tilde{\underline{\xi}}(p)$, and the poles of $W(p)/p$, i.e., the zeros $p = \pm 1/c_{SCH}$ of Δ_{SCH} (cf. (12.37)) (c_{SCH} =Scholte wave speed), and the pole $p = 0$. The former two poles are associated with the Scholte waves along the fluid/solid boundary of the fluid/solid configuration; the pole $p = 0$ will be shown to be associated with the up- and downgoing plane waves that exist in the vertical region above and below the strip S. The three possible distributions of the singular points in the complex $p-$plane are shown in Figure 12.4. Note that we always have $c_S < c_P$. In addition, it can be proved that $c_{SCH} < \min\{c_f, c_P, c_S\}$. Since the application of Cauchy's theorem in connection with the deformation of the path of integration in the complex $p-$plane requires the integrands to be single-valued, branch cuts are, in accordance with (12.19) and (12.25), introduced along $\mathrm{Im}(p) = 0$ and $1/c_{f,P,S} < |\mathrm{Re}(p)| < \infty$, i.e., where $\mathrm{Re}(\gamma_{f,P,S}) = 0$. In the cut $p-$plane, we then have $\mathrm{Re}[\gamma_{f,P,S}(p)] > 0$. Depending on the position of the point of observation, three cases are distinghuised for the deformation of the contour L^+ in (12.50) in the complex $p-$plane (Figure 12.5). First, if $\chi > 0$ the contour is deformed into the right half of the complex $p-$plane. Secondly, if $\chi = 0$ the contour remains unchanged and runs along L^+ . Finally, if $\chi < 0$ the contour is deformed into the left half of the complex $p-$plane, in which case the contribution from the pole $p = 0$ is to be taken into account. In this procedure the deformed paths of integration in (12.49) are obtained as $p = p^B(\chi, x_3, \tau)$ in the upper half of the $p-$plane, together with their images $p = p^{B^*}$ with respect to the real axis, where p^B is given by

$$p^B(\chi, x_3, \tau) = \chi\tau/(\chi^2 + x_3^2) + i(\tau^2 - T_B^2)^{1/2}|x_3|/(\chi^2 + x_3^2), \qquad (12.55)$$

with $T_B < \tau < \infty$, where $T_B = (\chi^2 + x_3^2)^{1/2}/c$ is the arrival time of the body

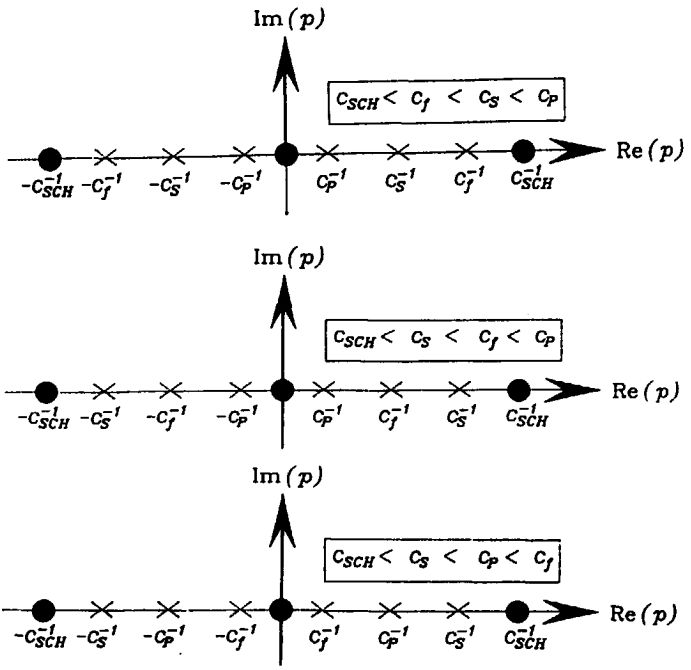

Figure 12.4: The three possible distributions of the singular points in the complex $p-$plane.

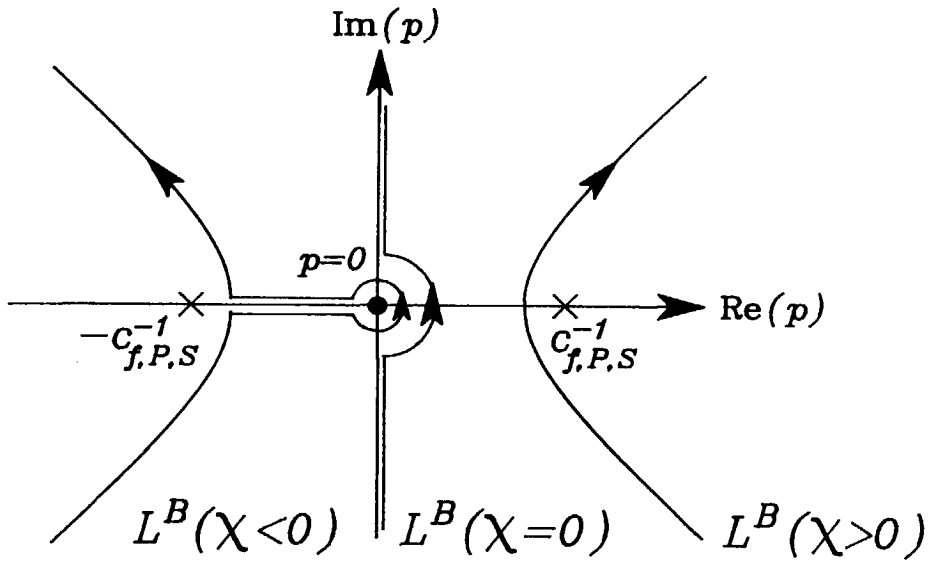

Figure 12.5: The contour L^B in the complex $p-$plane for the three different cases of $\chi < 0, \chi = 0, \chi > 0$.

wave.

Body-Wave Contributions

Introducing in (12.50) τ as the variable of integration, we find the body-wave contribution

$$\underline{\hat{FE}}^B = \hat{\Phi}(s)\underline{\hat{G}}^B(\chi, x_3, s), \tag{12.56}$$

where

$$\underline{\hat{G}}^B(\chi, x_3, s) = \int_{\tau=T_B}^{\infty} \underline{g}^B(\chi, x_3, \tau)\exp(-s\tau)d\tau, \tag{12.57}$$

in which

$$\underline{g}^B(\chi, x_3, \tau) = (1/\pi)\mathrm{Im}\{[W(p^B)/p^B]\underline{\tilde{\varepsilon}}(p^B)(\partial p^B/\partial\tau)\}H(\tau - T_B). \tag{12.58}$$

In (12.58), $\partial p^B/\partial\tau$ is the one-dimensional Jacobian given by

$$\partial p^B/\partial\tau = \chi/(\chi^2 + x_3^2) + i[\tau/(\tau^2 - T_B^2)^{1/2}]|x_3|/(\chi^2 + x_3^2). \tag{12.59}$$

In the derivation of (12.56), the part associated with $p = p^B$ and $p = p^{B^*}$ have been taken together and Schwarz's reflection principle has been used in the integrand. Equation (12.56) is the contribution from the integration along the contour L^B and is identified as a cylindrical wave motion. The space-time expressions for the body-waves follow by applying the convolution theorem to (12.56) and Lerch's theorem on the uniqueness of the Laplace transform with real, positive transform parameter (see Widder, 1946):

$$\underline{FE}^B = H(t - T_B)\int_{\tau=T_B}^{t} \Phi(t-\tau)\underline{g}^B(\chi, x_3, \tau)d\tau, \tag{12.60}$$

where H denotes again the Heaviside unit step function (cf. (12.44)).

Plane Wave Contributions

The contribution of the residue of the integrand in (12.50) at the simple pole $p = 0$ is found as

$$\underline{PW} = H(-\chi)\hat{\Phi}(s)W(0)\underline{\tilde{\varepsilon}}(0)\exp(-s|x_3|/c), \tag{12.61}$$

where H denotes again the Heaviside unit step function. It is identified as the plane wave that is excited above the strip source in the fluid and below the strip

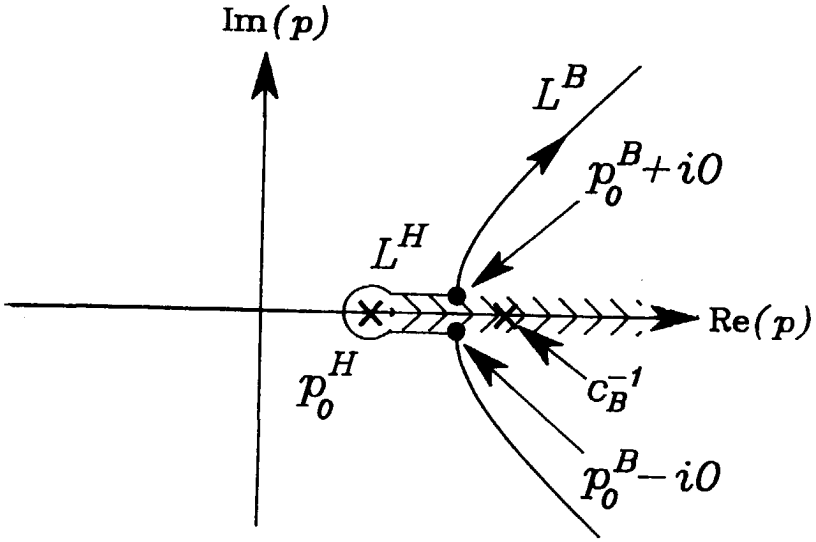

Figure 12.6: The contours L^H and L^B in the complex $p-$plane for the case that the deformed path is tempted to cross a branch cut.

source in the solid. (Note that in the domain D^+ given by (12.53), the region $0 \leq x_1 < a$ leads to $\chi < 0$ in the term for which $\chi = x_1 - a$.) The space-time expression for the plane wave simply follows as

$$\underline{PW}(\chi, x_3, t) = H(-\chi)W(0)\underline{\tilde{e}}(0)\Phi(t - T_{PL}), \tag{12.62}$$

where $T_{PL} = |x_3|/c$ is its arrival time.

Head Wave Contribution

In the deformation of the path of integration from L^+ to the path where (12.54) holds, it is not permitted to cross any of the branch cuts introduced in the complex $p-$plane. In the case that a branch point $p = p_0^H = 1/c_{f,P,S}$ has a smaller absolute value than the point $p = p_0^B$ where $p = p^B$ is tempted to cross the real axis, a loop integral L^H around the relevant branch cut associated with p_0^H and joining the points $p_0^B - i0$ and $p_0^B + i0$ has to be supplemented (Figure 12.6). Along this loop, too, the parameterization (12.54) has to be carried out. The relevant values of p in the upper and lower halves of the $p-$plane are found as $p = p^H(\chi, x_3, \tau)$ and its image $p = p^{H^*}(\chi, x_3, \tau)$ with

respect to the real axis, respectively, where p^H is given by

$$p^H(\chi, x_3, t) = \begin{cases} \chi\tau/(\chi^2 + x_3^2) + (T_B^2 - \tau^2)^{1/2}|x_3|/(\chi^2 + x_3^2) + i0 & \text{when } \chi < 0\,, \\ \chi\tau/(\chi^2 + x_3^2) - (T_B^2 - \tau^2)^{1/2}|x_3|/(\chi^2 + x_3^2) + i0 & \text{when } \chi > 0\,, \end{cases} \tag{12.63}$$

with $T_H < \tau < T_B$ where

$$T_H = p_0^H|\chi| + [(p_0^B)^2 - (p_0^H)^2]^{1/2}|x_3|. \tag{12.64}$$

The contribution of the loop integral around the branch is given by

$$\underline{\hat{FE}}^H = \hat{\Phi}(s)\underline{\hat{G}}^H(\chi, x_3, s), \tag{12.65}$$

where

$$\underline{\hat{G}}^H(\chi, x_3, s) = H(t - T_H)\int_{\tau=T_H}^{t} \underline{g}^H(\chi, x_3, \tau)\exp(-s\tau)d\tau, \tag{12.66}$$

in which

$$\underline{g}^H(\chi, x_3, \tau) = (1/\pi)\mathrm{Im}\{[W(p^H)/p^H]\tilde{\underline{e}}(p^H)(\partial p^H/\partial\tau)\}H(T_B - \tau). \tag{12.67}$$

In (12.67), $\partial p^H/\partial\tau$ is the one-dimensional Jacobian given by

$$\partial p^H/\partial\tau = \begin{cases} \chi/(\chi^2 + x_3^2) - [\tau/(T_B^2 - \tau^2)^{1/2}]|x_3|/(\chi^2 + x_3^2) & \text{when } \chi < 0\,, \\ \chi/(\chi^2 + x_3^2) + [\tau/(T_B^2 - \tau^2)^{1/2}]|x_3|/(\chi^2 + x_3^2) & \text{when } \chi > 0\,. \end{cases} \tag{12.68}$$

The contribution from the integration along the contour L^H is identified as a cylindrical head wave. The space-time expressions for the head waves follow by applying the convolution theorem to (12.65) and Lerch's theorem on the uniqueness of the Laplace transform with real, positive transform parameter (see Widder, 1946):

$$\underline{FE}^H = H(t - T_H)\int_{\tau=T_H}^{t} \Phi(t - \tau)\underline{g}^H(\chi, x_3, \tau)d\tau. \tag{12.69}$$

Due to the three different wave speeds in the fluid/solid configuration, three types of head waves can occur. Which type of head wave occurs in a specific wave problem depends on the ordering of the three wave speeds and on the

Table 12.1: The head waves that can occur in the fluid/solid configuration.

ordering of wave speeds	head waves in fluid	head waves in solid
$c_f < c_S < c_P$	P to f conversion S to f conversion	P to S conversion
$c_S < c_f < c_P$	P to f conversion	f to S conversion P to S conversion
$c_S < c_P < c_f$		P to S conversion f to P conversion f to S conversion

horizontal offset from source to receiver. For the three possible orderings of these wave speeds (cf. Figure 12.4), the head waves are listed in table 12.1.

The space-time expression for the total wave motion in the fluid/solid configuration that is generated by the strip source at the plane interface is now simply found by adding the three contributions (12.60), (12.62) and (12.69):

$$\underline{FE} = \underline{PW} + \underline{FE}^H + \underline{FE}^B. \tag{12.70}$$

The wave fronts corresponding to the body waves, the head waves, the plane waves and the Scholte waves that are generated by the strip source in the fluid/solid configuration are, for the three possible orderings of the wave speeds, shown in Figures 12.7-12.9.

Numerical Results

Synthetic seismograms of the particle velocity in the fluid and in the solid close to the strip source are presented for the volume injection rate strip source problem. The fluid medium properties are taken to be $\rho^f = 1.0 * 10^3$ kg/m^3 and $\kappa = 4.4*10^{-10}$ Pa^{-1}; the solid medium properties are taken to be $\rho^s = 2.5*10^3$ kg/m^3 and $\lambda = \mu = 10^{10}$ Pa. The corresponding fluid, $P-$ and $S-$wave speeds are:

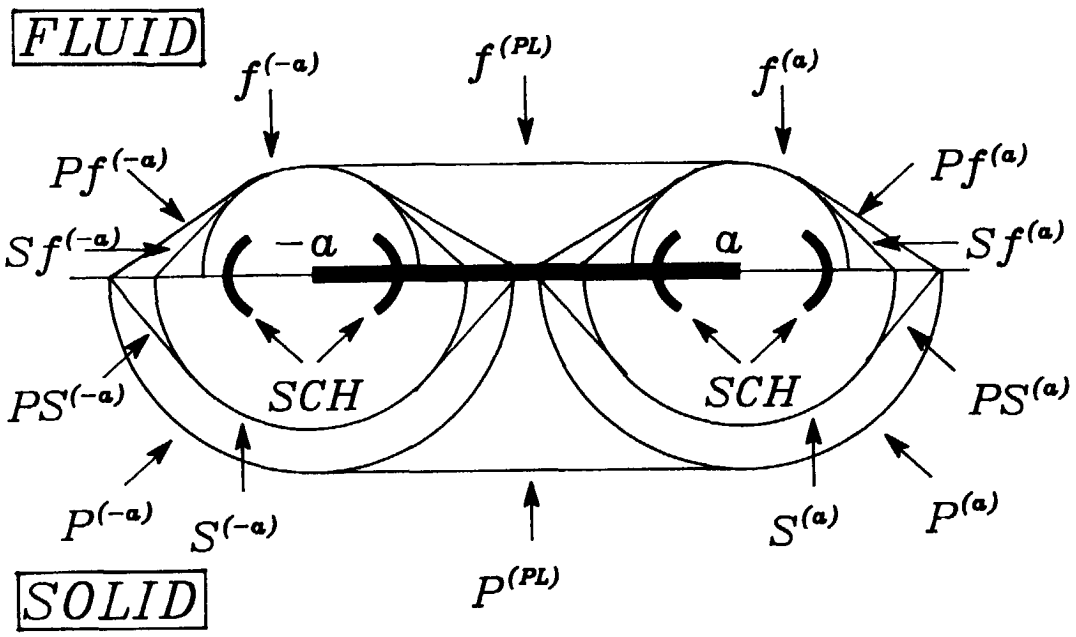

Figure 12.7: The different wave fronts generated by the strip source at the plane fluid/solid interface for the case that $c_f < c_S < c_P$. The wave fronts of the fluid, $P-, S-$, and Scholte waves are indicated by f, P, S, and SCH, respectively. The P to f, S to f and P to S conversion waves are denoted by Pf, Sf and PS, respectively. The waves originating from the left edge of the strip source have the superscript $(-a)$, the ones originating from the right edge of the strip source have the superscript (a). The wave fronts of the plane fluid and $P-$waves are indicated by $f^{(PL)}$ and $P^{(PL)}$, respectively.

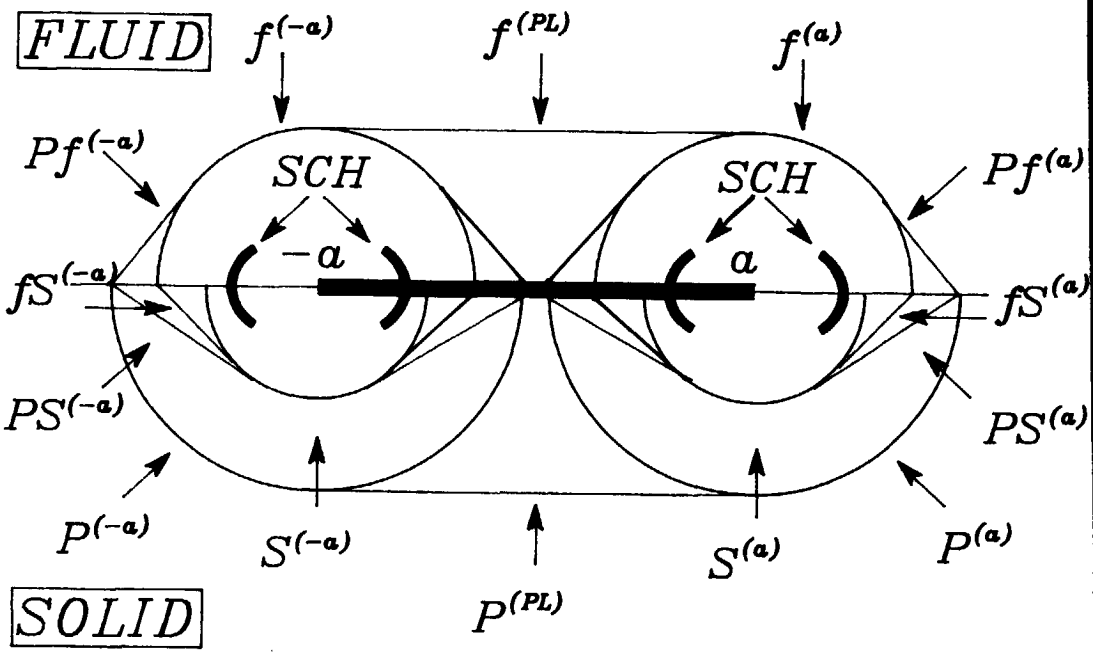

Figure 12.8: The different wave fronts generated by the strip source at the plane fluid/solid interface for the case that $c_S < c_f < c_P$. The wave fronts of the fluid, $P-, S-$, and Scholte waves are indicated by f, P, S, and SCH, respectively. The P to f, f to S and P to S conversion waves are denoted by Pf, fS and PS, respectively. The waves originating from the left edge of the strip source have the superscript $(-a)$, the ones originating from the right edge of the strip source have the superscript (a). The wave fronts of the plane fluid and $P-$waves are indicated by $f^{(PL)}$ and $P^{(PL)}$, respectively.

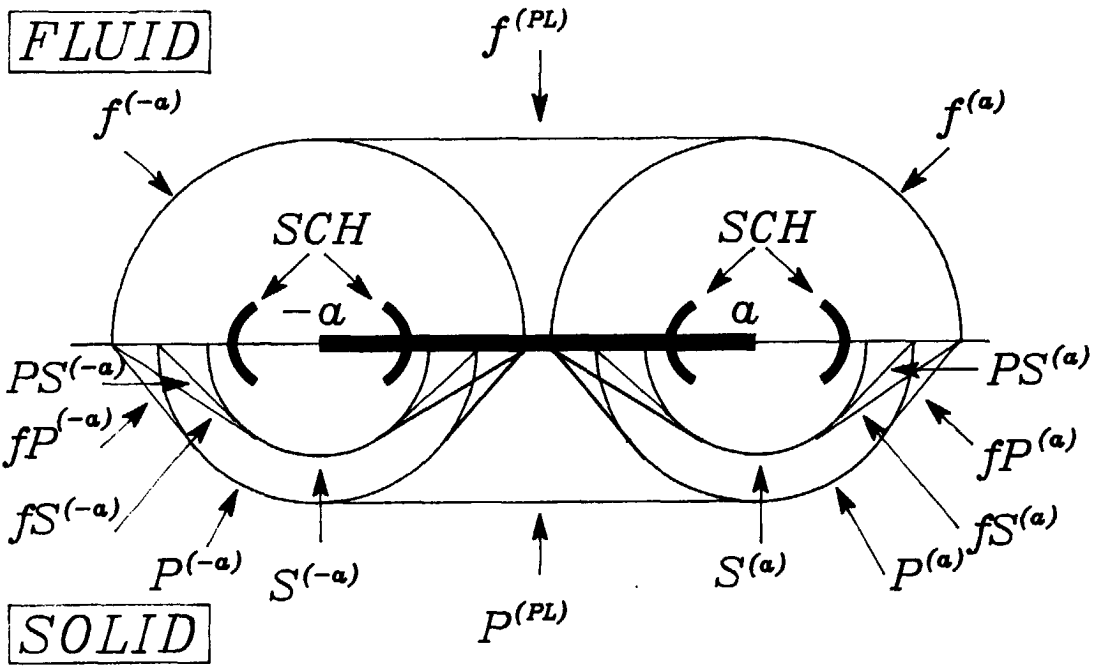

Figure 12.9: The different wave fronts generated by the strip source at the plane fluid/solid interface for the case that $c_P < c_S < c_f$. The wave fronts of the fluid, $P-, S-$, and Scholte waves are indicated by f, P, S, and SCH, respectively. The f to P, f to S and P to S conversion waves are denoted by fP, fS and PS, respectively. The waves originating from the left edge of the strip source have the superscript $(-a)$, the ones originating from the right edge of the strip source have the superscript (a). The wave fronts of the plane fluid and $P-$waves are indicated by $f^{(PL)}$ and $P^{(PL)}$, respectively.

$c_f = 1507$ m/s, $c_P = 3464$ m/s and $c_S = 2000$ m/s. Along the strip

$$S = \{-a < x_1 < a, x_3 = 0\} \tag{12.71}$$

the strip source introduces a spatially uniformly distributed volume injection rate. The injection rate per unit length in the x_2-direction and unit width in the x_1-direction is $\Phi(t)/2a$ with $\Phi(t)$ as the wavelet. For the test problem we took as source signature

$$\Phi_V(t) = A \exp(-\delta t) \sin(\omega t) H(t), \tag{12.72}$$

where $H(t)$ is the Heaviside unit step function (cf. (11.27)), A the source strength amplitude, δ the damping coefficient and ω the angular frequency. In our computations we take a strip source for which a=1 m. Four synthetic seismograms are presented that represent the particle velocity close to the strip source; two of them show the different waves generated by the strip source in the fluid and two of them show the different waves generated by the strip source in the solid. The synthetic seismograms for the fluid apply to an array of 21 receivers that are located 0.15 m apart and 1 m above the fluid/solid interface. The first receiver of this array is located above the center of the strip source. The synthetic seismograms for the solid apply to an array of 21 receivers that are located 0.15 m apart and 1 m below the fluid/solid interface. The first receiver of this array is located below the center of the strip source (Figure 12.10). For the computation of these seismograms we took as source parameters $A = 1$ N/m, $\delta = 2 * 10^4$ s^{-1} and $\omega = 2\pi * 5 * 10^3$ rad/s; this wavelet has a frequency of $5 * 10^3$ Hz and its first peak dominates the wave shape (see Figure 12.11). The seismograms in Figures 12.12 and 12.13 represent the horizontal and vertical fluid particle velocities w_1 and w_3, respectively, and the seismograms in Figures 12.14 and 12.15 represent the horizontal and vertical solid particle velocities v_1 and v_3, respectively.

Both in the seismograms of the receivers in the fluid and in the solid a scale is used such that the different wave phenomena are clearly visible. As a consequence, some of the wave peaks in the seismograms had to be clipped.

The computer program was written in Fortran 77. The time convolutions occurring in the expressions for the particle velocity were evaluated numerically

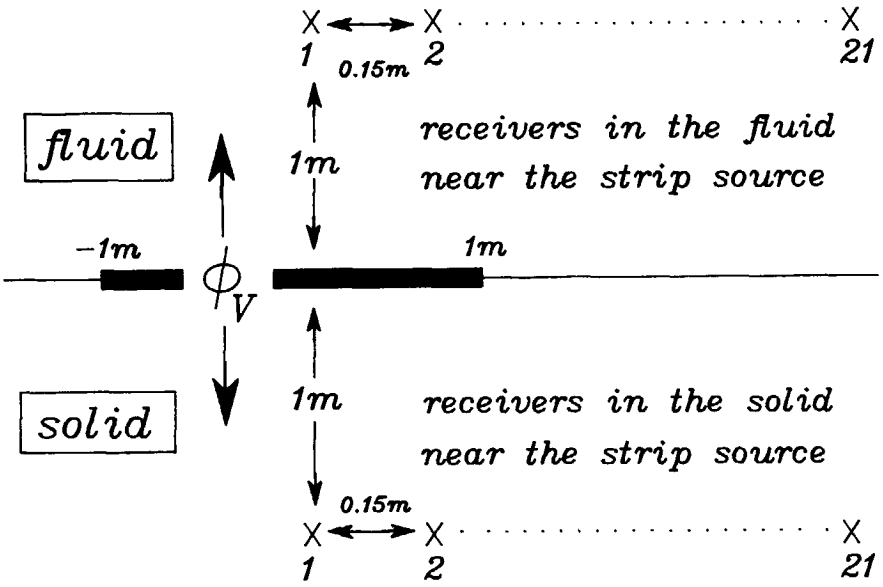

Figure 12.10: The array of 21 receivers in the fluid above the strip source and the array of 21 receivers in the solid below the strip source.

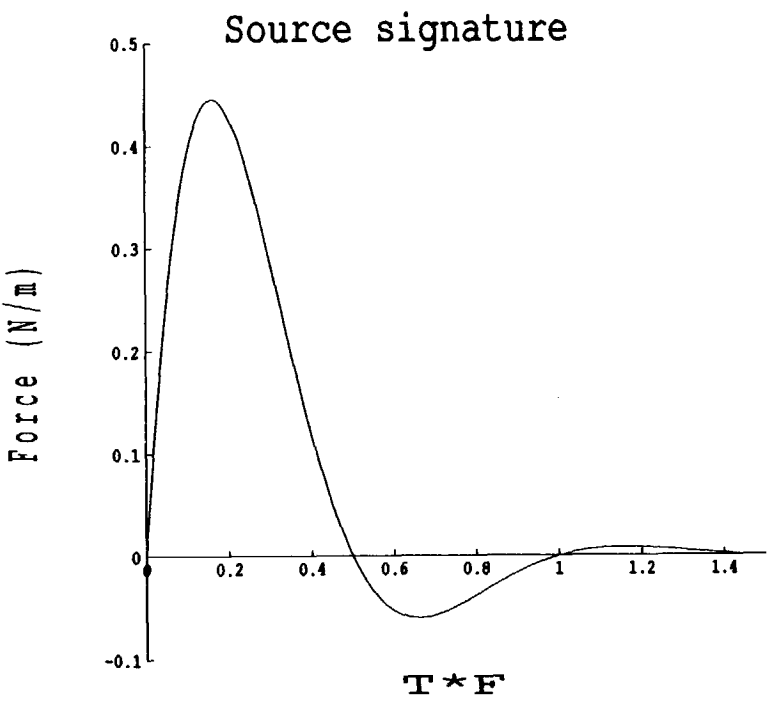

Figure 12.11: The source signature of the strip source for the source parameters $A = 1$ N/m, $\delta = 2 * 10^4$ s^{-1} and $\omega = 2\pi * 5 * 10^3$ rad/s (f=$5 * 10^3$ Hz).

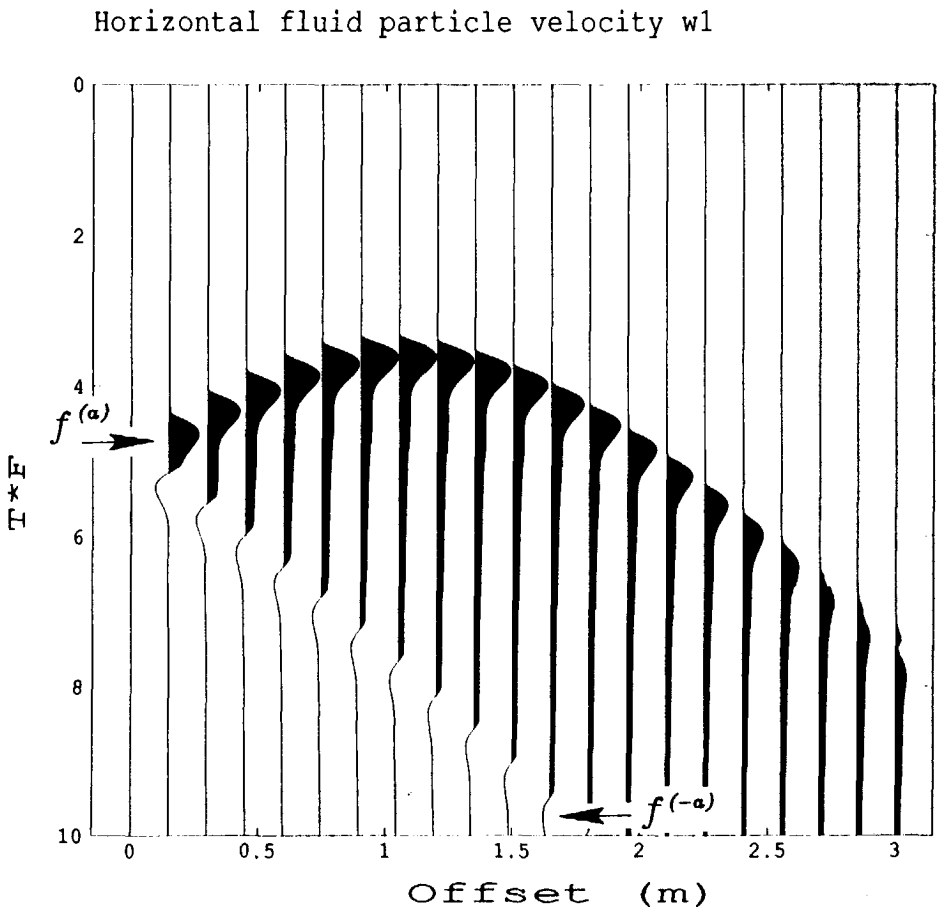

Figure 12.12: The horizontal component of the fluid particle velocity for the 21 shallow receivers for the volume injection rate strip source. The fluid waves are indicated by f. The wave originating from the left edge of the strip source has the superscript $(-a)$, the one originating from the right edge of the strip source has the superscript (a).

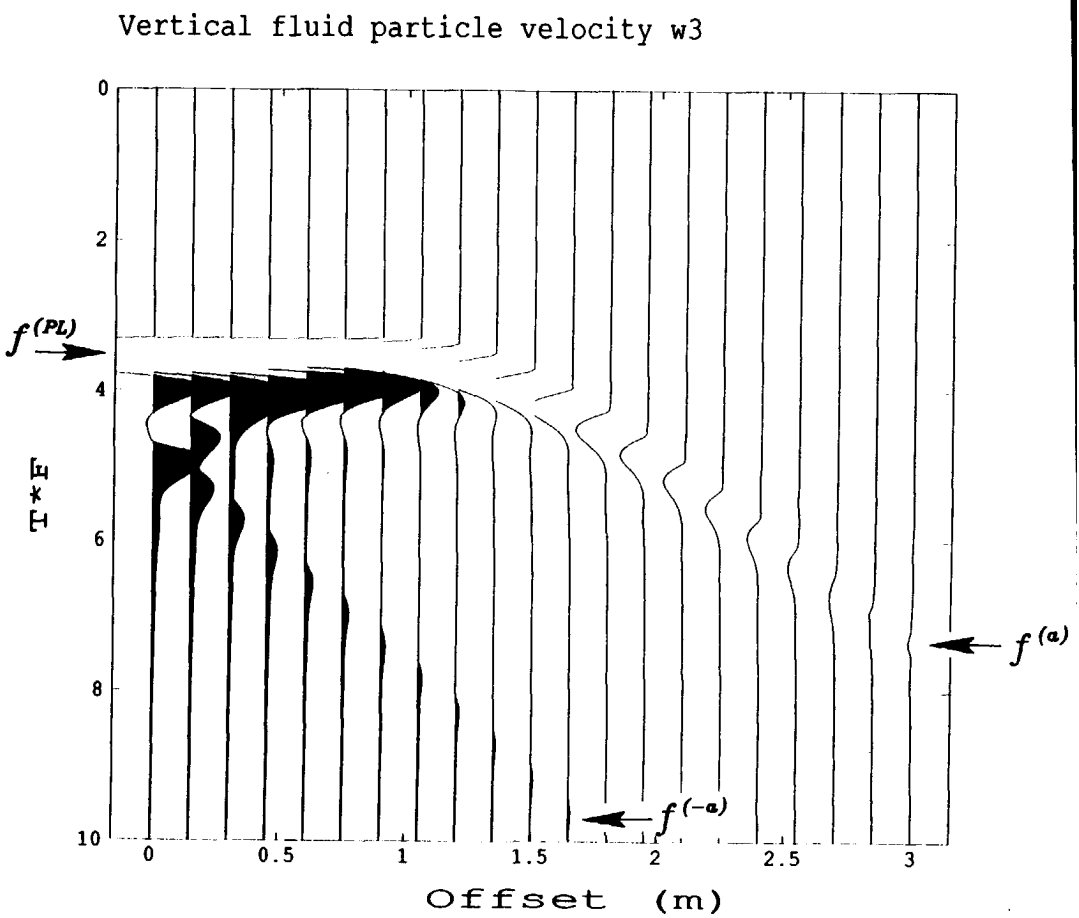

Figure 12.13: The vertical component of the fluid particle velocity for the 21 shallow receivers for the volume injection rate strip source. The fluid waves are indicated by f. The wave originating from the left edge of the strip source has the superscript $(-a)$, the one originating from the right edge of the strip source has the superscript (a). The plane fluid wave is indicated by $f^{(PL)}$.

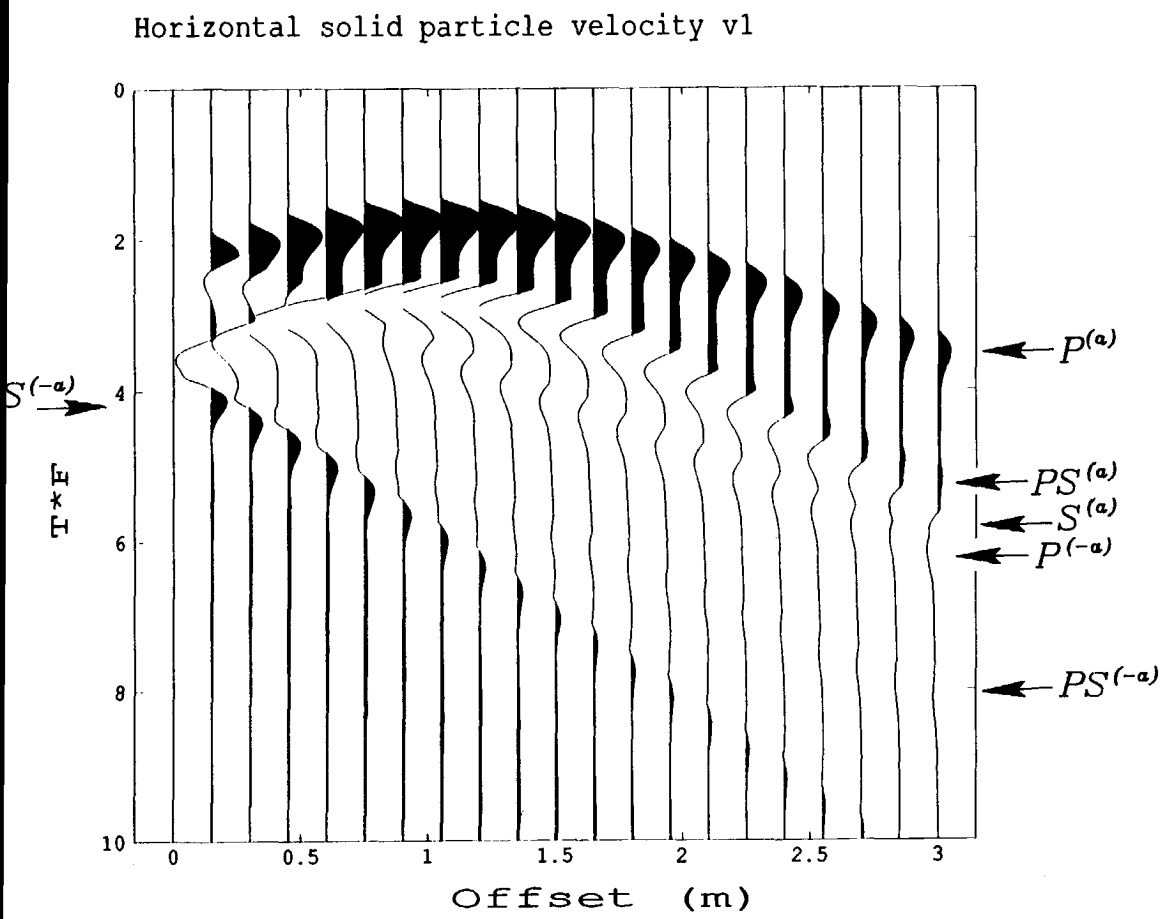

Figure 12.14: The horizontal component of the solid particle velocity for the 21 shallow receivers for the volume injection rate strip source. The $P-, PS-$, and $S-$waves are indicated by P, PS and S, respectively. The waves originating from the left edge of the strip source have the superscript $(-a)$, the ones originating from the right edge of the strip source have the superscript (a). The Rayleigh waves have a too small amplitude to show up.

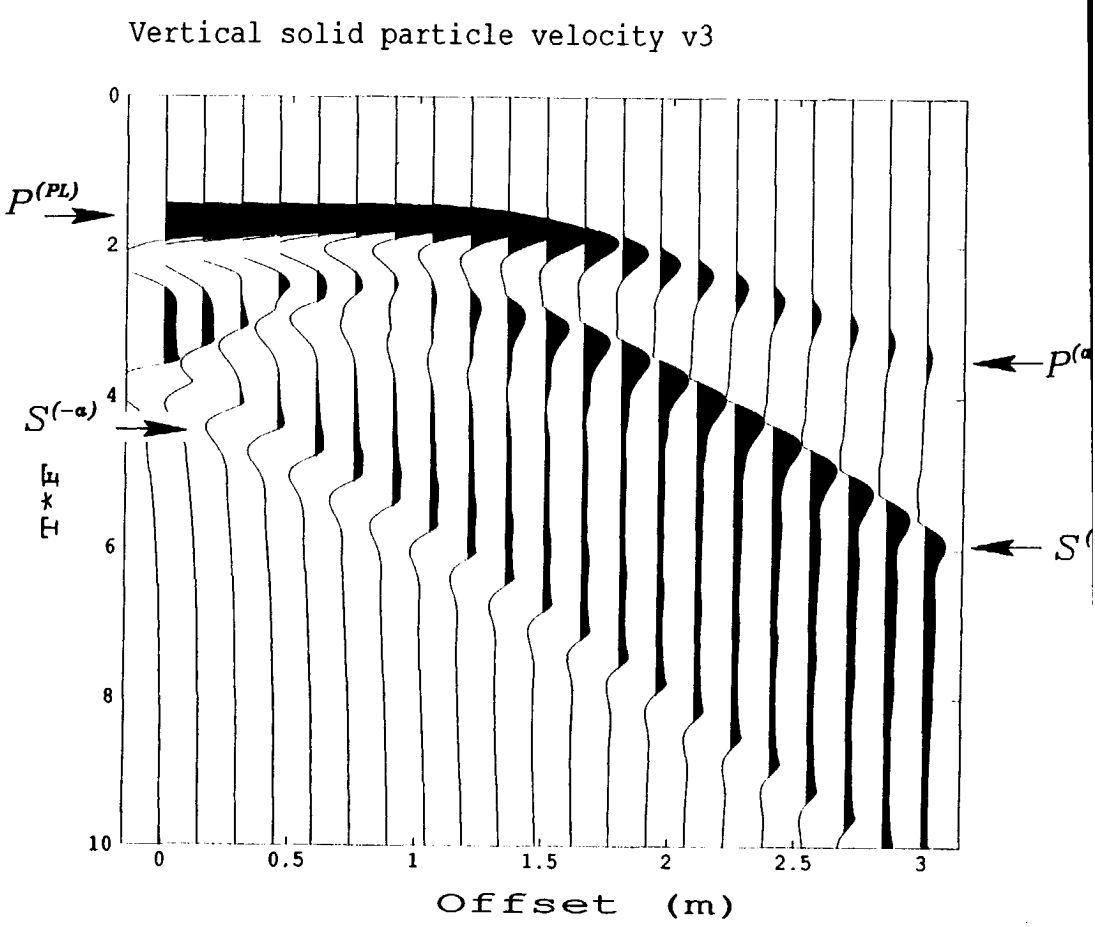

Figure 12.15: The vertical component of the solid particle velocity for the 21 shallow receivers for the volume injection rate strip source. The $P-, PS-$, and $S-$waves are indicated by P, PS and S, respectively. The waves originating from the left edge of the strip source have the superscript $(-a)$, the ones originating from the right edge of the strip source have the superscript (a). The plane $P-$wave is indicated by $P^{(PL)}$. The Rayleigh waves have a too small amplitude to show up.

with the aid of a subroutine of the NAG library (NAG (1988)). The relative accuracy for the determination of these time convolutions was set to 10^{-6}. To avoid numerical difficulties in the computation of the fluid wave or of the $P-$wave in case the Cagniard-De Hoop contour runs closely along the pole $p = 0$ in the complex $p-$plane, an analytically integrable part was separated off from the relevant Green's function so that the remaining part was easy to integrate numerically.

For each receiver the synthetic data were computed at 300 time intervals of $2\pi/30\omega$ m $\cdot$ s. Because the source signature is a highly damped sinusoid, the wave field quantities at a point of observation are expected to drop to a very small value shortly after the arrival of the first peak of the different wave constituents. To save a lot of computation time, the negligibly small field values at these instants have been automatically put equal to zero. With the above measures, the CPU-time needed for each of the two seismograms for the receivers in the fluid was about 1.0 hour and for each of the two seismograms for the receivers in the solid about 1.5 hour on a Vax 8250 computer. The main part of the computation time was spent on the evaluation of the time convolutions of the source signature with the relevant Green's functions.

The seismograms in Figures 12.12-12.15 clearly show the different fluid, $P-$, $S-$ and P to S headwave conversion waves originating from the two edges of the strip source. In addition, we see in the seismogram of the vertical component of the fluid particle velocity w_3 the plane fluid wave contribution that exists above the strip source, while in the seismogram of the vertical component of the solid particle velocity v_3 we see the plane $P-$wave contribution that exists below the strip source. The P to f and S to f conversion waves and the Rayleigh waves have a too small amplitude to show up. The corresponding wave fronts applying to this test case for which $c_f < c_S < c_P$ are drawn in Figure 11.16.

The synthetic seismograms in Figures 12.12-12.15 have been computed for a source with a high frequency (5 kHz), in order to bring out clearly the characteristics of the wave motions generated. In problems of applied geophysics much lower frequencies usually occur. Since the presented solution method is suited for all frequencies, it can be used for low-frequency problems as well.

Chapter 13

NUMERICAL RESULTS

As has already been mentioned in Chapter 9, we want to test our finite-element method for some two-dimensional acoustic wave problems in order to avoid the extensive use of computer storage capacity and computation time associated with three-dimensional problems. For the former, it is still possible to illustrate the specific advantages of the use of our elements. The main difference with the three-dimensional case are the local expansion functions. The elementary regions into which the domain of computation is discretized are now triangles (simplices in R^2) instead of tetrahedra (simplices in R^3).

As test configurations we take the ones introduced in the Chapters 10-12, i.e., the fluid halfspace (Figure 10.1), the solid halfspace (Figure 11.1) and the fluid/solid configuration (Figure 12.1). In the case that the media present in these configurations are taken to be homogeneous, the exact solutions are the relevant Cagniard-De Hoop solutions given in these chapters.

The finite-element method is used to perform the spatial discretization and leads, for each of the test problems, to a square system of linear, first-order, ordinary differential equations as far as the time coordinate t is concerned. In it, the global expansion coefficients used in the global representations of the acoustic wave field quantities occur as fundamental unknown time functions. Its general form is given by

$$\underline{\underline{M}}\,\partial_t \underline{x} = \underline{\underline{K}}\,\underline{x}, \tag{13.1}$$

where $\underline{\underline{M}}$ and $\underline{\underline{K}}$ are square matrices and $\underline{x} = \underline{x}(t)$ is the vector with the unknown time functions. In our computational method we apply a finite-element

discretization in the time direction, too. Thus the time functions are approximated by a sequence of time expansion functions defined on the discretized time axes. We take both for the time weighting and expansion functions so called 'hat' functions. These are piecewise linear functions that have value one in one of the discrete time points of the discretized time axes and zero in the neighbouring points. Substitution of these time representations in (13.1) leads to the system of equations

$$[\underline{\underline{M}} - (1/3)\Delta t\,\underline{\underline{K}}]\underline{x}^{n+1} = (4/3)\Delta t\,\underline{\underline{K}}\underline{x}^{n} + [\underline{\underline{M}} + (1/3)\Delta t\,\underline{\underline{K}}]\underline{x}^{n-1} \tag{13.2}$$

where $\underline{x}^n = \underline{x}(t^n)$ is the value of the vector with the time functions at the instant $t = t^n$. The scheme in (13.2) is a two-step method in the time direction. Therefore, we need besides the initial value $\underline{x}^0$, that follows from the acoustic wave problem, also an estimate of $\underline{x}^1$ to start the marching-on-in-time procedure. To this end we use at the start of the procedure the one-step Euler method:

$$\underline{\underline{M}}\underline{x}^1 = [\underline{\underline{M}} + \Delta t\,\underline{\underline{K}}]\underline{x}^0. \tag{13.3}$$

The above described time discretization procedure is used in the time integration of the different systems of differential equations that arise from the test problems. The test problems are discussed separately below.

Fluid halfspace

At the boudary of the halfspace a strip source is present that exerts along the strip

$$S = \{-a < x_1 < a, x_3 = 0\} \tag{13.4}$$

a spatially uniformly distributed normal force on the fluid medium. (Figure 10.1). The force per unit length in the x_2-direction and unit width in the x_1-direction is $\Phi_\perp(t)/2a$ with $\Phi_\perp(t)$ as the wavelet. We have taken as the source signature

$$\Phi_\perp(t) = A\exp(-\delta t)\sin(\omega t)H(t), \tag{13.5}$$

where $H(t)$ is the Heaviside unit step function (cf. (10.20)), A the source strength amplitude, δ the damping coefficient and ω the angular frequency. In our computations we have taken a strip source for which a=0.25 m, A = -1 N/m, $\delta = 2 * 10^3 s^{-1}$ and $\omega = 2\pi * 5 * 10^2$ rad/s (f = 0.5 kHz).

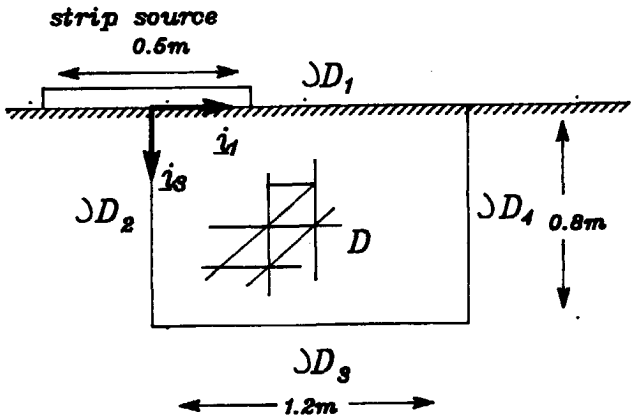

Figure 13.1: Domain of computation D with its four boundaries $\partial D_1, \partial D_2, \partial D_3$ and ∂D_4. The horizontal distance between ∂D_2 and ∂D_4 is 1.2 m; the vertical distance between ∂D_1 and ∂D_3 is 0.8 m. Domain D is discretized into an 18×12 grid.

As domain of finite-element computation D a rectangle is chosen that has a boundary ∂D_1 that is coincident with the boundary of the halfspace, a boundary ∂D_2 that is coincident with the plane of symmetry of the configuration ($x_1 = 0, x_3 \in R$) and the two boundaries ∂D_3 and ∂D_4 that together form an artificial boundary that restricts the domain of computation D (Figure 13.1). On the part of ∂D_1 where the strip source is not present, tractionfree boundary conditions are imposed whereas on the remaining part of ∂D_1 the strip source prescribes the scalar traction. On the boundary ∂D_2 the appropriate symmetry conditions are prescribed. Finally, the normal component of the particle velocity has been put equal to zero at the artificial boundaries ∂D_3 and ∂D_4. These boundaries are taken so far from the strip source that the (artificial) reflections against them can not reach the receivers within the chosen time window. As far as time is

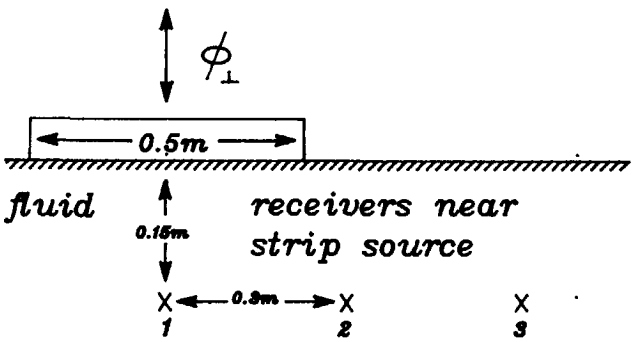

Figure 13.2: The array of 3 receivers in the fluid near the strip source.

concerned, we introduce the normalized time coordinate $t^{norm} = t * f$, where f is the frequency of excitation of the strip source.

First the finite-element solution in a homogeneous fluid halfspace is tested against the corresponding Cagniard-De Hoop solution. The fluid properties are taken to be $\rho^f = 1.0 * 10^3$ kg/m^3 and $\kappa = 4.4 * 10^{-10}$Pa^{-1}. The fluid wave speed is then $c_f = 1507$ m/s. The spatial fluid wave length Λ_f follows then as $\Lambda_f = c_f/f \approx 3$ m. As window for the normalized time we choose $t^{norm} \in [0.0\text{ s}, 0.5\text{s}]$. The seismograms for an array of 3 receivers are computed that are located 0.3 m apart at a depth of 0.15 m. The first receiver of this array is located below the center of the strip source (Figure 13.2). The vertical distance between the strip source and the boundary ∂D_3 is taken to be 0.8 m and the horizontal distance between the center of the strip source and the boundary ∂D_4 is taken to be 1.2 m. These distances ensure that the artificial reflections of the generated waves do not reach the receivers within the chosen time window. The spatial discretization is shown in Figure 13.1: we took 18 steps in the horizontal direction and 12 steps

in the vertical direction. Consequently, we have 45 discretization steps per wave length Λ_f. In the time direction we have taken a number of 80 time steps for our time window. The synthetic seismograms for the horizontal and the vertical particle velocities for the array of three receivers are presented in Figure 13.3 and Figure 13.4, respectively. The solid lines represent the exact Cagniard-De Hoop solution, the dashed line the finite-element solutions with the Cartesian elements and the dotted line the finite-element solution with the Face elements. We observe that the solution with the Face elements is a little better than the one with the Cartesian elements. However, the CPU time used in the computations with the Face elements was about 3 hours and with the Cartesian elements about 1 hour. For the homogeneous case, the finite-element method that makes use of the Cartesian elements is more efficient than the one that uses Face elements.

Next, the performance of the two different types of elements is tested for an acoustic halfspace wave problem with an inhomogeneous fluid. We take a strip source with the same parameters as used in the homogeneous fluid wave problem except that now $a = 0.3$ m. In the region R1 $= \{-0.1 < x_1 < 0.1,\ x_3 > 0\}$ the fluid properties are taken to be $\rho^{f(1)} = 1.0{*}10^3$ kg/m^3 and $\kappa^{(1)} = 4.4{*}10^{-10}$Pa^{-1}. The fluid wave speed in R1 is then $c_f^{(1)} = 1507$ m/s and the spatial wave length $\Lambda_f^{(1)} = 1.5$ m. In region R2 $= \{-\infty < x_1 < -0.1 \vee 0.1 < x_1 < \infty,\ x_3 > 0\}$ the fluid properties are taken to be $\rho^{f(2)} = 1.0{*}10^4$ kg/m^3 and $\kappa^{(2)} = 4.4{*}10^{-10}$Pa^{-1}. The fluid wave speed in R2 is then $c_f^{(2)} = 477$ m/s and the spatial wave length $\Lambda_f^{(2)} = 0.95$ m. Further, we have between the regions R1 and R2 fluid/fluid interfaces at $\{x_1 = -0.1, x_3 > 0\}$ and $\{x_1 = 0.1, x_3 > 0\}$ (Figure 13.5). The media in the two regions R1 and R2 show a relatively large contrast in their volume density of mass.

Synthetic seismograms have been computed for two receivers, the first one at the position (0.075 m, 0.1 m) which is in the region R1 and the second one at the position (0.125 m, 0.1 m) which is in the region R2. As window for the normalized time we choose $t^{norm} = [0.0\text{ s}, 0.25\text{ s}]$. The vertical distance between the strip source and the boundary ∂D_3 is taken to be 0.4 m and the horizontal distance between the center of the strip source and the boundary ∂D_4 is taken to be 0.4 m (see Figure 13.5). These distances ensure that the artificial reflections of the generated waves do not reach the receivers within the chosen time window.

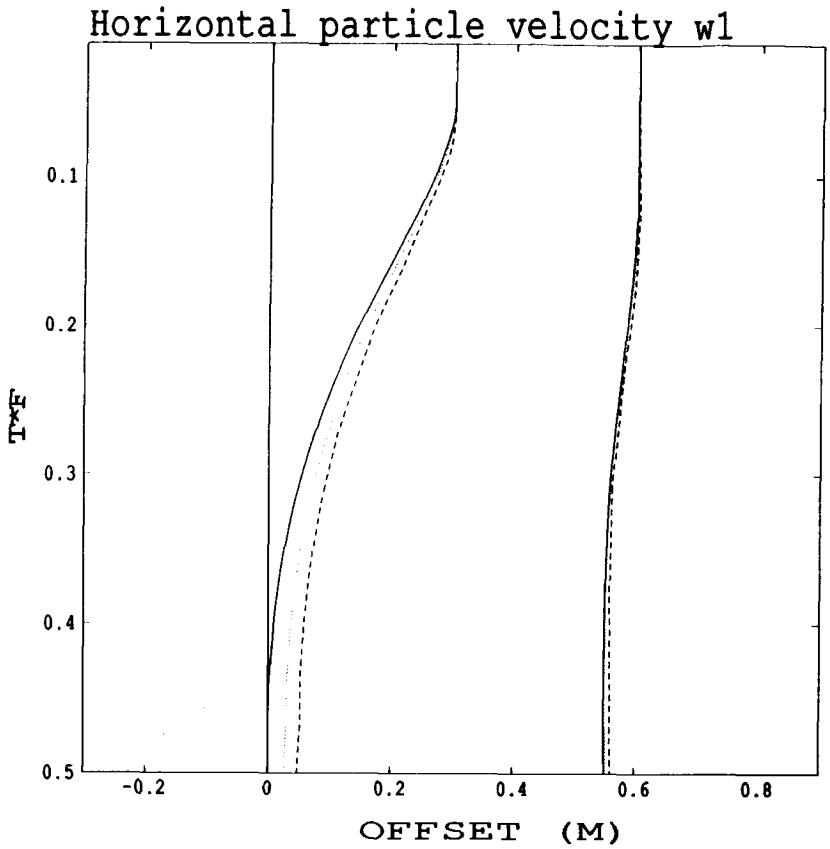

Figure 13.3: The horizontal component of the particle velocity for the three receivers for the normal force strip source. The solid line is the Cagniard-De Hoop solution, the dashed line the finite-element solution where Cartesian elements have been used and the dotted line the finite-element solution where Face elements have been used.

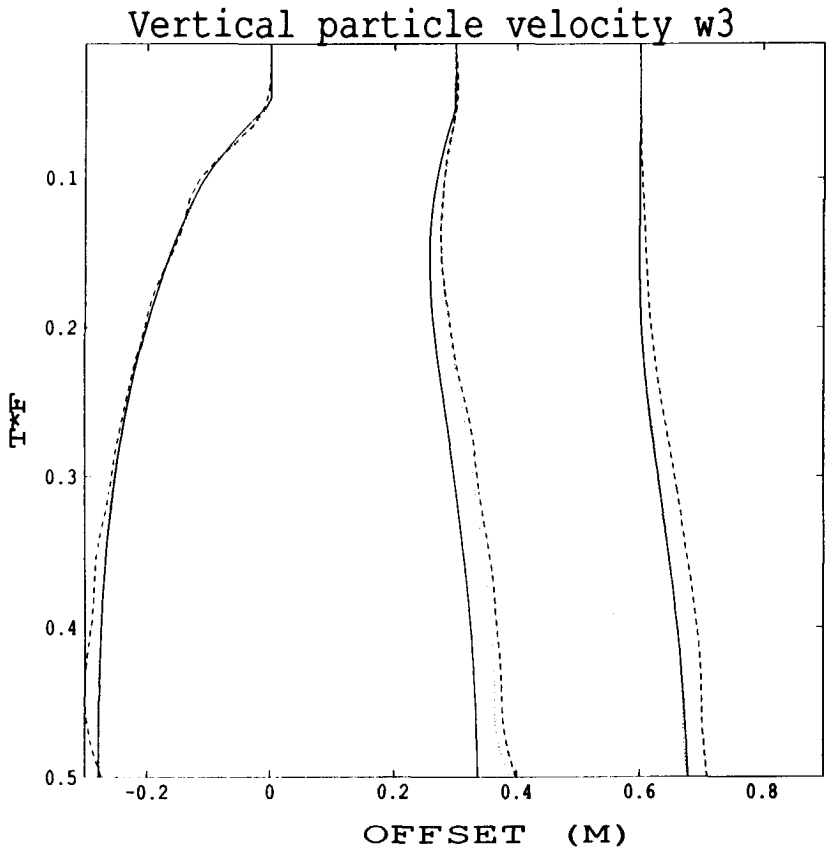

Figure 13.4: The vertical component of the particle velocity for the three receivers for the normal force strip source. The solid line is the Cagniard-De Hoop solution, the dashed line the finite-element solution where Cartesian elements have been used and the dotted line the finite-element solution where Face elements have been used.

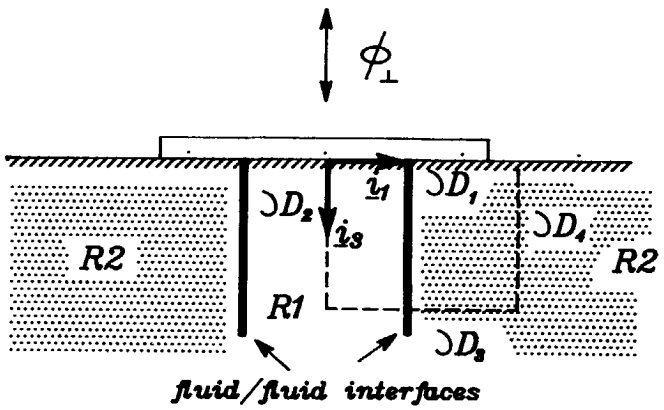

Figure 13.5: The inhomogeneous fluid halfspace with the regions R1=$\{-0.1 < x_1 < 0.1,\ x_3 > 0\}$ and R2=$\{-\infty < x_1 < -0.1 \vee 0.1 < x_1 < \infty,\ x_3 > 0\}$. At $\{x_1 = 0.1, x_3 > 0\}$ there is a fluid/fluid interface. The horizontal distance between ∂D_2 and ∂D_4 is 0.4 m; the vertical distance between ∂D_1 and ∂D_3 is 0.4 m. Domain D is discretized into a 4×4 grid.

First, the finite-element computations with Cartesian and Face elements are performed for a spatial discretization of 4 steps in the horizontal direction and 4 steps in the vertical direction of the domain of computation D (see Figure 13.5). The synthetic seismograms of the particle velocities are presented in Figures 13.6 and 13.7. The solid line is the solution with Face elements and the dashed line is the solution with Cartesian elements. Next, the computations with the Cartesian elements are performed for two grids with an increased number of discretization steps in the horizontal direction. In Figures 13.8 and 13.9 the dashed line is the finite-element solution with Cartesian elements for a grid with 8 steps in the horizontal direction and 4 steps in the vertical direction and in Figures 13.10 and 13.11 they are the relevant solutions for a grid with 12 steps in the horizontal direction and 4 steps in the vertical direction. In these seismograms the solid line is the finite-element solution with the Face elements for the 4×4 grid. We observe that by increasing the number of discretization steps in the horizontal direction the solution with Cartesian elements more and more approximates the one computed with the Face elements. The CPU time needed for the finite-element solution using the Cartesian elements for the finest grid is about 17 minutes and for the finite-element solution using the Face elements about 11 minutes. For this problem we observe that the finite-element method that uses the Face elements is more efficient than the one using Cartesian elements.

Solid halfspace

For the solid halfspace only finite-element computations with Cartesian elements have been performed because for this case the symmetry of the stress (following from the balance of angular momentum) does not give rise to extra difficulties. In case Face elements are used, the symmetrization of the expansion of the stress becomes a problem. Because the individual local Face expansion functions are not symmetric, this condition on the stress has to be enforced by supplementary (local) equations. How this is to be implemented is still an unsolved problem.

The finite-element computations are performed for a homogeneous solid halfspace. At the boudary of it a strip source is present that exerts along the strip (cf. (13.4)) a spatially uniformly distributed normal force on the solid medium (Figure 11.1). The force per unit length in the x_2-direction and unit width in

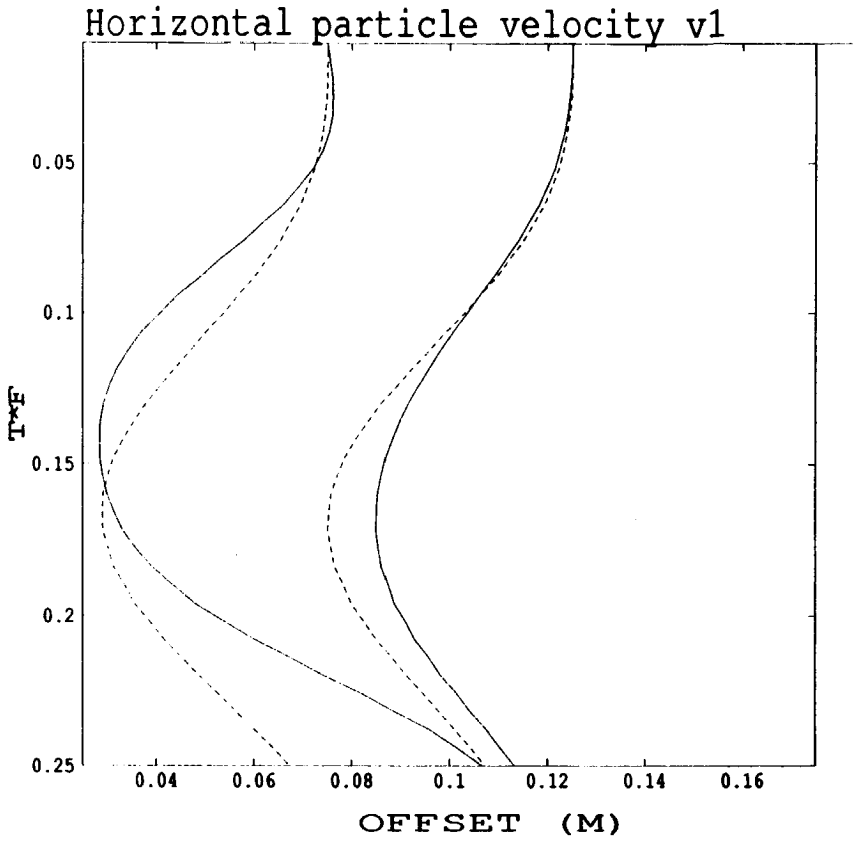

Figure 13.6: The horizontal particle velocity for the two receivers near the fluid/fluid interface for the normal force strip source problem. The solid line represents the finite-element solution with the aid of Face elements, the dashed line represents the one with the aid of Cartesian elements. For both methods we used a 4×4 grid.

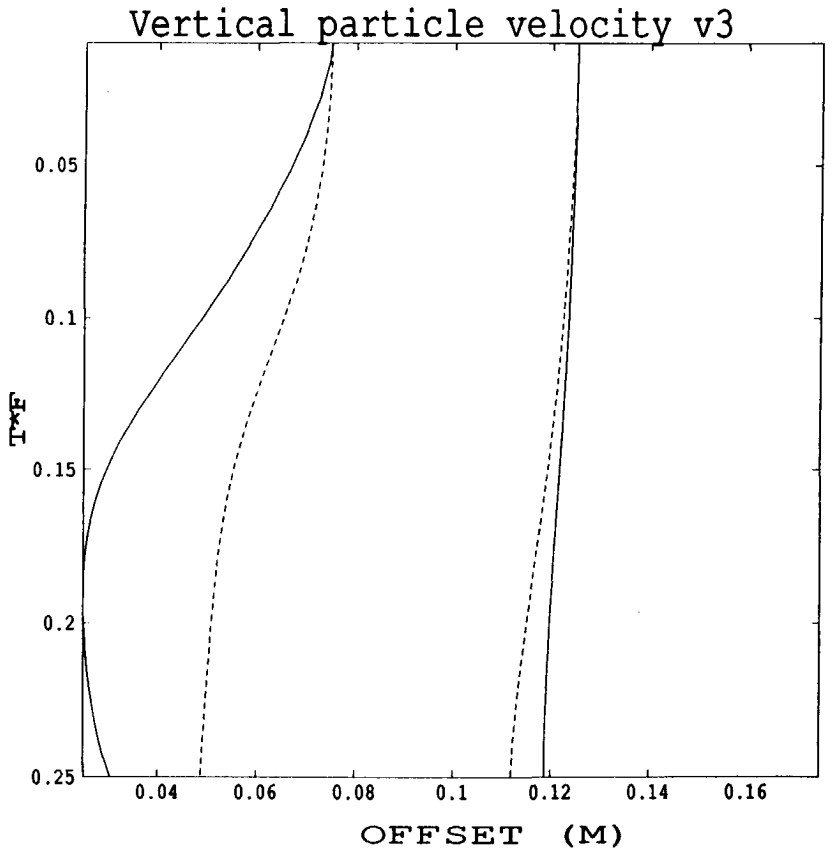

Figure 13.7: The vertical particle velocity for the two receivers near the fluid/fluid interface for the normal force strip source problem. The solid line represents the finite-element solution with the aid of Face elements, the dashed line represents the one with the aid of Cartesian elements. For both methods we used a 4×4 grid.

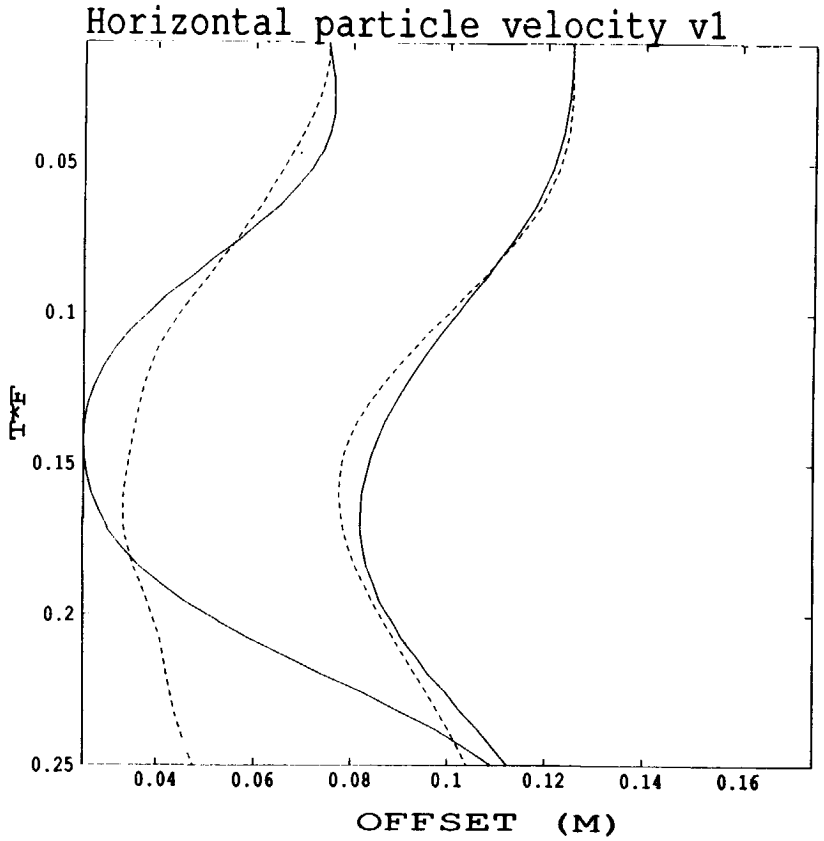

Figure 13.8: The horizontal particle velocity for the two receivers near the fluid/fluid interface for the normal force strip source problem. The solid line represents the finite-element solution with the aid of Face elements for a 4×4 grid, the dashed line represents the one with the aid of Cartesian elements for a 8×4 grid.

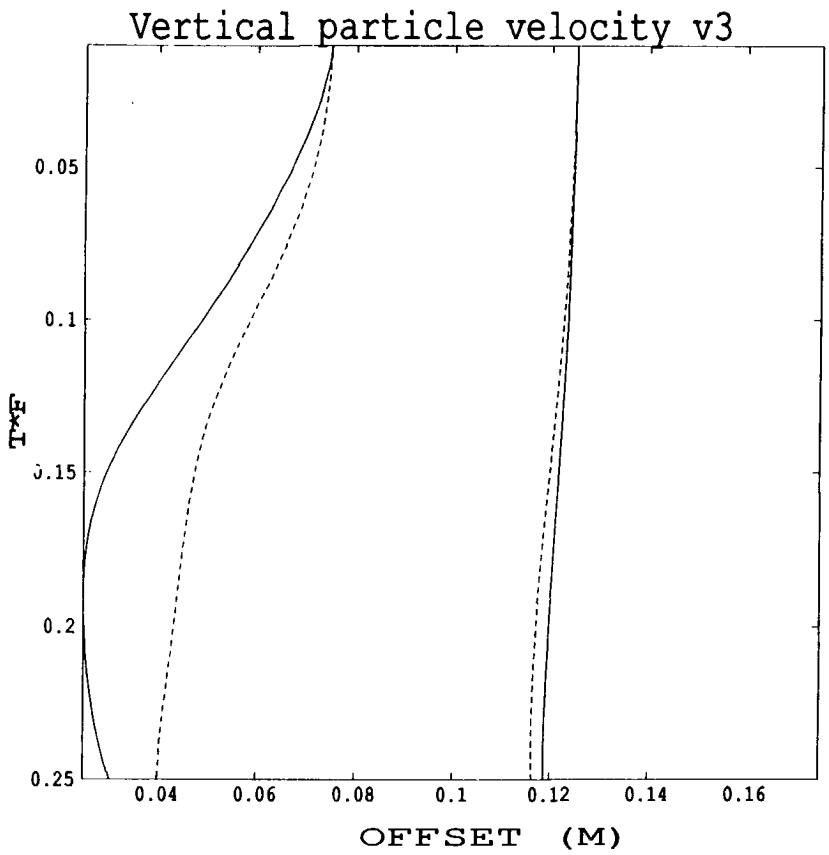

Figure 13.9: The vertical particle velocity for the two receivers near the fluid/fluid interface for the normal force strip source problem. The solid line represents the finite-element solution with the aid of Face elements for a 4×4 grid, the dashed line represents the one with the aid of Cartesian elements for a 8×4 grid.

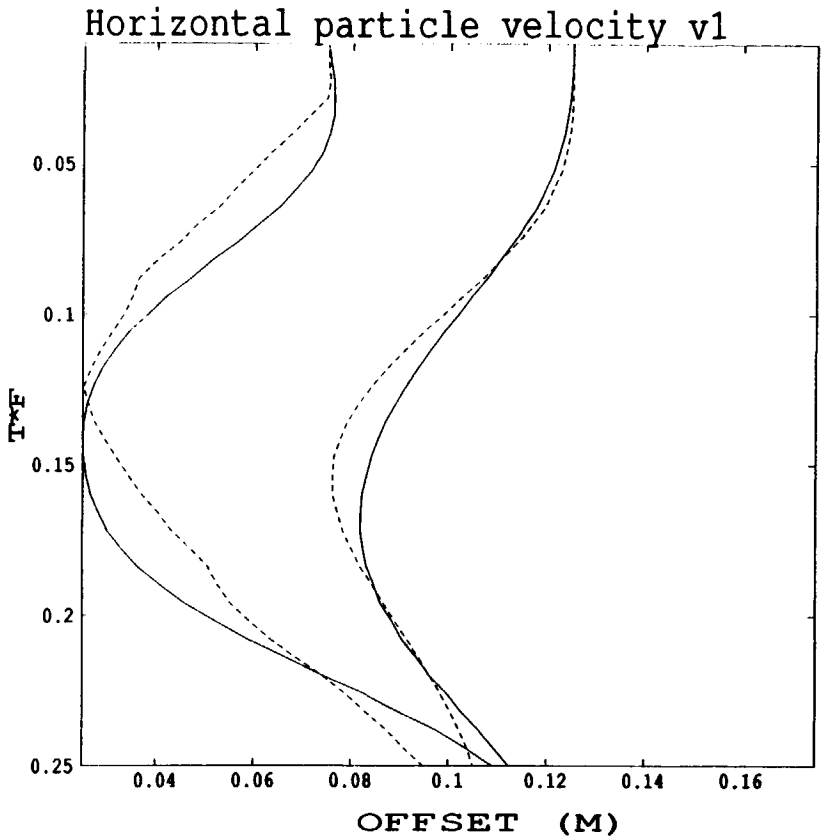

Figure 13.10: The horizontal particle velocity for the two receivers near the fluid/fluid interface for the normal force strip source problem. The solid line represents the finite-element solution with the aid of Face elements for a 4×4 grid, the dashed line represents the one with the aid of Cartesian elements for a 12×4 grid.

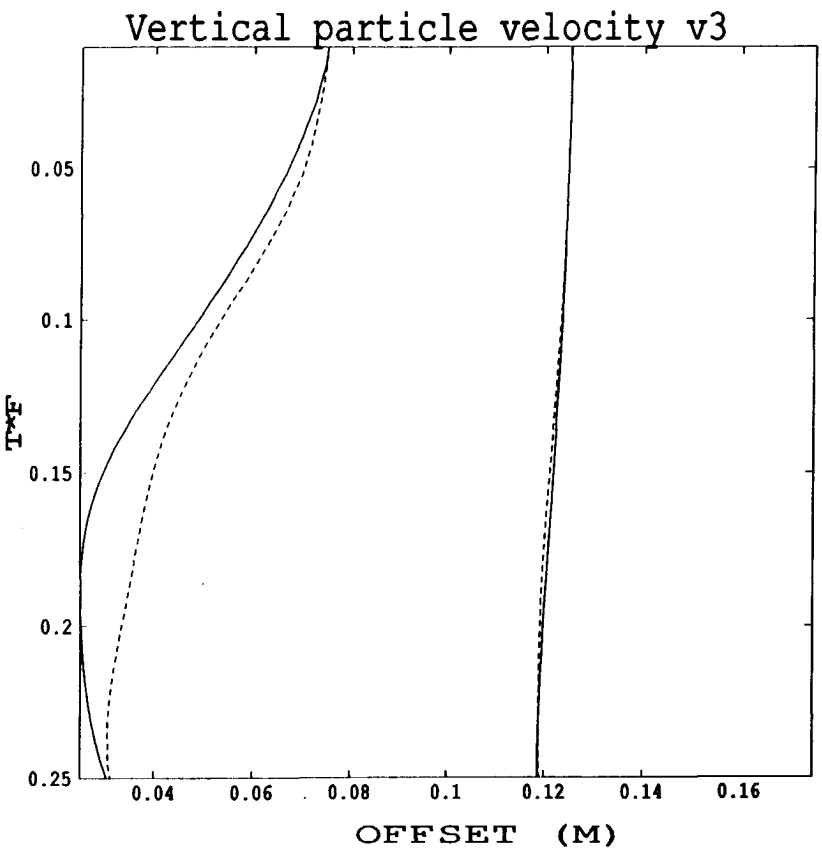

Figure 13.11: The vertical particle velocity for the two receivers near the fluid/fluid interface for the normal force strip source problem. The solid line represents the finite-element solution with the aid of Face elements for a 4×4 grid, the dashed line represents the one with the aid of Cartesian elements for a 12×4 grid.

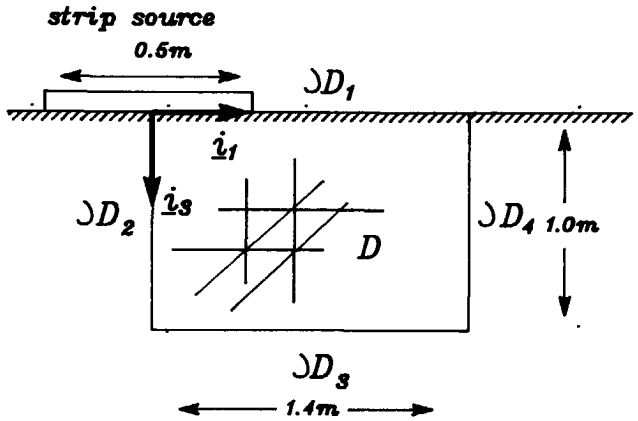

Figure 13.12: Domain of computation D with its four boundaries $\partial D_1, \partial D_2, \partial D_3$ and ∂D_4. The horizontal distance between ∂D_2 and ∂D_4 is 1.4 m; the vertical distance between ∂D_1 and ∂D_3 is 1.0 m. Domain D is discretized into a 7×5 grid.

the x_1−direction is $\Phi_\perp(t)/2a$ where the wavelet $\Phi_\perp(t)$ is given by (13.5). As source parameters we have taken a=0.25 m, $A = 1$ N/m, $\delta = 2 * 10^3$ s^{-1} and $\omega = 2\pi * 1.0 * 10^3$ rad/s (f = 1.0 kHz).

Similar to the computations for the fluid halfspace, the domain of finite-element computation D is a rectangle with a boundary ∂D_1 that is coincident with the boundary of the halfspace, a boundary ∂D_2 that is coincident with the plane of symmetry of the configuration ($x_1 = 0, x_3 \in R$) and two boundaries ∂D_3 and ∂D_4 that together form an artificial boundary that restricts the domain of computation D (Figure 13.12). On the part of ∂D_1 where the strip source is not present, tractionfree boundary conditions are required whereas on the remaining part of ∂D_1 the strip source prescribes the solid traction. On the boundary ∂D_2 the appropriate symmetry conditions are prescribed. Finally,

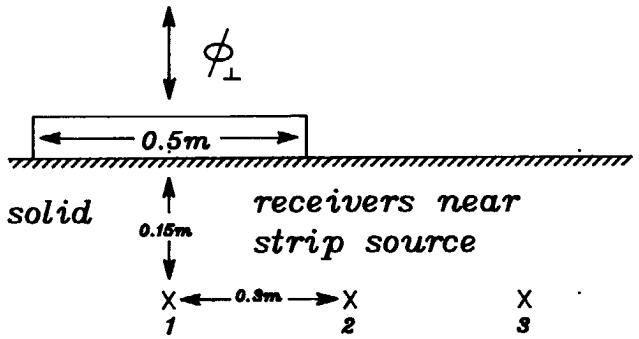

Figure 13.13: The array of 3 receivers in the solid near the strip source.

the normal component of the particle velocity has been put equal to zero at the artificial boundary ∂D_3 and ∂D_4. These boundaries are taken so far from the strip source that the (artificial) reflections of the waves generated by it can not reach the receivers within the chosen time window. As far as time is concerned, we introduce the normalized time coordinate $t^{norm} = t * f$, where f is the frequency of excitation of the strip source. As far as the medium properties are concerned, we take $\rho^s = 2.5 * 10^3$ kg/m^3 and $\lambda = \mu = 1.0 * 10^{10}$ N. The $P-$ and $S-$wave speeds are then $c_P = 3464$ m/s and $c_S = 2000$ m/s. The spatial $P-$ and $S-$wave lengths Λ_P and Λ_S follow then as $\Lambda_P = c_P/f \approx 3.5$ m and $\Lambda_S = c_S/f \approx 2$ m. As window for the normalized time we have chosen $t^{norm} \in$ [0.0 s, 0.5s]. The seismograms for an array of 3 receivers are computed that are located 0.3 m apart at a depth of 0.15 m. The first receiver of this array is located below the center of the strip source (Figure 13.13). The vertical distance between the strip source and the boundary ∂D_3 is taken to be 1.0 m and the

horizontal distance between the center of the strip source and the boundary ∂D_4 is taken to be 1.4 m. These distances ensure that the artificial reflections of the generated waves don't reach the receivers within the chosen time window. The spatial discretization is shown in Figure 13.12 where we took 7 steps in the horizontal direction and 5 steps in the vertical direction. Consequently, we have 20 discretization steps per $S-$wave length Λ_S. In the time direction we have taken a number of 50 time steps for our time window. The synthetic seismograms for the horizontal and the vertical particle velocities for the array of three receivers are presented in Figure 13.14 and Figure 13.15, respectively. The solid lines represent the exact Cagniard-De Hoop solution and the dashed lines the finite-element solutions with the Cartesian elements. The CPU time used in the computations with the Cartesian elements was about 26 minutes.

Fluid/solid configuration

Numerical results are presented for a fluid/solid configuration in which the fluid and solid are homogeneous (Figure 12.1). The properties of the solid are taken to be $\rho^s = 2.5 * 10^3 \mathrm{kg/m^3}$ and $\lambda = \mu = 10^{10}$ N. The $P-$ and $S-$wave speeds are then $c_P = 3464$ m/s and $c_S = 2000$ m/s, respectively. For the fluid properties we have taken $\rho^f = 1.0 * 10^3 \mathrm{kg/m^3}$ and $\kappa = 4.4 * 10^{-10} \mathrm{Pa^{-1}}$. The fluid wave speed is then $c_f = 1507$ m/s.

At the plane interface

$$I = \{x_1 \in R, x_3 = 0\} \tag{13.6}$$

between the fluid and the solid, a strip source is present that introduces a spatially uniformly distributed volume injection rate along the strip (13.4). The injection rate per unit length in the x_2-direction and unit width in the x_1-direction is $\Phi_\perp(t)/2a$ where the wavelet $\Phi_\perp(t)$ is given by (13.5). As source parameters we have taken $A = 1$ N/m, $\delta = 2 * 10^3 \mathrm{s^{-1}}$ and $\omega = 2\pi * 1.0 * 10^3$ rad/s ($f = 1.0$ kHz). For the chosen frequency of the excitation of the strip source the spatial wave lengths of the fluid, $P-$ and $S-$wave in the configuration are $\Lambda_f \approx 1.5m, \Lambda_P \approx 3.5m$ and $\Lambda_S \approx 2m$, respectively.

On the part $S \cap I$ of the interface the strip source generates a finite difference between the vertical component of the fluid particle velocity and the

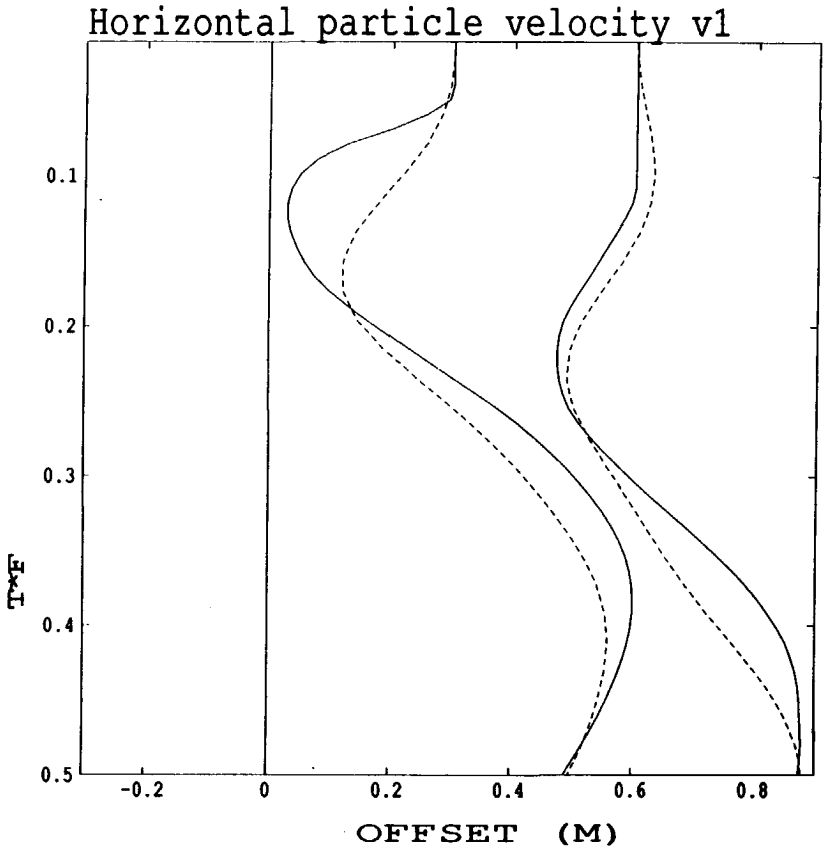

Figure 13.14: The horizontal component of the particle velocity for the three receivers for the normal force strip source. The solid line is the Cagniard-De Hoop solution, the dashed line the finite-element solution where Cartesian elements have been used.

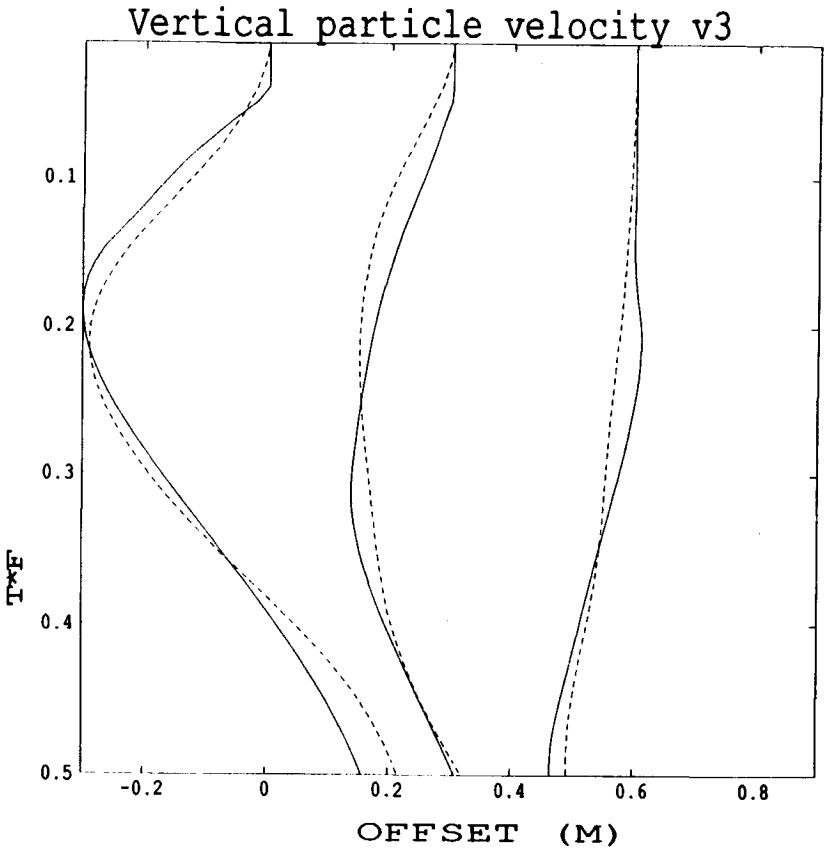

Figure 13.15: The vertical component of the particle velocity for the three receivers for the normal force strip source. The solid line is the Cagniard-De Hoop solution, the dashed line the finite-element solution where Cartesian elements have been used.

vertical component of the solid particle velocity. On the part $I \setminus S$ of the interface, where the strip source is not present, the vertical component of the fluid particle velocity is equal to the vertical component of the solid particle velocity. The scalar traction in the fluid is at each point of the interface I, equal to the normal component of the traction in the solid. Finally, the tangential component of the traction in the solid is at the interface I equal to zero. In general, the tangential component of the fluid particle velocity is unequal to the tangential component of the solid particle velocity at I. We test to finite-element solutions agains the exact Cagniard-De Hoop for the fluid/solid medium. In both finite-element methods we use Cartesian elements in the fluid and solid parts of the configuration. In the first method, denoted by Cartesian finite-element method, all acoustic wave field quantities are continuous by construction across the fluid/solid interface while in the second method, denoted by Face finite-element method, the vertical component of the particle velocity may jump by a finite amount through this interface. The last method reflects the principle of the Face elements.

We compute the particle velocity for two receivers near the fluid/solid interface. One receiver is present in the fluid and one is present in the solid. Both receivers have equal horizontal offset and have a vertical offset from the fluid/solid interface of 0.1 m. Computations are performed for the case that we have a strip source of infinite extent ($a \rightarrow \infty$) and for one of a finite extent in which case the receivers are placed at a part of the interface where the strip source is not present. (Figure 13.16).

First we show the results for the receivers for a the strip source of infinite extent ($a \rightarrow \infty$). For this case the domain of finite-element computation D is a rectangle with two vertical boundaries ∂D_2 and ∂D_4 that intersect the strip source. At these boundaries we require the vertical component of the particle velocity to be zero. Further, we have the two boundaries ∂D_1 and ∂D_3 that are the artificial boundaries that restrict the domain of computation D. (Figure 13.17). We perform the computations for a spatial grid that has 6 step in the horizontal direction and 9 steps in the vertical direction. As far as the shortes spatial wave length Λ_f is concerned, we have 9 steps per wave length. For the window of the normalized time coordinate we have taken $t_{norm} =$

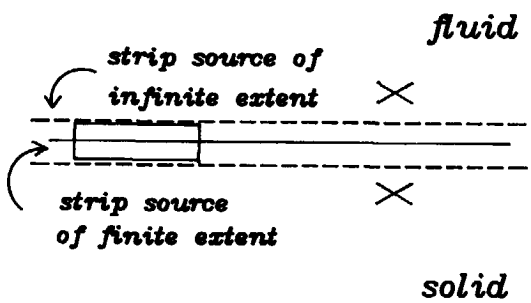

Figure 13.16: The 2 receivers near the fluid/solid interface that have equal horizontal offset and a vertical offset from the fluid/solid interface of 0.1 m.

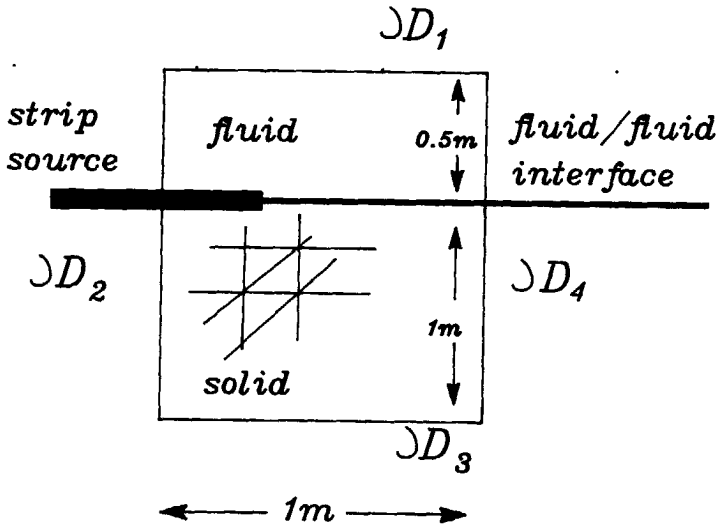

Figure 13.17: Domain of computation D with its four boundaries $\partial D_1, \partial D_2, \partial D_3$ and ∂D_4. The horizontal distance between ∂D_2 and ∂D_4 is 1.0 m; the vertical distance between ∂D_1 and the fluid/solid interface is 0.5 m and between ∂D_3 and the fluid/solid boundary 1.0 m. Domain D is discretized into a 6×9 grid.

$[0.0s, 0.25s]$ that has been discretized into a union of 50 time intervals. The artificial boundaries ∂D_1 and ∂D_3 have been taken so far from the strip source that the (artificial) reflections of the waves generated by it can not reach the receivers within the chosen time window.

The synthetic seismograms for the horizontal and the vertical components of the particle velocities for the receiver in the fluid and in the solid are represented in the Figures 13.18-13.21.

In the synthetic seismograms the solid lines are the exact Cagniard-De Hoop solutions, the dashed lines the solutions obtained by the Cartesian finite-element method and the dotted lines the Face finite-element solutions. For each receiver, both finite element methods needed about 1 hour CPU time.

We observe that the finite-element method using the Cartesian elements and that that uses the Face elements give an equally well approximation of the exact solution.

In the second numerical experiment, we compute the particle velocity for a strip source of finite extent where the two receivers are placed at a part of the interface where no strip source is present. The extent of the strip source is taken to be 0.5 m ($a = 0.25m$). As domain of finite-element computation we take the same as the one for the previous experiment, except that now the boundary ∂D_2 is coincident with the plane of symmetry of the configuration and ∂D_4 is an artificial boundary. We have also taken the same source parameters, time window and discretization of the spatial and time domain as have been used in the computations for the infinitely extended strip source.

The synthetic seismograms for the horizontal and the vertical components of the particle velocities for the receiver in the fluid and in the solid are represented in the Figures 13.22-13.25.

In the synthetic seismograms the solid lines are the exact Cagniard-De Hoop solutions, the dashed lines the solutions obtained by the Cartesian finite-element method and the dotted lines the Face finite-element solutions. For each receiver, both finite element methods needed about 1 hour CPU time.

We observe that the Face finite-element method gives a better approximation of the exact solution than the Cartesian finite-element method.

Concluding remarks

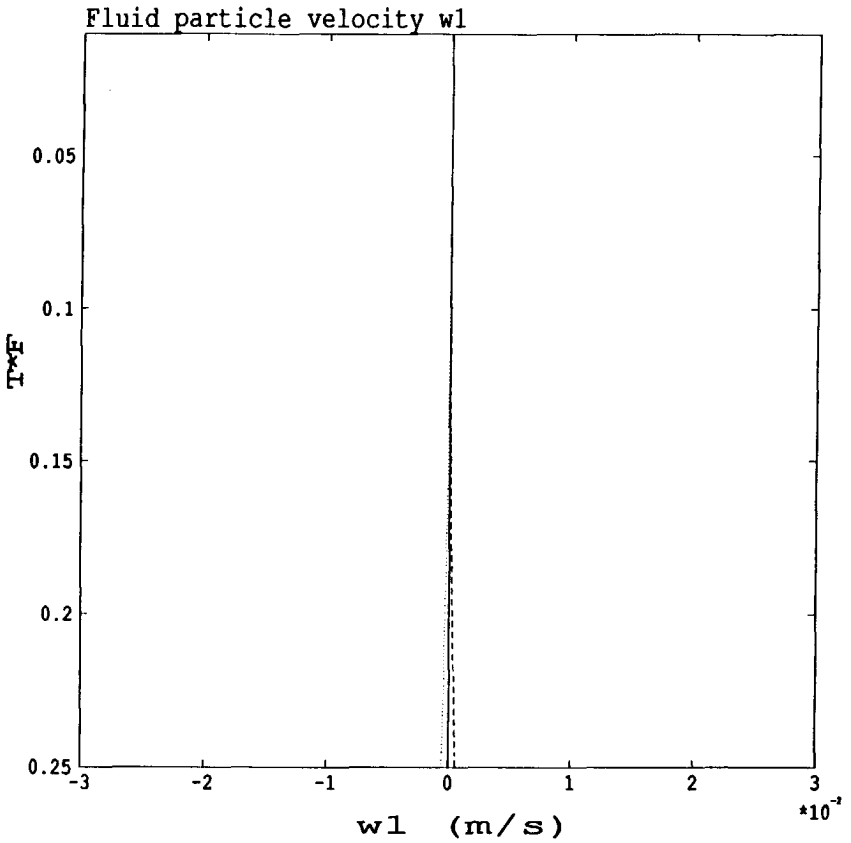

Figure 13.18: The horizontal component of the fluid particle velocity for the receiver in the fluid for the volume injection rate strip source of infinite extent. The solid line is the Cagniard-De Hoop solution, the dashed line the Cartesian finite-element method solution and the dotted line the Face finite-element method solution. have been used.

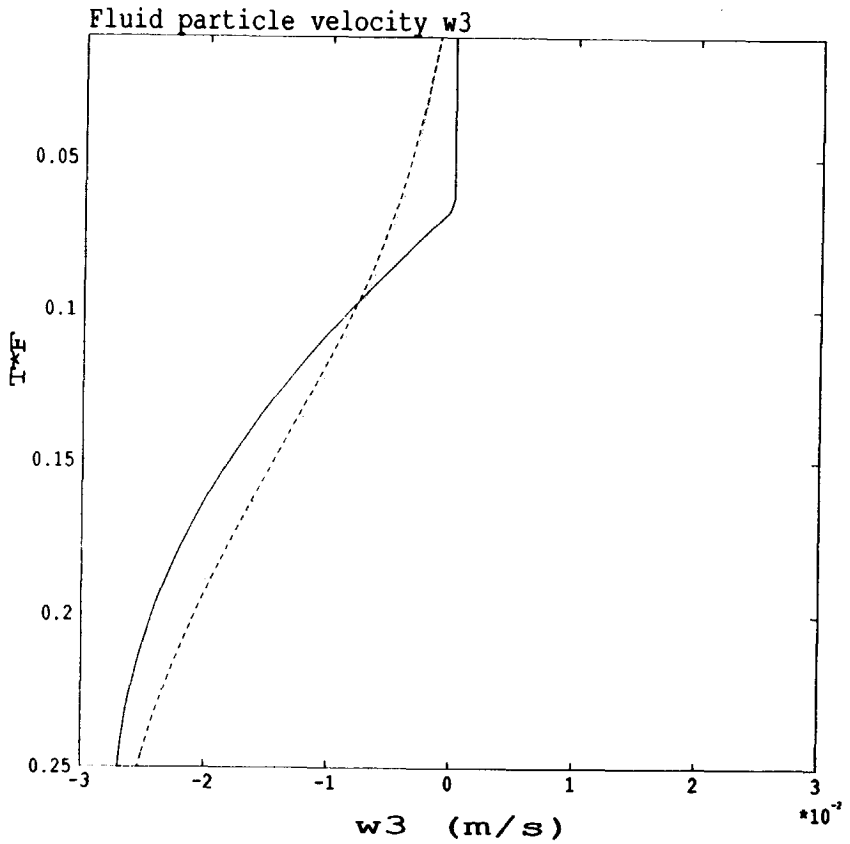

Figure 13.19: The vertical component of the fluid particle velocity for the receiver in the fluid for the volume injection rate strip source of infinite extent. The solid line is the Cagniard-De Hoop solution, the dashed line the Cartesian finite-element method solution and the dotted line the Face finite-element method solution.

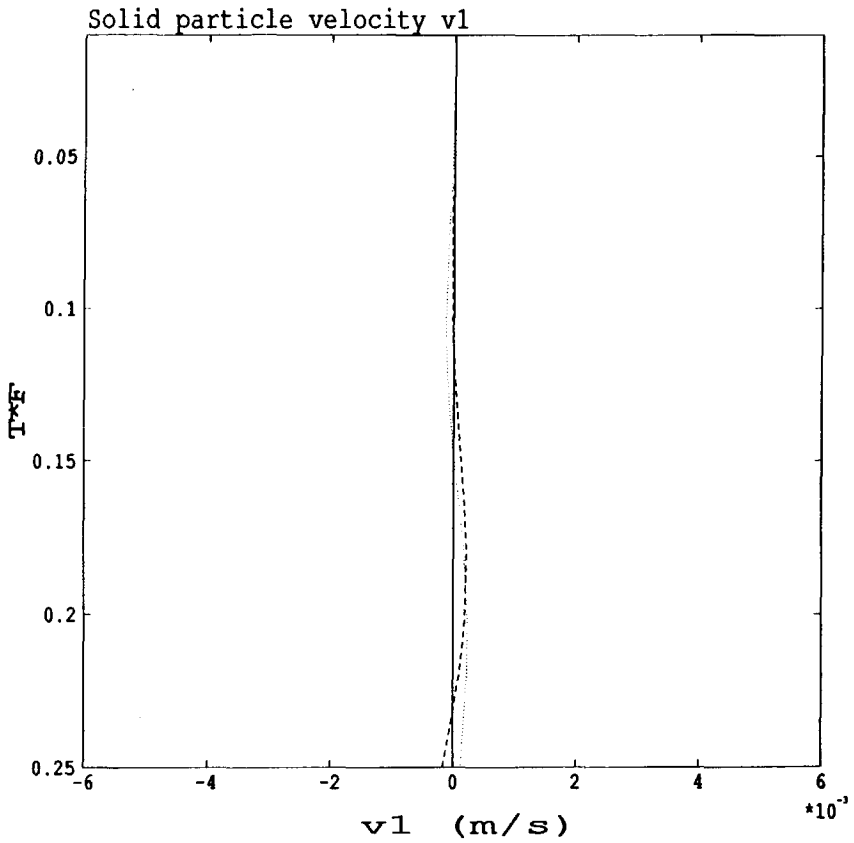

Figure 13.20: The horizontal component of the solid particle velocity for the receiver in the solid for the volume injection rate strip source of infinite extent. The solid line is the Cagniard-De Hoop solution, the dashed line the Cartesian finite-element solution and the dotted line the Face finite-element solution.

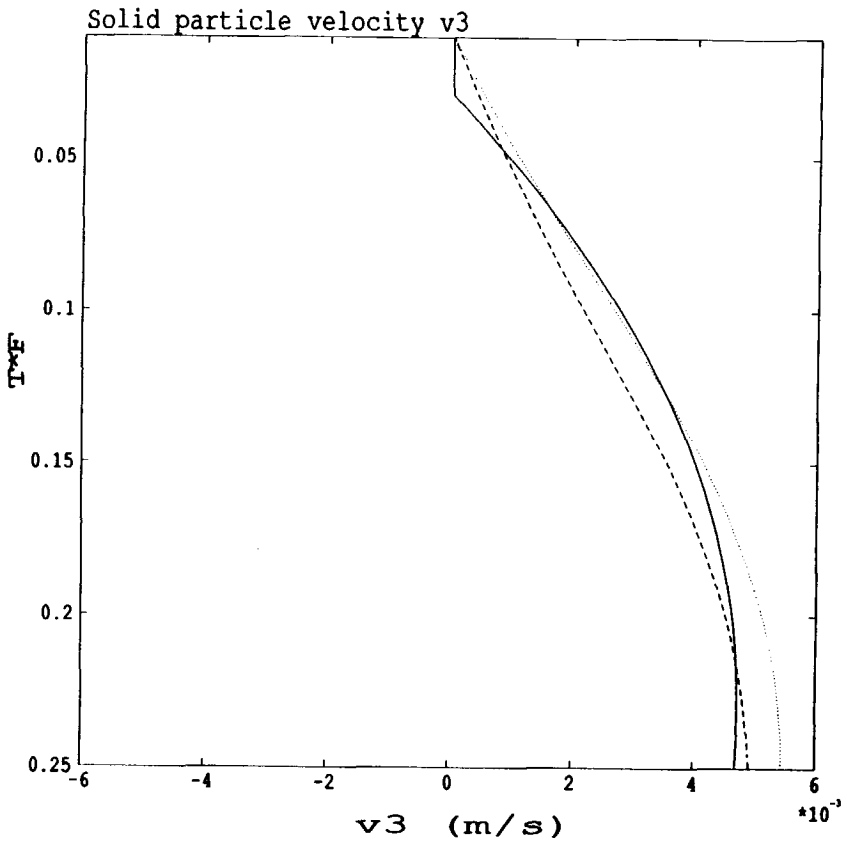

Figure 13.21: The vertical component of the solid particle velocity for the receiver in the solid for the volume injection rate strip source of infinite extent. The solid line is the Cagniard-De Hoop solution, the dashed line the Cartesian finite-element solution and the dotted line the Face finite-element solution.

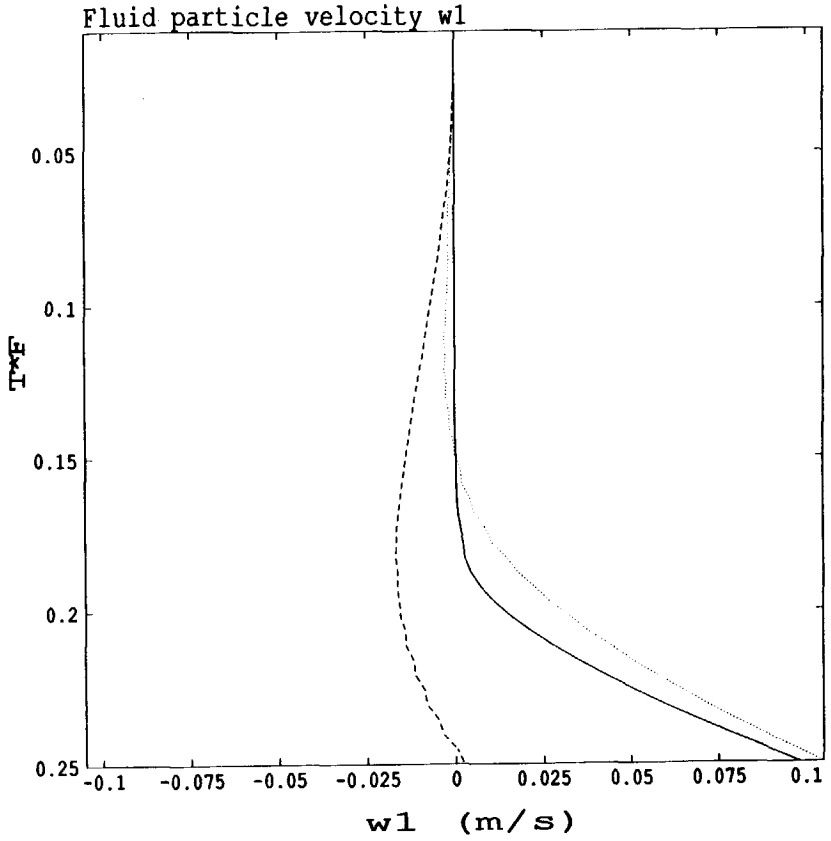

Figure 13.22: The horizontal component of the fluid particle velocity for the receiver in the fluid for the volume injection rate strip source of finite extent. The solid line is the Cagniard-De Hoop solution, the dashed line the Cartesian finite-element method solution and the dotted line the Face finite-element method solution. have been used.

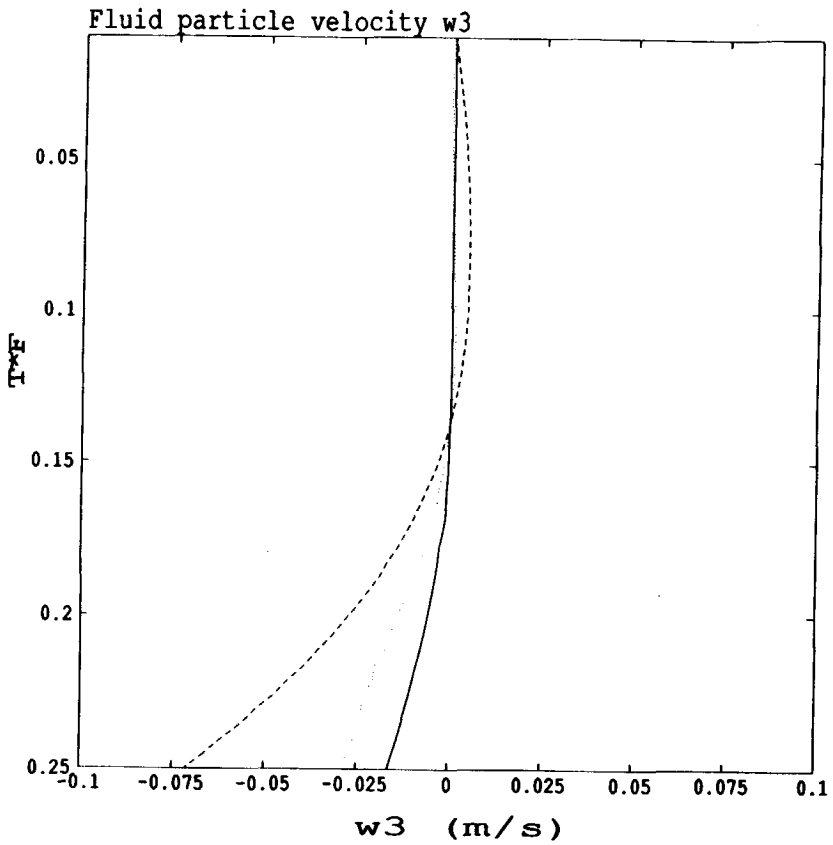

Figure 13.23: The vertical component of the fluid particle velocity for the receiver in the fluid for the volume injection rate strip source of finite extent. The solid line is the Cagniard-De Hoop solution, the dashed line the Cartesian finite-element method solution and the dotted line the Face finite-element method solution.

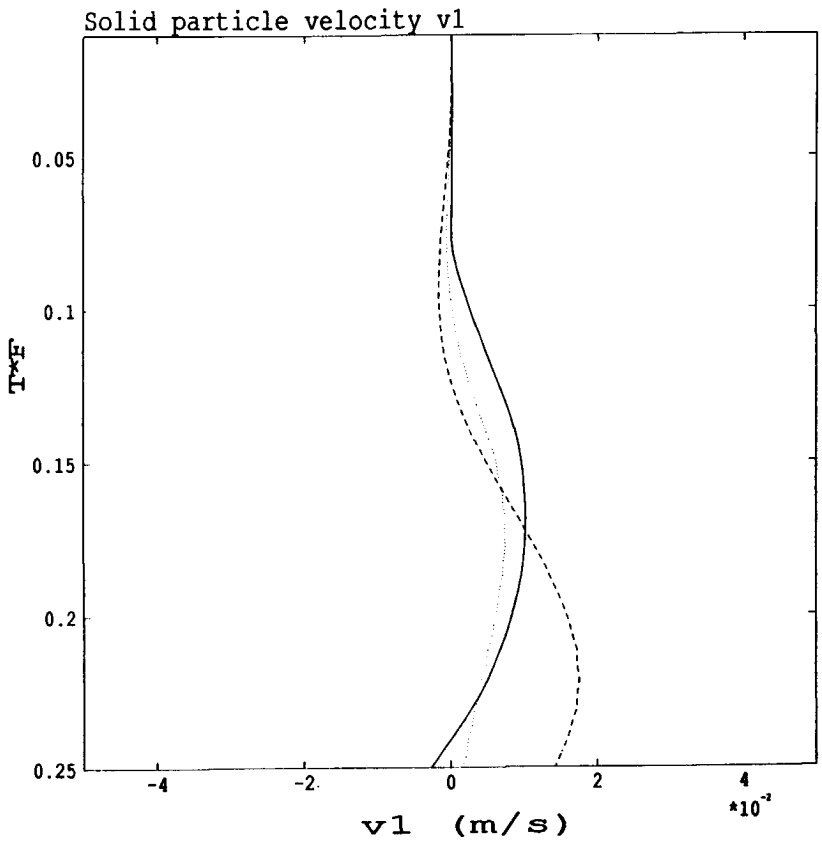

Figure 13.24: The horizontal component of the solid particle velocity for the receiver in the solid for the volume injection rate strip source of finite extent. The solid line is the Cagniard-De Hoop solution, the dashed line the Cartesian finite-element solution and the dotted line the Face finite-element solution.

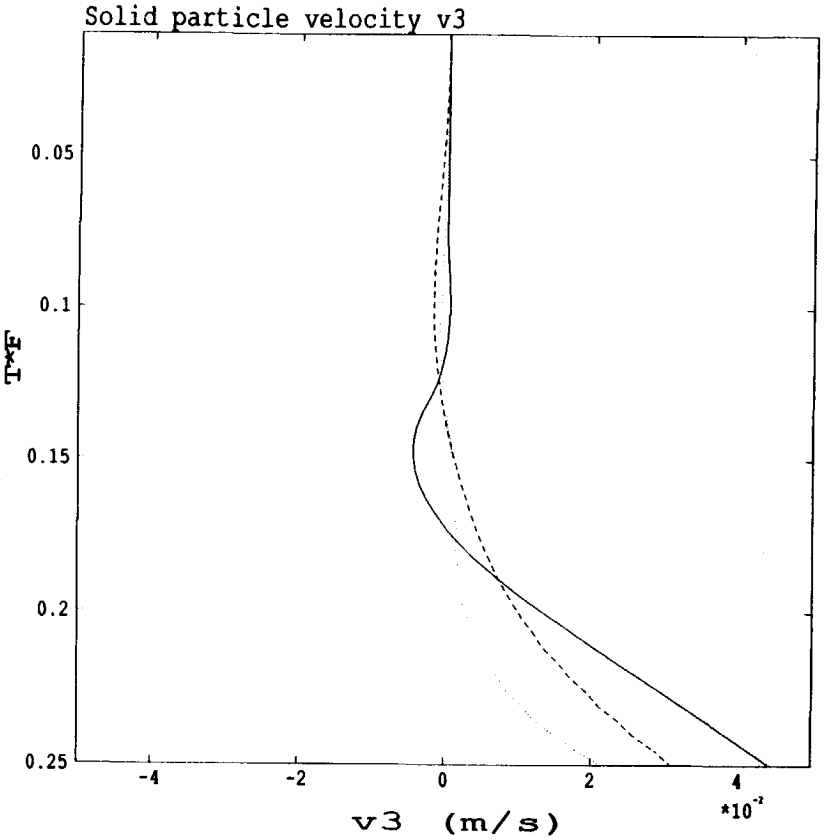

Figure 13.25: The vertical component of the solid particle velocity for the receiver in the solid for the volume injection rate strip source of finite extent. The solid line is the Cagniard-De Hoop solution, the dashed line the Cartesian finite-element solution and the dotted line the Face finite-element solution.

From the results it can be concluded that the finite-element solution gives results that approach the exact solution for the test cases when the mesh size diminishes. For the inhomogeneous configuration, where a relatively large contrast is considered, it is shown that the use of Face elements is superior to the use of Cartesian elements with a required refinement of the mesh near interfaces. The implementation of the Face elements for the stress requires additional local relationships between the expansion coefficients such that symmetry of the global representations is enforced. This problem has not been solved yet.

Appendix A

EVALUATION OF THE ELEMENT INTEGRALS

In this appendix the different integrals that show up in the finite-element formulation of the space-time acoustic wave problem will be evaluated. The relevant domain integrals in R^2 are all extended over a triangle and in R^3 over a tetrahedron; The triangle under consideration will be denoted by $T2$, its vertices by $\{P(0),\ P(1),\ P(2)\}$ and the corresponding barycentric coordinates (i.e., the linear interpolation functions) by $\{\lambda(0), \lambda(1), \lambda(2)\}$. The tetrahedron under consideration will be denoted by $T3$, its vertices by $\{P(0),\ P(1),\ P(2),\ P(3)\}$ and the corresponding barycentric coordinates (i.e., the linear interpolation functions) by $\{\lambda(0),\ \lambda(1),\ \lambda(2),\ \lambda(3)\}$. The integrands in these integrals either do not contain the barycentric coordinates or do contain one of them or the product of two or three of them. Such integrals will, in a more general setting, be evaluated below.

The evaluation of the integrals over $T3$ is most easily carried out by introducing three out of the four variables $\{\lambda(0),\ \lambda(1),\ \lambda(2),\ \lambda(3)\}$ as the variables of integration, and using for the fourth variable the relation $\lambda(0) + \lambda(1) + \lambda(2) + \lambda(3) = 1$. To keep the relevant scheme as flexible as possible, we let $\{I, J, K, L\} =$ cycl $\{0, 1, 2, 3\}$, where "cycl" stands for "cyclic permutation of", take $\lambda(I), \lambda(J)$ and $\lambda(K)$ as the variables of integration, and replace $\lambda(L)$ by $1 - \lambda(I) - \lambda(J) - \lambda(K)$.

Similarly, for the evaluation of the integrals over $T2$ we introduce two out of the three variables $\{\lambda(0), \lambda(1), \lambda(2)\}$ as the variables of integration, and use for

the third variable the relation $\lambda(0)+\lambda(1)+\lambda(2)=1$. To keep also this scheme as flexible as possible, we let $\{I,J,K\}=$ cycl $\{0,1,2\}$, take $\lambda(I)$ and $\lambda(J)$ as the variables of integration, and replace $\lambda(K)$ by $1-\lambda(I)-\lambda(J)$.

Integral over $T3$ containing no barycentric coordinate in the integrand

The case where the integrand over $T3$ contains no barycentric coordinate has as a typical example the volume V of $T3$. For this we obtain

$$\begin{aligned} V &= \int_{x\in T3} dx_1dx_2dx_3 \qquad (A.1)\\ &= \frac{\partial(x_1,x_2,x_3)}{\partial(\lambda(I),\lambda(J),\lambda(K))}\int_0^1 d\lambda(K)\int_0^{1-\lambda(K)} d\lambda(J)\int_0^{1-\lambda(K)-\lambda(J)} d\lambda(I), \end{aligned}$$

in which $\partial(x_1,x_2,x_3)/\partial(\lambda(I),\lambda(J),\lambda(K))$ denotes the three-dimensional Jacobian of the transformation from $\{x_1,x_2,x_3\}$ to $\{\lambda(I),\lambda(J),\lambda(K)\}$ as the variables of integration. Carrying out the integrations at the right-hand side, we arrive at

$$V=\frac{\partial(x_1,x_2,x_3)}{\partial(\lambda(I),\lambda(J),\lambda(K))}(1/6) \qquad (A.2)$$

or

$$\frac{\partial(x_1,x_2,x_3)}{\partial(\lambda(I),\lambda(J),\lambda(K))}=6V. \qquad (A.3)$$

This expression for the three-dimensional Jacobian is used in the further evaluations of integrals over $T3$.

Integral over $T2$ containing no barycentric coordinate in the integrand

A typical example where the integrand over $T2$ contains no barycentric coordinate is the area A of $T2$. For this we obtain, assuming that $T2$ lies in the x_1,x_2- plane,

$$\begin{aligned} A &= \int_{x\in T2} dx_1dx_2 \qquad (A.4)\\ &= \frac{\partial(x_1,x_2)}{\partial(\lambda(I),\lambda(J))}\int_0^1 d\lambda(J)\int_0^{1-\lambda(J)} d\lambda(I) \end{aligned}$$

in which $\partial(x_1,x_2)/\partial(\lambda(I),\lambda(J))$ denotes the two-dimensional Jacobian of the transformation from $\{x_1,x_2\}$ to $\{\lambda(I),\lambda(J)\}$ as the variables of integration. Car-

rying out the integrations at the right-hand side, we arrive at

$$A = \frac{\partial(x_1, x_2)}{\partial(\lambda(I), \lambda(J))}(1/2) \tag{A.5}$$

or

$$\frac{\partial(x_1, x_2)}{\partial(\lambda(I), \lambda(J))} = 2A. \tag{A.6}$$

This expression for the two-dimensional Jacobian is used in the further evaluations of integrals over $T2$.

Integrals over $T3$ containing the barycentric coordinates in the integrand

For the typical integral over $T3$ that contains the barycentric coordinates in its integrand we consider

$$\begin{aligned} I3(a,b,c,d) &= \int_{\boldsymbol{x}\in T3} [\lambda(I)]^a [\lambda(J)]^b [\lambda(K)]^c [\lambda(L)]^d dx_1 dx_2 dx_3 \\ &= 6V \int_0^1 d\lambda(K) \int_0^{1-\lambda(K)} d\lambda(J) \int_0^{1-\lambda(K)-\lambda(J)} \\ &\quad [\lambda(I)]^a [\lambda(J)]^b [\lambda(K)]^c [1-\lambda(I)-\lambda(J)-\lambda(K)]^d d\lambda(I) \\ &\quad \text{with } a>0, b>0, c>0, d>0, \end{aligned} \tag{A.7}$$

where (A.3) has been used to change from $\{x_1, x_2, x_3\}$ to $\{\lambda(I), \lambda(J), \lambda(K)\}$ as the variables of integration. Obviously,

$$I3(0,0,0,0) = V. \tag{A.8}$$

Integration by parts in the integral with respect to $\lambda(I)$ yields

$$\begin{aligned} &\int_0^{1-\lambda(K)-\lambda(J)} [\lambda(I)]^a [\lambda(J)]^b [\lambda(K)]^c [1-\lambda(I)-\lambda(J)-\lambda(K)]^d d\lambda(I) \\ &= (a+1)^{-1} d \int_0^{1-\lambda(K)-\lambda(J)} [\lambda(I)]^{a+1} [\lambda(J)]^b [\lambda(K)]^c \\ &\quad [1-\lambda(I)-\lambda(J)-\lambda(K)]^{d-1} d\lambda(I). \end{aligned} \tag{A.9}$$

Using (A.9) in (A.7) we obtain the recurrence relation

$$I3(a,b,c,d) = (a+1)^{-1} d\, I3(a+1,b,c,d-1). \tag{A.10}$$

Since (A.7) is completely symmetrical in all its parameters, (A.10) holds for the increase of any of the four parameters by one and decreasing any other parameter by one. Using the property of the factorial function

$$(a+1)! = (a+1)(a)! \text{ with } 0! = 1, \tag{A.11}$$

the recurrence relation (A.10) is satisfied by taking for $I3(a,b,c,d)$ the expression

$$I3(a,b,c,d) = \frac{a!b!c!d!}{(a+b+c+d+p)!}p!V, \tag{A.12}$$

where p is as yet arbitrary and (A.8) has been taken into account. Using (A.8) again, it also follows that

$$\begin{aligned} I3(a,b,c,d+1) &= I3(a,b,c,d) - I3(a+1,b,c,d) \\ &\quad - I3(a,b+1,c,d) - I3(a,b,c+1,d). \end{aligned} \tag{A.13}$$

Substitution of (A.13) in (A.12) leads to

$$p = 3. \tag{A.14}$$

Collecting the results, we arrive at

$$I3(a,b,c,d) = \frac{a!b!c!d!3!}{(a+b+c+d+3)!}V. \tag{A.15}$$

This formula can also be found in Zienkiewicz and Taylor (1989, p.139).

Integrals over $T2$ containing the barycentric coordinates in the integrand

For the typical integral over $T2$ that contains the barycentric coordinates in its integrand we consider

$$\begin{aligned} I2(a,b,c) &= \int_{x \in T2} [\lambda(I)]^a [\lambda(J)]^b [\lambda(K)]^c dx_1 dx_2 \\ &= 2A \int_0^1 d\lambda(J) \int_0^{1-\lambda(J)} [\lambda(I)]^a [\lambda(J)]^b [1-\lambda(I)-\lambda(J)]^c d\lambda(I) \\ &\quad \text{with } a > 0, b > 0, c > 0, \end{aligned} \tag{A.16}$$

where (A.6) has been used to change from $\{x_1, x_2\}$ to $\{\lambda(I), \lambda(J)\}$ as the variables of integration. Obviously,

$$I2(0,0,0) = A. \tag{A.17}$$

Integration by parts in the integral with respect to $\lambda(I)$ yields

$$\int_0^{1-\lambda(J)} [\lambda(I)]^a [\lambda(J)]^b [1-\lambda(I)-\lambda(J)]^c d\lambda(I) \tag{A.18}$$

$$= (a+1)^{-1} c \int_0^{1-\lambda(J)} [\lambda(I)]^{a+1} [\lambda(I)]^b [1-\lambda(I)-\lambda(J)]^{c-1} d\lambda(I).$$

Using (A.18) in (A.16) we obtain the recurrence relation

$$I2(a,b,c) = (a+1)^{-1} c \; I2(a+1,b,c-1). \tag{A.19}$$

Since (A.16) is completely symmetrical in all its parameters, (A.19) holds for the increase of any of the four parameters by one and decreasing any other parameter by one. Using the property of the factorial function

$$(a+1)! = (a+1)(a)! \text{ with } 0! = 1, \tag{A.20}$$

the recurrence relation (A.19) is satisfied by taking for $I2(a,b,c)$ the expression

$$I2(a,b,c) = \frac{a!b!c!}{(a+b+c+p)!} p! A, \tag{A.21}$$

where p is as yet arbitrary and (A.17) has been taken into account. Using (A.17) again, it also follows that

$$I2(a,b,c+1) = I2(a,b,c) - I2(a+1,b,c) - I2(a,b+1,c). \tag{A.22}$$

Substitution of (A.22) in (A.21) leads to

$$p = 2. \tag{A.23}$$

Collecting the results, we arrive at

$$I2(a,b,c) = \frac{a!b!c!2!}{(a+b+c+2)!} A. \tag{A.24}$$

This formula can also be found in Zienkiewicz and Taylor (1989, p.139).

REFERENCES

ACHENBACH, J.D. 1973. *Wave propagation in elastic solids.* Amsterdam: North Holland Publ. Co.

AKI, K., and RICHARDS, P.G. 1980. *Quantitative seismology.* San Francisco: W.H. Freeman & Co.

ALTERMAN, Z.S., and KARAL, F.C. 1968. Propagation of elastic waves in layered media by finite-difference methods. *Bulletin of the Seismological Society of America* 58:367-398.

ALTERMAN, Z.S., and LOEWENTHAL, D. 1970. Seismic waves in a quarter and three-quarter plane. *Geophysical Journal of the Royal Astronomical Society* 20:101-126.

BAJER, C.I. 1986. Triangular and tetrahedral space-time finite elements in vibration analysis. *International Journal for Numerical Methods in Engineering* 23:2031-2048.

BELLMAN, R., and KALABA, R. 1956. On the principle of invariant imbedding and propagation through inhomogeneous media. *Proceedings of the National Academy of Sciences (USA)* 42:629-632.

BOORE, D.M. 1972. Finite-difference methods for seismic wave propagation in heterogeneous media. In *Methods of computational physics,* eds. B. Alder, S. Fernback, and M. Rotenberg, pp. 1-37. New York: Academic Press Inc.

BROMWICH, T.J.I'A. 1902. Note on the wave surface of a dynamical medium, aeolotropic in all respects. *Proceedings of the London Mathematical Society* 34:307-321.

DHATT, G., and TOUZOT, G. 1984. *The finite element method displayed.* New York: John Wiley & Sons, Inc.

EMERMAN, S.H., SCHMIDT, W., and STEPHEN, R.A. 1982. An implicit finite-difference formulation of the elastic wave equation. *Geophysics* 47:1521-1526.

GUPTA, P.K., BENNETT, L.A., and RAICHE, A.P. 1987. Hybrid calculations of the three-dimensional electromagnetic response of buried conductors. *Geophysics* 52:301-306.

VAN DER HIJDEN, J.H.M.T. 1987. *Propagation of transient elastic waves in stratified anisotropic media.* Amsterdam: North Holland Publ. Co.

DE HOOP, A.T. 1985. A time-domain energy theorem for scattering of plane acoustic waves in fluids. *Journal of the Acoustical Society of America* 77:11-14.

—- 1985. A time-domain energy theorem for the scattering of plane elastic waves. *Wave Motion* 7:569-577.

—- 1988. Large-offset approximations in the modified Cagniard method for computing synthetic seismograms: a survey. *Geophysical Prospecting* 36:465-477.

—- 1988. Time-domain reciprocity theorems for acoustic wave fields in fluids with relaxation. *Journal of the Acoustical Society of America* 84:1877-1882.

DE HOOP, A.T., and VAN DER HIJDEN, J.H.M.T. 1985. Seismic waves generated by an impulsive point source in a solid/fluid configuration with a plane boundary. *Geophysics* 50:1083-1090.

DE HOOP, A.T., and STAM, H.J. 1988. Time-domain reciprocity theorems for the elastodynamic wave fields in solids with relaxation and their application to inverse problems. *Wave Motion* 10:479-489.

ILAN, A. 1978. Stability of finite difference schemes for the problem of elastic wave propagation in a quarter plane. *Journal of Computational Physics* 29:389-403.

ILAN, A., and LOEWENTHAL, D. 1976. Instability of finite-difference schemes due to boundary conditions in elastic media. *Geophysical Prospecting* 24:431-453.

ILAN, A., UNGAR, A., and ALTERMAN, Z.S. 1975. An improved representation of boundary conditions in finite-difference schemes for seismological problems. *Geophysical Journal of the Royal Astronomical Society* 43:727-745.

KELLY, K.R., WARD, R.W., TREITEL, S., and ALFORD, R.M. 1976. Synthetic seismograms: a finite-difference approach. *Geophysics* 41:2-27.

KUMMER, B., and BEHLE, A. 1982. Second-order finite-difference modeling of SH-wave propagation in laterally inhomogeneous media. *Bulletin of the Seismological Society of America* 72:793-808.

LAMB, H. 1957. *Hydrodynamics.* 6th ed. Cambridge: Cambridge Univ. Press.

LEE, K.H., PRIDMORE, D.F., and MORRISON, H.F. 1981. A hybrid three-dimensional electromagnetic modeling scheme. *Geophysics* 46:796-805.

LOVE, A.E.H. 1959. *A treatise on the mathematical theory of elasticity.* 4th ed. Cambridge: Cambridge Univ. Press.

MARFURT, K.J. 1984. Accuracy of finite-difference and finite-element modeling of the scalar and elastic wave equations. *Geophysics* 49:533-549.

MIKLOWITZ, J. 1978. *The theory of elastic waves and waveguides.* Amsterdam: North Holland Publ. Co.

MITCHELL, A.R. 1977. Finite element methods in time dependent problems. In *The state of the art in numerical analysis,* ed. D. Jacobs, pp. 671-697. London: Academic Press Inc.

MUR, G., and DE HOOP, A.T. 1985. A finite-element method for computing three-dimensional electromagnetic fields in inhomogeneous media. *IEEE Transactions on Magnetics* MAG-21:2188-2191.

NABER, L. 1980. *Topological methods in Euclidian Spaces.* Cambridge: Cambridge Univ. Press.

NAG FORTRAN LIBRARY MANUAL MARK 13 1988. *Numerical Algorithms Group*. Oxford, subroutine D01AJF.

PAO, Y.H., and MOW, C.C. 1973. *Diffraction of elastic waves and dynamic stress concentrations*. New York: Crane, Russak.

LORD RAYLEIGH 1899. On double refraction. *Scientific Papers 1*. Cambridge: Cambridge Univ. Press, 111-119.

REDDY, J.N. 1986. *Applied functional analysis and variational methods in engineering*. New York: McGraw-Hill Book Co.

SMITH, W.D. 1975. The application of finite-element analysis to body wave propagation problems. *Geophysical Journal of the Royal Astronomical Society* 42:747-768.

STAM, H.J., and DE HOOP, A.T. 1990. Theoretical considerations on a finite-element method for the computation of three-dimensional space-time elastodynamic wave fields. *Wave Motion* 12:67-80.

VIRIEUX, J. 1984. SH-wave propagation in heterogeneous media: Velocity-stress finite-difference method. *Geophysics* 49:1933-1957.

—- 1986. P-SV wave propagation in heterogeneous media: Velocity-stress finite-difference method. *Geophysics* 51:889-901.

WIDDER, D.V. 1946. *The Laplace transform*. Princeton: Princeton Univ. Press.

WILTON, D.T. 1978. Acoustic radiation and scattering from elastic structures. *International Journal for Numerical Methods in Engineering* 13:123-138.

WHITTAKER, E.T., and WATSON, G.N. 1950. *A course of modern analysis*. 4th ed. Cambridge: Cambridge.

ZIENKIEWICZ, O.C., 1983. Finite elements in the time domain. In *State-of-the art surveys on finite element technology*, eds. A.K. Noor, and W.D. Pilkey, pp. 405-449.

ZIENKIEWICZ, O.C., and MORGAN, K. 1983. *Finite elements and approximation.* New York: John Wiley & Sons, Inc.

ZIENKIEWICZ, O.C., WOOD, W.L., HINE, N.W. and TAYLOR, R.L. 1984. A unified set of single step algorithms, Part 1: General formulation and applications. *International Journal for Numerical Methods in Engineering* 20:1529-1552.

ZIENKIEWICZ, O.C., and TAYLOR, R.L. 1989. *The finite element method, Basic formulation and linear problems.* 4th. ed. London: McGraw-Hill Book Co.

SAMENVATTING

De numerieke modellering van akoestische golfproblemen heeft talrijke toepassingsgebieden. Voorbeelden zijn: de exploratiegeofysica, de akoestische beeldvorming voor medische doeleinden en het niet-destructief onderzoek aan mechanische constructies. In al deze toepassingen is men geïnteresseerd in de akoestische golfverschijnselen in ruimte en tijd in sterk inhomogene en mogelijk anisotrope vloeistoffen en vaste stoffen, en de kwantitatieve bepaling van de grootheden die de golfbeweging karakteriseren (de scalaire spanning in vloeistoffen (tegengestelde van de druk), de tensoriële spanning in vaste stoffen en de deeltjessnelheden in beide media), is het uiteindelijke doel. Voor eenvoudige configuraties, zoals de geometrieën die zich schikken in coördinatenstelsels waarin de geldende akoestische golfvergelijkingen separeerbaar zijn, kunnen analytische oplossingen voor golfpropagatie- en verstrooiingsproblemen worden geconstrueerd. Voor meer gecompliceerde configuraties is het echter noodzakelijk van numerieke methoden gebruik te maken. Eén van de numerieke methoden die bekend staat om haar eenvoud is de eindige-differentiemethode. Hoewel de eindige-differentiemethode met haar coördinaatlijnroosterstructuur het voordeel heeft van de eenvoud, geeft zij moeilijkheden met het modelleren van willekeurige randen en discontinuïteitsvlakken in de materiaaleigenschappen die niet samenvallen met zo'n rooster. De willekeurig georienteerde randen en vlakken kunnen echter zonder moeilijkheden worden aangepakt met de meer gecompliceerde eindige-elementenmethode, die niet beperkt is tot een speciale roosterstructuur.

Vanwege de beperkingen van de geheugenruimte en de rekentijd op de computer, moet men het domein van numerieke berekening, zowel in de eindige-differentiemethode als in de eindige-elementenmethode, zo veel mogelijk beperken. Nu zijn er voor een éénduidige oplossing van het akoestische golfprobleem in een

begrensd gebied D naast de daarin geldende differentiaalvergelijkingen ook voorwaarden nodig op de rand ∂D van D. Om golfbewegingen te berekenen die zich nog niet zo ver van de bronnen af hebben uitgebreid, voldoen de juiste nulcondities op ∂D mits ∂D buiten het gebied wordt gekozen waar de golfbeweging tot dusver is doorgedrongen. Toegestane nulcondities zijn van het Dirichlet- of van het Neumanntype. Het onderscheid is als volgt. Voor de randvoorwaarde van het Neumanntype wordt de normale component van de deeltjessnelheid voorgeschreven op de rand die grenst aan een vloeistof en de spanning wordt voorgeschreven op het gedeelte van de rand die grenst aan een vaste stof. Voor de randvoorwaarde van het Dirichlettype wordt de scalaire vloeistof spanning voorgeschreven op het gedeelte van de rand dat grenst aan een vloeistof, terwijl de deeltjessnelheid wordt voorgeschreven op het gedeelte van de rand dat grenst aan een vaste stof. In de meeste gevallen wordt het domein van numerieke berekening D voor zo'n procedure veel te groot. Dientengevolge moet het domein D kleiner worden genomen en moet men er rekening mee houden, dat de golfbeweging de rand ∂D heeft bereikt en dat door ∂D heen akoestische straling plaats vindt van D af. Het type randvoorwaarde dat deze straling in het oneindige buitengebied met eenvoudige akoestische eigenschappen modelleert, is een belangrijk onderwerp van het huidige theoretische onderzoek.

Om randvoorwaarden te construeren die de straling van golven door ∂D heen van D af modelleren, wordt het domein D van de eindige-elementenberekening ingebed in een omringend medium, de "inbedding". In onze analyse nemen wij een ruimte-tijdreciprociteitstheorema van het tijdconvolutietype als uitgangspunt. Dit wordt toegepast op de gediscretiseerde versie $[D]$ van D en zijn inbedding D_0. In een reciprociteitstheorema van dit type komen twee toestanden voor die in één en hetzelfde domein in ruimte en tijd kunnen bestaan. We identificeren één van de twee toestanden met het werkelijke akoestische golfveld, terwijl het andere wordt beschouwd als een hulptoestand die als passend te kiezen overblijft. Voor de bronnen die in de hulptoestand voorkomen, wordt een rij van gelokaliseerde bronverdelingen gekozen die gedefinieerd zijn op $[D]$. Elk van deze bronnen is gedefinieerd op één van de elementaire gebieden waarin D is onderverdeeld en is gelijk aan nul buiten zo'n gebied. De hulptoestand heeft, evenals het werkelijke golfveld, geen bronnen in de inbedding D_0. Voor de medi-

umeigenschappen in $[D]$ en D_0 van de hulptoestand worden die van de inbedding genomen. De ermee overeenkomende golfveldgrootheden, die gerelateerd zijn aan de gelokaliseerde bronverdelingen in een medium zoals de inbedding, zijn onze "gediscretiseerde" Greense functies. Er wordt aangenomen, dat deze analytisch kunnen worden bepaald. Substitutie van deze keuzen voor de hulptoestand in het reciprociteitstheorema levert relaties op tussen de waarden van de akoestische golfveldgrootheden, gewogen over ieder van de definitiegebieden van de gelokaliseerde bronverdelingen en de contrast- en primaire bronnen in $[D]$. Deze relaties dienen als de niet-lokale randvoorwaarden voor onze hybride eindige-elementenmethode.

De combinatie van de twee oplossingsmethoden, een eindige-differentie- of een eindige-elementenmethode voor het begrensde domein met een gecompliceerd medium en een analytische voor de eenvoudige inbedding, staat bekend als een hybride methode. In dit proefschrift wordt zo'n methode gepresenteerd, die numeriek akoestische golfproblemen in ruimte en tijd oplost in een configuratie die bestaat uit vloeistof- en/of vastestofgedeelten. De vloeistoffen en de vaste stoffen worden lineair, lokaal en instantaan reagerend genomen en tijdinvariant in hun mechanische gedrag. In één of ander begrensd domein D^{SC} wordt het medium willekeurig inhomogeen en anistroop ondersteld. De inbedding van dit domein is een vloeistof of een vaste stof met zulke eenvoudige eigenschappen, dat haar Greense functie geconstrueerd kan worden met behulp van analytische methoden.

De akoestische golfvelden in het vloeistofdomein worden gekarakteriseerd door hun deeltjessnelheid en hun scalaire spanning. De akoestische golfvelden in de vaste stof worden gekarakteriseerd door de deeltjessnelheid en hun tensoriële spanning. Deze grootheden worden beschouwd als de fundamentele toestandsgrootheden. We kiezen het begrensde domein van numerieke berekening D zodanig, dat $D^{SC} \subset D$. De berekening van de golfvelden in D wordt uitgevoerd door een eindige-elementenmethode die in het bijzonder geschikt is om de voorwaarden op willekeurig gevormde randen en vlakken van het vaste/vaste stof-, vloeistof/vloeistof- en het vaste stof/vloeistoftype te hanteren.

In een aantal technische problemen, meestal van het statische, d.w.z. tijdonafhankelijke, type kan de eindige-elementenmethode gebaseerd worden op een

variationeel principe. Zo'n principe zegt, dat de oplossing van het probleem een stationair punt is van een passend geconstrueerde functionaal (bijvoorbeeld het minimum van de potentiële energie opgeslagen in het systeem). Voor problemen waarvoor geen variationeel principe beschikbaar is, wordt de methode van de gewogen residuen gewoonlijk benut om tot een eindige-elementenformulering te komen. Bij onze aanpak zullen we als uitgangspunt een akoestisch ruimte-tijd reciprociteitstheorema van het tijdcorrelatietype gebruiken. In een reciprociteitstheorema van dit type komen twee toestanden voor die in één en hetzelfde domein in ruimte en tijd kunnen bestaan. We identificeren één van de twee toestanden met het werkelijke akoestische golfveld waarvoor een numerieke benadering moet worden geconstrueerd, terwijl het andere wordt beschouwd als een hulptoestand die passend te kiezen overblijft. We laten zien, dat speciale keuzen voor de hulptoestanden leiden tot een zekere weegprocedure toegepast op de vergelijkingen die de golfbeweging bepalen, d.w.z. de bewegingsvergelijking en de deformatievergelijking. Vervolgens worden er speciale lokale representaties voor het akoestische golfveld ontwikkeld, die speciaal geschikt zijn voor het hanteren van de voorwaarden die gelden op discontinuïteitsvlakken in sterk inhomogene media.

Met het oog op de tijdinvariantie van de configuratie waarin het golfveld voorkomt, discretizeren we de geometrie in elementaire subdomeinen die cylindrisch zijn in de tijdrichting in de vier dimensionale ruimte-tijd. In de driedimensionale ruimte nemen we het tetraeder als het elementaire subdomein. Met deze keuze bestaat de gediscretiseerde geometrie uit prisma's in ruimte-tijd. In overeenstemming hiermee, worden de lokale functies genomen als het produkt van een functie van de plaats en een functie van de tijd. De hoekpunten van de tetraeders vormen de knooppunten van de plaatsdiscretisatie. In ieder hoekpunt van een tetraeder dat samenvalt met een knooppunt dat zich niet op een discontinuïteitsvlak in de materiaaleigenschappen bevindt (een enkelvoudig knooppunt), worden de vectoriële en tensoriële toestandsgrootheden gerepresenteerd door hun componenten ten opzichte van een gekozen Cartesiaans achtergrondassenstelsel. In ieder hoekpunt van een tetraeder dat samenvalt met een knooppunt dat zich op een vlak van discontinuïteit in de materiaaleigenschappen bevindt (een meervoudig knooppunt), worden de vectoriële en tensoriële

toestandsgrootheden die continu zijn door dit vlak heen opnieuw gerepresenteerd ten opzichte van het gekozen Cartesiaanse achtergrondassenstelsel, terwijl diegenen die één of meer componenten hebben die een eindige sprong kunnen vertonen door dit vlak heen, worden gerepresenteerd ten opzichte van passend gekozen lokale basisvectoren. De richtingen van deze lokale basisvectoren worden zodanig gekozen, dat er in de resulterende representaties van de toestandsgrootheden exact aan de continuïteitsvoorwaarden op het vlak van discontinuïteit in de materiaaleigenschappen wordt voldaan (d.w.z. in machineprecisie).

Voor een éénduidige (numerieke) oplossing van het golfprobleem in het inhomogene en anisotrope begrensde domein van numerieke berekening D hebben we randvoorwaarden nodig op zijn buitenrand ∂D. In onze hybride methode representeren we de toestandsgrootheden op ∂D door integraalbetrekkingen die de gediscretiseerde Greense functies van de inbedding en de gelokaliseerde bronverdelingen die de inhomogeniteiten in D representeren bevatten. Veronderstel, dat de inbedding een vloeistof is, dan definiëren we in de vloeistofgedeelten van D^{SC} contrastvolumebronnen die van nul verschillen in die subdomeinen waar de vloeistofeigenschappen een contrast vertonen ten opzichte van de inbedding. Omdat de invloed van de vastestofgedeelten in D^{SC} niet kan worden beschreven met behulp van contrastvolumebronnen, wordt deze gerepresenteerd door oppervlakte bronnen van het vloeistoftype op de vloeistof/vaste stof overgangen. Als de inbedding een vaste stof is, definiëren we in de vastestofgedeelten van D^{SC} contrastvolumebronnen die van nul verschillen in die subdomeinen waar de vastestofeigenschappen een contrast vertonen ten opzichte van de inbedding en modelleren we de invloed van de vloeistof gedeelten in D^{SC} met behulp van oppervlaktebronnen van het vastestoftype op de vaste stof/vloeistof overgangen. De relevante integraalvoorstellingen volgen uit de akoestische ruimtetijdreciprociteitstheorema's van het tijdconvolutietype door in deze theorema's hulptoestanden te kiezen die overeenkomen met geschikte gelokaliseerde bronverdelingen (de gediscretiseerde Greense functies) van de inbedding. Voor een homogene inbedding kunnen deze analytisch worden berekend. Om het akoestische golfveld in de inbedding te bepalen, benutten we daarna de oppervlakte- en volumebronintegraalrepresentaties, gebruik makend van de nu bekende waarden van het akoestische golfveld op de randen van de oppervlaktebronnen en in de

contrastvolumebrondichtheden.

Numerieke resultaten illustreren de methode voor een aantal tweedimensionale configuraties. Voor de gevallen van een oppervlaktebron van eindige breedte op de rand van een halfoneindige vloeistof of een halfoneindige vaste stof en op het scheidingsvlak van een halfoneindige vloeistof en een halfoneindige vaste stof is ook de analytische oplossing van het probleem bepaald met behulp van de Cagniard-De Hoop methode. Deze gevallen dienen als test voor de correctheid en de nauwkeurigheid van de numerieke programmatuur.